Electron-Transfer Processes at Semiconductor/ Liquid Interfaces and Metal/Nanogap Junctions

Thesis by

Florian Gstrein

In Partial Fulfillment of the Requirements
For the Degree of Doctor of Philosophy

California Institute of Technology
Pasadena, California

2004

(Defended January 20, 2004)

This thesis is dedicated to my uncle

Hofrat
Dr. H. Peter Wagner
Meteorologist
(1944 - 2001)

Acknowledgments

A wise and slightly cynical postdoctoral scholar in the Lewis group once told me as he was pacing up and down the noble hallways of Noyes, “The only thing people are really interested in when reading your thesis are the acknowledgements. So acknowledge everyone and everything!” If this statement is correct, I had better do justice to the expectations of my readership! I have done my best in compiling the following list of people who all have made important contributions to my Ph.D. thesis and I apologize for any omissions.

It gives me great pleasure to thank my advisor, Prof. Nathan S. Lewis, for his outstanding mentorship and friendship. Nate is an exceptional advisor, inspiring scientist and without a shadow of a doubt the smartest man I have ever met. The most important thing I have learned from Nate is that experimental science can only be done by approaching a scientific question thoroughly and carefully from various angles and by carrying out the appropriate control experiments.

Dr. Helfried Näfe (Max Planck Institute for Metals Research, Stuttgart, FRG) and Dr. Dimitrij I. Bronin (Institute of High-Temperature Electrochemistry, Russian Academy of Sciences, Ural Branch, Ekaterinburg, Russian Federation) were the most influential mentors in my pre-Caltech days. Their shining example and integrity as researchers left me with no other choice but to pursue academic research.

I would like to thank my co-advisors, Prof. Michael Roukes and Prof. James C. Hone, who is now at Columbia University. Michael not only allowed me to work in his magnificent laboratory in the Department of Physics, but he also fully integrated me into his research group. Not many outsiders belong to the inner circle of the Roukes group, and I am grateful for Michael’s genuine and continued interest in my research project. Jim, the *force extraordinaire* behind the NIRT project, pursued together with me many projects and

I am looking forward to our collaboration on various levels in the future. I also learned from Jim that you can buy an entire lab on eBay, but that you cannot “buy” a car from him.

There are many members of the Lewis and Roukes group who have worked with me closely on several projects. Tom Hamann did an outstanding job in synthesizing many of the osmium compounds for the ZnO project and in studying their self-exchange properties. Dr. William Royea and David Michalak worked with me closely on studies of the surface recombination behavior of silicon. In particular, Dave carried out most of the rf-conductivity measurements. I would like to thank Prof. Adrian Lew (Stanford University) and Dr. Reiner Nürnberg (Weierstrass Institute, Berlin) for many useful discussions regarding the TeSCA simulations. The NIRT project was a collaborative effort of many people. Jim’s leading role has already been mentioned. My friend Dr. Srivatsan Nagarajan came up with many original ideas regarding this project and contributed in setting up the early instrumentation. Working with Leon Bellan, who did his senior thesis work with me, was the most pleasant experience I had at Caltech. Leon contributed greatly in setting up the measurement system in its present form. I would also like to thank Ali Hussain (Scherer group), Carol Garland (TEM work) and Drs. Hongxin Tang, Darron Young, Hidehiro Yoshida, and Henk Postma (all Roukes group) for their helping hands with many NIRT experiments.

I am also indebted to many Lewis group members present and past for good discussions and their support, especially, Dr. Shawn “Sean” Briglin, Lauren “Lorraine” Webb, Jordan Katz, Prof. George Coia (the wise old postdoc), Prof. Sami Anz, Dr. Will Royea, Dr. Rob Rossi, Dr. Glen Walker, Prof. Mike Freund, Dr. Bruce Brunschwig, Dr. Jae-Joon Lee, Dr. Arnel Fajardo and two exceptional administrative assistants of Nate’s, Nannette Pettis and Sherry Feick. Among all Lewis groupies, Mr. David J. Michalak stands out as an exceptional scientist, co-worker, film maker, co-actor, and great friend.

I would like to thank the remaining members of my Ph.D. committee, Prof. Rudy Marcus for all the beautiful theory without which none of the experimental work in this thesis would have made much sense and Prof. Bill Goddard for two exceptionally well-taught classes, which convinced me that I better stay far away from computational chemistry. Many of the experiments would have been impossible without Mike Roy and Guy Duremberg (Instrument Shop), Tom Dunn (Electrical Shop), and the great Nils Apslund (Roukes Group).

Last but certainly not least I would like to thank the many outstanding people that I met during graduate school for their friendship, love and spiritual support. In no particular order these individuals are Adri Lew and Patri Strass (now at Stanford), Alex Bäcker, Eva Peral, Veronica & Pablito (all Pasadena), Julian Chaubell & Nance (Pasadena), Mathias Libedinsky (now in Jerusalem), Ronen Almog (now at the Technion in Haifa), Mathias Zielonka, Alejandra Engelberg, and Sebastian (all Pasadena), Eva Rüba (now in Vienna), Christoph Sonnlechner (now in Vienna), Ines Schwetz (now in Graz), and my dear landlords and friends Robert and Carolyn Volk (San Marino).

Finally, I would like to thank my family back in Austria, first and foremost my parents, Hans-Jürgen & Edith Gstrein, and my sister, Marlis, for their relentless moral support and good humor during all the ups (and the rare downs) of the past five years.

Abstract

This thesis presents recent progress made in the understanding of charge-transfer kinetics and charge-carrier dynamics at semiconductor/liquid interfaces and presents a study of the charge-transport characteristics of nanostructured electrodes for the study of electron tunneling through molecules.

It is shown that n-ZnO/H_2O-A/A^- junctions (where A/A^- corresponds to $[Fe(CN)_6]^{3-/4-}$, $[Co(bpy)_3]^{3+/2+}$, or $[OsL_2L']^{3+/2+}$) display energetic and kinetic behavior of unprecedented ideality for the experimental determination of robust rate constants for electron transfer from n-type semiconductors to electron acceptors in solution. The reorganization energies of these redox couples were for the first time determined independently through NMR line-broadening experiments. Semiconductor/liquid contacts with an electrochemical driving force larger than the driving force at the point of optimum exoergicity showed lower rate constants than contacts with a lower driving force. The rate constant for charge transfer of the junction with the highest driving force increased when the driving force was lowered. This was done by decreasing the pH of the contacting electrolyte, which shifted the conduction-band edge of the OH-terminated n-ZnO to more positive values. This indicates that the contact with the largest driving force operated in the inverted regime of charge transfer. The rate constant of the contact with the lowest driving force ($\Delta G^{o'} << 0.7$ eV), on the other hand, decreased when the conduction-band edge was shifted to more positive values, which indicates that the low-driving force contact operated in the normal regime of charge transfer. These results provide for the first time a direct and credible experimental indication that semiconductor/liquid contacts can indeed operate in the inverted regime. Semiconductor/liquid contacts, which had a similar driving force but different reorganization energies showed the expected dependence of the rate constant on the reorganization energy consistent with Marcus theory.

The experimentally observed charge-carrier decay dynamics for a variety of chemically treated Si surfaces can be consistently explained with reference to their interfacial energetics. Low effective surface recombination velocities (*SRVs*) were observed for systems capable of undergoing interfacial charge-transfer reactions that produce an accumulation of holes or an accumulation of electrons at the Si surface. In conjunction with near-surface channel conductance measurements, it was revealed that the formation of an accumulation of holes or the formation of an accumulation of electrons and not a reduced density of electrical trap sites on the surface, is primarily responsible for the long charge-carrier lifetimes observed for Si surfaces. Digital simulations incorporating a generalized Shockley-Read-Hall model for surface recombination revealed that effective surface recombination velocities < 10 cm s^{-1} can be produced by surfaces having a density of electrical traps as large as 10^{12} cm^{-2} provided that the surface is in accumulation or inversion due to charge-transfer equilibration with the redox-active electrolyte. Silicon in contact with aqueous fluoride solutions exhibit low *SRV*s. Some reports in the past have suggested that the defect density of Si in acidic solutions is reduced by the protonation of defect sites. Alternatively, this study shows that an accumulation of electrons at the surface can lead to low *SRVs*. The degree of band bending and *SRVs* of Si(111) in contact with a variety of aqueous fluoride solutions were determined for the first time at open circuit conditions. The accumulation of electrons at the surface is responsible for the low effective *SRVs* in NH_4F and buffered HF solutions. The reversible protonation of basic defect sites might be important for the low *SRV* of n-Si(111)/$H_2SO_{4(aq)}$ contacts but plays a minor role in the recombination behavior of Si in contact with aqueous fluoride solutions.

Electromigration-induced breaking of metal nanowires is a promising new method that has recently been employed in the formation of metal-molecule-metal tunnel junctions. The electrical characteristics of unmodified electrodes have not been thoroughly

studied. In this work, the current *vs.* voltage (*J vs. E*) characteristics of electron-tunnel junctions formed by the electromigration of metal nanowires without a molecule bridging the gap were explored in detail. Junctions displayed *J vs. E* characteristics with a variety of shapes and current magnitudes. The low-temperature *J vs. E* curves of some junctions showed regions of zero conductivity near zero bias. Such features were absent in the data collected for other tunnel junctions. These differences notwithstanding, a common pattern was discerned in that the low-bias resistances of the vast majority of the junctions decreased by an order of magnitude or more with increasing temperature. The features detected in this study are consistent with the Coulomb blockade effect. We attribute the blockade behavior to metal atom clusters or islands located in the nano-sized gap region. This assignment is compatible with the mechanism of electromigration. In support of this interpretation, it was found that the low-bias resistance *vs.* temperature curves were well described by Abeles' model for electron tunneling in granular metal junctions. Additional support for the assignment was obtained from TEM studies of gold junctions with chromium adhesion layers, where the images showed the presence of a thin granular film bridging the electrodes.

Table of Contents

Chapter 4. Electron-Transfer Processes at Metal/Nanogap Junctions

List of Figures

List of Tables

CHAPTER 1 *Introduction to Electron-Transfer Processes at Semiconductor/Liquid Interfaces and Metal/Nanogap Junctions*

1.1 OVERVIEW

For a long time, electrochemists have viewed the electrode simply as an electronic conductor of low resistivity that serves as a source or sink of electrons. The influence of charge-transfer kinetics and charge-carrier dynamics at the surface of an electrode have only been vaguely connected to the electronic and energetic properties of individual charge carriers in the electrode and the electronic interaction of that electrode with a redox couple in solution. According to the late Heinz Gerischer (1919-1994), by many considered to be the field's most influential proponent, the modern concept of electrode kinetics is largely due to the introduction of semiconductors as electrode materials and the advent of electron-transfer theory.[1]

This thesis presents recent progress made in our understanding of charge-transfer kinetics and charge-carrier dynamics at semiconductor/liquid interfaces and presents an investigation of the fundamental properties of nanostructured electrodes for the study of electron tunneling through molecular bridges and solvents. In Chapter 2 of this thesis, ZnO (0001) single-crystal electrodes in contact with a series of non-adsorbing redox couples in solution are presented as model systems of unprecedented ideality for the study of the energetics of electron-transfer processes. Chapter 3 of this thesis shows that the dynamics of charge carrier recombination at the semiconductor/liquid interface can be consistently explained through reference to the interfacial energetics. The same concept can also be applied to the complex but technologically relevant charge-carrier dynamics at the surface of Si single crystals in contact with aqueous fluoride etching solutions. Chapter 4 deviates from the field of semiconductor electrochemistry somewhat and addresses charge-transfer processes in metal nanoelectrodes separated by less than 1 nanometer. Such experiments are important in understanding the energetics of electron tunneling through solvents and molecular bridges.

The present chapter serves as an introduction to an important concept underlying the field of semiconductor electrochemistry: the electrostatics of the semiconductor/liquid interface. The electrostatics of this junction will be developed in a mathematically rigorous fashion using Poisson's equation and the Gauss relation. Special concepts regarding the kinetics of charge transfer across the semiconductor/liquid interface and the Shockley-Read-Hall model of charge-carrier recombination will be introduced in Chapter 2 and Chapter 3, respectively. The energetics of electron tunneling will be discussed in Chapter 4.

1.2 ENERGETICS OF THE SEMICONDUCTOR/LIQUID INTERFACE

One of the most fundamental properties of semiconductor electrodes is that diffuse double layers can not only exist in the form of ionic double layers, which are so familiar from studies involving metallic electrodes, but can also exist in form of diffuse space-charge layers inside the semiconductor electrode itself. This space-charge layer usually dominates the capacitance of the electrode. Conceptually, this space-charge layer is identical with semiconductor-metal junctions and models developed by physicists have thus been successfully adapted for semiconductor/liquid junctions.

The energy band diagrams of an n-type semiconductor and a p-type semiconductor in contact with a liquid are shown in Figure 1.1 (a) before and after equilibration of the Fermi levels together with the charge-carrier profiles for electrons and holes. The equilibration processes at semiconductor/liquid junctions involving either n-type or p-type electrodes are so closely related that the description will be restricted to the case of an n-type semiconductor. The equilibration process and the definition of parameters of a p-type semiconductor/liquid junction follow from Figure 1.1 (a).

Figure 1.1 Band Diagrams and Charge-Carrier Profiles of n-type and p-type Semiconductor/Liquid Junctions.

The reference energy has been shifted from the vacuum level to an arbitrary value on the electrochemical energy scale (for instance cell potential). (a) Before charge equilibration, the energy bands and charge-carrier profiles are uniform and the entire semiconductor is neutral. To achieve depletion the electrochemical potential or the Fermi level of the solution is more positive (in the case of p-type more negative) than the Fermi level, $\boldsymbol{E}_{\mathbf{F}}$, of the semiconductor. As a result electrons (in the case of p-type: holes) are injected from the conduction band (in the case of p-type: valence band) to acceptor species in solution. The charge transfer will continue until the initial difference in the Fermi levels is neutralized. After charge equilibration a depletion layer is formed in the semiconductor, i.e., a non uniform charge distribution in the semiconductor. An excess of positive charges (p-type: negative charges) in the depletion width W and in the solution an excess of negative charges (p-type: positive charges) evolves. This results in a electric potential gradient (band bending) in the semiconductor. The parameter qV_n is defined as the difference between $\boldsymbol{E}_{\mathbf{F}}$ and $\boldsymbol{E}_{\mathbf{cb}}$, and qV_s is the surface barrier of the junction. The surface barrier can be modulated by the applied potential (E_app) and is typically expressed as $V_\mathrm{s} = V_\mathrm{bi} + E_\mathrm{app}$. The surface barrier of the junction in the absence of an applied potential (V_bi) is referred to as the built-in voltage. The barrier height of the junction, Φ_B is defined as $\Phi_\mathrm{B} = qV_\mathrm{n} + qV_\mathrm{s}$. Subscript “n” and “p” denote n-type or p-type semiconductor, respectively. (b) Three special equilibrium conditions for an n-type semiconductor: (I) flat-band condition (no difference in Fermi levels or Fermi level of the semiconductor is shifted accordingly by applying an external potential) (II) inversion (very positive solution potential), and (III) accumulation (very negative solution potential). Parameters are explained in the text.

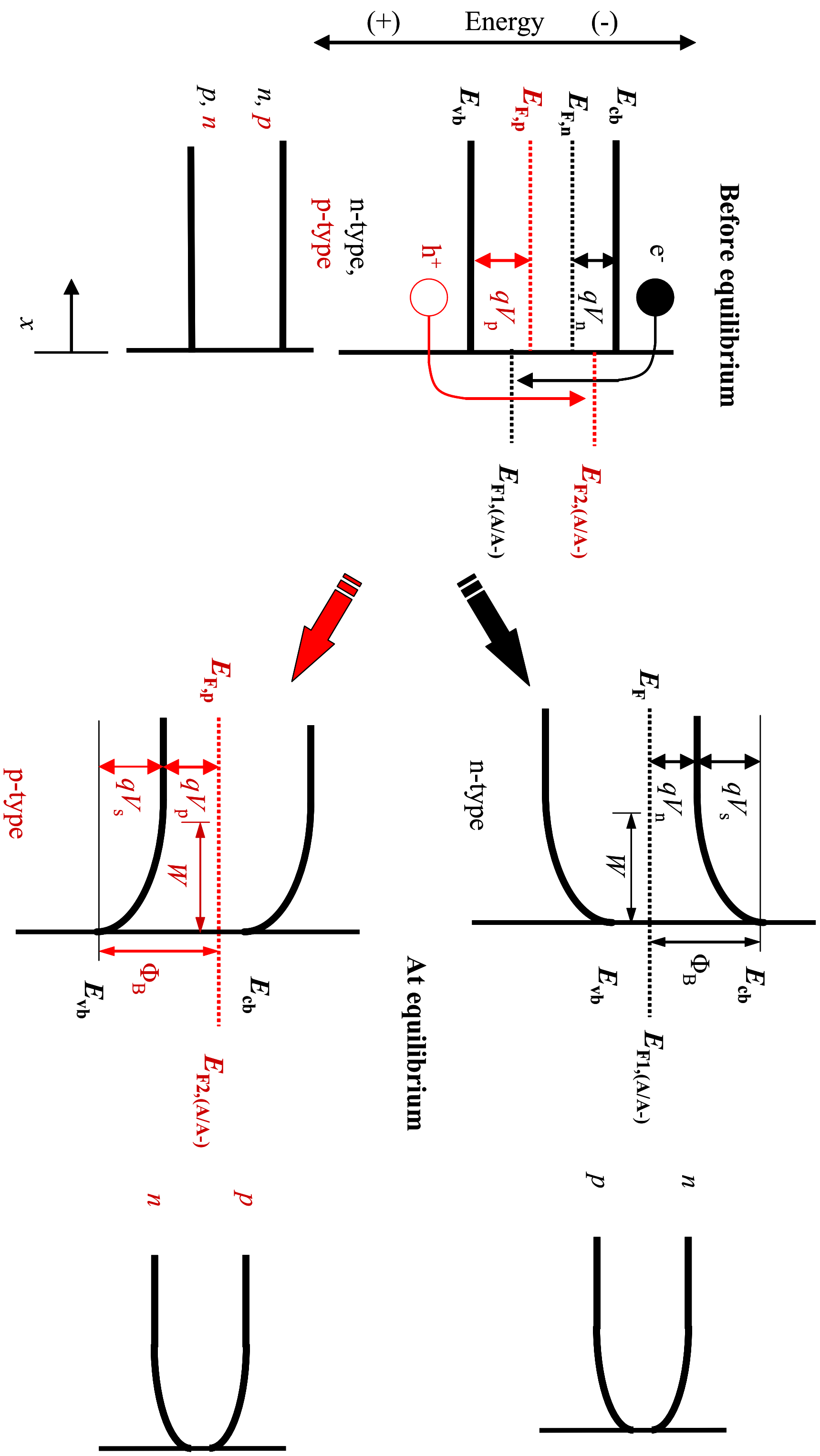
Before equilibrium
(+) Energy (-)
e-
h+
E_{cb}
$E_{F,n}$
$E_{F,p}$
E_{vb}
qV_n
qV_p
n-type,
p-type
n, p
p, n
x
$E_{F1,(A/A-)}$
$E_{F2,(A/A-)}$
At equilibrium
n-type
E_F
qV_s
qV_n
W
Φ_B
E_{cb}
E_{vb}
$E_{F1,(A/A-)}$
n
p
p-type
$E_{F,p}$
qV_s
qV_p
W
Φ_B
E_{cb}
E_{vb}
$E_{F2,(A/A-)}$
p
n

Figure 1.1 (a)

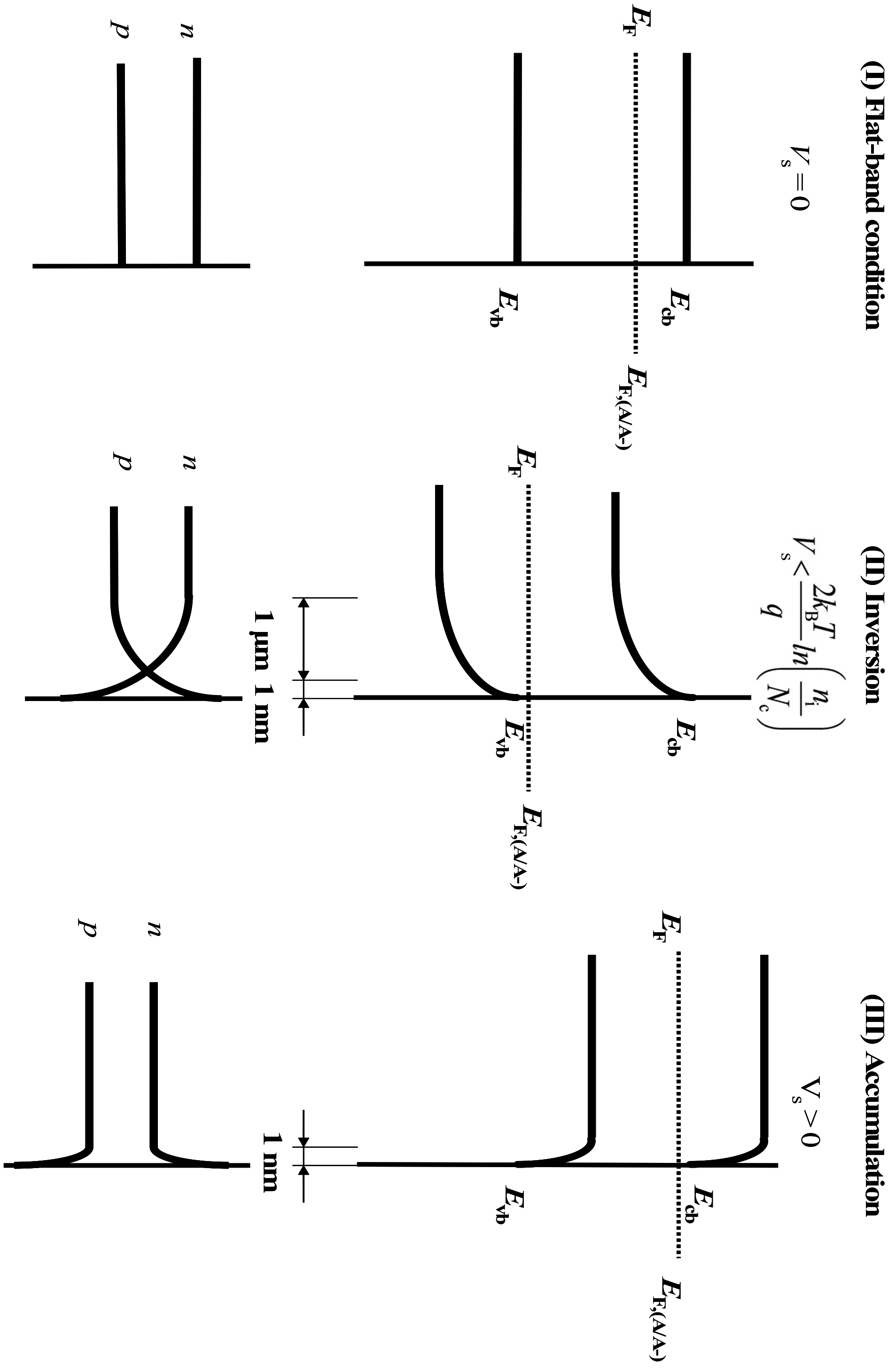
(I) Flat-band condition
V_s = 0
E_F
E_cb
E_vb
E_F,(A/A-)
n
p
(II) Inversion
V_s < 2k_BT/q ln(n_i/N_c)
E_F
E_cb
E_vb
E_F,(A/A-)
n
p
1 μm
1 nm
(III) Accumulation
V_s > 0
E_F
E_cb
E_vb
E_F,(A/A-)
n
p
1 nm

Figure 1.1 (b)

The electrochemical potential of a semiconductor is given by its Fermi level, $\boldsymbol{E}_{\mathbf{F}}$, whereas the electrochemical potential of the solution is related to the formal reduction potential by the Nernst equation ($\boldsymbol{E}_{\mathbf{F,\ A/A-}}$ = q $E_{\mathrm{A/A-}}$). To achieve depletion $\boldsymbol{E}_{\mathbf{F}}$ needs to be more negative than $\boldsymbol{E}_{\mathbf{F,\ A/A-}}$. To achieve equilibrium where no net-charge transfer is thermodynamically possible between the semiconductor and the solution, the semiconductor will inject electrons to acceptor species in solution until the two Fermi levels are equilibrated. Since the number of states per unit energy in the liquid far exceeds the number of available states in the semiconductor, little negative movement of $\boldsymbol{E}_{\mathbf{F,\ A/A-}}$ is expected and the equilibrium position of the Fermi levels after equilibration essentially coincides with the initial electrochemical potential of the solution. Due to the limited number of states in the semiconductor, $\boldsymbol{E}_{\mathbf{F}}$ will become more positive as electrons are inject to accpetor species in solution.

Since the number of charges that are transferred usually exceeds the number of dopant atoms present per atom layer by far, a space-charge region evolves; the depth over which dopant atoms are ionized is referred to as the depletion width (W). The larger the initial difference between the two Fermi levels is, the wider one expects the depletion width to be. The positive charges in the space-charge region need to be neutralized by a negative counter charge in the solution. Since a net charge density exists in the semiconductor and in the solution phase, a potential gradient on both sides of the junction has to evolve. The relationship between the charge density, ρ, and the potential, Φ, is given by the one-dimensional Poisson's equation:

$$\frac{d^2\Phi}{dx^2} = -\frac{\rho}{\varepsilon\varepsilon_0} \qquad \text{(Eq. 1.1)}$$

where ε_0 and ε denote the permittivity of free space and the dielectric constant of the semiconductor, respectively. The surface charge is given by the Gauss relation:

$$\left.\frac{d\Phi}{dx}\right|_{x=0} = -\frac{Q}{\varepsilon\varepsilon_0};\ V = \Phi - \Phi_{\text{bulk}}$$

(Eq. 1.2)

$$\left.\frac{dV}{dx}\right|_{V=V_{bi}} = \frac{Q}{\varepsilon\varepsilon_0}.$$

where Q is the net positive surface charge, V is the band bending function, and V_s is the surface barrier of the junction. The surface barrier can be modulated by the applied potential (E_{app}) and is typically expressed as $V_s = V_{\text{bi}} + E_{\text{app}}$. The surface barrier of the junction in the absence of an applied potential (V_{bi}) is referred to as the built-in voltage. For $|\boldsymbol{E}_{\mathbf{cb}}\text{-}\boldsymbol{E}_{\mathbf{F}}| > 3k_B\mathrm{T}$ and $|\boldsymbol{E}_{\mathbf{F}}\text{-}\boldsymbol{E}_{\mathbf{vb}}| > 3k_B\mathrm{T}$, the electron and hole densities, n and p, respectively, as a function of V are given by a Boltzmann relationship:[2, 3]

$$n = n_b \exp\left(-\frac{qV}{k_B T}\right)$$

(Eq. 1.3)

$$p = p_b \exp\left(\frac{qV}{k_B T}\right).$$

Charge neutrality holds in the bulk of the crystal such that $N_D\text{-}N_A = n_b\text{-}p_b$, where N_D, N_A, n_b and p_b denote the donor concentration, accpetor concentration, bulk electron concentration and bulk hole concentration, respectively. Using Eq. 1.1 and Eq. 1.3 and expressing the potential in terms of V, Poisson's equation can we written as

$$\frac{d^2\mathrm{V}}{dx^2} = \frac{\mathrm{q}}{\varepsilon\varepsilon_0}\left[\underbrace{N_{\mathrm{D}} - N_{\mathrm{A}} + p_{\mathrm{b}} \cdot \exp\left(\frac{qV}{k_B T}\right) - n_b \cdot \exp\left(-\frac{qV}{k_B T}\right)}_{\rho/q}\right].$$

(Eq. 1.4)

Multiplying each side of Eq. 1.4 with $2(dV/dx)$, substituting (N_D-N_A) with (n_b-p_b), integrating once and applying the boundary condition $dV/dx = 0$ when $V = 0$ leads to a general expression of the Poisson equation, which typically cannot be solved analytically unless simplifying assumptions are made:

$$\left(\frac{d\mathrm{V}}{dx}\right)^2 = \frac{2\mathrm{q}}{\varepsilon\varepsilon_0}\cdot\left\{(n_b - p_\mathrm{b})\cdot V + \left(\frac{k_\mathrm{B}T}{q}\right)n_\mathrm{b}\left[\exp\left(-\frac{qV}{k_\mathrm{B}T}\right)-1\right]\right. \qquad \text{(Eq. 1.5)}$$
$$\left.-\left(\frac{k_\mathrm{B}T}{q}\right)p_\mathrm{b}\left[\exp\left(\frac{qV}{k_\mathrm{B}T}\right)-1\right]\right\}.$$

The simplifying assumptions leading to the so-called Schottky model are that the density of minority carriers and the free-electron and free-hole concentration are negligible and that the space-charge region is depleted to a distance $x = W$.[3-5] The charge density equals $qn_b = q(N_D\text{-}N_A)$. Substituting this relation into Eq. 1.4 and integrating successively yields

$$\frac{d\mathrm{V}}{dx} = \frac{\mathrm{q}}{\varepsilon\varepsilon_0}\left[N_\mathrm{D} - N_\mathrm{A}\right](W - x) \qquad \text{(Eq. 1.6)}$$

and

$$V = \frac{q}{2\varepsilon\varepsilon_0}\left[N_\mathrm{D} - N_\mathrm{A}\right](W - x)^2$$
$$V_\mathrm{bi} = \frac{q}{2\varepsilon\varepsilon_0}\left[N_\mathrm{D} - N_\mathrm{A}\right]W^2;\ \ x = 0. \qquad \text{(Eq. 1.7)}$$

For moderately doped semiconductors, the width of the depletion layer is typically on the order of micrometers.[4-6]

Two interesting cases arise, when an n-type semiconductor contacts a liquid phase with either a highly reducing (negative) or highly oxidizing (positive) electrochemical potential, see Figure 1.1 (b). For highly negative electrochemical potentials, $V_\mathrm{S} > 0$, a large concentration of majority carries (here: electrons) accumulates in the space-charge.

Assuming that the Boltzmann approximation still holds and using the boundary conditions $V = V_s$ at $x=0$, Eq. 1.4 can be simplified and solved with respect to the distance x:

$$\left(\frac{dV}{dx}\right) = \left(\frac{2k_B T n_b}{\varepsilon\varepsilon_0}\right)^{1/2} \cdot \left[\exp\left(-\frac{qV}{2k_B T}\right)\right] \qquad \text{(Eq. 1.8)}$$

$$x = \left(2k_B T\varepsilon\varepsilon_0 / q^2 n_b\right)^{1/2} \cdot \left[\exp\left(\frac{qV}{2k_B T}\right) - \exp\left(\frac{qV_s}{2k_B T}\right)\right].$$

According to Eq. 1.8, V decreases in n-type Si within approximately 100 Å to a value of -$k_B T/q$.[4, 5] The small width of the accumulation layer makes intuitive sense because the excess majority carriers need not reside on dopant atom as in the case of depletion, but can also reside on lattice atoms of the semiconductor.[6] The opposite case, inversion, arises when $V_s < 2k_B T/q \ln(n_i/N_c)$ where N_c and n_i denote the effective density of states in the conduction band and the intrinsic electron concentration, respectively.[3] Poisson's equation and the width of the inversion layer are given by:

$$\left(\frac{dV}{dx}\right) = \left(\frac{2k_B T p_b}{\varepsilon\varepsilon_0}\right)^{1/2} \cdot \left[\exp\left(\frac{qV}{2k_B T}\right)\right] \qquad \text{(Eq. 1.9)}$$

$$x = \left(2k_B T\varepsilon\varepsilon_0 / q^2 p_b\right)^{1/2} \cdot \left[\exp\left(-\frac{qV}{2k_B T}\right) - \exp\left(-\frac{qV_{bi}}{2k_B T}\right)\right].$$

From solid state theory[3] p_b is given by

$$p_b = n_b^{-1} \cdot N_c N_v \cdot \exp\left(-\frac{E_g}{k_B T}\right) \qquad \text{(Eq. 1.10)}$$

where N_v and E_g are the effective density of states in the valence band and the band gap of the semiconductor, respectively. The width of the inversion layer has dimensions similar to those of the accumulation layer.[4, 5]

The differential capacitance of the semiconductor/liquid junction is readily derived from the space charge per unit area. Using Eq. 1.2 and Eq. 1.5 the space charge can be computed in both the general form (Eq. 1.11) and in the simplified form using the Schottky approximation for depletion (Eq. 1.12):.

$$Q = A\varepsilon_0\varepsilon \left.\frac{dV}{dx}\right|_{x=0} = \sqrt{\frac{2\varepsilon_0\varepsilon\cdot A^2}{\beta}\cdot q\cdot\left\{n_b\cdot\left(e^{-\beta V_s}+\beta V_s-1\right)-p_b\cdot\left(e^{\beta V_s}+\beta V_s-1\right)\right\}} \qquad \text{(Eq. 1.11)}$$

$$Q = \sqrt{\frac{2\varepsilon_0\varepsilon\cdot A^2}{\beta}\cdot q\cdot(n_b-p_b)\cdot\left(\beta\cdot V_s-1\right)}. \qquad \text{(Eq. 1.12)}$$

The parameter β denotes q/k_BT. A general formula for the differential capacitance is obtained by differentiating the space charge with respect to V_s:

$$C = \frac{dQ}{dV_s} = \sqrt{\frac{\varepsilon_0\varepsilon\cdot A^2\cdot q\left[n_b\cdot\left(1-e^{-\beta V_s}\right)-p_b\cdot\left(e^{\beta V_s}+1\right)\right]^2}{2\beta\cdot\left[n_b\cdot\left(e^{-\beta V_s}+\beta V_s-1\right)-p_b\cdot\left(e^{\beta V_s}+\beta V_s-1\right)\right]}} \qquad \text{(Eq. 1.13)}$$

The surface potential (V_s) can be modulated at will by means of an applied potential (E_{app}). Substituting V_s with $V_s = V_{\mathrm{bi}} + E_{\mathrm{app}}$, using the Schottky approximation for depletion and the charge neutrality relation and after proper rearrangement, the familiar Mott-Schottky expression[4, 5, 7] for the differential capacitance is obtained:.

$$C^{-2} = \frac{2}{\varepsilon_0\varepsilon\cdot q\cdot\left(N_{\mathrm{D}}-N_{\mathrm{A}}\right)A^2}\cdot\left(V_{\mathrm{bi}}+E_{app}-\frac{1}{\beta}\right). \qquad \text{(Eq. 1.14)}$$

Since the electrostatic potential cannot be measured directly, differential capacitance measurements offer the most valuable information about the electrostatics of the junction. If the semiconductor/liquid junction is under depletion, and the differential capacitance can be unambiguously related to the space-charge capacitance, the Mott-Schottky expression can be employed to determine V_{bi} and the surface-electron concentration can therefore be determined experimentally.

It is worthwhile to summarize the three main situations to be found in the double layer of a semiconductor:

(a) accumulation layer, where the excess charge has the same sign as the majority carrier in the bulk crystal and is constituted mainly by these carriers, not ionized donors or acceptors; the width of the accumulation layer is on the order of 100 Å;
(b) depletion layer, where the excess charge has the opposite sign of the majority carrier and consists mainly of ionized donors or accpetors for n- or p-type specimens, respectively; the width of the depletion layer is usually on the order of micrometers;
(c) inversion layer, where the excess charge carrier adjacent to the surface has the opposite sign of the majority carrier in the bulk crystal and is mainly constituted by minority carriers; the width of the inversion layer is on the order of 100 Å.

1.3 COMPARISON BETWEEN SEMICONDUCTOR AND METAL ELECTRODES

Semiconductor electrodes are ideally suited for the study of interfacial charge-transfer reactions.[8] The complications of kinetic studies involving metal electrodes originate mainly from the fact that the electron concentration at the surface of the metal cannot be directly determined experimentally[9, 10] and is therefore implicitly contained in the rate law. Due to the high density of states in the metal, double layer charges induced at the Fermi level of the metal can reside within a few Å of the surface.[11] While in a n-type semiconductor electrodes only electrons with energies of ($\boldsymbol{E}_{\mathbf{cb}}$ -3 $k_{\mathrm{B}}T < \boldsymbol{E} < \boldsymbol{E}_{\mathbf{cb}}$) are occupied by free electrons and need therefore be considered for electron flow from the semiconductor to the solution, the measured rate constant for electron flow from a metal electrode is a summation of energy dependent rate constants. Each rate constant describes interfacial charge transfer from every occupied electronic state to acceptor states in solution and is characterized by its own activation energy and surface electron concentration. Neither the individual energy-dependent rate constants nor the electron concentrations have been measured to date. As a consequence, the interfacial flux at optimum exoergicty for charge transfer, which usually far exceeds the mass-transport limit, will always dominate the interfacial charge carrier flux. Thus, key predictions from electron-transfer theory like the existence of the inverted regime can not be studied with metal electrodes.[12] Due to the limited concentration of electrons at the surface of the semiconductor, the charge carrier fluxes are expected to be far smaller than the mass transport limit.[8]

1.4 REFERENCES

1 Gerischer, H., The Impact of Semiconductors on the Concepts of Electrochemistry. **1990,** 35, 1677.

2 Pierret, R. F., *Advanced Semiconductor Fundamentals*. ed. Neudeck, G. W.; Pierret, R. F.; Addison-Wesley Publishing Company: Reading, MA, 1987; VI.

3 Sze, S. M., *The Physics of Semiconductor Devices*. Wiley: New York, 1981.

4 Morrison, S. R., *Electrochemistry at Semiconductor and Oxidized Metal Electrodes*. Plenum Press: New York, 1980.

5 Morrison, S. R., *The Chemical Physics of Surfaces*. Plenum Press: New York and London, 1990.

6 Tan, M. X.; Laibinis, P. E.; Nguyen, S. T.; Kesselman, J. M.; Stanton, C. E.; Lewis, N. S., *Principles and Applications of Semiconductor Photoelectrochemistry.* In *Progress in Inorganic Chemistry, Vol 41*, Ed. John Wiley & Sons Inc.: New York, 1994; 41, 21.

7 Gerischer, H., *Semiconductor Photoelectrochemistry.* In *Physical Chemistry: An Advanced Treatise*, Ed. Eyring, H.; Henderson, D.; Yost, W., Academic: New York, 1970; 9A, 463.

8 Fajardo, A. M.; Lewis, N. S., Free-Energy Dependence of Electron-Transfer Rate Constants at Si/Liquid Interfaces. *J. Phys. Chem. B.* **1997,** 101, (51), 11136.

9 Marcus, R. A., Chemical and Electrochemical Electron-Transfer Theory. *Ann. Rev. Phys. Chem.* **1964,** 15, 155.

10 Bard, A. J.; Faulkner, L. R., *Electrochemical Methods: Fundamentals and Applications*. John Wiley & Sons: New York, 1980.

11 Stratton, J. A., *Electromagnetic Theory*. McGraw-Hill: New York, 1971.

12 Chidsey, C. E. D., Free-Energy and Temperature Dependence of ET on Au. *Science* **1991,** 251, 919.

CHAPTER 2 *Energetics of Electron-Transfer Reactions at the n-type ZnO(0001)/Liquid Interface*

2.1 INTRODUCTION

The Marcus description of outer-sphere electron-transfer reactions has been extensively studied for electron transfer between molecular electron acceptor and donor species in homogeneous solution.[1] Agreement between theory and experiment has been demonstrated in numerous cases.[2-6] However, attempts to compare the Marcus treatment of charge-transfer at semiconductor/liquid contacts with experiments are rare. A study of charge-transfer kinetics at the n-Si/CH_3OH viologen$^{2+/+}$ interface indeed verified the predicted dependence of interfacial charge-transfer rate constants, k_{et}, on changes in standard free energies.[7, 8] In order to advance our understanding of interfacial charge-transfer kinetics in terms of the Marcus formalism a systematic study of the relationship between k_{et} and both the driving force for electron transfer and the reorganization energy, is necessary.[9-11]

Attempts to extend investigations at the n-Si/CH_3OH viologen$^{2+/+}$ interface to semiconductor liquid contacts other than those involving InP[12] have so far been thwarted due to a lack of control over the surface chemistry of electrical defects at the solid/liquid interface. Without extraordinarily low defect densities, adsorption and surface state-dominated kinetics govern the interfacial charge-transfer processes and thereby preclude analysis of the desired interfacial kinetic events.[10, 11]

In order to address the question of the driving-force and reorganization-energy dependence of interfacial rate constants, we will revert to a large band gap semiconductor, ZnO, first studied over 30 years ago.[13-21] These early reports suggest that robust kinetic measurements can be performed at n-ZnO electrodes in contact with redox couples in aqueous solution. ZnO electrodes were studied in the 1960s by Dewald[19-21] and Morrison and co-workers.[13-15] Both authors noted a linear relationship between the logarithm of current density and applied voltage with a slope of 60 mV/decade indicating that ZnO/ liquid contacts exhibit a first-order kinetic dependence in the surface electron concentration.[13-16, 19-21] However, only a few of the redox couples studied, notably $[Fe(CN)_6]^{3-/4-}$, showed the expected first-order dependence of the interfacial rate on the concentration of the redox acceptor species in the solution phase.[15]

An interesting result of these early studies is the small frequency dispersion of the differential capacitance measurements, which allowed a reliable determination of surface electron concentration and the position of the band edges versus a fixed reference electrode.

Attempts to extract rate constants from steady-state *j-E* data for further mechanistic studies, however, were thwarted by several facts. Most of these simple metal-ion-based redox systems studied by Morrison[15] such as Ce^{4+} (in HNO_3 and H_2SO_4), $IrCl_6^{2-}$, V^{3+} (in HCl), and $Ag(NH_3)_2^+$ are known to adsorb onto hydroxylated surfaces or to involve complex inner-sphere electron-transfer pathways. Little follow up of these early experiments has occurred over the following three decades.[22]

In order to study the dependence of the rate constant on both the reorganization energy and the driving force, one-electron redox couples covering a wide range of reorganization energies and formal reduction potentials are needed. For experiments aimed at elucidating the driving force dependence of the interfacial rate constant, a series of redox couples with formal reduction potentials spanning more than 400 mV is needed. The reorganization energy for this series of redox couples needs to be constant. We will employ a series of osmium(III/II) polybipyridyl compounds with various ligand substitutions of the general formula $[OsL_2L']^{3+/2+}$. The letter L represents 2,2’-dipyridyl, “bpy”, or 4,4’-dimethy-2,2’dipyridyl, “dmbpy”, and L’ represents 2,2’-dipyridyl, “bpy”, 4,4’-dimethy-2,2’dipyridyl, “dmbpy”, two imidazole ligands “$(Him)_2$”, or two 1-methylimidazole ligands, “$(MeHim)_2$“. To study the reorganization energy dependence of interfacial charge-transfer reactions, the electrochemical driving force should remain constant. Pentaamminepyridineruthenium(III/II), $[Ru(NH_3)_5py]^{3+/2+}$, and tris(bipyridine)cobalt(III/II), $[\text{Co(bpy)}_3]^{3+/2+}$, and $[\text{Os(dmbpy)}_2(\text{Him})_2]^{3+/2+}$ have been selected to conduct a first rigorous examination of the reorganization-energy dependence of k_{et}. The reorganization energies of these compounds span a range from 0.7 to 2.3 eV.[23, 24] Rate constants will be obtained by steady state *j-E* measurements along with differential capacitance measurements to determine the concentration of surface electrons. The reorganization energies of the osmium(III/II) polybipyridyl compounds will be determined independently by measuring their self-exchange rate constants in NMR line-broadening experiments.

2.2 BACKGROUND

For an intramolecular electron-transfer event between a donor and acceptor species at a fixed distance, the rate constant, $k_{\text{D-A}}$ (units: sec^{-1}), is described by Marcus theory.[1, 25-28] In the classical limit the quantum mechanical treatment of homogenous electron-transfer reactions results into the following expression for $k_{\text{D-A}}$ [1, 24]

$$k_{\text{D-A}} = \underbrace{\frac{2\pi}{\hbar}\cdot\overline{H_{\text{AB}}^2}\cdot\frac{1}{\left(4\pi\left(\lambda_{\text{i}}+\lambda_{\text{o}}\right)\cdot k_{\text{B}}T\right)^{1/2}}}_{\nu_{\text{e}}}\cdot\underbrace{\left\{\exp\left[\frac{-\left(\lambda_{\text{i}}+\lambda_{\text{o}}+\Delta G^{o'}\right)^2}{4k_{\text{B}}T\left(\lambda_{\text{i}}+\lambda_{\text{o}}\right)}\right]\right\}}_{\kappa_{\text{n}}} \tag{Eq. 2.1}$$

In this expression the rate constant is related to a pre-exponential term, ν_{e}, and the so-called nuclear or Franck-Condon term κ_{n}. H_{AB} is the electronic matrix element, which describes the electronic coupling between the reactant and product states. In case of the nuclear term, the activation energy to reach the transition state is split up into the free energy of the electron-transfer reaction, $\Delta G^{\text{o}'}$, and inner and outer-sphere contributions of donor and acceptor species to the reorganization energy, λ_{i} and λ_{o}, respectively.

For a semiconductor electrode, the concentration of surface electrons, n_{S}, is a parameter that can be measured and controlled experimentally by changing the electrode potential. Thus, in addition to the acceptor concentration [A], n_S must appear explicitly in the expression for the current density $j(E)$.[9-11, 28-31]

$$j(E) = -q \cdot k_{et} \cdot [A] \cdot n_S \qquad \text{(Eq. 2.2)}$$

The rate constant, k_{et}, therefore has units of cm^4 s^{-1}. The kinetic behavior of a semiconductor/liquid junction differs in several important aspects from systems involving metal electrodes. The rate constant is independent of the applied potential E, since the applied potential drops almost exclusively within the space-charge region of the semiconductor electrode with a negligible potential drop across the electrical double layer (Helmholtz layer) of the solid/liquid interface. Therefore, the current density, j, varies with E because n_S is related to the electron concentration in the bulk, n_b, through a Boltzmann-type relationship:[31, 32]

$$n_s = \underbrace{n_b \cdot \exp\left(-q \cdot V_{bi} \big/ k_B T\right)}_{n_{so}} \cdot \exp\left(-q \cdot E \big/ k_B T\right) \qquad \text{(Eq. 2.3)}$$

where k_B is Boltzmann's constant, and V_{bi} denotes the built-in voltage of the junction. Figure 2.1 introduces the thermodynamic and kinetic parameters of a general semiconductor/liquid junction. Ionized surface states and the Helmholtz layer are explicitly considered in the energy diagram. The Galvani (or inner) potential, Ψ_o, distributes itself over several regions of the semiconductor/liquid interface: (1) the space-charge layer in the semiconductor, characterized by the surface potential, Ψ_S, and the space charge of electrons, holes and immobile donors and acceptors in the lattice, q_{sc} , (2) a region of trapped charges in surface states, characterized by a surface state charge q_{ss}, (3) a Helmholtz layer formed by adsorbed ions or ionized surface groups and characterized by the Helmholtz potential, $q \cdot V_H$ and the adsorbed charge q_{ad} and last but not least (4) the double layer associated with ionic counter charge in the electrolyte, q_{el}. Charge neutrality demands that $q_{sc} + q_{ss} + q_{ad} + q_{el} = 0$. Since the distribution of the Galvani potential

Figure 2.1 Thermodynamic and Kinetic Parameters of a General Semiconductor/ Liquid Junction in the Presence of Ionized Surface States.

$\boldsymbol{E}_{\mathbf{cb}}$ and $\boldsymbol{E}_{\mathbf{vb}}$ are the conduction and valence band edge, respectively. qV_{bi} denotes the built-in-voltage at the point of zero charge, and Φ_{B} the barrier height. At equilibrium the Fermi level of the semiconductor $\boldsymbol{E}_{\mathbf{F,sc}}$ equals the cell potential $\boldsymbol{E}_{\mathbf{F,\ A/A^-}}$. The inner potential, Ψ_{o}, is distributed over the surface potential, Ψ_{S}, and the Helmholtz potential, qV_{H}. The barrier height for electron transfer can be changed by varying qV_{H} (for instance through pH changes) and by changing $\boldsymbol{E}_{\mathbf{F,\ A/A^-}}$. If the junction is biased away from equilibrium (E<0), the concentration of surface electrons, n_{s}, becomes larger than the concentration of surface electrons at equilibrium, n_{so}, with the result that a non-zero net current density, *j(E)*, flows.

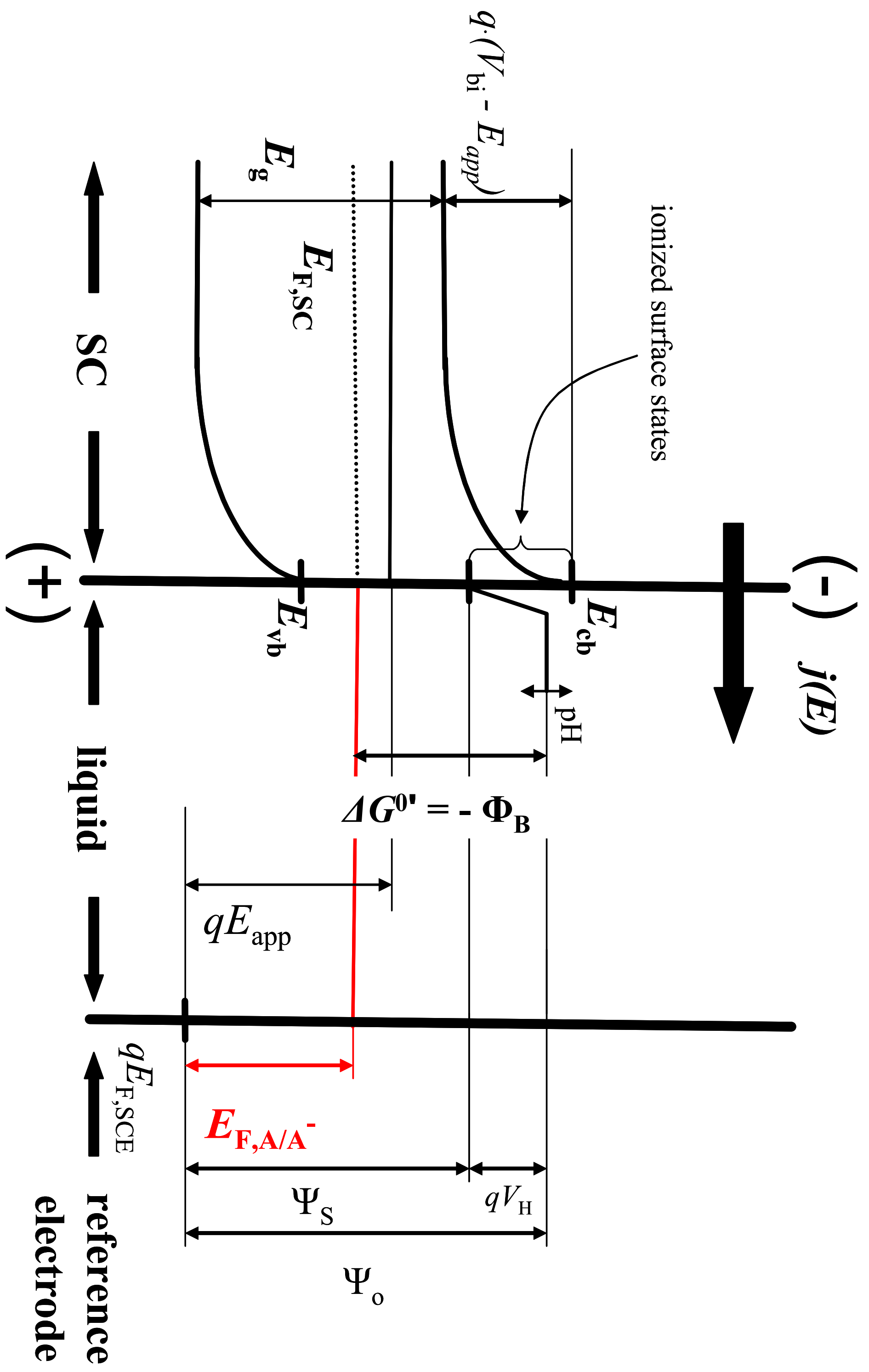
SC
liquid
reference electrode
(+)
(-)
j(E)
E_g
E_F,SC
q·(V_bi - E_app)
ionized surface states
E_vb
E_cb
pH
ΔG^0' = - Φ_B
qE_app
qE_F,SCE
E_F,A/A^-
Ψ_S
qV_H
Ψ_o

Figure 2.1

cannot be measured directly, the most valuable information regarding the charge distribution is obtained from differential capacitance measurements. The space-charge region is a result of the equilibration of the two Fermi levels, $\boldsymbol{E}_{\mathbf{F,sc}}$ (Fermi level of the semiconductor) and $\boldsymbol{E}_{\mathbf{F,\ A/A-}}$ (Fermi level of the redox couple in the electrolyte), which is facilitated by the transfer of electrons between the bands of the semiconductor and the redox couple in solution such that the net rate of electron transfer is zero at equilibrium. The surface charge is larger than at equilibrium when an external bias is applied through the back contact of the semiconductor with the result that a net current $j(E)$ flows, see Eq. 2.3. The thickness of the space-charge region is 100-1000 times the thickness of the Helmholtz layer and the latter is insensitive to electron transfer and is solely determined by the adsorption and desorption of ions. For metal oxide semiconductors, V_H is found to be a function only of the pH of the solution, see Eq. 2.5.[29, 33-35]

According to Figure 2.1, the energy of a solvated electron with respect to a reference electrode is given by its Galvani potential and thus the driving force for electron transfer from n-ZnO(0001) to a redox couple in solution can not only be changed by varying $\boldsymbol{E}_{\mathbf{F,\ A/A-}}$ but also by varying the pH of the supporting electrolyte. Both the Zn-rich and the O-rich surface of ZnO are known to be OH-terminated after etching.[33-35]

Lohmann uses a free-energy *ansatz* to derive the relationship between the *pH* and the Helmholtz potential (V_{H}).[35]

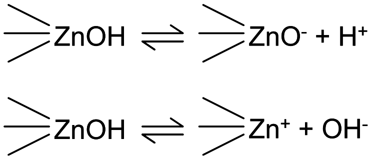

$$\mu^{o}_{ZnOH} + RT \cdot ln\ a_{ZnOH} = \mu^{o}_{ZnO^-} + RT \cdot ln\ a_{ZnO^-} + \mu^{o}_{H^+} + RT \cdot ln\ a_{H^+} - F \cdot V_{\mathrm{H}}$$
$$\mu^{o}_{ZnOH} + RT \cdot ln\ a_{ZnOH} = \mu^{o}_{Zn^+} + RT \cdot ln\ a_{Zn^+} + \mu^{o}_{OH^-} + RT \cdot ln\ a_{OH^-} + F \cdot V_{\mathrm{H}} \qquad \text{(Eq. 2.4)}$$

$$V_{\mathrm{H}} = const + \frac{RT}{2F} \cdot ln \frac{a_{ZnO^-}}{a_{Zn^+}} - \frac{2.3 \cdot RT}{F} \cdot pH$$

If the activity coefficient of ZnO^- ($a_{\mathrm{ZnO-}}$) and of Zn^+ ($a_{\mathrm{Zn+}}$) in Eq. 2.4 are assumed to stay constant, every pH unit change will result in a 55 mV shift in V_{H}. Thus, as depicted in Figure 2.1, the band-edge position of a metal oxide semiconductor can be shifted with respect to a fixed reference simply by varying the pH of the contacting aqueous electrolyte.

Several attempts to derive expressions for the rate constant of heterogeneous electron transfer between semiconductor electrodes and acceptor species in solution have so far been undertaken. These attempts encompass simple collisional models[30, 33] and an electronic coupling model adapting Marcus' treatment of electron transfer at the interface of two immiscible liquids.[12, 36] A final electronic coupling model for the rate law, Eq. 2.5,[37] based on the Fermi Golden Rule uses the same formalism as Eq. 2.1:

$$j(E) = -q \cdot \frac{2\pi}{\hbar} \cdot \left\{ \overline{H^{2}_{\mathrm{AB,sc}}} \right\} \cdot \left\{ \frac{1}{\left(4\pi\lambda_{\mathbf{A,sc}} k_{\mathrm{B}} T\right)^{1/2}} \right\} \cdot \left\{ \beta_{\mathrm{sc}}^{-1} \right\} \cdot \left\{ \frac{l_{\mathrm{sc}}}{d_{\mathrm{sc}}^{2/3} \cdot (6/\pi)^{1/3}} \right\} \cdot$$

$$\left\{ \exp\left[-\left[\overbrace{\left(\boldsymbol{E_{CB}} - qE_{\mathrm{F,\,A/A^{-}}} \right)}^{\Delta G^{o\prime}} + \lambda_{\mathbf{A,sc}} \right]^{2} \Big/ 4\pi\lambda_{\mathbf{A,sc}} k_{\mathrm{B}} T \right] \right\} \cdot [A] \cdot n_{\mathrm{s}}(E) \qquad \text{(Eq. 2.5)}$$

In Eq. 2.5 β_{sc}^{-1} is the coupling attenuation factor, l_{sc} the effective coupling length in the semiconductor, $\lambda_{\mathbf{A,sc}}$ denotes the reorganization energy of the acceptor species near the semiconductor electrode[36, 38] and d_{sc} denotes the atomic density. The subscript 'sc' indicates parameters for a semiconductor electrode.

In order to obtain reliable rate constants from steady state *j-E* data for further mechanistic studies, two stringent conditions must be met.[10, 11] First, the rate law of Eq. 2.2 must be obeyed, which means that the observed rate must be first order in both the acceptor concentration $[A]$ and surface-electron concentration n_s . While the first order dependence in $[A]$ and n_s can be qualitatively inferred from steady state *j-E* data, an independent and reliable method must be used in determining the value of n_s. Secondly, the band-edges positions of the semiconductor electrode need to remain remain unchanged with respect to a reference electrode when $[A]$ is varied.

2.3 EXPERIMENTAL

2.3.1 Electrode Preparation

Hydrothermally grown n-type ZnO (0001) single crystals were purchased from Atomergic Corp., Farmingdale NY (1 crystal: **ZnO3**) and Commercial Crystal Laboratories, Inc. Naples, FL (2 crystals: **ZnO1** and **ZnO2**). Electrochemical experiments reported in this work were confined to the Zn-rich surface, (0001). The crystals were approximately 10 × 10 × 1 mm^3 in dimensions. The conductivity of the crystals was reported by the manufacturer to be in the range of 10 to 10^4 Ω cm. No data on the nature of the dopant or the mobility of the charge carrier were available from the supplier.

Due to the high cost of ZnO single crystals and due to their limited availability, a polishing procedure was developed which allowed individual crystals to be reused for multiple electrochemical experiments. The single crystal was removed from the sample holder, cleaned, and mounted to a polishing fixture (South Bay Technology Inc., San Clemente, CA), which exactly maintained the crystallographic orientation of the sample. The mounting block was flattened with respect to the tungsten carbide linings of the polishing fixture using #320 SiC paper (Struers, Denmark). The crystal was mounted to the mounting block with the Zn-rich crystal face facing up using adhesive glue (softening point of 80^oC; Crystal Bound, South Bay Technology Inc., San Clemente, CA). The glue was allowed to solidify and a weight was placed on the crystal to ensure that the crystal remained flush with respect the mounting block. Approximately 50 μm of the surface were removed by grinding with #800 SiC paper, followed by #1000 SiC paper and #1200 SiC paper (all Struers Denmark) and a 50 g weight. For polishing water-based diamond suspensions of grain size 6, 3 and 1 μm (all South Bay Technology Inc., San Clemente, CA) were employed for approximately 60 min at each polishing grain size. After each polishing step the surface was inspected microscopically and polishing was continued until no further improvement of the surface quality was noticed. The final polishing step was accomplished by chemically polishing the surface in a silica/KOH suspension (50-100 nm, pH > 10, South Bay Technology Inc., San Clemente, CA) for at least 45 min. This produced a damage-free surface. The orientation of the crystals were tested before and after polishing with an X-ray Laue camera (Thomas Holzheu, CAMET Research Inc., Goleta CA), and no miscut was introduced before and after the polishing.

Reports in the literature suggest a wide range of metals and alloys as suitable ohmic contact materials for ZnO. Both electroplated indium[20, 21] and Ga-In eutectic[39] were tested and found to be suitable since they gave linear *J-E* curves when contacted with ZnO. In all work described subsequently, the polished ZnO crystal was mounted to the mounting block with the O-rich face pointing up using adhesive glue (Crystal Bound). The surface was roughened using Precision Alumina powder 22 microns (South Bay Technology Inc., San Clemente, CA). Ga-In eutectic, prepared by wetting an In shot (Alfa Aesar 40338) with Ga (Aldrich 26,326-5), was scratched onto approximately 80 % of the oxygen-rich face of the crystals. Prior to the application of the ohmic contact, etching of the O-rich face with concentrated phosphoric acid was necessary to improve the wetting of the Ga-In eutectic. After removal from the crystal bound and cleaning in acetone and isopropanol, a tinned copper wire (0.32 mm^2 cross sectional area) was glued to the Ga-In eutectic using silver print (GC electronics 22-201, Rockford IL) and served as the back-face contact.

The sample holder consisted of a glass tube (diam. 15 mm) into which the crystal and the back-face contact were placed. The back-face contact was sealed by filling the inverted glass tube with low-melting apiezon wax (softening point 120 ^{o}C) to a height of approximately 20 mm. The apiezon wax could be readily removed by dichloromethane. The electrode area was defined by using black insulating paint (prepared by dissolving 3.6 g of Apiezon wax in 20 ml of hexanes) and it was made sure that all edges of the crystal were covered with wax. The exact electrode area was determined photographically and was typically 0.2-0.3 cm^2.

Before experiments involving freshly polished ZnO crystals, the electrode was etched in concentrated phosphoric acid (Aldrich 21,510-4) for seven min, rinsed with 18 MΩ cm nanopure water (Barnstead NANOPure filter) and blown dry with $N_{2(g)}$. The etching time of seven min was in accordance with Dewald's recommendation[20, 21] of one minute per μm of plastically deformed region, which evolved during polishing. In subsequent measurements the ZnO electrodes were dipped into phosphoric acid to remove unwanted adsorbed species from the surface.

2.3.2 Electrochemical Measurements

All electrochemical experiments were carried out in a custom-made 4 neck round bottom flask with a 29/42 ground glass joint to hold the ZnO electrode. The three 9/20 ground glass joints on the side held a EG&G bridging tube into each of which a standard aqueous saturated calomel electrode (SCE, Fisher Scientific 13-620-52), a Pt gauze counter electrode (with an apparent surface area approximately 20 times larger than the area of the ZnO electrode), and a 2 mm diameter Pt working electrode (Bioanalytical Systems, West Lafayette, IN), which was used to measure the cell potential and the limiting currents, were immersed. The cell was designed such that a minimum amount of solution (10 ml) could be used. Deaerated conditions were established by bubbling $N_{2(g)}$ or $Ar_{(g)}$ through the cell solution. All experiments involving Os-polybipyridyl compounds were carried out at 0 ^{o}C. Experiments involving the remaining redox compounds were carried out at room temperature.

After an electrode was etched, it was immersed in the supporting electrolyte for at least 10 min before it was transferred to the electrochemical cell. This procedure proved helpful in getting reproducible results. All solutions were stirred with a magnetic stir bar. Nitrogen flow was terminated before the experiment to prevent bubbles from getting trapped on the electrode surface. For each series of measurements, the short circuit current of the ZnO-electrode was measured. *J-E* data and the open circuit potential were recorded before an after the differential capacitance measurements. Solution potentials were recorded before and after each experiment with respect to SCE and differed in no case by more than 5 mV.

Current-potential data were obtained with a Schlumberger Instruments Electrochemical Interface Model SI1287. The scan rate was 20 mV/sec and usually three cycles were employed. The current-potential data were corrected for the resistance of the electrochemical cell, R_{cell}, and the concentration overpotential of the cell solution, η_{overpot}, see Eq. 2.6. The cell resistance was obtained from the high-frequency intercept of the impedance spectra, which was independent of the bias but differed from the bulk resistance of the crystal. The concentration overpotential[40] can be calculated from the mass transport limiting currents and used in the potential correction, see Eq. 2.7. However, the concentration overpotential correction was in no case larger than 20 mV.

$$E_{\text{corr}} = E - J \cdot R_{\text{cell}} - \eta_{\text{overpot}} \approx E - J \cdot R_{\text{cell}} \qquad \text{(Eq. 2.6)}$$

$$\eta_{\text{overpot}} = \left(\frac{RT}{F}\right)\left[ln\left(\frac{j_{\text{A,lim}}}{-j_{\text{C,lim}}}\right) - ln\left(\frac{j_{\text{A,lim}} - j_{\text{J-E}}}{j_{\text{J-E}} - j_{\text{C,lim}}}\right)\right] \qquad \text{(Eq. 2.7)}$$

In Eq. 2.6 and Eq. 2.7 R denotes the gas constant, F is Faraday's constant, J is the measured current (A), $j_{\text{J-E}}$ the measured current density (A/cm^2) and E the applied potential. The mass-transport-limited cathodic and anodic current densities, $j_{\text{A,lim}}$ and $j_{\text{C,lim}}$, respectively, were measured for each cell solution with a one-sided Pt-foil, which had approximately the same geometric surface area as the respective ZnO electrode. *J-E* data were fitted to the full diode equation:[32]

$$j = -j_o\left(exp\left(-\frac{qE_{\text{corr}}}{\gamma \cdot k_{\text{B}}T}\right) - 1\right) \qquad \text{(Eq. 2.8)}$$

where γ is the so-called diode quality factor, which is unity for the ideal case of a semiconductor/liquid contact that is first order in surface electron concentration.

Differential capacitance measurements were performed with a Schlumberger Instruments Model 1260 Impedance Gain-Phase Analyzer interfaced to Model SI1287. The C_{diff}^{-2}-E behavior of the semiconductor/liquid contact was recorded for DC biases stepped in 50 mV increments over a potential range of 0 to 0.8 V versus SCE. A 10 mV AC signal was superimposed on the DC bias. Each capacitance measurement consisted of frequency sweeps in the range of 10-10^5 Hz. In order to derive the desired space-charge capacitance from the impedance data, all spectra were fitted to an equivalent circuit. Figure 2.2 shows a possible equivalent circuit and its simplifications. Circuit (a) contains most of the possible non-ideal contributions to the impedance. The equivalent circuit assumed in this work was circuit (c), which consists of the cell resistance R_{cell} in series with two parallel components R_{sc} and C_{sc} representing the resistance and capacitance of the space-charge region, respectively. Based on circuit (c), the appropriate equations relating the impedance to the space-charge capacitance are

$$\boldsymbol{Z} = R_{\text{cell}} + \frac{R_{\text{sc}}}{1-\omega^2 C_{\text{sc}}^2 R_{\text{sc}}^2} - i \cdot \frac{R_{\text{sc}}^2 \cdot C_{\text{sc}}\omega}{1-\omega^2 C_{\text{sc}}^2 R_{\text{sc}}^2} \qquad \text{(Eq. 2.9)}$$

$$C_{\text{sc}} = \frac{1+\sqrt{1-\dfrac{4\cdot Z_{im}^2}{R_{\text{sc}}^2}}}{2\omega\cdot Z_{im}} \qquad \text{(Eq. 2.10)}$$

where Z_{im} is the imaginary part of the total impedance $\boldsymbol{Z}$ and ω is the angular frequency.

The general formula for the differential capacitance and the simplified formula using the Schottky approximation was developed in Chapter 1.2, see Eq. 1.13 and Eq. 1.14, respectively. If C_{diff} can be set equal to C_{sc}, dopant density (N_{D}) and flat-band potential (E_{fb}; note $E_{\text{fb}} = -V_{\text{bi}}$) are obtained by fitting the C_{diff}^{-2}-E data to the Mott-Schottky equation:[11, 29, 32-34]

$$C_{\text{sc}}^{-2} = \frac{2}{q\cdot\varepsilon\varepsilon_{\text{o}}\cdot N_{\text{D}}\cdot A^2}\cdot\left(E - E_{\text{fb}} - \frac{k_{\text{B}}T}{q}\right) \qquad \text{(Eq. 2.11)}$$

$$\Phi_{\text{B}} = -\Delta G^{\text{o}'} = E^{o'}{}_{\text{F,A/A-}} - E_{\text{fb}} - \frac{k_{\text{B}}T}{q}\cdot\ln\left(\frac{N_{\text{c}}}{N_{\text{D}}}\right) \qquad \text{(Eq. 2.12)}$$

Figure 2.2 Equivalent Circuit and Its Simplifications.

Circuit (a) contains most of the possible non-ideal contributions to the impedance. Subscript "*sc*" denotes space charge, "*ss*" surface state, "*H*" Helmholtz, "cont" refers to the back face contact. Circuit (b) represents the case where contributions from the Helmholtz double layer, the back face contact are negligible. Circuit (c) represents the ideal equivalent circuit that allows for an unambiguous identification of the space-charge capacitance.

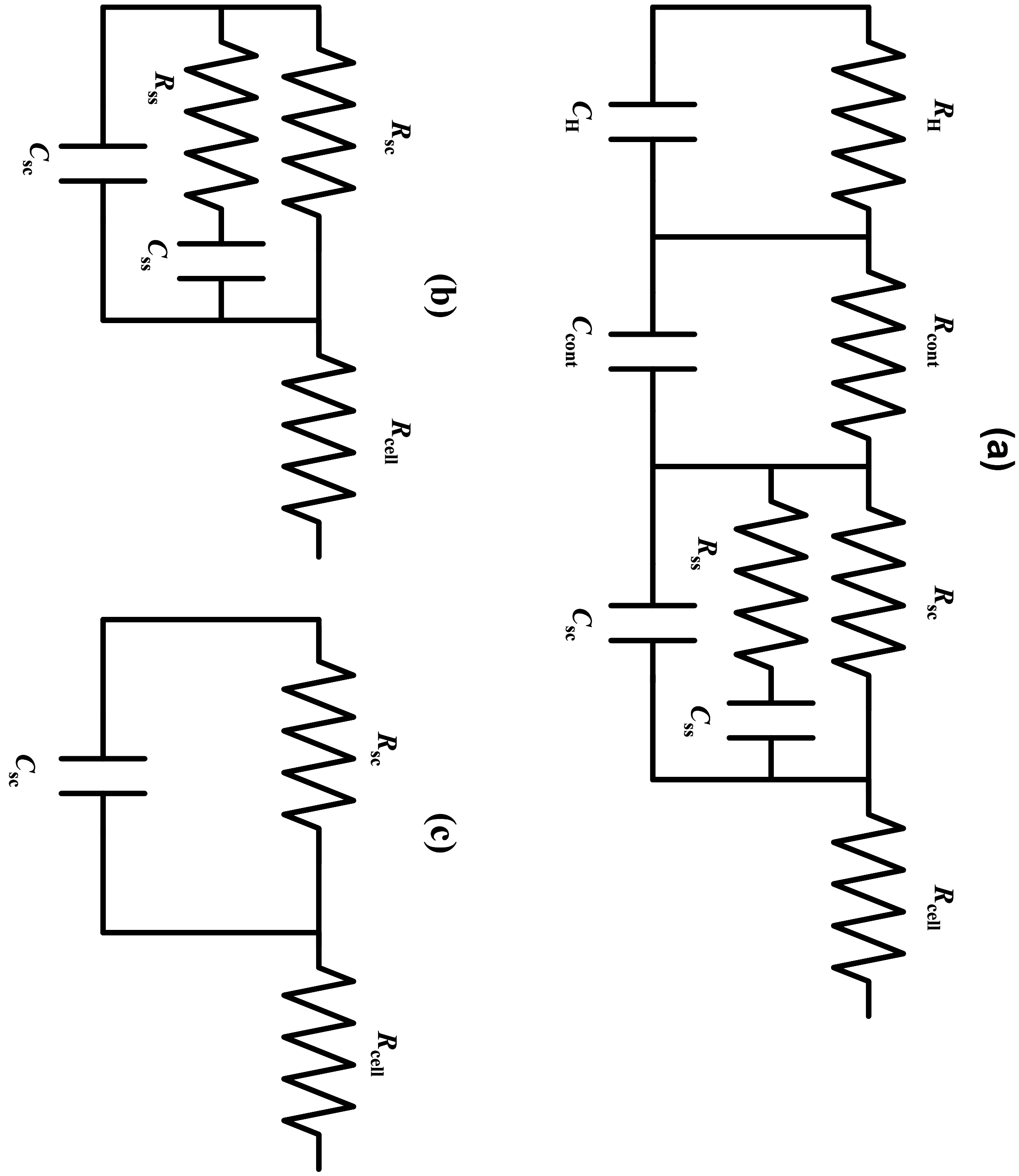
(a)
R_H
C_H
R_cont
C_cont
R_sc
R_ss
C_sc
C_ss
R_cell
(b)
R_sc
R_ss
C_sc
C_ss
R_cell
(c)
R_sc
C_sc
R_cell

Figure 2.2

where ε is the dielectric constant (8.7 for ZnO),[41] ε_o the permittivity of free space and A the surface area of the semiconductor electrode. With knowledge of N_D and E_{fb} the barrier height, Φ_B, at the formal reduction potential $E^{o'}_{F,A/A-}$ can be determined. N_c is the effective density of states in the conduction band[32] and was found to be 3.8×10^{18} cm^{-3} for ZnO.[42]

2.3.3 Redox Compounds and Solutions

Potassium ferrocyanide trihydrate $K_4[Fe(CN)_6]\cdot3H_2O$ (Aldrich, 99.99+ %) and potassium ferricyanide $K_3[Fe(CN)_6]$ (J.T. Baker, A.C.S. reagent) were recrystallized from hot water. Crystals were washed with ice cold water and diethylether and then dried *in vacuo*.

2.3.3.1 Synthesis of Trisbipyridinecobalt(III) Chloride

Approximately 1 g of cobaltous chloride $CoCl_2\cdot6H_2O$ (J.T. Baker, A.C.S.) was dissolved in a minimum amount of methanol (EM Science, OmniSolv). One equivalent of 2,2-dipyridyl (Aldrich, 99+%) was dissolved in methanol and added to the cobaltous chloride solution. The solution was stirred for ~20 min. Methanol was removed *in vacuo* and the dry compound was re-dissolved in water and oxidized with a ~30% stoichiometric excess of bromine (EM Science, GR). The solution was then transferred to a cation exchange column containing Sephadex C-25 CM resin (Aldrich 27,124-1). Without the oxidation step two distinct bands were formed corresponding to $[Co^{II}(bpy)_3]^{2+}$ and $[Co^{III}(bpy)_3]^{3+}$. After the oxidation step a single band was observed, in addition to narrow bands of low- and high-charged impurities. A stoichiometric amount of ammonium hexafluorophosphate (Aldrich, 99.9%) was used to precipitate the compound. Since the solubility of the PF_6-salts in water was too low, PF_6^- was exchanged for Cl^- in an anion exchange column containing Sephadex DEAE A-25 resin (Aldrich 27,127-6). Water was removed *in vacuo*, the compound was dissolved in methanol, recrystallized by adding diethylether, washed with ice-cold water and diethylether and finally dried *in vacuo*

Figure 2.3 Chemical Structures of Redox Compounds Used in This Work.

Each compound is identified by a roman numeral. These roman numerals are referred to throughout the text. (**I**) tris(bipyridine)osmium(III/II) or $[Os(bpy)_3]^{3+/2+}$, (**II**) tris(dimethylbipyridine)osmium(III/II) or $[Os(dmbpy)_3]^{3+/2+}$, (**III**) bis(bipyridine)bis(imidazole)osmium(III/II) or $[Os(bpy)_2(Him)_2]^{3+/2+}$, (**IV**) bis(dimethylbipyridine)bis(imidazole)osmium(III/II) or $[Os(dmbpy)_2(Him)_2]^{3+/2+}$, and (**V**) bis(bipyridine)bis(n-methylimidazole)osmium(III/II) or $[Os(bpy)_2(n\text{-}Meim)_2]^{3+/2+}$, (**VI**) chemical structures of tris(bipyridine)cobalt(III/II) or $[Co(bpy)_3]^{3+/2+}$, (**VII**) pentaaminepyridineruthenium(III/II) $Ru(NH_3)_5py$ and (**VIII**) ferro/ferricyanide $[Fe(CN)_6]^{3-/4-}$. Formal reduction potentials and reorganization energies are described in the text.

(I)

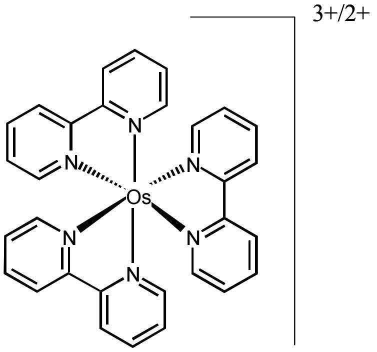

(II)

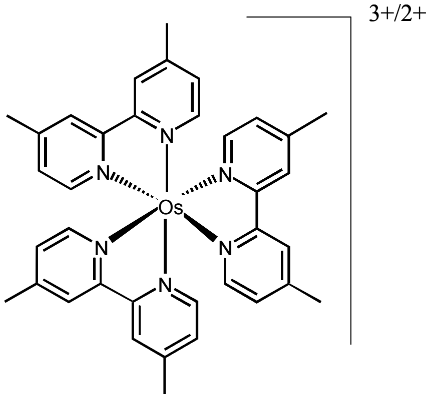

(III)

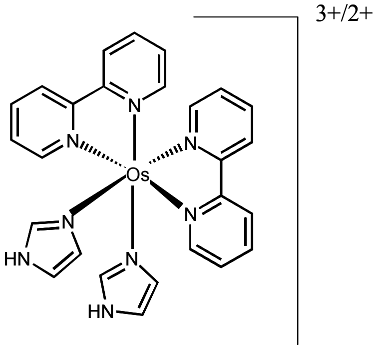

(IV)

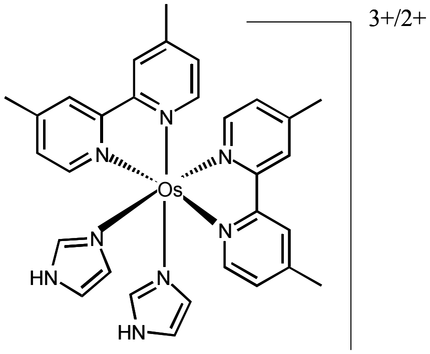

(V)

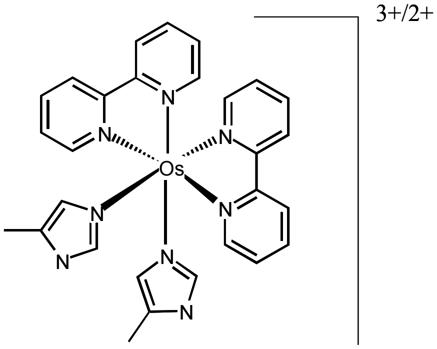

Figure 2.3

(VI)

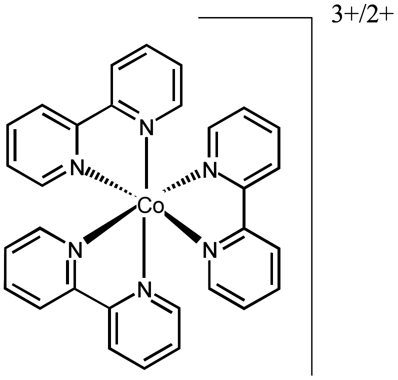

(VII)

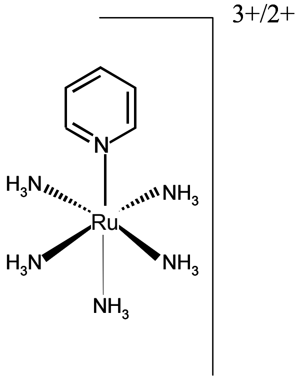

(VIII)

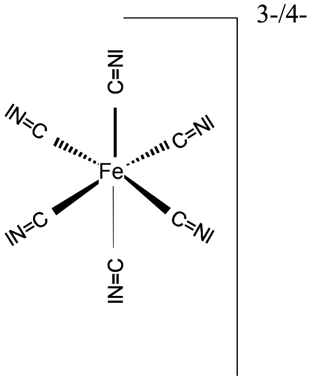

Figure 2.3 continued

overnight. The yield was 80 %. Chemical Analysis (theoretical values in brackets): $[Co(bpy)_3](PF_6)_3$: C 37.44 (36.22), N 8.30 (8.70) , H 2.5 (2.5); $[Co(bpy)_3](Cl)_3 \cdot 3.5(H_2O)$: C 50.47 (51.7), N 11.79 (12.06), H 4.48 (4.48). NMR of $[Co(bpy)_3](Cl)_3 \cdot 3.5(H_2O)$ (chemical shifts are referenced to the residual protons of acetone-d4): ^{1}H-bpy: 9.21 (d), 8.82 (t), 8.09 (t), 7.78 (d).

2.3.3.2 Synthesis of Pentaaminepyridineruthenium(II) Hexafluorophosphate

The ruthenium precursor $[Ru^{III}(NH_3)_5Cl]Cl_2$ (0.5 g, Strem, 98%) was dissolved in 150 ml nanopure water. Approximately 0.88 g of silver trifluromethane sulfonate (Aldrich, 99+%) was dissolved in water and added to the solution. The solution was stirred for 3 hours to allow AgCl to coagulate. Silver chloride was then removed by filtration. Approximately 10 g of pyridine (Aldrich, 99+%) were added to the solution and the reaction was allowed to proceed under reducing conditions (Zn-amalagam: 16 g Zn-mossy; amalagamation with 0.2 g $HgCl_2$) and under red light for one hour. The solution was then filtered and the solvents were removed *in vacuo*. The compound was dissolved in a minimum amount of water and transferred to an ion exchange column containing Sephadex C-25 CM resin. Solution and eluants were deaerated with nitrogen. Three distinctive bands formed. The highly colored orange band was collected and the compound was precipitated by adding 0.57 g of sodium hexaflurophosphate (Aldrich, 20,805-1). The precipitate was collected, washed with ice-cold water and diethylether and dried *in vacuo*. The yield was 50 %. Chemical analysis (theoretical values are in brackets): C 11.11 (10.82), N 14.89 (15.14), H 3.53 (3.63). NMR (chemical shifts are referenced to the residual protons of acetone-d6): ^{1}H-py: 8.80 (d), 7.75 (t), 7.32 (t), $^1H\text{-}NH_3$: 3.11 (n.a.), 2.61 (n.a.).

2.3.3.3 Synthesis of Os-polybipyridyl Compounds

The synthesis and measurement of reorganization energies of the Os-polybipyridyl compounds used in this study were carried out by Thomas W. Hamann; details are described in his candidacy report.[23] The precursor materials ammonium hexachloroosmate(IV) ($(NH_4)_2[OsCl_6]$, Aldrich 20,970-4), potassium hexachloroosmate(IV) ($K_2[OsCl_6]$, Aldrich 45,907-0), dipyridyl (bpy, Aldrich D21,630-5), 4,4'-dimethyl-2,2'-dipyridyl (dmbpy, Aldrich 24,573-9), imidazole (him, Aldrich 43,615-1), n-methyl imidazole (n-meim, Aldrich 19,988-5), ammonium hexafluorophosphate (NH_4PF_6, Aldrich 21,659-3), and tetrabutylammonium chloride (TBAC; Fluka 86853) were all used as received. All solvents are reagent grade and used as received. Water was obtained from a Barnstead NANOPure filter with a resistivity > 18 MΩ cm.

All compounds were characterized by elemental analysis and mass spectroscopy. The PF_6^{2-} salts had mass percentage values for carbon, nitrogen, and hydrogen which corresponded to the theoretical values. For Cl salts, however, the mass percentage were significantly lower for carbon and nitrogen and slightly higher for H, which can be accounted for by the addition of 5 equivalents of water.

Synthesis of $[OsB_3]Cl_2$ where B = bpy or dmbpy To $(NH_4)_2[OsCl_6]$ (0.25g / 0.56 mmol) was added 3.5 equivalents of B in a 50 mL round bottom flask and dissolved in 20 mL ethylene glycol. The solution was heated to reflux with rapid stirring under argon for one hour, then allowed to cool to room temperature. Sometimes $K_2[OsCl_6]$ was used as the starting material; in this case KCl was filtered from solution after cooling and the procedure continued as follows. 100 mL of saturated aqueous NH_4PF_6 was added to the solution which was then filtered yielding a dark green product which was washed with cold water and diethyl ether. The product was dried in air overnight, then purified on an activated neutral alumina column using acetonitrile as the eluent. A dark green band was collected, and the solvent removed *in vacuo*. The dark residue was dissolved in a minimal amount of acetone and precipitated by addition of diethyl ether. The product, $[OsB_3](PF_6)_2$, was filtered and dried *in vacuo*. Yields in excess of 80% were obtained. A sephadex DEAE-A25 ion-exchange column was prepared with NaCl and H_2O. The product was dissolved in 250 mL of acetonitrile and diluted to 2.5 L with H_2O. This dilute solution was eluted through the sephadex column and the solvent was stripped off. The residue was dissolved in a minimal amount of methanol and precipitated by addition of cold diethyl ether. The dark green precipitate was filtered and dried *in vacuo*. A nearly quantitative yield was recovered. Alternatively, $[OsB_3](PF_6)_2$ was dissolved in 100 mL acetone and a concentrated solution of TBAC in acetone was added during vigorous stirring. The insoluble $[OsB_3]Cl_2$ precipitated out of solution, was filtered, washed with acetone and ether, then dried *in vacuo*. Chemical Analysis (theoretical values in brackets): $[Os(bpy)_3]Cl_2$: C 41.38 (49.38), N 10.80 (11.52) , H 3.23 (3.32); mass spectroscopy observed m/z (calculated value) = 660.2 g (658.8 g) $[Os(dmbpy)_3](PF_6)_2$: C 41.81 (41.86), N 7.89 (8.14), H 3.49 (3.51); $[Os(dmbpy)_3]Cl_2$: C 46.25 (53.13), N 8.79 (10.33), H 4.57 (4.46); mass spectroscopy observed m/z (calculated) = 743.3 g (742.9 g)

Synthesis of $[OsB_2L_2]Cl_2$ where L = him or n-meim To $(NH_4)_2[OsCl_6]$ (1.1g / 2.3 mmol) were added 2 equivalents of B to a 50 mL round bottom flask and dissolved in 35 mL ethylene glycol. The solution was heated to reflux with rapid stirring under argon for one hour, then allowed to cool to room temperature. Sometimes $K_2[OsCl_6]$ was used as the starting material; in this case KCl was filtered from solution after cooling and the procedure continued as follows. Approximately 100 mL of cold 1M aqueous $Na_2S_2O_4$ was slowly added to solution to reduce any $[OsCl_2B_2]^+$ that may have formed and precipitate $[OsCl_2B_2]$. The solution was cooled in an ice bath for 1 hour, then a black precipitate was collected. The precipitate was washed with cold water and diethyl ether and used without further purification for further reactions. 5-20 equivalents of L were added to the dried product in a 100 mL round bottom flask and dissolved in 50 mL of ethylene glycol. The solution was heated to reflux with rapid stirring under argon for 2-10 hours, then allowed to cool to room tem-

perature. 100 mL of saturated aqueous NH_4PF_6 (or $NaPF_6$) was added to the solution which was then filtered yielding a dark brown product which was washed with cold water and diethyl ether. The product was dried in air overnight, then purified on an activated neutral alumina column using acetonitrile as the eluent. A brown band was collected, and the solvent removed *in vacuo*. The brown residue was dissolved in a minimal amount of acetone and precipitated by addition of diethyl ether. The product was filtered and dried under vacuum. Yields in excess of 30% were obtained. The product was dissolved in 250 mL of acetonitrile and diluted to 2.5 L with H_2O. This dilute solution was eluted through a sephadex DEAE-A25 ion-exchange column and the solvent was stripped off. The residue was dissolved in a minimal amount of methanol and precipitated by addition of cold diethyl ether. The brown precipitate was filtered and dried *in vacuo*. A nearly quantitative yield was recovered. Alternatively, $[OsB_2L_2](PF_6)_2$ was dissolved in 100 mL acetone and a concentration solution of TBAC in acetone was added during vigorous stirring. The insoluble $[OsB_2L_2]Cl_2$ precipitated out of solution, was filtered, washed with acetone and ether, then dried *in vacuo*. Chemical analysis: $[Os(him)_2(bpy)_2](PF_6)_2$: C 33.56 (33.60), N 11.77 (12.06), H 2.46 (2.58); $[Os(him)_2(bpy)_2]Cl_2$: C 41.42 (44.01), N 14.21 (15.78), H 3.64 (3.42); mass spectroscopy: observed m/z (calculated value) = 639.1 g (638.7 g); $[Os(him)_2(dmbpy)_2](PF_6)_2$: C 36.65 (36.55), N 11.13 (11.37), H 3.31 (3.25); $[Os(him)_2(dmbpy)_2]Cl_2$: C 45.00 (47.01), N 12.29 (14.63), H 4.55 (4.18); $[Os(n\text{-}Meim)_2(bpy)_2](PF_6)_2$: C 35.34 (35.12), N 11.53 (11.71), H 2.81 (2.93); $[Os(him)_2(bpy)_2]Cl_2$: C 40.90 (45.55), N 13.02 (15.18), H 3.63 (3.80); mass spectroscopy: observed m/z (calculated value) = 667.1 g (666.8 g);
The oxidized species of all osmium compounds were produced *in situ* by bulk electrolysis using a carbon mesh electrode.

2.3.3.4 Buffer Systems and Supporting Electrolyte

All electrochemical experiments were carried out in aqueous, buffered solutions containing 1 M KCl (Aldrich, 99+%) as the supporting electrolyte. Water was obtained from a Barnstead NANOPure filter with a resistivity > 18 MΩ cm. To adjust the pH of the solution, a borax buffer BO_2^-/HBO_2 (0.05M $Na_2B_4O_7 \cdot 10\ H_2O$, Aldrich, A.C.S. reagent), phosphate buffer $H_2PO_4^-/HPO_4^{2-}$ (0.02 M KH_2PO_4, Mallinckrodt, AR), and imidazole buffer ($6 < pH < 8$) were used. The pH was adjusted with concentrated $HCl_{(aq)}$ The pH was determined before and after the experiment with a glass combination pH electrode (ORION 9202BN, Beverly, MA). All experiments involving **ZnO1** and **ZnO2** were carried out in the imidazole buffer. Experiments involving **ZnO3** were carried out in the borax or phosphate buffer.

2.4 RESULTS

Three ZnO electrodes (**ZnO1**, **ZnO2**, and **ZnO3**) were used. In this chapter the results leading to the determination of rate constants for charge transfer are presented in great detail for electrode **ZnO1**, while only the main results are listed for the remaining two electrodes, **ZnO2** and **ZnO3**. The semiconductor/liquid junction must follow two stringent criteria for the reliable determination of rate constants: ideal energetic and ideal kinetic behavior. The kinetic behavior is evaluated by current density *versus* voltage measurements (J-E measurements) and is considered to be ideal if the rate law (Eq. 2.2) applies,[9-11, 13, 15, 20, 21, 28-30, 33] i.e., the semiconductor/liquid junction shows a pseudo-first order dependence in both the surface electron concentration (n_s) and the acceptor concentration ($[A]$). The energetic behavior of the junction is evaluated by differential capacitance *versus* voltage measurements (C_{diff}-E measurements). The behavior is considered to be ideal if C_{diff} shows no frequency dispersion. Furthermore, the energetic position of the conduction-band edge needs to remain unchanged with respect to a reference electrode when $[A]$ is varied. Chapter 2.4.1 is devoted to the electrostatics of the n-type ZnO(0001)/liquid interface, and the results of the *J-E* measurements are discussed in Chapter 2.4.2. Individual data sets are identified by the ZnO electrode, the redox compound and the pH of the buffer (e.g. **ZnO1_II_pH8**: electrode ZnO1 in contact with $[Os(dmbpy)_3]^{3+/2+}$ in buffer of pH 8).

2.4.1 Results of C_{diff}-*E* Measurements

The results of the C_{diff}-*E* measurements for contacts involving electrode **ZnO1** and the Osmium polybipyridyl compounds depicted in Figure 2.3 (a) are summarized in Table 2.1. A typical Bode plot representative of the majority of the semiconductor/liquid junctions studied in this work is presented in Figure 2.4. The Bode plots are shown for two applied potentials, 0.8 V and 0.2 V *vs.* SCE, and reveal that the energetics of this junction (Table 2.1: **ZnO1_II_pH8**) were close to being ideal. The impedance *vs.* frequency plot in the double-logarithmic representation was linear and the phase angles were close to -90^o which indicates that the impedance is dominated by a simple capacitance. The impedance deviated from linearity only at frequencies larger than 5 kHz due to the large series resistance of the junction. To obtain the correct value of the differential capacitance (C_{diff}), the impedance spectra were fit to the equivalent circuit in Figure 2.2 (c) for frequencies ranging from 100 Hz to 5 kHz. The slope of the curve in the double-logarithmic plot of impedance *vs.* frequency was equal to -1, indicating that the imaginary part of the impedance, represented by Eq. 2.10, was essentially equal to $(\omega C_{diff})^{-1}$. Additionally, in the frequency range used for the determination of the differential capacitance no frequency dispersion of the capacitance was observed. If frequency dispersion were present the magnitude of the slope would be smaller than 1.[43] The impedance spectra for a given potential *vs.* SCE did not change when the acceptor concentration is changed. .

It should be noted that starting with frequencies larger than 50 kHz a second relaxation process becomes visible. Since impedance measurements at frequencies larger

Figure 2.4 Representative Bode Plot for a n-ZnO(0001)/H_2O Junction.

The Bode plot is shown for n-ZnO(0001) in contact with $[Os(dmbpy)_3]^{3+/2+}$ in a buffer of pH 8. (Table 2.1: **ZnO1_II_pH8**). Circles denote impedance data for an applied potential of 0.8 V *vs.* SCE and squares indicate data for an applied potential of 0.2 V *vs.* SCE. The filled circles and the filled squares denote an acceptor concentration of 5 mM, while the open circles and open squares indicate an acceptor concentration of approximately 0.5 mM. The energetics of the **ZnO1_II_pH8** junction were ideal. The linearity of the impedance *vs.* frequency in the double-logarithmic plot and phase angles close to -90^{o} indicate that the system behaves as a simple capacitor over the frequency range of $10\text{-}5\times10^{3}$ Hz. The slope of the curve was -1 indicating that no frequency dispersion was present. At frequencies higher than 5×10^{3} the impedance deviated from linearity due to the high series resistance of 2500 Ω . This junction yielded a flat-band potential (E_{fb}) of -0.147 ± 0.001 V *vs.* SCE for high acceptor concentrations (5 mM) and $E_{fb} = -0.145 \pm 0.001$ V *vs.* SCE for low acceptor concentrations (0.5 mM). The dopant density (N_D) was equal to 1.19×10^{15} cm^{-3}. At low frequencies some noise was present, which was removed for clarity.

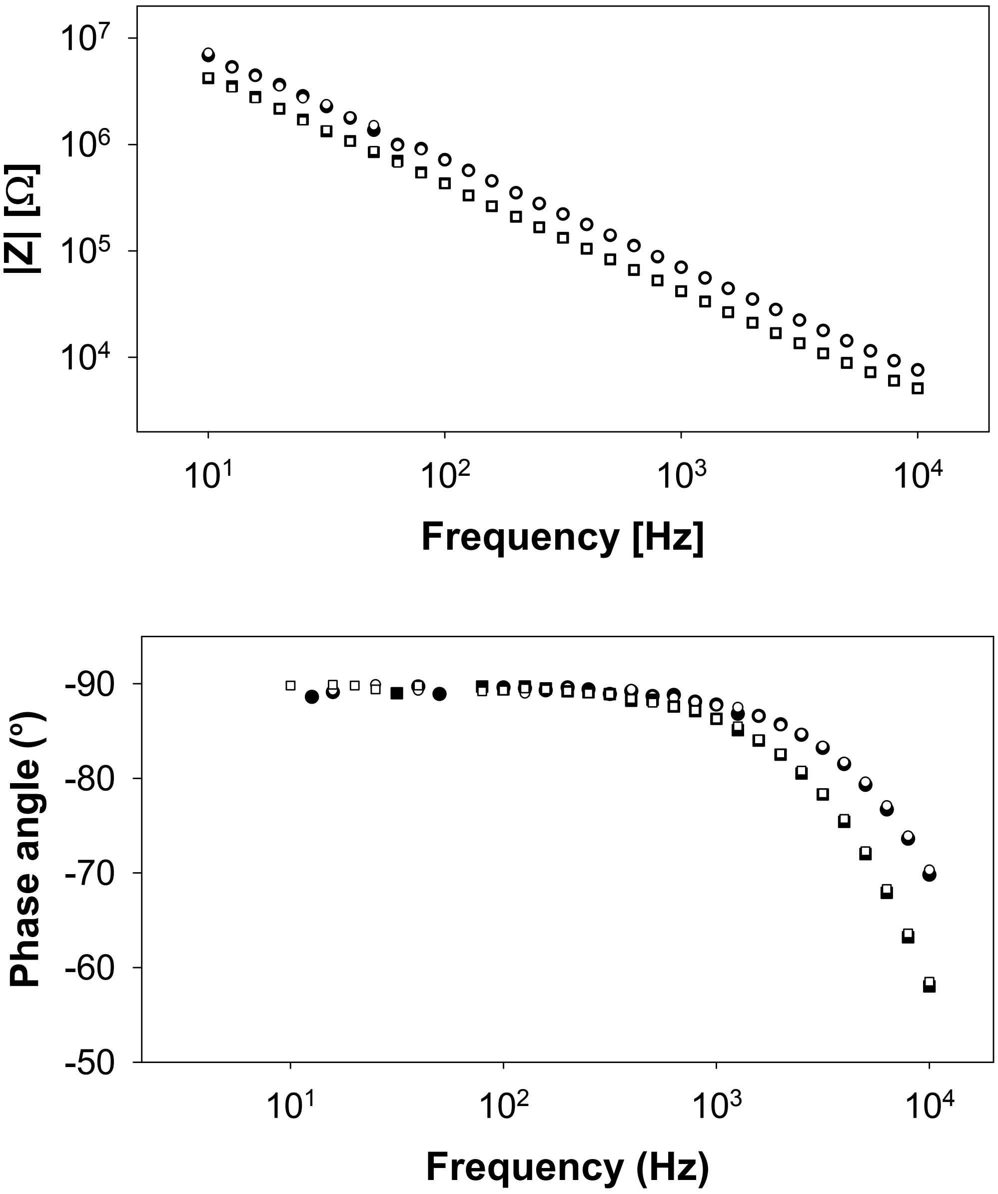

10^7
10^6
10^5
10^4
|Z| [Ω]
10^1
10^2
10^3
10^4
Frequency [Hz]
-90
-80
-70
-60
-50
Phase angle (°)
10^1
10^2
10^3
10^4
Frequency (Hz)

Figure 2.4 (a)

TABLE 2.1. Impedance data for junctions **ZnO1_I_pH8-ZnO1_V_pH8**

E (V)	R_s (Ω)	C_{sc} (nF)	ΔC_{sc} (%)	E (V)	R_s (Ω)	C_{sc} (nF)	ΔC_{sc} (%)
Zn_I_pH8	5 mM						
0.80	2656	2.229	0.35	0.40	2736	2.922	0.29
0.75	2675	2.282	0.40	0.35	2733	3.066	0.31
0.70	2684	2.350	0.40	0.30	2750	3.247	0.27
0.65	2696	2.413	0.41	0.25	2748	3.456	0.28
0.60	2656	2.502	0.35	0.20	2724	3.727	0.30
0.55	2689	2.587	0.32	0.15	2761	4.098	0.25
0.50	2722	2.689	0.33	0.10	2838	4.654	0.29
0.45	2742	2.792	0.35				
Zn_II_pH8	5 mM						
0.80	2711	2.255	0.23	0.40	2735	2.962	0.25
0.75	2634	2.317	0.25	0.35	2740	3.109	0.24
0.70	2790	2.378	0.28	0.30	2725	3.293	0.20
0.65	2707	2.449	0.28	0.25	2751	3.506	0.19
0.60	2735	2.533	0.20	0.20	2775	3.785	0.22
0.55	2768	2.623	0.21	0.15	2805	4.169	0.20
0.50	2750	2.722	0.19	0.10	2835	4.750	0.21
0.45	2730	2.832	0.21				
Zn_III_pH8	5 mM						
0.80	2619	2.275	0.22	0.40	2660	3.004	0.19
0.75	2586	2.334	0.35	0.35	2648	3.164	0.18
0.70	2594	2.409	0.20	0.30	2693	3.347	0.16
0.65	2610	2.484	0.19	0.25	2663	3.571	0.18
0.60	2628	2.564	0.20	0.20	2697	3.864	0.17
0.55	2616	2.653	0.20	0.15	2743	4.278	0.15
0.50	2625	2.758	0.17	0.10	2778	4.923	0.06
0.45	2633	2.870	0.18				
Zn_IV_pH8	5 mM						
0.80	2424	2.274	0.34	0.40	2439	3.010	0.29
0.75	2514	2.337	0.33	0.35	3414	3.174	0.21
0.70	2501	2.401	0.36	0.30	2433	3.362	0.22
0.65	2458	2.476	0.33	0.25	2408	3.597	0.23
0.60	2498	2.566	0.30	0.20	2420	3.899	0.22
0.55	2490	2.656	0.28	0.15	2455	4.343	0.06
0.50	2431	2.759	0.34	0.10	2499	5.032	0.07
0.45	2448	2.875	0.25				
Zn_V_pH8	5 mM						
0.80	2709	2.284	0.12	0.40	2728	3.005	0.12
0.75	2699	2.343	0.12	0.35	2727	3.168	0.12
0.70	2705	2.408	0.15	0.30	2724	3.358	0.07
0.65	2648	2.487	0.13	0.25	2760	3.590	0.08
0.60	2708	2.567	0.12	0.20	2748	3.891	0.08
0.55	2696	2.657	0.11	0.15	2837	4.317	0.17
0.50	2713	2.756	0.13	0.10	2836	4.999	0.05
0.45	2728	2.873	0.12				

E (V)	R_s (Ω)	C_{sc} (nF)	ΔC_{sc} (%)	E (V)	R_s (Ω)	C_{sc} (nF)	ΔC_{sc} (%)
Zn_I_pH8	**0.5 mM**						
0.80	**2658**	**2.242**	**0.23**	**0.40**	**2670**	**2.932**	**0.18**
0.75	**2598**	**2.303**	**0.23**	**0.35**	**2704**	**3.079**	**0.17**
0.70	**2680**	**2.366**	**0.20**	**0.30**	**2708**	**3.255**	**0.13**
0.65	**2604**	**2.435**	**0.21**	**0.25**	**2700**	**3.466**	**0.15**
0.60	**2659**	**2.516**	**0.21**	**0.20**	**2738**	**3.732**	**0.14**
0.55	**2659**	**2.603**	**0.15**	**0.15**	**2753**	**4.112**	**0.08**
0.50	**2701**	**2.700**	**0.18**	**0.10**	**2797**	**4.679**	**0.09**
0.45	**2691**	**2.804**	**0.20**				
Zn_II_pH8	**0.5 mM**						
0.80	**2675**	**2.255**	**0.18**	**0.40**	**2706**	**2.963**	**0.17**
0.75	**2629**	**2.316**	**0.18**	**0.35**	**2716**	**3.118**	**0.11**
0.70	**2579**	**2.385**	**0.19**	**0.30**	**2696**	**3.297**	**0.10**
0.65	**2638**	**2.452**	**0.20**	**0.25**	**2724**	**3.512**	**0.12**
0.60	**2668**	**2.535**	**0.17**	**0.20**	**2724**	**3.791**	**0.12**
0.55	**2648**	**2.624**	**0.16**	**0.15**	**2759**	**4.183**	**0.12**
0.50	**2710**	**2.718**	**0.18**	**0.10**	**2801**	**4.781**	**0.11**
0.45	**2650**	**2.833**	**0.16**				
Zn_III_pH8	**0.5 mM**						
0.80	**2688**	**2.265**	**0.23**	**0.40**	**2768**	**2.949**	**0.43**
0.75	**2837**	**2.301**	**0.46**	**0.35**	**2682**	**3.118**	**0.19**
0.70	**2704**	**2.374**	**0.41**	**0.30**	**2732**	**3.290**	**0.19**
0.65	**2588**	**2.451**	**0.33**	**0.25**	**2712**	**3.504**	**0.14**
0.60	**2697**	**2.532**	**0.37**	**0.20**	**2753**	**3.783**	**0.18**
0.55	**2594**	**2.616**	**0.42**	**0.15**	**2758**	**4.168**	**0.16**
0.50	**2763**	**2.703**	**0.43**	**0.10**	**2798**	**4.755**	**0.15**
0.45	**2768**	**2.824**	**0.43**				
Zn_IV_pH8	**0.5 mM**						
0.80	**2613**	**2.276**	**0.32**	**0.40**	**2605**	**2.999**	**0.30**
0.75	**2513**	**2.340**	**0.27**	**0.35**	**2622**	**3.160**	**0.20**
0.70	**2577**	**2.404**	**0.31**	**0.30**	**2605**	**3.339**	**0.19**
0.65	**2633**	**2.482**	**0.29**	**0.25**	**2659**	**3.559**	**0.21**
0.60	**2536**	**2.564**	**0.31**	**0.20**	**2650**	**3.837**	**0.24**
0.55	**2569**	**2.653**	**0.28**	**0.15**	**2665**	**4.241**	**0.05**
0.50	**2569**	**2.754**	**0.29**	**0.10**	**2716**	**4.829**	**0.05**
0.45	**2574**	**2.872**	**0.23**				
Zn_V_pH8	**0.5 mM**						
0.80	**2647**	**2.291**	**0.09**	**0.40**	**2676**	**3.019**	**0.09**
0.75	**2630**	**2.350**	**0.13**	**0.35**	**2723**	**3.173**	**0.07**
0.70	**2659**	**2.417**	**0.12**	**0.30**	**2680**	**3.358**	**0.10**
0.65	**2638**	**2.492**	**0.08**	**0.25**	**2706**	**3.587**	**0.10**
0.60	**2648**	**2.573**	**0.06**	**0.20**	**2709**	**3.882**	**0.10**
0.55	**2667**	**2.665**	**0.07**	**0.15**	**2750**	**4.296**	**0.07**
0.50	**2632**	**2.768**	**0.10**	**0.10**	**2820**	**4.926**	**0.11**
0.45	**2680**	**2.886**	**0.06**				

than 100 kHz become somewhat difficult to execute due to the inductance of the connecting cables,[43] this relaxation process could not be explored in greater detail. The series resistance of the system was more or less constant with applied potential and on the order of 2600 Ω for electrode **ZnO1** and 6600 Ω for electrode **ZnO2**. It should be noted that this series resistance was only partly due to the high ohmic resistance of the sample. After the electrochemical measurements were completed, the ohmic resistance of the sample was determined by covering the front of the sample, which was originally exposed to the solution, with Ga-In eutectic. The measured impedance was purely resistive and as expected independent of frequency. The resistance was equal to 1000 Ω in the case of electrode **ZnO1** and equal to 2500 Ω in the case of electrode **ZnO2**. In accordance with the impedance spectra, the *J-E* characteristics were ohmic (i.e., linear) and showed no rectifying behavior due to a Schottky barrier at the semiconductor metal back contact. This indicates that the relaxation process that became visible at the highest frequencies was not due to a bulk property of the crystal or due to the back contact, but was a property of the semiconductor/liquid contact. Since surface state capacitances are typically on the order of 0.1 μF cm^{-2} for a surface state density of 10^{10}cm^{-2},[29] the relaxation process in question has a relaxation frequency (f_r) > 50 kHz and might therefore be associated with surface states since the relaxation frequency for this process would be $f_r = [C\text{ss}\times\text{area}\times R]^{-1} = [10^{-7}\times 0.255\times(2500-1000)]^{-1} = 10$ kHz.

Since the differential capacitance showed no signs of frequency dispersion or signs of large concentration-dependent shifts the differential capacitance was set equal to the space-charge capacitance. If this assumption is correct than the Mott-Schottky plot of C_{diff}^{-2} *vs. E* should be linear. According to Eq. 2.11, the dopant density can be calculated from the slope and the flat-band potential can be calculated from the intercept of the regression curve with the abscissa. The Mott-Schottky plots for junctions **ZnO1_I_pH8** to **ZnO1_V_pH8** are shown in Figure 2.5. The results of all C_{diff} *vs. E* measurements are summarized in Table 2.2. As expected, C_{diff}^{-2} *vs. E is* linear. The r^2 values were in all cases 0.998 or better. These regression factors are acceptable, although Mott-Schottky plots for ideal semiconductor/liquid junctions typically yield r^2 better than 0.999.[7]

With the knowledge of E_{fb} the surface electron concentration (n_s) can be computed both for equilibrium conditions and for the situation where a potential is applied to the back contact (see Eq. 2.3). Since E_{fb} enters the equation for n_s (see Eq. 2.3) and subsequently the equation for k_{et} (see Eq. 2.2) in the exponent, care was taken to determine E_{fb} in statistically meaningful ways. As mentioned above, the impedance data were fit to the equivalent circuit shown in Figure 2.2 (c). The fitting routine yielded an average parameter for C_{diff} and a value for its standard deviation (ΔC_{diff}). The standard deviation was in no case larger than 0.43 %. The three intercepts per acceptor concentration shown in Figure 2.5 correspond to the linear regression fits of C_{diff}, $C_{diff} + \Delta C_{diff}$, and $C_{diff} - \Delta C_{diff}$. The small standard deviations resulted in minimal shifts of E_{fb}, typically on the order of 2 mV. To prove the validity of the rate law, *j-E* measurements were carried out at two different acceptor concentrations. The lower accpetor concentrations (approximately 0.5 mM) were obtained by diluting the 5 mM solution by a factor of 10. To ensure that no shifts in the band-edge positions occurred during dilution, C_{diff} -E measurements were also carried for the diluted solutions. The results are listed in Table 2.2. For the vast majority of the junctions the band-edge positions remained stable within 15 mV following dilution. Junctions with differences in the flat-band potential of more than 25 mV were typically not considered for the determination of reliable rate constants. The E_{fb} values determined by extrapolation of data in the Mott-Schottky plots (see Figure 2.5) were: -0.155 V ± 0.001 V *vs.* SCE (low [A]) and -0.150 V ± 0.002 *vs.* SCE for junction **ZnO1_I_pH8** under low and high acceptor concentrations, respectively; -0.145 V ± 0.001 V *vs.* SCE (low [A]) and -0.147 V ± 0.001 *vs.* SCE (high [A]) for junction **ZnO1_II_pH8;** -0.147 V ± 0.001 V *vs.* SCE (low [A]) and -0.135 V ± 0.002 *vs.* SCE (high [A]) for **ZnO1_III_pH8**; -0.137 V ± 0.000 V *vs.* SCE (low [A]) and -0.132 V ±

Figure 2.5 Mott-Schottky Plots for Junctions ZnO1_I_pH8 to ZnO1_V_pH8.

Mott-Schottky plots for junctions **ZnO1_I_pH8** to **ZnO1_V_pH8**. In addition to Mott-Schottky plot covering the entire potential range, regions where the linear regression fits intercept with the abscissa are shown. In each plot data for high acceptor concentrations (5 mM, filled circles and dashed lines) and low accpetor concentrations (approximately 0.5 mM, open circles and solid lines) are shown. The three fits per acceptor concentration correspond to the actual fit of C_{diff}, $C_{\mathrm{diff}} + \Delta C_{\mathrm{diff}}$, and $C_{\mathrm{diff}} - \Delta C_{\mathrm{diff}}$. (a) **ZnO1_I_pH8**: E_{fb} = -0.155 V ± 0.001 V *vs.* SCE (low [A]), E_{fb} = -0.150 V ± 0.002 *vs.* SCE (high [A]), $N_{\mathrm{D}} = (1.17 \pm 0.02)\times10^{15}$ cm^{-3}. (b) **ZnO1_II_pH8**: E_{fb} = -0.145 V ± 0.001 V *vs.* SCE (low [A]), E_{fb} = -0.147 V ± 0.001 *vs.* SCE (high [A]) , $N_{\mathrm{D}} = (1.19 \pm 0.01)\times10^{15}$ cm^{-3}. (c) **ZnO1_III_pH8**: E_{fb} = -0.147 V ± 0.001 V *vs.* SCE (low [A]), E_{fb} = -0.135 V ± 0.002 *vs.* SCE (high [A]), $N_{\mathrm{D}} = (1.19 \pm 0.01)\times10^{15}$ cm^{-3}. (d) **ZnO1_IV_pH8**: E_{fb} = -0.137 V ± 0.000 V *vs.* SCE (low [A]), E_{fb} = -0.132 V ± 0.001 *vs.* SCE (high [A]), $N_{\mathrm{D}} = (1.20 \pm 0.02)\times10^{15}$ cm^{-3}. (e) **ZnO1_V_pH8**: E_{fb} = -0.142 V ± 0.001 V *vs.* SCE (low [A]), E_{fb} = -0.125 V ± 0.002 *vs.* SCE (high [A]), $N_{\mathrm{D}} = (1.19 \pm 0.02)\times10^{15}$ cm^{-3}. The geometrical surface area for the electrode was 0.255 cm^2.

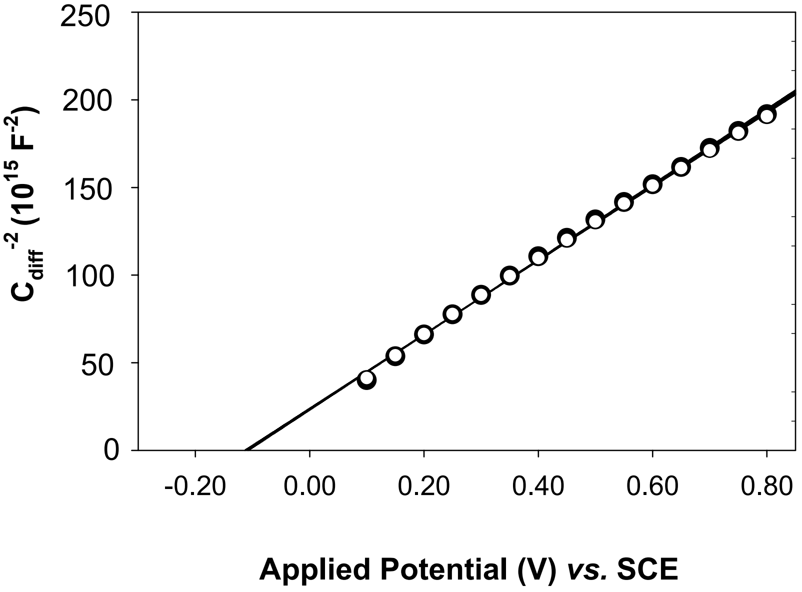
250
200
150
100
50
0
C_{diff}^{-2} (10^{15} F^{-2})
-0.20
0.00
0.20
0.40
0.60
0.80
Applied Potential (V) *vs.* SCE

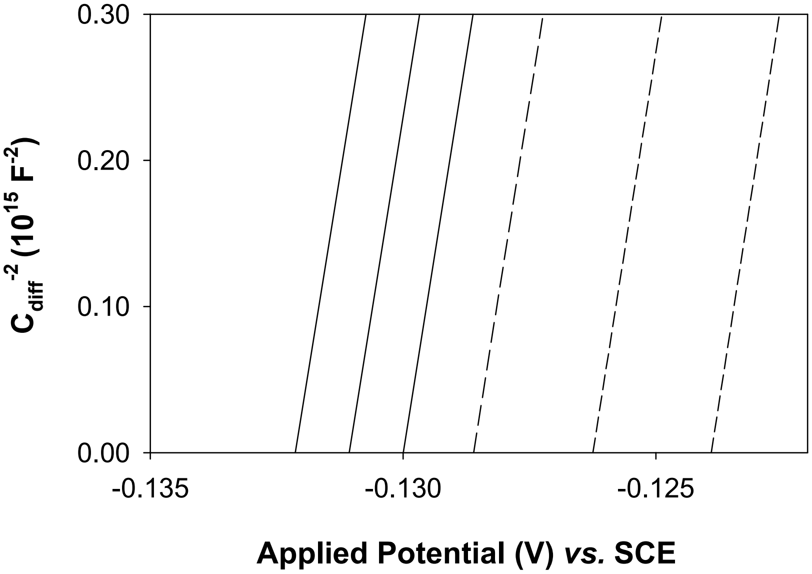
0.30
0.20
0.10
0.00
C_{diff}^{-2} (10^{15} F^{-2})
-0.135
-0.130
-0.125
Applied Potential (V) *vs.* SCE

Figure 2.5 (a)

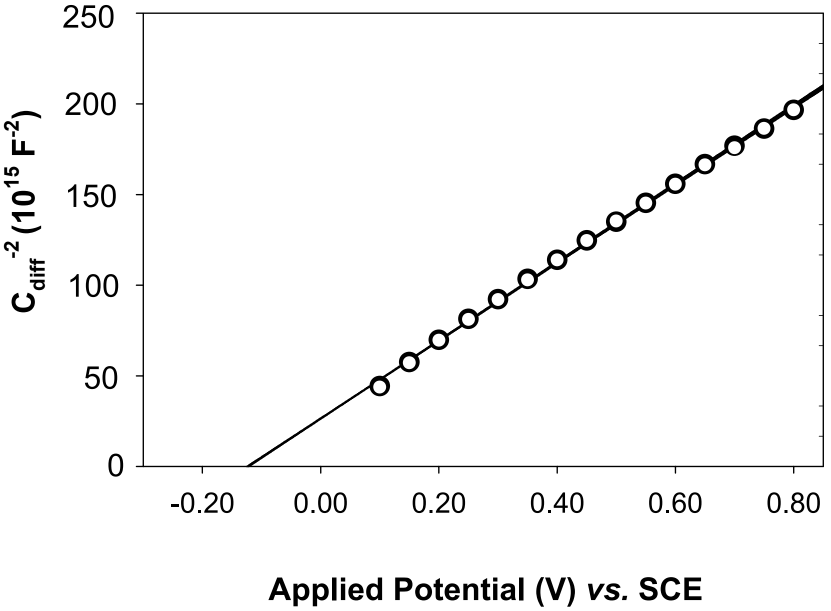
250
200
150
100
50
0
C_{diff}^{-2} (10^{15} F^{-2})
-0.20
0.00
0.20
0.40
0.60
0.80
Applied Potential (V) *vs.* SCE

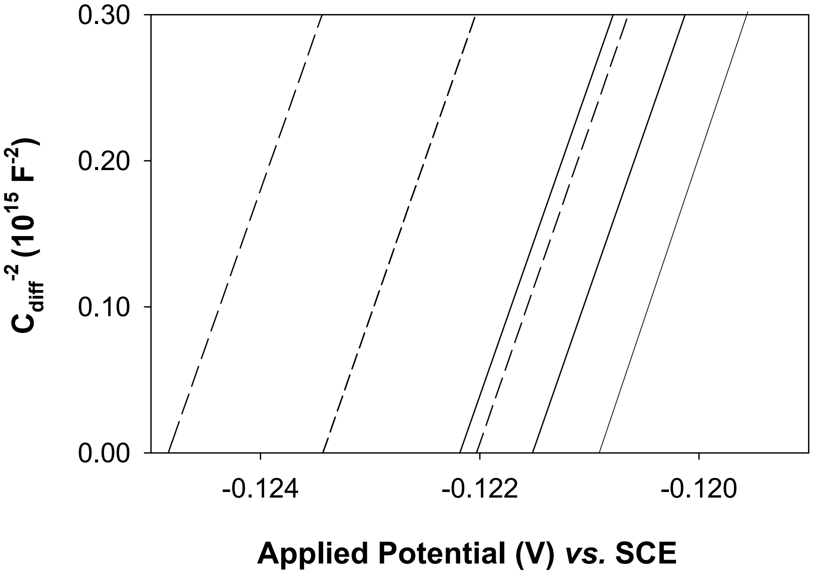
0.30
0.20
0.10
0.00
C_{diff}^{-2} (10^{15} F^{-2})
-0.124
-0.122
-0.120
Applied Potential (V) *vs.* SCE

Figure 2.5 (b)

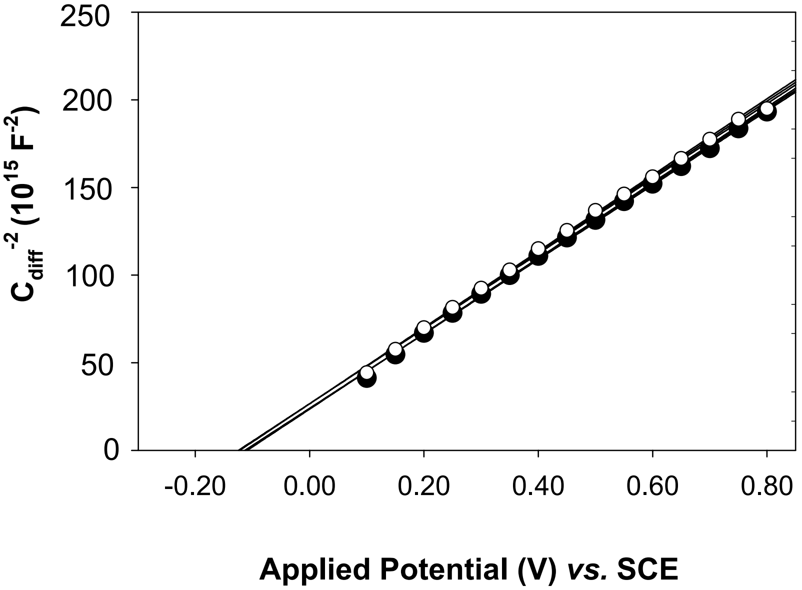

250
200
150
100
50
0
-0.20
0.00
0.20
0.40
0.60
0.80
C_{diff}^{-2} (10^{15} F^{-2})
Applied Potential (V) *vs.* SCE

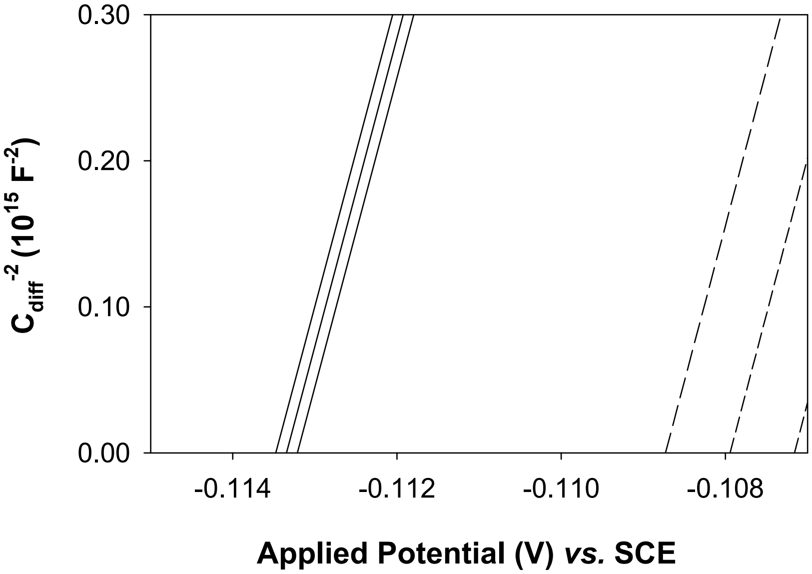

0.30
0.20
0.10
0.00
-0.114
-0.112
-0.110
-0.108
C_{diff}^{-2} (10^{15} F^{-2})
Applied Potential (V) *vs.* SCE

Figure 2.5 (c)

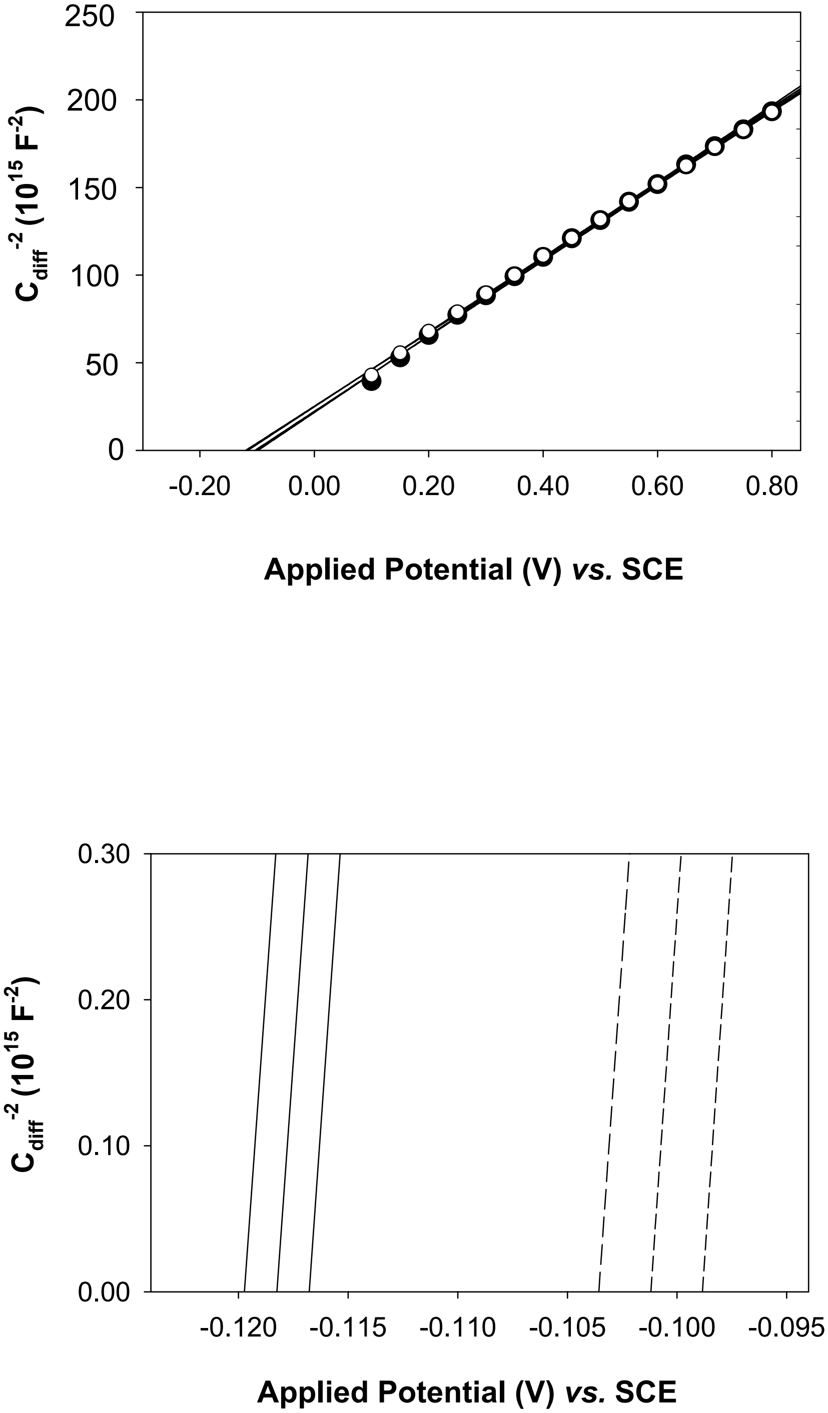
250
200
150
100
50
0
C_{diff}^{-2} (10^{15} F^{-2})
-0.20
0.00
0.20
0.40
0.60
0.80
Applied Potential (V) *vs.* SCE
0.30
0.20
0.10
0.00
C_{diff}^{-2} (10^{15} F^{-2})
-0.120
-0.115
-0.110
-0.105
-0.100
-0.095
Applied Potential (V) *vs.* SCE

Figure 2.5 (d)

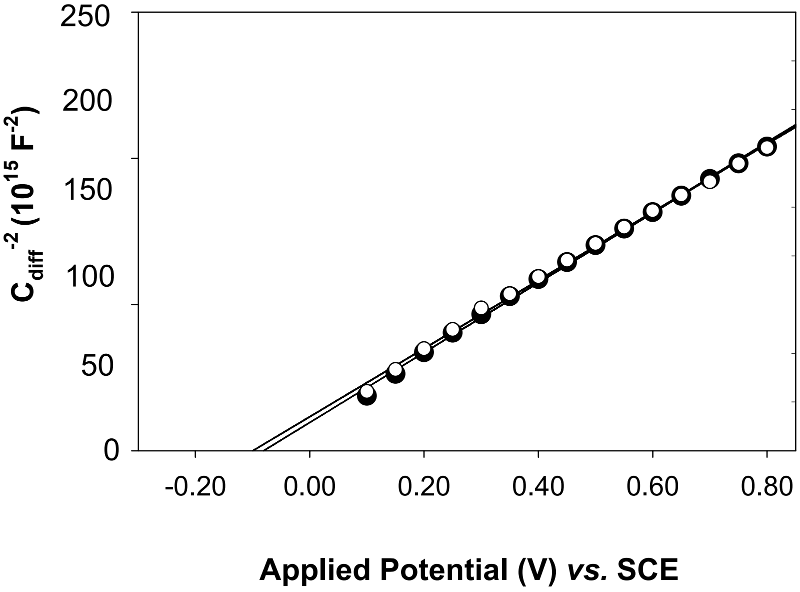
C_{diff}^{-2} (10^{15} F^{-2})
250
200
150
100
50
0
-0.20
0.00
0.20
0.40
0.60
0.80
Applied Potential (V) *vs.* SCE

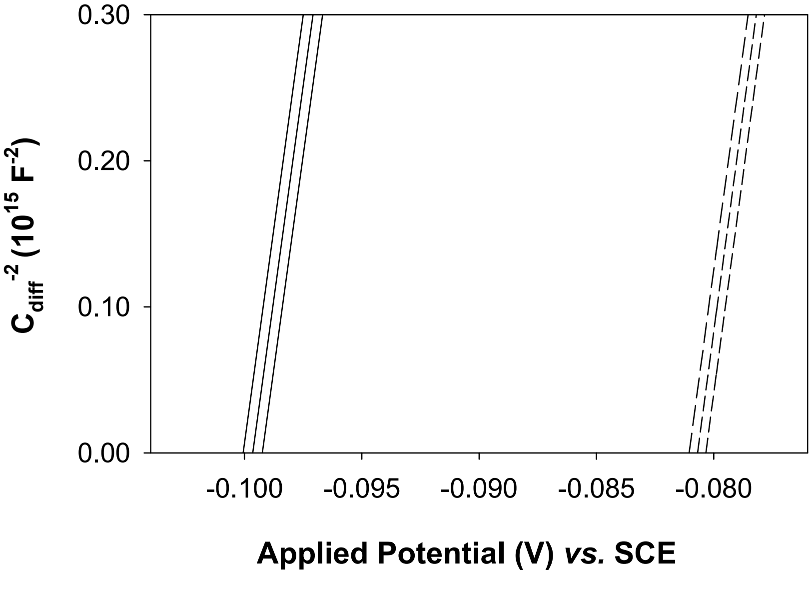
C_{diff}^{-2} (10^{15} F^{-2})
0.30
0.20
0.10
0.00
-0.100
-0.095
-0.090
-0.085
-0.080
Applied Potential (V) *vs.* SCE

Figure 2.5 (e)

TABLE 2.2. Average values of the flat-band potential (E_{fb}) and of the dopant density (N_{D}) for the n-ZnO(0001)/liquid junctions.

The subscripts “5 mM” and “0.5 mM” denote high and low acceptor concentrations,

	E_{fb} (V) *vs.* SCE	10^{15} N_{D} (cm^{-3})	$E_{\text{fb, 0.5 mM.}}$	10^{15} $N_{\text{D, 5 mM}}$	$E_{\text{fb, 0.5 mM.}}$	10^{15} $N_{\text{D, 0.5 mM}}$
ZnO1_I_pH6.8	**-0.069±0.014**	**1.15±0.01**	**-0.082**	**1.15**	**-0.056**	**1.16**
ZnO1_II_pH6.8	**-0.092±0.006**	**1.15±0.01**	**-0.087**	**1.14**	**-0.097**	**1.15**
ZnO1_IV_pH6.8	**-0.048±0.007**	**1.15±0.02**	**-0.042**	**1.13**	**-0.054**	**1.16**
ZnO1_V_pH6.8	**-0.071±0.002**	**1.16±0.01**	**-0.071**	**1.16**	**-**	**-**
ZnO1_I_pH8	**-0.152±0.003**	**1.17±0.02**	**-0.150**	**1.16**	**-0.155**	**1.18**
ZnO1_II_pH8	**-0.146±0.001**	**1.19±0.01**	**-0.147**	**1.19**	**-0.145**	**1.19**
ZnO1_III_pH8	**-0.141±0.007**	**1.19±0.01**	**-0.135**	**1.20**	**-0.147**	**1.18**
ZnO1_IV_pH8	**-0.134±0.003**	**1.20±0.01**	**-0.132**	**1.19**	**-0.137**	**1.21**
ZnO1_V_pH8	**-0.133±0.010**	**1.19±0.02**	**-0.125**	**1.18**	**-0.142**	**1.21**
ZnO1_I_pH6.0	**-0.010±0.013**	**1.24±0.00**	**-0.022**	**1.24**	**0.001**	**1.24**
ZnO1_I_pH7.8	**-0.130±0.007**	**1.24±0.01**	**-0.123**	**1.24**	**-0.136**	**1.24**
ZnO1_IV_pH6	**0.042±0.013**	**1.23±0.01**	**0.030**	**1.22**	**0.054**	**1.23**
ZnO1_IV_pH7.8	**-0.100±0.002**	**1.33±0.01**	**-0.101**	**1.33**	**-0.098**	**1.34**

	E_{fb} (V) *vs.* SCE	10^{15} N_{D} (cm^{-3})	$E_{\text{fb, 0.5 mM.}}$	10^{15} $N_{\text{D, 5 mM}}$	$E_{\text{fb, 0.5 mM.}}$	10^{15} $N_{\text{D, 0.5 mM}}$
ZnO2_I_pH6.8	**-0.069±0.014**	**1.15±0.01**	**-0.082**	**1.15**	**-0.056**	**1.16**
ZnO2_II_pH6.8	**-0.127±0.006**	**1.60±0.01**	**-0.121**	**1.60**	**-0.132**	**1.61**
ZnO2_IV_pH6.8	**-0.114±0.010**	**1.63±0.02**	**-0.104**	**1.61**	**-0.123**	**1.65**
ZnO2_I_pH8	**-0.193±0.006**	**1.66±0.01**	**-0.188**	**1.65**	**-0.198**	**1.67**
ZnO2_II_pH8	**-0.187±0.014**	**1.63±0.05**	**-0.174**	**1.59**	**-0.199**	**1.67**
ZnO2_III_pH8	**-0.192±0.012**	**1.68±0.01**	**-0.182**	**1.67**	**-0.203**	**1.68**
ZnO2_IV_pH8	**-0.180±0.001**	**1.65±0.01**	**-0.180**	**1.66**	**-0.180**	**1.64**
ZnO2_V_pH8	**-0.181±0.009**	**1.68±0.01**	**-0.173**	**1.68**	**-0.190**	**1.69**
ZnO2_I_pH6.5	**-0.014±0.001**	**1.19±0.01**	**-0.013**	**1.18**	**-0.014**	**1.19**
ZnO2_II_pH6.5	**-0.030±0.003**	**1.15±0.02**	**-0.032**	**1.13**	**-0.028**	**1.16**
ZnO2_III_pH6.5	**-0.007±0.008**	**1.23±0.03**	**0.001**	**1.21**	**-0.014**	**1.26**
ZnO2_IV_pH6.5	**0.001±0.007**	**1.28±0.01**	**0.008**	**1.27**	**-0.005**	**1.29**
ZnO2_V_pH6.5	**-0.018±0.002**	**1.23±0.02**	**-0.016**	**1.21**	**-0.019**	**1.24**

0.001 *vs.* SCE (high [A]) for **ZnO1_IV_pH8**; -0.142 V ± 0.001 V *vs.* SCE (low [A]) and -0.125 V ± 0.002 *vs.* SCE (high [A]) **ZnO1_V_pH8**. The results obtained for the remaining junctions are summarized in Table 2.2. Under depletion conditions, the slope of the Mott-Schottky plots can be used to determine the dopant density (N_D), see Eq. 2.11. For a given electrode and pH the dopant densities were essentially equal within acceptable deviations. The dopant density of electrode **ZnO1** averaged over all junctions was $(1.20 \pm 0.05)\times10^{15}$ cm^{-3} and the average N_D of electrode **ZnO2** was $(1.65 \pm 0.03)\times10^{15}$ cm^{-3}. After repolishing electrode **ZnO2** (data set: **ZnO2_I_pH6.5-ZnO2_V_pH6.5**) the dopant density shifted to significantly lower values $(1.22 \pm 0.05)\times10^{15}$ cm^{-3}. Individual results are shown in Table 2.2.

An alternative and statistically meaningful way of determining the E_{fb} of a ZnO electrode in contact with an electrolyte of constant pH is to plot the barrier height (Φ_B) at the formal reduction potential as a function of the formal reduction potential. The formal reduction potential was experimentally determined by measuring the half-wave potential ($E_{1/2}$) *vs.* SCE. According to Eq. 2.12, this should result in a linear relationship with a slope of 1. The intercept should correspond to the position of the conduction-band edge ($\boldsymbol{E}_{\mathbf{cb}}$). Barrier heights were computed using Eq. 2.12 and the averaged values of E_{fb} and N_D for a given junction (average of low and high accpetor concentrations). The results of this approach are depicted in Figure 2.6 (a) and Figure 2.6 (b) for electrode **ZnO1** and **ZnO2**, respectively. The $\boldsymbol{E}_{\mathbf{cb}}/q$ value was -0.303 ± 0.007 V *vs.* SCE for junctions involving **ZnO1** and a buffer solution of pH 8 (**ZnO1_I_pH8-ZnO1_V_pH8**). At pH 6 the $\boldsymbol{E}_{\mathbf{cb}}/q$ value was -0.230 ± 0.032 V *vs.* SCE (**ZnO1_I_pH6.8-ZnO1_V_pH6.8)**. The $\boldsymbol{E}_{\mathbf{cb}}/q$ value for electrode **ZnO2** corresponded to -0.350 ± 0.009 V *vs.* SCE and -0.182 ± 0.014 V *vs.* SCE, for electrodes in contact with buffer of pH 8 (**ZnO2_I_pH8-ZnO2_V_pH8**) and buffer of pH 6.5 (**ZnO2_I_pH6.5-ZnO2_V_pH6.5**), respectively.

Figure 2.6 Plot of the Barrier Height *vs.* $E_{1/2}$ for Various n-ZnO(0001) Semiconductor/Liquid Contacts.

(a) Electrode **ZnO1**: Each compound is represented by a roman numeral. Filled circles denote data recorded at pH 8 (see Table 2.2: **ZnO1_I_pH8-ZnO1_V_pH8**); the linear regression slope was 1.043 and the r^2-value was 0.9996. The $\boldsymbol{E}_{\mathbf{cb}}/q$ value corresponds to the x-intercept and was -0.303 ± 0.007 V *vs.* SCE. Open circles denote data recorded at pH 6.8 (see Table 2.2: **ZnO1_I_pH6.8-ZnO1_V_pH6.8**); the linear regression slope was 1.051 and the r^2-value was 0.994. The $\boldsymbol{E}_{\mathbf{cb}}/q$ value corresponds to the x-intercept and was -0.230 ± 0.032 V *vs.* SCE. (b) Electrode **ZnO2**: Each compound is represented by a roman numeral. Filled circles denote data recorded at pH 8 (see Table 2.2: **ZnO2_I_pH8-ZnO2_V_pH8**); the linear regression slope was 1.025 and the r^2-value was 0.9995. The $\boldsymbol{E}_{\mathbf{cb}}/q$ value corresponds to the x-intercept and was -0.350 ± 0.009 V *vs.* SCE. Open circles denote data recorded at pH 6.5 for a repolished electrode (see Table 2.2: **ZnO2_I_pH6.5-ZnO2_V_pH6.5**); the linear regression slope was 1.038 and the r^2-value was 0.996. The $\boldsymbol{E}_{\mathbf{cb}}/q$ value corresponds to the x-intercept and was -0.182 ± 0.014 V *vs.* SCE.

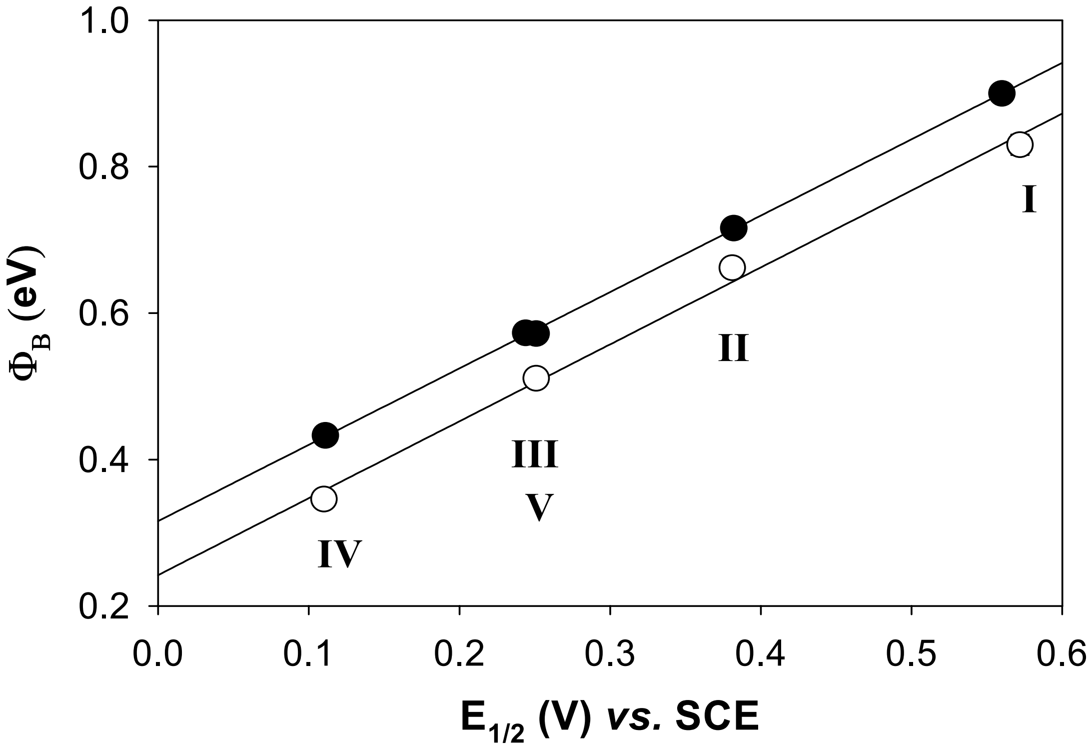

Figure 2.6 (a)

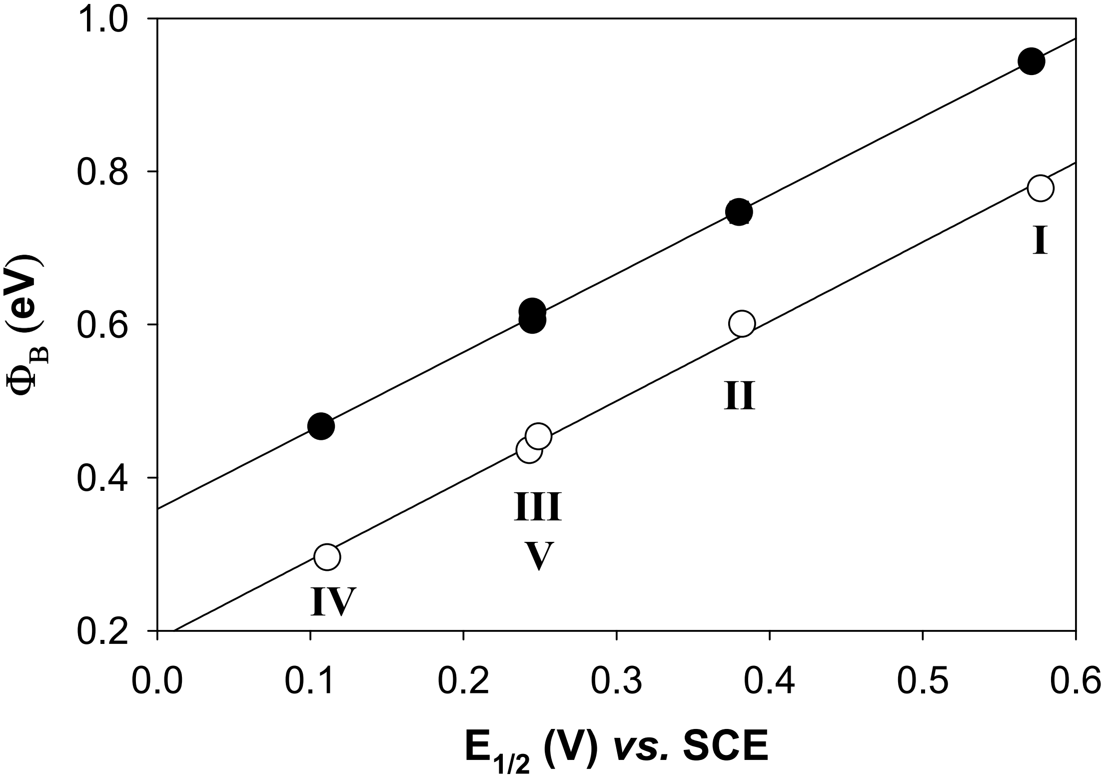

Figure 2.6 (b)

According to Eq. 2.4, E_{fb} and Φ_B of ZnO should shift by 54.2 mV ($2.3\times k_BT/q$) for every pH unit change.[29, 33-35] The measured shifts in E_{fb} and Φ_B compared favorably with the theoretical predictions. Changing the pH from 8 to 6.8 should result in a positive 65 mV shift in the band-edge position *vs.* SCE. The measured shift of **ZnO1** was 73 mV. The predicted shift the E_{fb} of **ZnO2** following a pH change from 8 to 6.5 is 81 mV; the measured shift was 72 mV.

The differences in the E_{fb} values of electrode **ZnO1** and **ZnO2** are noteworthy. Both electrodes were nominally from the same batch. The difference in N_D cannot account for the differences in E_{fb} as the dopant density would have to be almost an order of magnitude higher to account for the 50 mV difference. Morrison and co-workers[13, 14] mention unaccounted for differences in the flat-band potential of crystals of nominally identical N_D. These shifts were as high as 70 mV. It is difficult to compare the experimentally determined flat-band potentials of approximately -0.15 V to -0.18 V *vs.* SCE with data from the literature, since these reports are not in agreement with each other. Dewald mapped out the dependence of E_{fb} on the dopant density and the pH. According to Dewald's results, the E_{fb} at $N_D = 1.2\times10^{15}$ cm^{-3} can be estimated to be approximately -0.36 V *vs.* SCE.[20, 21] According to the results in Morrison's report, on the other hand , crystals with $N_D = 1.2\times10^{15}$ cm^{-3} should have a $E_{fb} = -0.14$ V *vs.* SCE, which compares favorably with the results of measurements reported in this study.[13, 14]

2.4.2 Results of *J-E* Measurements

All junctions presented in this study showed rectifying behavior and consequently followed the diode equation (Eq. 2.8). The cathodic current increased exponentially with bias and the anodic current showed limiting behavior, typical for diodes. The measured currents were low enough to be limited completely by kinetics and not by mass transport. Due the high cell resistance (see Table 2.1) the current×resistance drop (*JR* drop) was on the order of 30 mV for the highest currents measured in this study and thus the applied potential had to be corrected accordingly. In addition, the *J-E* data of some junctions were corrected for the concentration overpotential. Both corrective measures are explained in detail in Chapter 2.3.2 (Eq. 2.6 and Eq. 2.7). .

It should be noted that ZnO/liquid junctions with ideal diode quality factors and ideal potential shifts are a result of a careful optimization of the experimental system under investigation. Diode quality factors and potential shifts of ZnO in contact with Os compounds tended to be non-ideal ($\gamma > 1.5$) if the electrode was exposed to electrolytes of pH 8.7 or lower containing $[Fe(CN)_6]^{3-/4-}$. Since the point of zero charge (p.z.c) of ZnO is estimated to be close to 8.7[20, 21, 44, 45] the negatively charged $[Fe(CN)_6]^{3-/4-}$ might adsorb to the surface and introduce surface states in the energy gap. A lack of acceptor concentration dependence was noticed for some Os redox couple at pH > 8.00 indicating that the positively charged acceptor might adsorb to the surface at pH > p.z.c. Attempts to employ non-aqueous solvents like acetonitrile yielded non ideal junction characteristics with $\gamma \sim 2.00$, despite reports indicating ideal junction kinetics in acetonitrile.[22] When the same electrode was immersed into aqueous solutions $\gamma \sim 1$ were recorded.

Figure 2.7 (a)-(e) shows the dark *J-E* curves for five representative n-ZnO/liquid junctions (**ZnO1_I_pH8** to **ZnO1_V_pH8**). The applied potential (*E*) was corrected for the *JR* drop only. The diode quality factors (γ) and potential shifts following dilution are compiled in Table 2.3 for all junctions. The theoretical shifts were determined by measuring the limiting currents for the reduction of the accpetor species with a Pt microelectrode before and after *J-E* measurements. The expected shift corresponds to $(RT/F)\times\ln(J_{high,lim}/J_{low,lim})$. Diode quality factors were determined by fitting the J-E_{corr} characteristics with respect to the diode equation (Eq. 2.8). The maximum tolerable deviation of the measured shift from the theoretically expected value was set to 15 mV. Data with higher deviations were not considered for the determination of robust rate

Figure 2.7 Dark *J*-E_{corr} Characteristics for Junctions ZnO1_I_pH8 to ZnO1_V_pH8.

The shift as the solution was diluted by a factor of 10 is shown. The applied potential is referenced with respect to SCE and was corrected for the ohmic drop due to the cell resistance (R_{cell} ~ 2600 Ω). A tenfold higher acceptor concentration is expected to shift the *J*-*E* by 54.2 mV. Filled circles denote an acceptor concentration of 5 mM and open circles denote an acceptor concentration of approximately 0.5 mM. As detailed in the text the theoretical shifts were determined by measuring the limiting currents for the reduction of the accpetor species with a Pt microelectrode. Diode quality factors were determined by fitting the *J*-E_{corr} characteristics with respect to the diode equation (Eq. 2.8) (a) **ZnO1_I_pH8:** The shift was 37 mV (theor.: 52 mV), the diode quality factors for the high and low acceptor concentration were 1.02 and 1.05, respectively. (b) **ZnO1_II_pH8:** The shift was 53 mV (theor.: 53 mV), the diode quality factors for the high and low acceptor concentration were 1.02 and 1.08, respectively. (c) **ZnO1_III_pH8:** The shift was 51 mV (theor.: 54 mV), the diode quality factors for the high and low acceptor concentration were 1.02 and 1.03, respectively. (d) **ZnO1_IV_pH8:** The shift was 52 mV (theor.: 48 mV), the diode quality factors for the high and low acceptor concentration were 1.02, 1.03, respectively. (e) **ZnO1_V_pH8:** The shift was 63 mV (theor.: 54 mV), the diode quality factors for the high and low acceptor concentration were 1.04, 1.09, respectively. The geometrical surface area for the electrode was 0.255 cm^2.

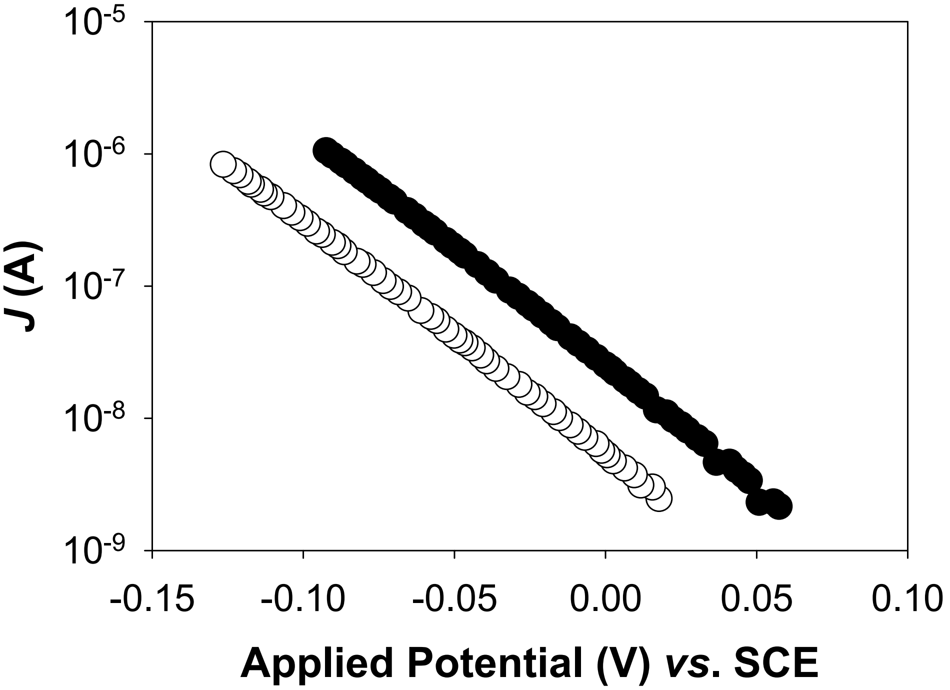
10-5
10-6
10-7
10-8
10-9
J (A)
-0.15
-0.10
-0.05
0.00
0.05
0.10
Applied Potential (V) *vs*. SCE

Figure 2.7 (a)

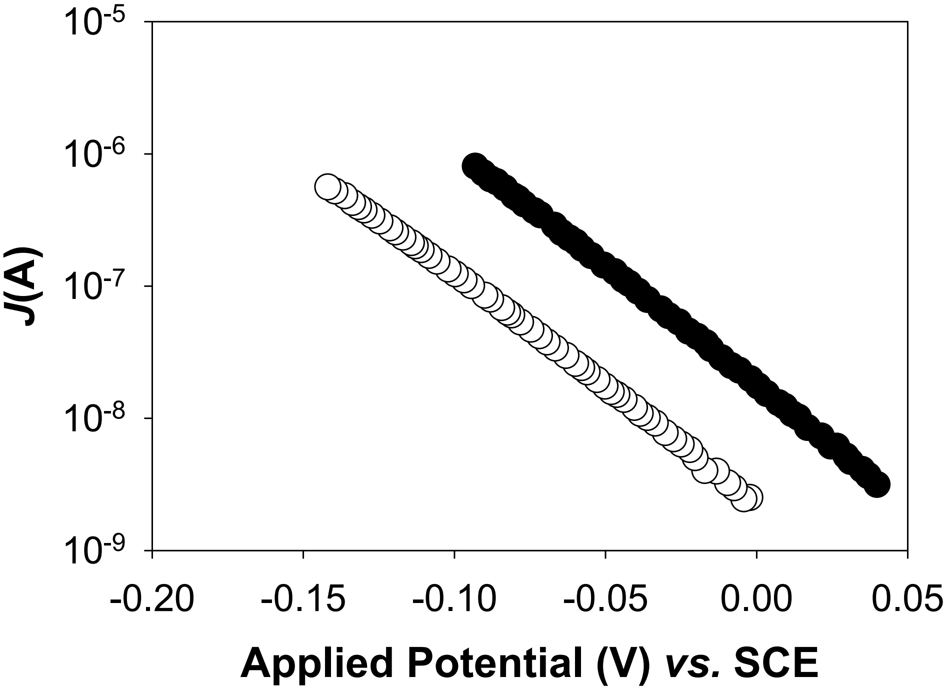

10^{-5}
10^{-6}
10^{-7}
10^{-8}
10^{-9}
J(A)
-0.20
-0.15
-0.10
-0.05
0.00
0.05
Applied Potential (V) *vs.* SCE

Figure 2.7 (b)

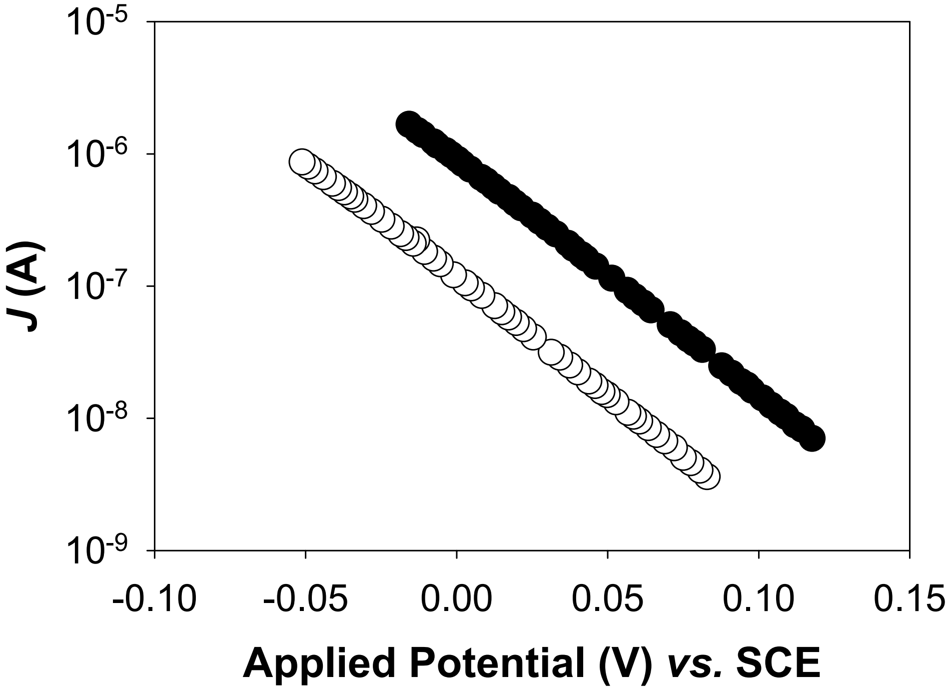

10^{-5}
10^{-6}
10^{-7}
10^{-8}
10^{-9}
J (A)
-0.10
-0.05
0.00
0.05
0.10
0.15
Applied Potential (V) *vs.* SCE

Figure 2.7 (c)

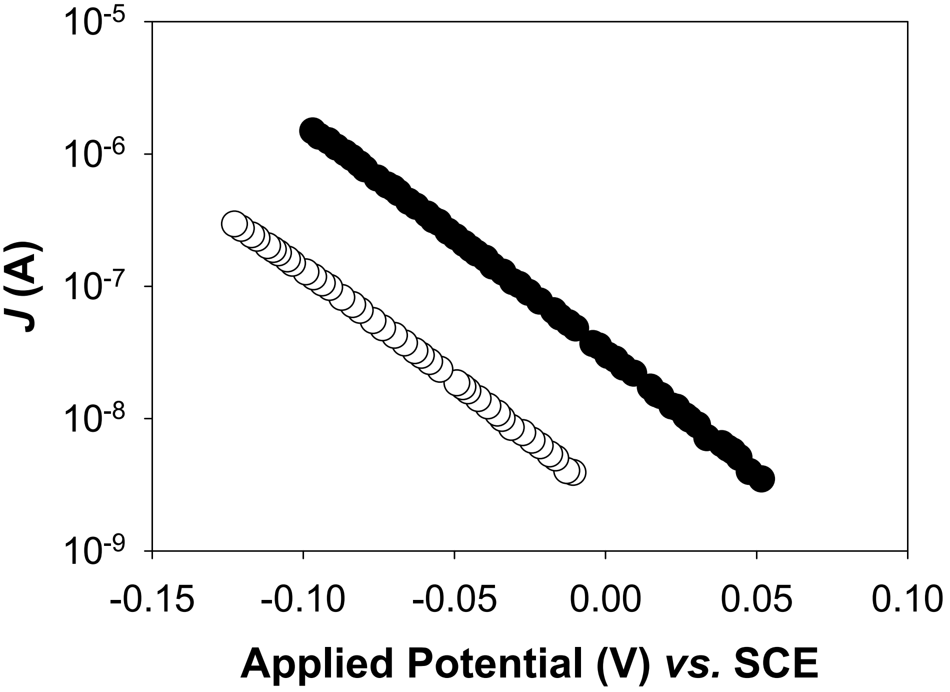
10^{-5}
10^{-6}
10^{-7}
10^{-8}
10^{-9}
J (A)
-0.15
-0.10
-0.05
0.00
0.05
0.10
Applied Potential (V) *vs.* SCE

Figure 2.7 (d)

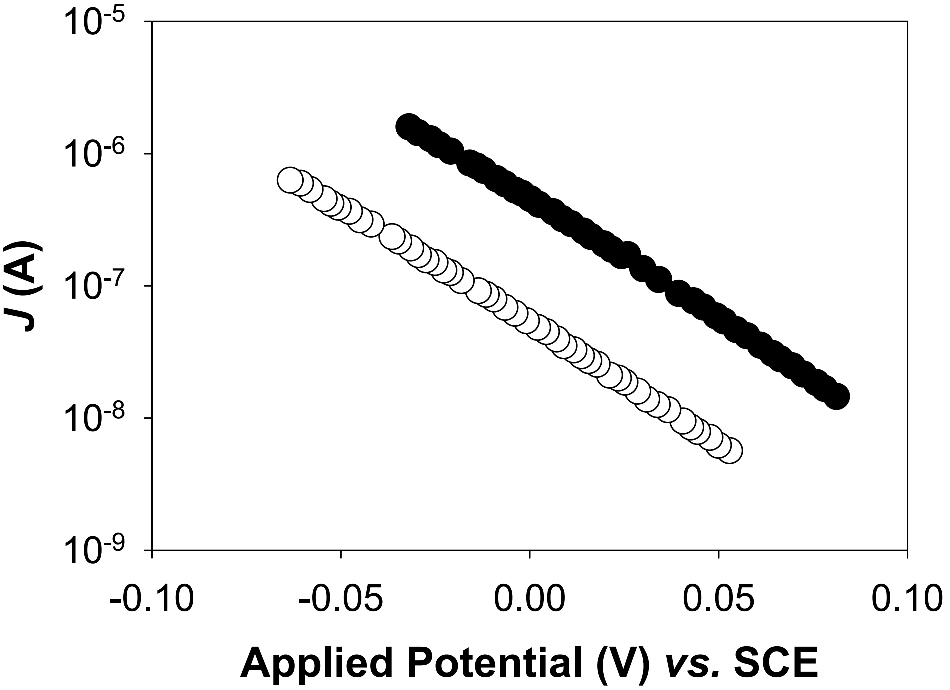
10^{-5}
10^{-6}
10^{-7}
10^{-8}
10^{-9}
J (A)
-0.10
-0.05
0.00
0.05
0.10
Applied Potential (V) *vs.* SCE

Figure 2.7 (e)

TABLE 2.3. *J-E* Data for n-ZnO(0001)/liquid junctions

	γ (5 mM)	**γ (0.5 mM)**	**E shift (theor. value) (mV)**
ZnO1_I_pH6.8	1.05	1.06	37 (47)
ZnO1_II_pH6.8	1.05	1.06	85 (70)
ZnO1_IV_pH6.8	1.04	1.07	58 (52)
ZnO1_V_pH6.8	1.06	1.1	38 (48)
ZnO1_I_pH8	1.02	1.05	37 (52)
ZnO1_II_pH8	1.02	1.08	53 (53)
ZnO1_III_pH8	1.02	1.03	51 (54)
ZnO1_IV_pH8	1.02	1.03	52 (48)
ZnO1_V_pH8	1.04	1.09	62 (54)
ZnO1_I_pH6.0	1.07	1.08	42 (51)
ZnO1_I_pH7.8	1.06	1.06	52 (58)
ZnO1_IV_pH6	1.02	1.11	55 (50)
ZnO1_IV_pH7.8	1.01	1.03	48 (52)

	γ (5 mM)	**γ (0.5 mM)**	**E shift (theor. value) (mV)**
ZnO2_I_pH6.8	1.05	1.06	48 (47)
ZnO2_II_pH6.8	1.03	1.1	67 (70)
ZnO2_IV_pH6.8	1.02	1.03	54 (52)
ZnO2_I_pH8	1.04	1.06	40 (52)
ZnO2_II_pH8	1.04	1.09	52 (53)
ZnO2_III_pH8	1.03	1.03	52 (54)
ZnO2_IV_pH8	1.03	1.03	53 (48)
ZnO2_V_pH8	1.05	1.11	50 (54)
ZnO2_I_pH6.5	1.08	1.08	48 (50)
ZnO2_II_pH6.5	1.04	1.07	45 (54)
ZnO2_III_pH6.5	1.05	1.03	40 (49)
ZnO2_IV_pH6.5	1	1.02	64 (65)
ZnO2_V_pH6.5	1.04	1.06	50 (60)

constants. The *J-E* data in Figure 2.7 (a)-(e) are plotted as ln(-*J*) *vs*. E_{corr}. After correcting for the cell resistance and in some instances for the concentration overpotential, *J-E* data resulted in excellent linearity for the ln(-*J*) *vs. E* plots. For junction **ZnO1_I_pH8** the shift was 37 mV (theor.: 52 mV) and the γ values for high and low acceptor concentrations were 1.02 and 1.05, respectively. Junction **ZnO1_II_pH8** had a potential shift of 53 mV (theor.: 53 mV) and the γ values for high and low acceptor concentration were 1.02 and 1.08, respectively. For **ZnO1_III_pH8** the shift was 51 mV (theor.: 54 mV) and the γ values for high and low acceptor concentration were 1.02 and 1.03, respectively. Junction **ZnO1_IV_pH8** had a potential shift of 52 mV (theor.: 48 mV) and the γ values for high and low acceptor concentration were 1.02, 1.03, respectively. Finally, junction **ZnO1_V_pH8:** showed a potential shift of 63 mV (theor.: 54 mV) and γ values for high and low acceptor concentrations of 1.04, 1.09, respectively.

The fact that the measured potential shifts corresponded so closely to the theoretically predicted values indicates that all junction listed in Table 2.3 were pseudo-first order in acceptor concentration. Diode quality factors close to 1.0 attested that in addition all of the junctions in this investigation were pseudo-first order in surface electron concentration. The *J-E* data were therefore very robust and introduced little ambiguity in the determination of k_{et} values. Compared to other semiconductor/liquid junctions, the diode quality factors and potential shifts of n-ZnO/liquid junctions are of unprecedented ideality. Fajardo *et al.* report diode quality factors as large as 1.4 and deviations in the potential shifts as high as 20 mV as being acceptable for the determination of the rate constants at n-Si/CH_3OH junctions.[7, 8]

2.4.3 Determination of Electron-Transfer Rate Constants (k_{et})

The excellent adherence of electron-transfer processes at the ZnO/liquid interface to the rate law, allows robust rate constants (k_{et}) to be computed. This is done by dividing

TABLE 2.4. Barrier heights (Φ_B) and rate constants (k_{et}) for n-ZnO(0001)/liquid junctions.

	Φ_B(eV)	$E_{1/2}$ (V) *vs* SCE	10^{-19} k_{et} (cm^4 s^{-1})	10^{-19} k_{et} (cm^4 s^{-1}) *
ZnO1_I_pH6.8	0.830±0.014	0.572	1.6±1.0	1.0±0.7
ZnO1_II_pH6.8	0.662±0.006	0.381	3.2±1.8	1.6±1.2
ZnO1_IV_pH6.8	0.346±0.007	0.110	2.1±1.8	6.8±5.8
ZnO1_V_pH6.8	0.511±0.002	0.251	1.4±0.7	1.4±1.1
ZnO1_I_pH8	0.900±0.003	0.560	1.0±0.4	0.7±0.3
ZnO1_II_pH8	0.716±0.001	0.382	0.6±0.2	0.5±0.2
ZnO1_III_pH8	0.573±0.007	0.244	20.9±8.3	27.0±9.6
ZnO1_IV_pH8	0.433±0.003	0.111	8.8±3.5	8.9±3.1
ZnO1_V_pH8	0.572±0.010	0.251	0.7±0.3	0.9±0.3
ZnO1_I_pH6.0	0.778±0.013	0.581	0.9±0.5	0.5±0.3
ZnO1_I_pH7.8	0.886±0.007	0.570	0.3±0.1	0.3±0.1
ZnO1_IV_pH6	0.269±0.013	0.124	0.3±0.2	2.4±2.0
ZnO1_IV_pH7.8	0.405±0.002	0.120	1.5±0.4	3.1±1.3

* alternative way of k_{et} determination (method B, see text for details)

	Φ_B(eV)	$E_{1/2}$ (V) *vs* SCE	10^{-19} k_{et} (cm^4 s^{-1})	10^{-19} k_{et} (cm^4 s^{-1}) *
ZnO2_I_pH6.8	0.834 ± 0.014	0.576	1.6±1.0	3.8±2.4
ZnO2_II_pH6.8	0.686±0.006	0.379	4.1±1.9	3.9±1.5
ZnO2_IV_pH6.8	0.405±0.010	0.111	8.1±3.8	16.0±6.3
ZnO2_I_pH8	0.944±0.006	0.571	2.7±1.3	2.6±0.7
ZnO2_II_pH8	0.747±0.014	0.380	1.0±0.5	1.8±0.5
ZnO2_III_pH8	0.617±0.012	0.245	20.9±10.0	69.1±18.6
ZnO2_IV_pH8	0.467±0.001	0.107	28.3±13.5	38.0±10.3
ZnO2_V_pH8	0.606±0.009	0.245	0.9±0.4	1.5±0.4
ZnO2_I_pH6.5	0.778±0.001	0.577	0.3±0.2	0.6±0.3
ZnO2_II_pH6.5	0.601±0.003	0.382	0.3±0.1	0.2±0.1
ZnO2_III_pH6.5	0.436±0.008	0.243	2.2±1.3	4.3±2.5
ZnO2_IV_pH6.5	0.296±0.007	0.111	0.7±0.4	1.9±1.1
ZnO2_V_pH6.5	0.454±0.002	0.249	0.3±0.2	0.3±0.2

the current density (j) by ($qn_s[A]$), see Eq. 2.2. The acceptor concentration in Eq. 2.2 was assumed to be identical with the bulk value, which is considered to be a fair assumption for semiconductor electrodes.[46] The accpetor concentration was adjusted to the desired value by means of bulk electrolysis, so its value is known with high accuracy. The determination of k_{et} values is restricted to junctions with ideal energetics and potential shifts following dilution, which are close to the theoretical values. The determination of k_{et} was restricted to j-E data that were obtained for high acceptor concentrations (5 mM). The surface electron concentrations as a function of applied potential $n_s(E)$ was computed according to Eq. 2.3. Since the diode quality factors were close to unity, which indicates that J changed with E according to the diode equation, recombination mechanisms involving surface states can be ruled out. This means that statistically valid k_{et} values can be obtained simply by computing and then averaging k_{et} values over the entire forward bias range. It should be noted that other approaches in the literature had to restrict the computation of k_{et} values exclusively to the highest j values, because $\gamma > 1$ suggest that only at high j values charge transfer prevails over recombination pathways with higher γ values.[7, 8, 30] The biggest ambiguity in the present study is introduced by the relatively large standard deviations found for E_{fb}. The flat-band potential enters Eq. 2.3 in the exponent and even small deviations in E_{fb} have a dramatic effect on n_s and subsequently on k_{et}. A 55 mV uncertainty in E_{fb} for instance causes an order of magnitude change in k_{et}! To get a statistically relevant error estimate of the rate constant (Δk_{et}) a standard Gaussian error analysis was performed. The formula for Δk_{et} and the individual partial differentials with respect to [A], the surface area (A), E_{fb} and N_D are listed in Eq. 2.13.

$$\Delta k_{et} = \sqrt{\left(\frac{\partial k_{\mathrm{et}}}{\partial [A]}\right)^2_{\substack{E_{\mathrm{fb}},\\ A, N_{\mathrm{D}}}} \cdot (\Delta [A])^2 + \left(\frac{\partial k_{\mathrm{et}}}{\partial E_{\mathrm{fb}}}\right)^2_{\substack{[A],\\ A, N_{\mathrm{D}}}} \cdot (\Delta E_{\mathrm{fb}})^2 + \left(\frac{\partial k_{\mathrm{et}}}{\partial A}\right)^2_{\substack{E_{\mathrm{fb}},\\ [A], N_{\mathrm{D}}}} \cdot (\Delta A)^2 + \left(\frac{\partial k_{\mathrm{et}}}{\partial N_{\mathrm{D}}}\right)^2_{\substack{E_{\mathrm{fb}},\\ [A], A}} \cdot (\Delta N_{\mathrm{D}})^2}$$

$$\left(\frac{\partial k_{\mathrm{et}}}{\partial [A]}\right)_{\substack{E_{\mathrm{fb}},\\ A, N_{\mathrm{D}}}} = -\frac{k_{\mathrm{et}}}{[A]};\ \left(\frac{\partial k_{\mathrm{et}}}{\partial E_{\mathrm{fb}}}\right)_{\substack{[A],\\ A, N_{\mathrm{D}}}} = k_{\mathrm{et}} \cdot \frac{q}{k_B T};\ \left(\frac{\partial k_{\mathrm{et}}}{\partial A}\right)_{\substack{E_{\mathrm{fb}},\\ [A], N_{\mathrm{D}}}} = -\frac{k_{\mathrm{et}}}{\mathrm{A}};\ \left(\frac{\partial k_{\mathrm{et}}}{\partial N_{\mathrm{D}}}\right)_{\substack{E_{\mathrm{fb}},\\ [A], A}} = -\frac{k_{\mathrm{et}}}{N_{\mathrm{D}}} \qquad \text{(Eq. 2.13)}$$

Parameters $\Delta[A]$, ΔA, ΔE_{fb}, and ΔN_{D} denote the absolute errors in $[A]$, A, E_{fb} and N_{D}, respectively. The error for $\Delta[A]$ was chosen to be 1.506×10^{17} cm^{-3} and ΔA was chosen to be 0.02 cm^2.

As detailed in Chapter 2.4.1, two methods were used to statistically evaluate the junction energetics. Flat-band potentials and N_{D} values were determined for an individual semiconductor/liquid junction (specific electrode, redox couple, acceptor concentration and pH value) and an average value and standard deviation was calculated for E_{fb} and N_{D} considering the error from the fitting results of C_{diff}. Since high $[A]$ data were used in the determination of k_{et}, one way of computing k_{et} values of a given junction is to use the values of E_{fb} and N_{D} obtained for high $[A]$. This avoids the introduction of systematic errors by including an averaged value and is the method of choice if the E_{fb} values are considered to be accurate (method A). The rate constants computed in this way are listed together with the values for the barrier height ($\Phi_{\mathrm{B})}$ in Table 2.4. As values for ΔE_{fb}, and ΔN_{D}, the standard deviations obtained from the high and low $[A]$ data were considered. Since E_{fb} should be constant for a given electrode and pH, an alternative way of computing k_{et} values is to use the data obtained from the Φ_{B} *vs.* $E_{1/2}$, see Figure 2.6 (a)-(b). This approach results in an averaged value and standard deviation for the conduction-band edges ($\boldsymbol{E}_{\mathbf{cb}}$) by means of a linear regression method, which is representative for a specific electrode rather than a specific semiconductor/liquid contact. These averaged values for $\boldsymbol{E}_{\mathbf{cb}}$ can be easily converted into E_{fb} values and were used together with mean values for N_D to compute k_{et} (method B). The results of this alternative approach are presented in Table 2.4 (right most column). With one notable exception (**ZnO1_IV_pH6.0)**, k_{et} values computed by these two different methods gave results that either were within the range of error or introduced no significant deviations of the overall trend.

2.4.4 Trends in the k_{et} Values for n-Zn(0001)/Liquid Contacts.

In order to compare the rate constants with one another, ideally both the reorganization energies (λ) and electronic coupling elements need to be precisely known or need to be constant for the series of contacts under investigation. Since the reorganization energy enters the Frank Condon factor (see Eq. 2.5) in the exponent, knowledge of λ is of outmost importance. The reorganization energies (λ) of selected Os-polybipyridyl compounds were measured by means of NMR line broadening techniques[23] for the same experimental conditions that prevailed during charge-transfer rate measurements. The measurements were carried out in a pH 7.8 imidazole buffer (D_2O, 1 M KCl, deuterated imidazole + DCl) and in pH 5 buffer (D_2O, 1 M KCl, deuterated pthalic acid and DOH, $\vartheta \sim 2\ ^oC$). The self-exchange rate constant (k_{ex}) of $[Os(bpy)_2(4\text{-}Meim)_2]^{3+/2+}$ (this is a protonated analog to $[Os(bpy)_2(Him)_2]^{3+/2+}$) at pH 7.8 was $(1.10 \pm 0.33)\times10^8\ s^{-1}$, which corresponds to $\lambda = 0.66 \pm 0.04$ eV. The self-exchange rate constant of $[Os(bpy)_2(n\text{-}Meim)_2]^{3+/2+}$ at pH 7.8 was $(1.02 \pm 0.40)\times10^8\ s^{-1}$, which corresponds to $\lambda = 0.65 \pm 0.03$ eV. The self-exchange rate constant of $[Os(dmbpy)_3]^{3+/2+}$ at pH 7.8 was $(1.09 \pm 0.00)\times10^8\ s^{-1}$, which corresponds to $\lambda = 0.65 \pm 0.00$ eV. The reorganization energy of $[Os(dmbpy)_3]^{3+/2+}$ was re-measured in pH 5 buffer and gave the same result as in pH 7.8 buffer.

The values of λ are similar enough to allow for a direct comparison of k_{et} in terms of their electrochemical driving force and electronic coupling dependence. Selected k_{et}

Figure 2.8 Plots of Electron-Transfer Rate Constants (k_{et}) *vs.* Driving Force for Charge Transfer.

The determination of the rate constants is detailed in the text. The $\Delta G^{o'}$ values correspond to the barrier height values for equal accpetor and donor concentration ([A]=[A$^-$]). The data used to generate the plots are summarized in Table 2.4. Circles correspond to redox couple **I**, triangles down corresponds to redox couple **II**, squares correspond to redox couple **III**, diamonds correspond to redox couple **IV**, and triangles up correspond to redox couple **V**. (a) Data for **ZnO1_I_pH8-ZnO1_V_pH8** (filled symbols) and **ZnO2_I_pH8-ZnO2_V_pH8** (open symbols). (b) Data for **ZnO1_I_pH8**-**ZnO1_V_pH8** (filled symbols) and **ZnO1_I_pH6.8-ZnO1_V_pH6.8** (open symbols). (c) Data for **ZnO1_I_pH8** and **ZnO1_IV_pH8** (filled symbols) and **ZnO1_I_pH6** and **ZnO1_IV_pH6** (open symbols). Arrows indicate the shift in k_{et} when the pH of the buffer is lowered.

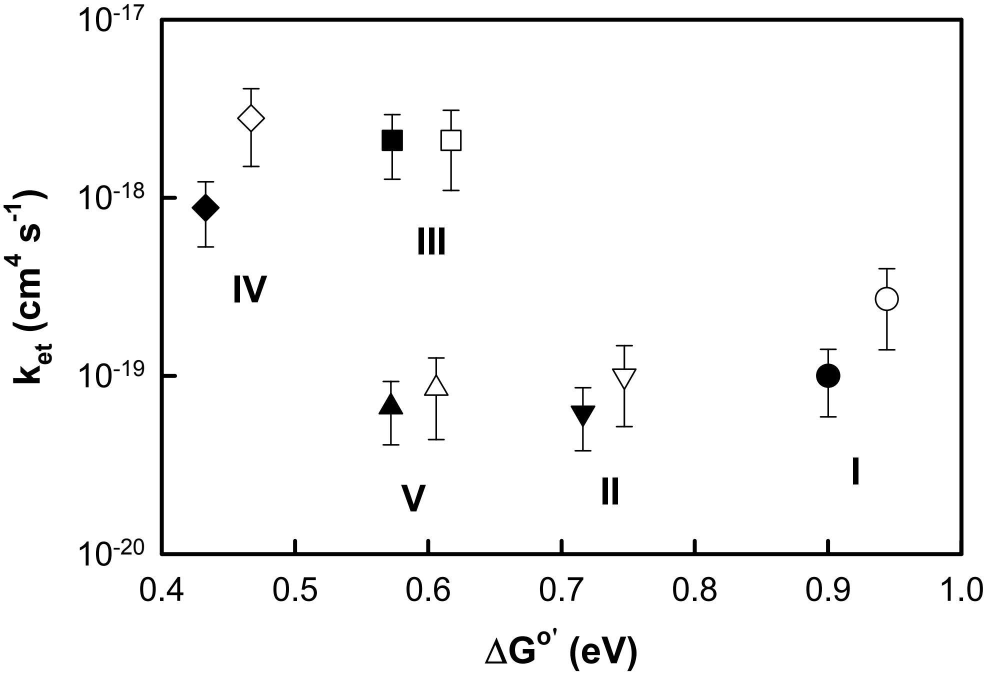
10^{-17}
10^{-18}
10^{-19}
10^{-20}
k_{et} (cm^4 s^{-1})
IV
III
V
II
I
0.4
0.5
0.6
0.7
0.8
0.9
1.0
$\Delta G^{o'}$ (eV)

Figure 2.8 (a)

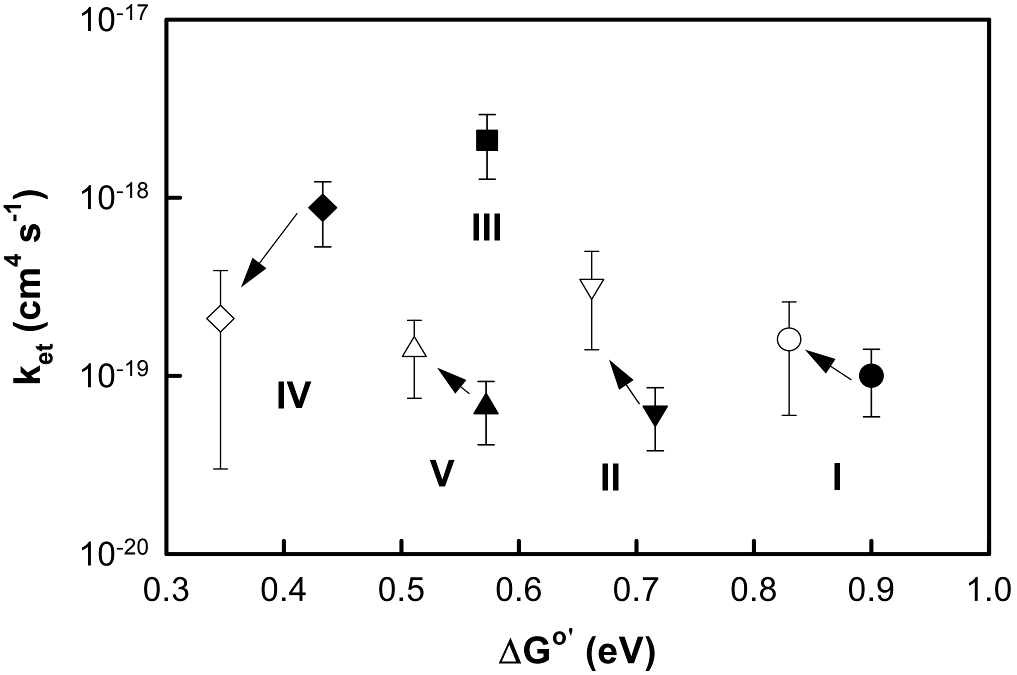
10^{-17}
10^{-18}
10^{-19}
10^{-20}
k_{et} (cm^4 s^{-1})
III
IV
V
II
I
0.3
0.4
0.5
0.6
0.7
0.8
0.9
1.0
$\Delta G^{o'}$ (eV)

Figure 2.8 (b)

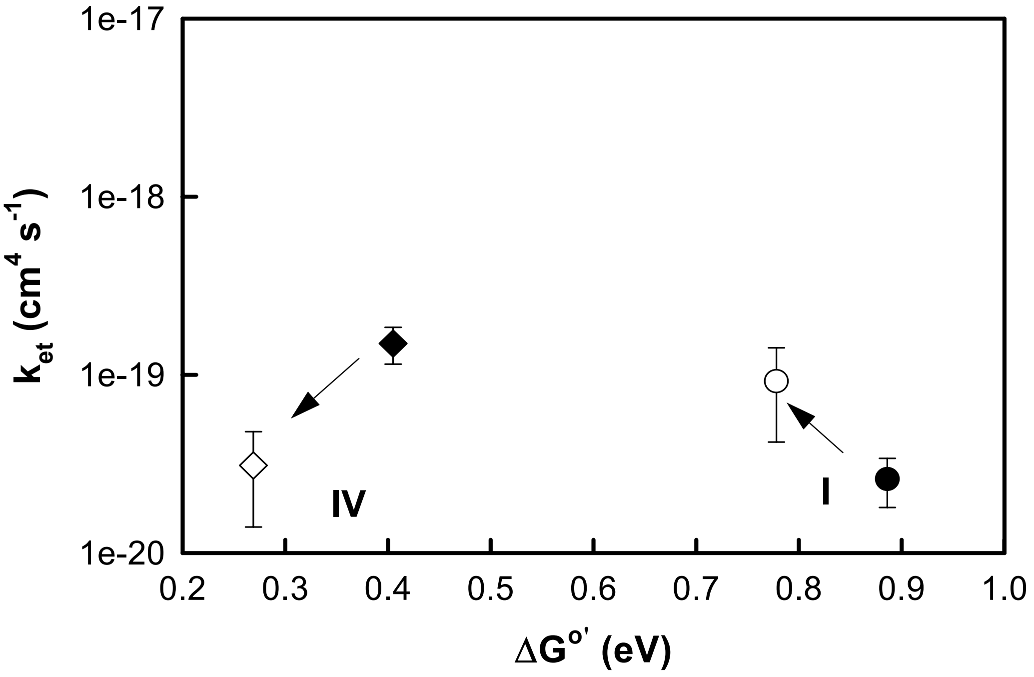
1e-17
1e-18
1e-19
1e-20
k_{et} (cm^4 s^{-1})
0.2
0.3
0.4
0.5
0.6
0.7
0.8
0.9
1.0
$\Delta G^{o'}$ (eV)
IV
I

Figure 2.8 (c)

values (computed using method A) are depicted in Figure 2.8 (a)-(c). The results at pH 8 for electrodes **ZnO1** and **ZnO2** are depicted in Figure 2.8 (a) for comparison. Although the k_{et} values for these two electrodes were somewhat different, the overall trend is comparable. The k_{et} values obtained for redox compound **III** were (20.9 ± 8.3)×10^{-19} cm^4 s^{-1} (**ZnO1_III_pH8**, Φ_B = 0.573 ± 0.007 eV) and (20.9 ± 10.0)×10^{-19} cm^4 s^{-1} (**ZnO2_III_pH8**, Φ_B = 0.617 ± 0.012 eV). The barrier height of this contact was similar to the reorganization energy of 0.66 eV and indicates that compound **III** operated close to the point of optimum exoergicity, see Eq. 2.5. The redox compound exhibiting the largest driving force for electron transfer, compound **I,** consistently gave lower k_{et} values than compound **III**: (1.0 ± 0.4)×10^{-19} cm^4 s^{-1} (**ZnO1_I_pH8**, Φ_B = 0.900 ± 0.003 eV) and (2.7 ± 1.3)×10^{-19} cm^4 s^{-1} (**ZnO2_I_pH8**, Φ_B = 0.944 ± 0.006 eV). Redox compound **II** followed this trend. Its rate constants, however, were slightly smaller than those of compound **I**, see Table 2.4. The redox compound with the lowest driving force, compound **IV**, had rate constants similar to those of compound **III**, (8.8 ± 3.5)×10^{-19} cm^4 s^{-1} (**ZnO1_IV_pH8**, Φ_B = 0.433 ± 0.003 eV) and (28.3 ± 13.5)×10^{-19} cm^4 s^{-1} (**ZnO2_IV_pH8**, Φ_B = 0.467±0.001 eV). Given the structural similarities of compound **V** and compound **III** and the similar driving forces for electron transfer, the rate constants obtained for n-ZnO in contact with **V** differed remarkably from those obtained for n-ZnO/ **III**: (0.7 ± 0.3)×10^{-19} cm^4 s^{-1} (**ZnO1_IV_pH8**, Φ_B = 0.572 ± 0.010 eV) and (0.9 ± 0.4)×10^{-19} cm^4 s^{-1} (**ZnO2_IV_pH8**, Φ_B = 0.467 ± 0.001 eV).

The observed trend for changes in k_{et} with pH are presented in Figure 2.8 (b) and (c). These experiments are especially interesting because they provide an alternative way of changing the driving force for electron transfer without changing the nature of the redox compound thereby keeping parameters like the electronic matrix element constant. In the case of electrode **ZnO1** the observed dependence of k_{et} with pH seems to suggest that the rate constant of electron transfer from ZnO to compound **I** and **II** increased with decreasing driving force. The rate constants for junctions **ZnO1_I_pH6.8** and **ZnO1_II_pH6.8** were $(1.6 \pm 1.0)\times10^{-19}$ cm^4 s^{-1} ($\Phi_B = 0.830 \pm 0.014$ eV) and $(3.2 \pm 1.8)\times10^{-19}$ cm^4 s^{-1} ($\Phi_B = 0.662 \pm 0.006$ eV). This trend was also observed for compound **I** at pH 6, see Table 2.4 and Figure 2.8 (c) (note that measurements at pH 6 and pH 7.8 were taken immediately after each other). With the exception of compound **V,** the reverse trend was observed for redox compounds with lower driving force. Compound **IV** showed a lower k_{et} at pH 6.8 and pH 6.0 than at pH 8, $k_{et} = (2.1 \pm 1.8)\times10^{-19}$ cm^4 s^{-1} (**ZnO1_IV_pH6.8**, $\Phi_B = 0.346 \pm 0.007$ eV) and $(0.3 \pm 0.2)\times10^{-19}$ cm^4 s^{-1} (**ZnO1_IV_pH6.0**, $\Phi_B = 0.269 \pm 0.013$ eV). For electrode **ZnO2** not enough results are available for a valid comparison of the rate constants. The measurements at pH 6.5 were taken after the electrode was repolished and this introduced a large shift in the flat-band potential and in the linear regression slope of the Mott-Schottky plot. A comparison of this data set with the rate constants at pH 8 therefore seems to be inappropriate.

Measurements at pH values smaller than 6.00 resulted in non-rectifying behavior for compounds with a low driving force, despite the fact that the driving force was still larger than 3 k_BT. At low pH values the surface of the ZnO electrode showed rapid signs of degradation, so measurements were restricted to pH values larger than 6.00.

2.4.5 Rate Constants of n-ZnO in Contact with $[Fe(CN)_6]^{3-/4-}$, $[Co(bpy)_3]^{3+/2+}$, or $[Ru(NH_3)_5py]^{3+/2+}$

In an earlier part of this study the reorganization energy dependence of ZnO/liquid contacts was studied.[47] The results of these measurements are presented in Table 2.5. The differential capacitance measurements showed ideal energetics. The junctions showed no frequency dispersion of the differential capacitance and the r^2 value for Mott-Schottky plots was typically 0.999 or better. Electrode **ZnO3** had a dopant density $N_D = 8\times10^{16}$ cm^{-3}. The flat-band potential of the as-received crystal was -0.212 ± 0.014 V *vs.* SCE

(**ZnO3_VIII_pH8.7**) and subsequently changed to -0.124 ± 0.012 V (**ZnO3_VIII_pH8.7a**) *vs.* SCE and -0.153 ± 0.014 V *vs.* SCE after repolishing (**ZnO3_VI_pH8.7**). The crystallographic orientation of the crystals was determined by single-crystal X-ray diffractometry and no significant changes in the orientation were detected before and after repolishing. It should be noted that despite higher dopant densities and higher pH values, E_{fb} values are more positive than the E_{fb} values of **ZnO1** and **ZnO2**.

With *J-E* measurements of n-ZnO/$[Fe(CN)_6]^{3-/4-}$ (compound **VIII**) contacts, we have confirmed previous reports[14-16] on the adherence of this system to the ideal rate law. The n-ZnO/$[Co(bpy)_3]^{3+/2+}$contact (compound **VI**) is another example of such an ideal system. However, the rate of interfacial electron transfer at n-ZnO in contact with $[Ru(NH_3)_5py]^{3+/2+}$ (compound **VII**) was found to be independent of the acceptor concentration, which might indicate that **VII** adsorbs to the surface, for instance via hydrogen bonds to the hydroxylated surface of n-ZnO. The results for n-ZnO/$[Fe(CN)_6]^{3-/4-}$ contacts, $k_{et} = (1.1 \pm 0.6)\times10^{-20}$ cm^4 s^{-1} and $\Phi_B = 0.6$ eV, agree well with Morrison's result of $k_{et} = 3\times10^{-20}$ cm^4 s^{-1} and $\Phi_B = 0.7$ eV. It is not clear whether $[Fe(CN)_6]^{3-/4-}$ can be used for further mechanistic studies of interfacial rate constants, since speculations about kinetic complications and cation effects were reported for rate constant measurements at metal electrodes.[48, 49] Compound **VIII** had a reorganization energy (λ) of 1.5 eV,[50-53] which according to Eq. 2.5 results in a $k_{et,max}$ of 2×10^{-17} cm^4 s^{-1}, which is in accordance with theoretical predictions.[37] Trisbipyridinecobalt(III/II) on the other hand is a very well-studied one-electron transition metal complex, for which the above stated complications do not exist. Hence this compound is particularly suited for mechanistic studies of k_{et}. The rate constant for electron transfer for this contact was found to be extremely small, $k_{et} = (2 \pm 0.4)\times10^{-25}$ cm^4 s^{-1}. The reorganization energy of compound **VI** is approximately 2.3 eV,[24] which is very high in comparison with the λ of Os-

TABLE 2.5. Results of rate constant measurements involving electrode ZnO3 and redox compounds **VI**, **VII**, **VIII**.

Experiments	γ **[-]**	**E shift [mV]**	$10^{-17} N_D$ **[cm^{-3}]**	$\Delta G^{o\prime}$ **[eV]**	k_{et} **[cm^4/sec]**
ZnO3_VIII_ph8.7 [a]	1.13	60 (61)	0.8	0.600±0.014	$(1.1\pm0.6)\times10^{-21}$
70/7 mM ([A]/[A]$^-$)					
7/7 mM (([A]/[A]$^-$)	1.10				
ZnO3_VIII_pH8.7a [b]	1.10	60 (61)	0.79	0.510±0.012	$(5\pm2)\times10^{-23}$
70/7 mM ([A]/[A]$^-$)					
7/7 mM ([A]/[A]-)	1.11	70(64)			
0.7/7 mM ([A]/[A]-)	1.14				
ZnO3_VII_pH7.0 [c]	1.05	0 (34)	0.9	0.350±0.012	N/A
7/1 mM ([A]/[A]$^-$)					
3.16/1 mM ([A]/[A]$^-$)	1.10				
ZnO3_VI_pH8.7 [d]	1.08	62 (61)	0.78	0.310±0.010	$(2.0\pm0.4)\times10^{-25}$
10/1 mM ([A]/[A]-)					
1/1 mM ([A]/[A]$^-$)	1.07				

[a] electrode used as received

[b] same electrode as in [a]; electrode was repolished

[c] same electrode as in [a]; re-etched

[d] same electrode as in [a]; repolished

polybipyridyl redox compounds ($\lambda = 0.66$ eV) or $[Fe(CN)_6]^{3-/4-}$($\lambda = 1.5$ eV). No literature values are available with which to compare the rate constant of n-ZnO/**VI** contacts, but the agreement of $k_{et,max} = 4\times10^{-18}$ cm^4 s^{-1} with the theoretical prediction especially in direct comparison with $[Fe(CN)_6]^{3-/4-}$, is satisfactory and gives a first indication for a pronounced reorganization energy dependence of k_{et}.

2.5 DISCUSSION

The most striking feature of n-ZnO/H_2O(A/A^-) contacts presented in this study are their ideal *J-E* characteristics. In prior studies most of the semiconductor/liquid junctions did not observe the simple rate law of Eq. 2.2.[9-11, 54, 55] Semiconductor/liquid junctions with rates that are first order in both the acceptor and surface electron concentration are therefore the exception rather than the rule. That is why most efforts to investigate the influence of driving force and reorganization energy on interfacial rate constants have thus been thwarted. With *J-E* measurements of n-ZnO/$[Fe(CN)_6]^{3-/4-}$ contacts, we have confirmed previous reports[14-16] on the adherence of this system to the ideal rate law. The n-ZnO/$[Co(bpy)_3]^{3+/2+}$ and n-ZnO/$[OsL_2L']^{3+/2+}$ contacts are further examples for such ideal systems.

In the first part of this chapter, the energetic behavior of n-ZnO/liquid contacts will be discussed with a special focus on the true value of the flat-band potential and the influence of surface states. In the second part the kinetic behavior of the n-ZnO/liquid contacts will be discussed in terms of the Marcus formalism.

2.5.1 Energetic Behavior of n-ZnO(0001)/Liquid Contacts

Following Morrison's and Dewald's discussion of the energetic behavior of ZnO[13-15, 20, 21] and the arguments used in numerous other reports,[10, 11, 29, 32-34] a straightforward explanation for the lack of frequency dispersion of C_{diff} is that the applied potential drops exclusively within the electrode leaving potentials at the solution side (Helmholtz) invariant. Therefore, it seems to be adequate to set the differential capacitance equal to the space-charge capacitance and analyze the results through use of the Mott-Schottky equation. A further implication of the above statement is that values for the flat-band potential must be independent of the concentration and nature of the acceptor species. This was shown to be the case for any given measurement series employing the same electrode with a maximum standard deviation of E_{fb} on the order of 15 mV.

No straightforward explanation, however, can be given at first sight for inconsistent E_{fb} values for different ZnO electrodes of nominally the same dopant density other than that these differences have its origins in different surface conditions. Morrison reports a standard deviation for E_{fb} of approximately 70 mV.[14] Despite the low frequency dispersion, the maximum deviation of E_{fb} for different electrodes of the same batch was 30 mV (**ZnO1** and **ZnO2**) and 90 mV (**ZnO3**). Especially, repolishing introduced large shifts in the flat-band potential although the crystallographic orientation was preserved during polishing and the surface showed no compositional changes as confirmed by X-ray photoelectron spectroscopy. The absence of a relaxation process in the impedance spectra associated with surface states and excellent diode quality factors do not necessarily imply that there are no surface states present at the n-ZnO/$H_2O(A/A^-)$ interface. One possibility is of course that the relaxation process associated with surface states is beyond the frequency range used in the impedance measurements. Another possibility is that the surface state capacitance does not appear in the impedance spectra of the semiconductor/ liquid contact because the surface states are desorbable or not reversibly charged within the period of the AC-signal.[14] Under certain conditions Gomes[56] was able to find evidence for a surface state capacitance in the impedance of n-ZnO/H_2O contacts. The appearance of a surface state capacitance was, however, accompanied by a strong frequency dispersion of C_{diff}, which was absent in this study.

Figure 2.9 Influence of Trap States on Mott-Schottky Plots.

The parameter $\boldsymbol{E}_{\mathbf{T}}$ denotes the energy level of trap states and N_T denotes the trap density. Under flat-band conditions traps at $\boldsymbol{E}_{\mathbf{T}}$ are fully occupied. As the Fermi level crosses $\boldsymbol{E}_{\mathbf{T}}$, traps are being ionized (surface region); $qV_{bi} = \boldsymbol{E}_{\mathbf{F}}' - \boldsymbol{E}_{\mathbf{T}}$. As the Fermi level becomes more positive than $\boldsymbol{E}_{\mathbf{T}}$, more and more traps are getting ionized deep into the space-charge region; $qV_{bi} > \boldsymbol{E}_{\mathbf{F}}' - \boldsymbol{E}_{\mathbf{T}}$. Mott-Schottky plots are linear because the impedance data are only obtained in region "3" of the Mott-Schottky plot. Extrapolation in region "3" results in erroneous values for the flat-band potential and erroneous values for the dopant densities ($N_D + N_T$) are derived from the slope.

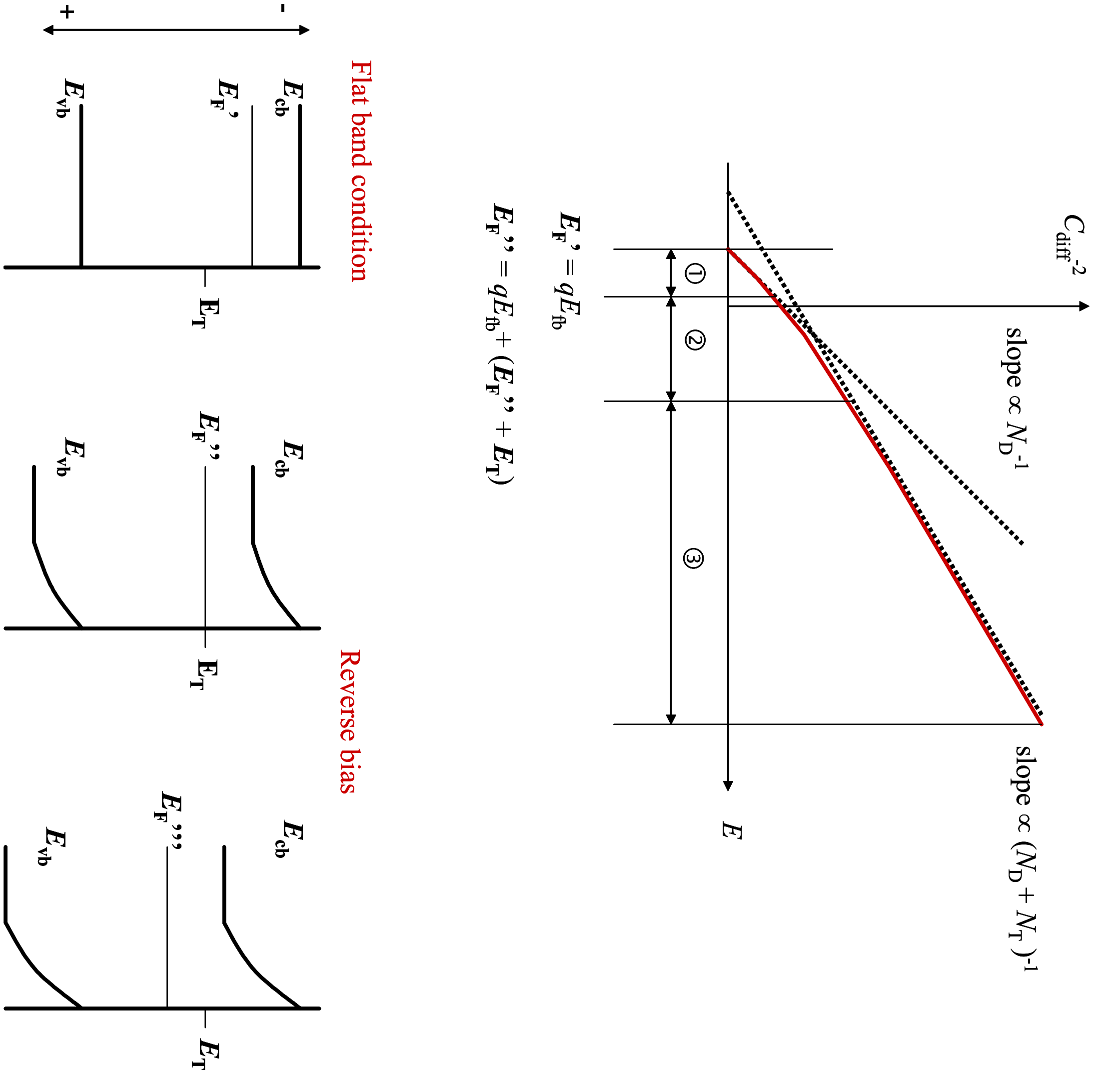
C_{diff}^{-2}
slope ∝ N_D^{-1}
slope ∝ $(N_D + N_T)^{-1}$
E
①
②
③
$E_F' = qE_{fb}$
$E_F'' = qE_{fb} + (E_F'' + E_T)$
Flat band condition
Reverse bias
-
+
E_{cb}
E_F'
E_{vb}
E_T
E_{cb}
E_F''
E_{vb}
E_T
E_{cb}
E_F'''
E_{vb}
E_T

Figure 2.9

It was noted in Chapter 2.4.1, that a surface-related relaxation process is found at frequencies higher than 10 kHz. This relaxation process might be associated with surface states. A possible explanation for the shifts in E_{fb} and N_D that are consistent with the findings of our study is given in Figure 2.9. The surface quality after polishing varies greatly from sample to sample. During grinding and polishing, trap states are introduced into the space-charge region. The plastically deformed region is 6 μm deep (grain size of the abrasive). Etching removes the plastically deformed region. According to Figure 2.9, changes in the slope and in the intercept can be caused by different density of trap states, i.e., different extent of surface damage. Trap states close to the flat-band potential will be fully occupied under flat-band conditions and for potentials more negative than E_{fb}, i.e., for forward bias. For positive potentials, however, as the Fermi level crosses $\boldsymbol{E}_{\mathbf{T}}$, traps are being ionized first in a region close to the surface. As the Fermi level becomes more positive than $\boldsymbol{E}_{\mathbf{T}}$ (reverse bias), more and more traps will be ionized and these ionized traps will penetrate deeply into the space-charge region. Mott-Schottky plots appear linear because impedance data were only obtained in region “3” of the Mott-Schottky plot, where traps throughout the space-charge region are ionized. Extrapolation of C_{diff}-E data in region “3” results in erroneous values for the flat-band potential and erroneous values for the dopant densities ($N_D + N_T$ instead of N_D) are derived from the slope of the Mott-Schottky plots. It should be noted that the r^2 values of electrodes **ZnO1** and **ZnO2** are not ideal and a slight curvature in the Mott-Schottky might be presented. These electrodes showed different apparent dopant densities and different values for the flat-band potential. The difference in the apparent dopant densities gives an indication on the order of magnitude of the trap density of approximately 10^{15} cm^{-3}. With a depletion width of 0.5 microns the trap density at the surface is estimated to be $N_{ss} \sim 5\times10^{10}$ cm^{-2}). According to Gerischer, the surface state capacitance for such a surface state density is on the order of 1×10^{7} F cm^{-2}.[29] If all traps are fully ionized, the resulting potential drop will be on the order of 100 mV., which is the right order of magnitude for the deviations that are measured for E_{fb}. The excellent r^2-values for electrodes with higher dopant density (**ZnO3**) is consistent with this picture. One expects E_{fb} to shift, but the slope of the Mott-Schottky plot is not affected since the trap density is much smaller than the dopant density, i.e., $N_D \sim N_D + N_T$. The excellent diode quality factors and the lack of Fermi-level pinning are also consistent with this interpretation. States on the surface are passivated during *J-E* measurement since all the data were collected for strong forward bias where all traps are fully occupied and do not play a significant role. As long as the Fermi level of the contacting phase does not cross $\boldsymbol{E_T}$ no Fermi level pinning is expected (traps are occupied) and the shifts in E_{fb} due to an erroneous extrapolation will be more or less consistent for a given electrode. This also explains the observation that the *j-E* data of some contacts are identical although the apparent flat-band potential differs by 90 mV (see Table 2.5: **ZnO3_VIII_pH8.7** and **ZnO3_VIIIa_pH8.7**).

In this context it is interesting to note that for low pH values (positive E_{fb} values) junctions appear to be non-rectifying although the $\Delta G^{o'}$ for electron transfer is larger than 3 k_BT. It might very well be the case that surface traps begin to influence the *J-E* data, once the band edges are positively shifted that far.

The implications of these findings, however, do not have much impact on the validity of the rate constants and the observed trends. The uncertainty in the dopant density is expected to play a minor role. As long as the deviations in E_{fb} are similar for all redox compounds, and the experimental evidence seems to suggest that this is indeed the case, these shifts in E_{fb} will introduce a constant offset in the rate constant, which can be dramatic (one order of magnitude), but which does not affect the overall trend. The uncertainty that this effect introduces in the absolute value of $\Delta G^{o'}$ will not change the picture in terms of whether electron transfer takes place in the inverted or non-inverted regime.

2.5.2 Kinetic Behavior of n-Zn(0001)/Liquid Contacts

The perfect adherence of the charge transfer kinetics at the n-ZnO/liquid interface to the rate law, which is unprecedented in the literature, is a striking result of this investigation. This is especially so in light of the numerous reports published for charge-transfer reactions at semiconductor/liquid interfaces, where a lack of adherence to the rate law has so far thwarted routine mechanistic investigations of interfacial charge-transfer reactions in terms of the Marcus formalism.[9-11, 54, 55] The data set presented in this study is thus ideally suited for an interpretation of the results in terms of the Marcus formalism and poses interesting questions for future research regarding the importance of electronic coupling.

An important feature of the approach adopted for this investigation is, that for the first time rate constant measurements were performed together with an independent determination of the reorganization energies of a homologous series of $[OsL_2L']^{3+/2+}$ redox compounds. The reorganization energies were found to be quite similar for all Os-polybipyridyl compounds used in this study and were independent of pH. This therefore permits a direct comparison of the k_{et} values in terms of their electrochemical driving force, pH dependence and electronic coupling dependence.

The theoretical predictions for the rate constant as a function of the electrochemical driving force are based on a Fermi Golden Rule expression for non-adiabatic electron transfer[37] and are shown in Figure 2.10 for 2 values of the reorganization energy, $\lambda = 0.66$ eV and $\lambda/2 = 0.33$ eV. Initially, it was assumed that the electronic coupling element is constant for the redox compounds in this study.

Based on the results of the barrier-height measurements and for a typical reorganization energy of the $[OsL_2L']^{3+/2+}$ redox couple of 0.66 eV, contacts with a low electrochemical driving force like n-ZnO/$[Os(dmbpy)_2(Him)_2]^{3+/2+}$ (**IV**) should be in the normal regime of electron transfer, while contacts like n-ZnO/$[Os(dmbpy)_3]^{3+/2+}$ (**II**) and n-ZnO/$[Os(bpy)_3]^{3+/2+}$ (**I**) should be in the inverted regime. Indeed, these two contacts showed a lower rate constant for electron transfer than n-ZnO/$[Os(bpy)_2Him_2]^{3+/2+}$ **(III)**. The rate constant of n-ZnO/**II**, however, is lower than the k_{et} of n-ZnO/**I**, which has the higher driving force. In order to test whether the high k_{et} value of n-ZnO/**III** is purely due to increased electronic coupling and not a result of a driving force dependence, several additional experiments were performed. First, one might argue that the imidazole ligands (Him) can deprotonate at higher pH values thus providing more effective electronic coupling to the ZnO electrode, which is assumed to have a positive surface potential at these pH values. If the imidazole ligand were subjected to deprotonation, the half wave potential ($E_{1/2}$) would shift by 55 mV per pH unit change in the deprotonated state.[40] The $E_{1/2}$ values were measured from pH 3 to pH 9 and the values were identical within 5 mV, which rules out that compound **III** provides a more effective coupling due to deprotonation. Another test is to replace the hydrogen atoms on the imidazole with a methyl group. The resulting compound, $[Os(bpy)_2(n\text{-}Meim)_2]^{3+/2+}$ (**V**), has an almost identical formal reduction potential and the n-ZnO/**V** contact thus has a very similar electrochemical driving force for electron transfer, which was confirmed through barrier height measurements. Surprisingly the resulting rate constant was lower than the rate constant of the n-ZnO/**III** by at least one order of magnitude. This suggests that the initial assumption that the homologous series of $[OsL_2L']^{3+/2+}$ redox compounds in contact with n-ZnO have constant electronic coupling is no longer valid. It would therefore be necessary to measure the electronic matrix element directly in order to investigate the mechanistic differences in the k_{et} values of contacts like n-ZnO/**III** and n-ZnO/**V**. Unfortunately, direct measurements of the electronic matrix element, for instance by measuring the temperature dependence of the maximum rate constant, are difficult to perform, short of being impossible. First, there are practical limitations since the temperature range that can be employed for such measurements in a solvent like water is

Figure 2.10 Plots of the Electron-Transfer Rate Constant as a Function of Driving Force and Reorganization Energy.

The plots were computed using the expression for the rate constant in Eq. 2.5. The solid line corresponds to a $\lambda = 0.66$ eV and the dotted line corresponds to a $\lambda = 0.34$ eV. The parameters in Eq. 2.5 were chosen as follows: $\Delta \boldsymbol{H}_{\mathbf{AB}}^{\mathbf{2}} = 5\times10^{-4}$ eV^2/state, $\beta^{-1} = 10^{-8}$ cm, $l_{sc} = 3\times10^{-8}$ cm, $d_{sc} = 4.22\times10^{22}$ cm^{-3}.

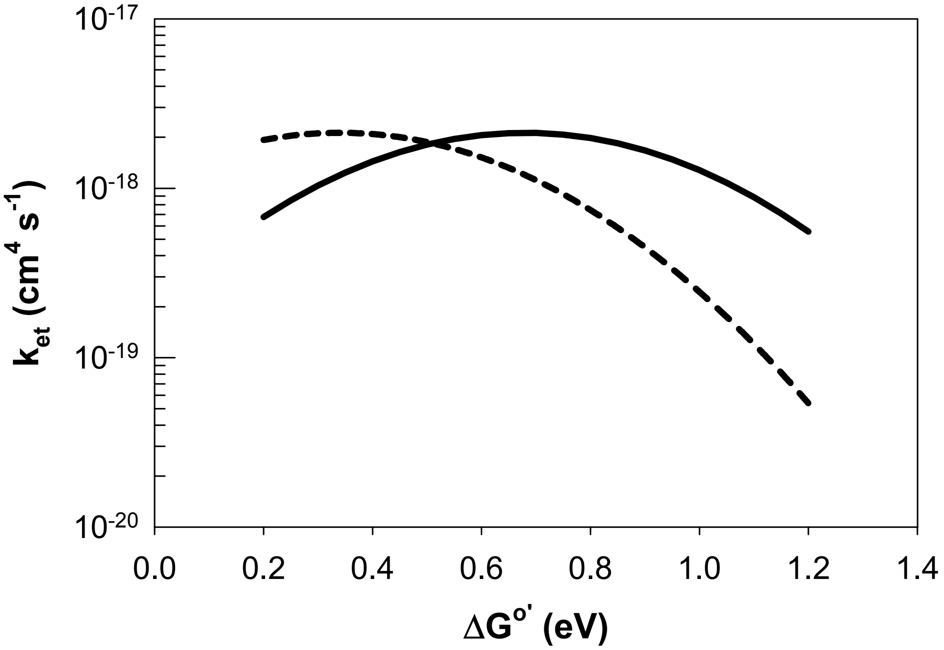

Figure 2.10

very limited and the stability of the redox compounds used at higher temperatures is questionable. Additionally, the $k_{\mathrm{et,max}}$ term, which explicitly contains the square of electronic matrix element, is only a weak function of T ($k_{\mathrm{et,max}}$ is proportional to $T^{-1/2}$), whereas the surface electron concentration (n_{s}) in the rate expression follows a Boltzmann distribution and thus depends strongly, that is exponentially, on T. Given the constraints that the solvent system poses on the temperature range and the high errors that characterize rate constant measurements, it seems to be unlikely that the weak temperature dependence of $k_{\mathrm{et,max}}$ can be extracted from *j-E* data which are dominated by the temperature dependence of n_{s}. This thwarts a robust determination of the square of the electronic matrix element.

As detailed in Chapter 2.2, metal oxide semiconductors provide an alternative and convenient way of changing the driving force for charge transfer. The band-edge position can be changed by varying the pH of the solution, see Eq. 2.4. Since the formal reduction potential of the redox couple does not change with pH, pH-dependent rate constant measurements provide a convenient way of varying the driving force by up to 100 mV (2 pH unit changes) using the same redox couple. This should enable measurements of the driving force dependence of k_{et} while keeping the electronic matrix element and the reorganization energy constant. The pH dependence of the rate constants, which is depicted in Figure 2.8 (b) and (c), indicates that contacts n-ZnO/**I** and n-ZnO/**II** might indeed operate in the inverted regime while contact n-ZnO/**IV** belongs into the normal regime, because the rate constants for n-ZnO/**I** and n-ZnO/**II** increases with decreasing driving force (inverted regime), while the rate constant for n-ZnO/**IV** decreases with decreasing driving force (normal regime). To our knowledge this is the first direct measurement of the kinetic behavior in the Marcus inverted region for interfacial electron transfer to date. It should however be noted that several papers, although all short of a direct proof, suggest that this kind of behavior might apply to some semiconductor/liquid contacts,[57] especially nanocrystalline TiO_2 solar cells.[58-60]

The inverted behavior also allows us to place the point of optimum exoergicity ($k_{et} = k_{et,max}$, i.e., $\Delta G^{o'} = \lambda_{sc}$) somewhere between 0.433 and 0.716 eV, which is in accordance with a $\lambda_{sc} = 0.66$ eV (a value which was derived from the investigation of self exchange reactions) and not with $\lambda_{sc} = \lambda/2$. Although the placement of the point of exoergicity might appear as a rather rough estimate, this result nevertheless presents an important result of this investigation. In self-exchange reactions, energy is necessary to reorganize the solvent dipoles of both the electron acceptor and the electron donor following a charge transfer event. In the case of interfacial charge transfer one might assume that only $\lambda/2$ is necessary, since the electron donor is replaced by an electrode and only the solvent dipoles of the acceptor need to reorganize. Due to image charge effects, however, Smith *et al.* placed the effective reorganization for interfacial charge transfer across a dielectric electrode of finite permittivity close to the self-exchange value of λ.[38] Measurements performed on the n-Si/viologen$^{2+/+}$ system come to a similar conclusion regarding the location of the point of optimum exogergicity.[7, 8]

Besides the driving force dependence, the results of this study also allow us to comment on the reorganization energy dependence of interfacial rate constants. According to the rate expression in Eq. 2.5, the rate constant will decrease with increasing reorganization energy. Indeed, redox compounds like $[Co(bpy)_3]^{3+/2+}$ with reorganization energies as high as 2.3 eV yielded the lowest rate constant of all ZnO contacts. The rate constant for n-ZnO/$Co(bpy)_3]^{3+/2+}$ at pH 8.7 was on the order of 10^{-25} cm^4 s^{-1}, which gives a clear indication of the reorganization energy dependence of k_{et}, especially when compared to $[Os(dmbpy)_2(Him)_2]^{3+/2+}$ at pH 6.8, which for a similar electrochemcial driving force and a $\lambda = 0.7$ eV yielded a rate constant on the order of 10^{-19} cm^4 s^{-1}. Clearly, more work is necessary to discern the reorganization energy-dependence of the rate constant. The possibility of changing the driving force at will by varying the pH might be an attractive way of balancing out small differences in the electrochemical driving force of redox compounds which have different reorganization energies, thus allowing the sole effect of the reorganization energy on the rate constant to be studied.

A final comment can be made regarding the magnitude of electronic coupling and the maximum rate constants for charge transfer. Based on the value for the electrochemical driving force and the value for the reorganization energy, the Franck Condon factors $k_{\mathrm{et,max}}$ can be calculated for each contact. Dividing the experimentally derived k_{et} values by the corresponding Franck Condon factor gives the maximum rate constant and thus an estimate for the electronic coupling. The maximum rate constant is on the order of 2×10^{-18} $\mathrm{cm^4\ s^{-1}}$ for n-ZnO in contact with $[\mathrm{Os(dmbpy)_2(Him)_2}]^{3+/2+}$ and $[\mathrm{Os(dmbpy)_2(Him)_2}]^{3+/2+}$ and 2×10^{-19} $\mathrm{cm^4\ s^{-1}}$ for n-ZnO in contact with $[\mathrm{Os(bpy)_3}]^{3+/2}$. The square of the electronic matrix element is therefore on the order of 10^{-4} $\mathrm{eV^2\ state^{-1}}$ for n-ZnO in contact with $[\mathrm{Os(dmbpy)_2(Him)_2}]^{3+/2+}$ and $[\mathrm{Os(dmbpy)_2(Him)_2}]^{3+/2+}$ and 10^{-5} $\mathrm{eV^2\ state^{-1}}$ for n-ZnO in contact with $[\mathrm{Os(bpy)_3}]^{3+/2}$. Compared to estimates regarding the electronic coupling at the n-Si/viologen$^{2+/+}$ interface the square of the electronic matrix element is 2 orders of magnitude higher than the value for n-ZnO contacts.[7, 8] As a point of caution it is noted that the true value of the flat-band potential might further lower the maximum rate constant by up to one order of magnitude which changes the estimate of the electronic coupling element accordingly.

2.6 CONCLUSIONS

In this work, n-ZnO/$\mathrm{H_2O}$-A/A$^-$ (where A/A$^-$ corresponds to $[\mathrm{Fe(CN)_6}]^{3-/4-}$, $[\mathrm{Co(bpy)_3}]^{3+/2+}$, or $[\mathrm{OsL_2L'}]^{3+/2+}$) displayed energetic and kinetic behavior of unprecedented ideality for the experimental determination of robust rate constants for electron transfer from n-type semiconductors to non-adsorbing, one-electron redox couple in solution. Differential capacitance measurements showed that Fermi level pinning is absent for the system under investigation and that the band edges of ZnO are fixed within 20 mV with respect to an electrochemical reference when the solution potential is changed.

The reorganization energies of the homologous series of $[OsL_2L']^{3+/2+}$compounds were for the first time determined independently by measuring the corresponding self-exchange rate constants in NMR line-broadening experiments. The reorganization energies of all the $[OsL_2L']^{3+/2+}$ compounds were found to be on the order of 0.7 eV. The driving force dependence and the influence of electronic coupling on the measured rate constants could therefore be interpreted in terms of Marcus theory.

Two methods were used to vary the driving force for electron transfer across the semiconductor/liquid interface. First, the driving force was changed by varying the formal reduction potential of the redox couple in solution. Contacts with an electrochemical driving force that was significantly larger than the driving force at the point of optimum exoergicity showed lower rate constants than contacts with lower driving force. Computation of the maximum rate constant, however, revealed that the square of the electronic matrix element was not constant for these contacts. An alternative way of changing the driving force for charge transfer was thus necessary to avoid the ambiguity of the former approach regrading the varying influence of electronic coupling. In this approach the driving force was changed by moving the band-edge position of the n-ZnO electrode with respect to the solution potential through variations of the pH of the electrolyte. With this approach the driving force dependence of charge transfer could be studied for the same redox compound in solution. The rate constant of the contact with the highest driving force ($\Delta G^{o'} >> 0.7$ eV) increased when the driving force was lowered by shifting the conduction band edge to more positive values. This indicates that the contact operates in the inverted regime. The rate constant of the contact with the lowest driving force ($\Delta G^{o'} << 0.7$ eV) decreased when the conduction band edge was shifted to more positive values. This indicates that the low-driving force contact operates in the normal regime. This investigation provides therefore the first direct and credible experimental indication that semiconductor/liquid contacts can operate in the inverted regime.

Semiconductor/liquid contacts, which had a similar driving force but a reorganization energy that differed by 1.6 eV showed the expected dependence of the rate constant on the reorganization energy consistent with Marcus theory.

2.7 REFERENCES

1 Marcus, R. A.; Sutin, N., Electron Transfers in Chemistry and Biology. **1985,** 811, (3), 265.

2 Fox, L. S.; Kozik, M.; Winkler, J. R.; Gray, H. B., Gaussian Free-Energy Dependence of Electron-Transfer Rates in Iridium Complexes. *Science* **1990,** 247, (4946), 1069.

3 Fleming, G. R.; Martin, J. L.; Breton, J., Rates of Primary Electron-Transfer in Photosynthetic Reaction Centers and Their Mechanistic Implications. *Nature* **1988,** 333, (6169), 190.

4 Gray, H. B.; Winkler, J. R., Electron Transfer in Proteins. *Annu. Rev. Biochem.* **1996,** 65, 537.

5 Maroncelli, M.; Macinnis, J.; Fleming, G. R., Polar-Solvent Dynamics and Electron-Transfer Reactions. *Science* **1989,** 243, (4899), 1674.

6 Closs, G. L.; Miller, J. R., Intramolecular Long-Distance Electron-Transfer in Organic-Molecules. *Science* **1988,** 240, (4851), 440.

7 Fajardo, A. M.; Lewis, N. S., Free-Energy Dependence of Electron-Transfer Rate Constants at Si/Liquid Interfaces. *J. Phys. Chem. B* **1997,** 101, (51), 11136.

8 Fajardo, A. M.; Lewis, N. S., Rate Constants for Charge Transfer Across Semiconductor-Liquid Interfaces. *Science* **1996,** 274, (5289), 969.

9 Koval, C. A.; Howard, J. N., Electron-Transfer at Semiconductor Electrode Liquid Electrolyte Interfaces. *Chem. Rev.* **1992,** 92, (3), 411.

10 Lewis, N. S., An Analysis of Charge-Transfer Rate Constants for Semiconductor Liquid Interfaces. *Annu. Rev. Phys. Chem.* **1991,** 42, 543.

11 Lewis, N. S., Progress in Understanding Electron-Transfer Reactions at Semiconductor/Liquid Interfaces. *J. Phys. Chem. B* **1998,** 102, (25), 4843.

12 Pomykal, K. E.; Fajardo, A. M.; Lewis, N. S., Theoretical and Experimental Upper Bounds on Interfacial Charge-Transfer Rate Constants between Semiconducting Solids and Outer-Sphere Redox Couples. *J. Phys. Chem.* **1996,** 100, (9), 3652.

13 Morrison, S. R.; Freund, T., Chemical Reactions of Electrons and Holes at ZnO/Electrolyte- Solution Interface. *Electrochim. Acta* **1968,** 13, (6), 1343.

14 Freund, T.; Morrison, S. R., Mechanism of Cathodic Processes on Semiconductor Zinc Oxide. *Surf. Sci.* **1968,** 9, (1), 119.

15 Morrison, S. R., Electron Capture by Ions at ZnO/Solution Interface. *Surf. Sci.* **1969,** 15, (3), 363.

16 Vandenberge, R. A.; Cardon, F.; Gomes, W. P., Electrochemical Reactivity of Redox Couple $Fe(CN)_6^{3-}/Fe(CN)_6^{4-}$ at Single-Crystal Zinc Oxide Electrode. *Surf. Sci.* **1973,** 39, (2), 368.

17 Gomes, W. P.; Freund, T.; Morrison, S. R., Chemical Reactions Involving Holes at Zinc Oxide Single Crystal Anode. *J. Electrochem. Soc.* **1968,** 115, (8), 818.

18 Gomes, W. P.; Freund, T.; Morrison, S. R., Chemical Reactions Involving Anodic Processes on a Single- Crystal Zinc Oxide Catalyst. *Surf. Sci.* **1969,** 13, (1), 201.

19 Dewald, J. F., Experiments on Electron Transfer Reactions at the ZnO Electrode. *J. Electrochem. Soc.* **1958,** 105, (3), C49.

20 Dewald, J. F., The Charge and Potential Distributions at the Zinc Oxide Electrode. **1960,** 39, (3), 615.

21 Dewald, J. F., The Charge Distribution at the Zinc Oxide-Electrolyte Interface. *J. Phys. Chem. Solids* **1960,** 14, 155.

22 Rodman, S.; Spitler, M. T., Determination of Rate Constants for Dark Current Reduction at Semiconductor Electrodes Using ZnO Single-Crystal Microelectrodes. *J. Phys. Chem. B* **2000,** 104, (40), 9438.

23 Hamann, T. W. Candidacy Report. California Institute of Technology, Pasadena, 2003.

24 Meyer, T. J.; Taube, H., *Electron Transfer Reactions*. In *Comprehensive Coordination Chemistry*, Ed. Wilkinson, S. G.; Gilliard, R. D.; McCleverty, J. A., Pergamon Press: New York, 1987; 1, 331.

25 Marcus, R. A., On Theory of Electron-Transfer Reactions .6. Unified Treatment for Homogeneous and Electrode Reactions. *J. Chem. Phys.* **1965,** 43, (2), 679.

26 Marcus, R. A., Theory of Oxidation-Reduction Reactions Involving Electron Transfer .5. Comparison and Properties of Electrochemical and Chemical Rate Constants. *J. Phys. Chem.* **1963,** 67, (4), 853.

27 Marcus, R. A., Theory of Oxidation-Reduction Reactions Involving Electron Transfer .1. *J. Chem. Phys.* **1956,** 24, (5), 966.

28 Marcus, R. A., Chemical + Electrochemical Electron-Transfer Theory. *Annu. Rev. Phys. Chem.* **1964,** 15, 155.

29 Gerischer, H., *Semiconductor Photoelectrochemistry.* In *Physical Chemistry: An Advanced Treatise*, Ed. Eyring, H.; Henderson, D.; Yost, W., Academic: New York, 1970; 9A, 463.

30 Gerischer, H., Electron-Transfer Kinetics of Redox Reactions at the Semiconductor Electrolyte Contact - a New Approach. *J. Phys. Chem.* **1991,** 95, (3), 1356.

31 Tan, M. X.; Laibinis, P. E.; Nguyen, S. T.; Kesselman, J. M.; Stanton, C. E.; Lewis, N. S., *Principles and Applications of Semiconductor Photoelectrochemistry.* In *Progress in Inorganic Chemistry*, Ed. John Wiley & Sons Inc: New York, 1994; 41, 21.

32 Sze, S. M., *The Physics of Semiconductor Devices*. Wiley: New York, 1981.

33 Morrison, S. R., *Electrochemistry at Semiconductor and Oxidized Metal Electrodes*. Plenum Press: New York, 1980.

34 Morrison, S. R., *The Chemical Physics of Surfaces*. Plenum Press: New York and London, 1990.

35 Lohmann, F., Der Einfluss des pH auf die Elektrischen und Chemischen Eigenschaften von Zinkoxidelektroden. **1966,** 70, (4), 428.

36 Marcus, R. A., Reorganization Free-Energy for Electron Transfers at Liquid Liquid and Dielectric Semiconductor Liquid Interfaces. *J. Phys. Chem.* **1990,** 94, (3), 1050.

37 Royea, W. J.; Fajardo, A. M.; Lewis, N. S., Fermi Golden Rule Approach to Evaluating Outer-Sphere Electron-Transfer Rate Constants at Semiconductor/Liquid Interfaces. *J. Phys. Chem. B* **1997,** 101, (51), 11152.

38 Smith, B. B.; Koval, C. A., An Investigation of the Image Potential at the Semiconductor Electrolyte Interface Employing Nonlocal Electrostatics. *J. Electroanal. Chem.* **1990,** 277, (1-2), 43.

39 Spitler, M. T., Personal Communication Regarding Ohmic Contact Materials for ZnO Single Crystal Electrodes, 1999.

40 Bard, A. J.; Faulkner, L. R., *Electrochemical Methods: Fundamentals and Applications*. John Wiley & Sons: New York, 1980.

41 Bhargava, R., *Properties of Wide Bandgap II-VI Semiconductors*. Inspec: London, 1997.

42 Madelung, O.; Schulz, M., *Landolt Boernstein, Numerical Data and Functional Relationships in Science and Technology, New Ser. Group III, Crystals and Solid State Physics*. Springer: Berlin; New York, 1987-.

43 Macdonald, J. R., *Impedance Spectroscopy. Emphasizing Solid Materials and Systems*. John Wiley, Inc.: New York, Chichester, Brisbane, Toronto, Singapore, 1987.

44 Blok, L., Ionic Double Layer at ZnO/Solution Interface .1. Experimental Point of Zero Charge. *J. Colloid Interface Sci.* **1970,** 32, (3), 518.

45 Blok, L., Ionic Double Layer at ZnO/Solution Interface .3. Comparison of Calculated and Experimental Differential Capacities. *J. Colloid Interface Sci.* **1970,** 32, (3), 533.

46 Royea, W. J.; Kruger, O.; Lewis, N. S., Frumkin Corrections for Heterogeneous Rate Constants at Semiconducting Electrodes. *J. Electroanal. Chem.* **1997,** 438, (1-2), 191.

47 Gstrein, F. Candidacy Report. California Institute of Technology, Pasadena, 2000.

48 Anson, F. C., Exchange Current Densities for Fe(II)-Fe(III) Solutions in Sulfuric Acid and Perchloric Acid. *Anal. Chem.* **1961,** 33, (7), 939.

49 Angell, D. H.; Dickinson, T., Kinetics of Ferrous/Ferric and Ferro/Ferricyanide Reactions at Platinum and Gold Electrodes .1. Kinetics at Bare-Metal Surfaces. *J. Electroanal. Chem.* **1972,** 35, (NMAR), 55.

50 Weaver, M. J.; Yee, E. L., Activation Parameters for Homogeneous Outer-Sphere Electron- Transfer Reactions - Comparisons between Self-Exchange and Cross Reactions Using Marcus Theory. *Inorg. Chem.* **1980,** 19, (7), 1936.

51 Takagi, H.; Swaddle, T. W., The Aqueous Hexacyanoferrate(II/III) Self-Exchange Reaction at High-Pressures. *Inorg. Chem.* **1992,** 31, (22), 4669.

52 Cho, K. C.; Cham, P. M.; Che, C. M., Kinetics of Electron-Transfer between Metal Hexacyanide Complexes. *Chem. Phys. Lett.* **1990,** 168, (3-4), 361.

53 Anast, J. M.; Margerum, D. W., Electron-Transfer Reactions of Copper(III) Peptide Complexes with Hexacyanoferrate(II). *Inorg. Chem.* **1982,** 21, (9), 3494.

54 Howard, J. N.; Koval, C. A., Kinetics of Reduction of Dimethylferrocenium Ion in Acetonitrile at Nearly Ideal Regions of N-Tungsten Diselenide Electrodes. *Anal. Chem.* **1994,** 66, (24), 4525.

55 Rosenbluth, M. L.; Lewis, N. S., Kinetic-Studies of Carrier Transport and Recombination at the Normal-Silicon Methanol Interface. *J. Am. Chem. Soc.* **1986,** 108, (16), 4689.

56 Gomes, W. P.; Cardon, F., Surface States at Single Crystal Zinc Oxide/Electrolyte Interface .1. Impedance Measurements. **1970,** 74, (5), 431.

57 Nakabayashi, S.; Itoh, K.; Fujishima, A.; Honda, K., Electron-Transfer Rates in Highly Exothermic Reactions on Semiconductor Electrolyte Interfaces, and the Deuterium-Isotope Effect. *J. Phys. Chem.* **1983,** 87, (26), 5301.

58 Heimer, T. A.; Bignozzi, C. A.; Meyer, G. J., Molecular-Level Photovoltaics - the Electrooptical Properties of Metal Cyanide Complexes Anchored to Titanium-Dioxide. *J. Phys. Chem.* **1993,** 97, (46), 11987.

59 Moser, J. E.; Gratzel, M., Observation of Temperature Independent Heterogeneous Electron- Transfer Reactions in the Inverted Marcus Region. *Chem. Phys.* **1993,** 176, (2-3), 493.

60 Lu, H.; Prieskorn, J. N.; Hupp, J. T., Fast Interfacial Electron-Transfer - Evidence for Inverted Region Kinetic-Behavior. *J. Am. Chem. Soc.* **1993,** 115, (11), 4927.

CHAPTER 3 *Effects of Interfacial Energetics on the Charge Carrier Dynamics at Silicon/Liquid Contacts*

3.1 INTRODUCTION

Low surface recombination velocities are important for surface passivation in Si-based electrical devices such as photovoltaics[1-3] and photoelectrochemical devices.[4]

Hydrogen-terminated Si (111) exhibits a low surface recombination velocity in contact with aqueous acids,[5, 6] and aqueous fluoride solutions[7] although the electrical properties of this surface rapidly degrade upon exposure to an air ambient.[7] Silicon surfaces exhibit a low effective surface recombination velocity when in contact with methanolic solutions of 1,1'-dimethylferrocenium ($Me_2Fc^{+/0}$),[8-10] as do Si surfaces in contact with I_2 or Br_2 in methanol, ethanol, or tetrahydrofuran (THF).[11-15]

The low surface recombination velocity (*SRV*) of Si in contact with iodine-containing electrolytes has been ascribed to the passivation of the Si surface resulting from Si-I bonding[14] or has in some cases been ascribed to passivation due to the formation of surface Si-alkoxide bonds.[11] Work preceding this study,[7] however, has indicated that another effect is important in producing the behavior observed in this system, and that the observed carrier recombination dynamics reflect low *effective SRV* values. These low effective *SRV* values are the result of an electrochemical charge-transfer reaction at the Si/liquid contact.[16-19] Specifically, interfacial charge transfer spontaneously produces an inversion layer on n-type Si samples contacting solutions which have sufficiently positive electrochemical potentials.[16-19] This accumulation of holes at the semiconductor surface produces low effective *SRV* values even if the surface actually has a significant number of electrically active defect sites.

In the present study, digital device simulations of the photoconductivity decay of Si surfaces under inversion or depletion conditions are reported for both low-level and high-level injection conditions. The digital simulations are compared with experimental results from surface recombination velocity measurements. The simulations are required to evaluate quantitatively the extent to which inversion conditions produce low effective surface recombination velocities in the presence of significant levels of electrically active defect states at the solid/liquid contact. The simulations also address the extent to which the experimentally observed data are consistent with expectations of conventional Shockley-Read-Hall recombination statistics for semiconductor/liquid contacts having various degrees of band bending.

The digital device simulations are complemented by an experimental study of Si/liquid contacts which produce an accumulation region in n-type Si, for instance n-Si/$CH_3OH{-}CoCp_2^{+/0}$ contacts. Electrochemically well-defined Si/liquid contacts which are accumulated are of great interest with respect to the recombination behavior of H-terminated Si surfaces in contact with aqueous fluoride solutions and aqueous acids. Hydrogen-terminated Si-surfaces have attracted widespread attention for their low *SRV* values and for their high apparent degree of electrical passivation.[5, 6, 20] Both of these properties have been associated with the high degree of structural perfection of H-terminated surfaces in contact with various acids or fluoride etching solutions. Royea *et al.* have shown that this surface rapidly degrades when exposed to air.[7] However, a self-consistent relationship between the degree of band-bending, the structural perfection of the surface and the surface recombination characteristics has yet to be rigorously established. For aerobic etching the *SRV* values decrease as the molarity of the acid solution increases, with *SRV* becoming less than 10^2 cm s^{-1}.[5] It should be noted that no apparent relationship exists between the acidity of the solution and the measured *SRV* value, since weakly dissociating acids like $HF_{(aq)}$ and $H_3PO_{4(aq)}$ essentially yield the same *SRV* values as very strong acids like $H_2SO_{4(aq)}$ as long as their molarities are in excess of 1 M.[5, 7] Despite numerous reports regarding the anodic oxidation of Si(111),[21-28] the pH-dependence of the open circuit potential in aqueous fluoride solutions,[26-28] and the kinetics of etching,[28-30] few reports exist that describe the nature of band bending of Si in contact with aqueous fluoride solutions.[28]

At present, two mechanisms have been envisioned to explain the low effective *SRV* values found for Si(111) in contact with acidic solutions and aqueous fluoride solutions. In the case of acids, Yablonovitch *et al.* have ascribed the low *SRV* values of Si(111) in contact with acids to the reversible protonation of weakly basic defect sites, such that the defect state density is almost completely eliminated (and *SRV* minimized) in strongly acidic aqueous solutions.[5, 20] Impedance spectroscopy measurements of the surface state capacitance of Si(111) in contact with fluoride solutions of various pH by Searson and co-workers,[31, 32] suggest that the surface trap density decreases with decreasing pH.

A second mechanism has been proposed, which is based on the influence that band bending has on the effective surface recombination velocity.[28, 33] An accumulation of electrons at the Si surface will lead to a low effective *SRV* value even for high surface trap densities $N_{T,s}$. Additionally, such a charge-transfer derived effect might provide a natural explanation of the relationships between the *SRV* of n-Si(111) in contact with various etching solutions and acids and the degree of structural perfection of the surface. Allongue *et al.* measured the built-in voltage of Si/H_2O contacts using differential capacitance measurements, which requires the n-type Si surface to be severely biased.[28] These authors argue that n-type Si surfaces are under accumulation in contact with aqueous fluoride solutions and that the degree of accumulation at the Si/H_2O contact is more or less invariant with the pH.[28]

To correlate the surface recombination behavior of Si/H_2O contacts with the degree of band bending, the surface recombination velocities of (111)-oriented n-type Si in aqueous fluoride solutions and 18 M $H_2SO_{4(aq)}$ were measured and the band bending of Si(111) in aqueous fluoride solutions were determined for the first time at open circuit conditions through measurements of the near-surface channel conductance of solution-gated n^+-p-Si(111)-n^+ devices. These techniques were also used to study Si/$CoCp_2^{+/0}$

contacts (strong accumulation) to corroborate the interpretations made for Si/H_2O contacts.

3.2 BACKGROUND

Recombination-Generation (R-G) is nature's way of restoring order in a semiconductor, when the equilibrium is perturbed for instance by a light pulse. The light pulse perturbation introduces an excess of charge carriers into the semiconductor. Figure 3.1 shows the various R-G processes, which will be considered in the computational studies and in the analysis of the experiments reported in this thesis. The capture of an electron and hole at the same midgap-trap site in the bulk of a semiconductor leads to the annihilation of a electron/hole pair. This recombination process is commonly referred to as Shockley-Read-Hall (*SRH*) recombination or indirect thermal or non-radiative R-G, because thermal energy is released during the recombination event.W. Shockley and W.T. Read[34]and independently R. N. Read[35] were the first to model and investigate this process. Recombination at trap centers can also occur in the depletion region of the semiconductor and is referred to as depletion region recombination. Recombination at surfaces is a very prominent recombination process in semiconductor/ liquid junctions and can be treated with the *SRH* model. In Auger recombination trapping at a mid gap center or direct band-to-band recombination occurs simultaneously with the collision of electrons in the conduction band. The energy which is released by the trapping subprocess is transferred during the collision to the second electron. Subsequently, this highly energetic electron loses its energy in a step-wise fashion through collisions with the lattice of the semiconductor. This step-wise loss of energy is referred to as thermalization. Auger recombination is prominent when one deals with high injection levels and/or highly doped semiconductors.[36]

Figure 3.1 Energy Band Visualization of Recombination Processes.

Various recombination processes are shown: (1) Shockley-Read-Hall recombination in the bulk of the semiconductor proceeds with a bulk recombination rate U_{br}.(2) Shockley-Read-Hall recombination in the depletion region proceeds with a depletion-region recombination rate U_{dr}. (3) surface recombination proceeds with a surface recombination rate U_{sr}. (4) Auger recombination: trapping at a band-gap center occurs simultaneously with the collision between two electrons; the highly energetic electron thermalizes and looses its energy in small steps through collision with the lattice. Processes (1)-(3) are referred to as indirect, non-radiative, or thermal recombination processes. Auger recombination is only prominent at high light intensities.

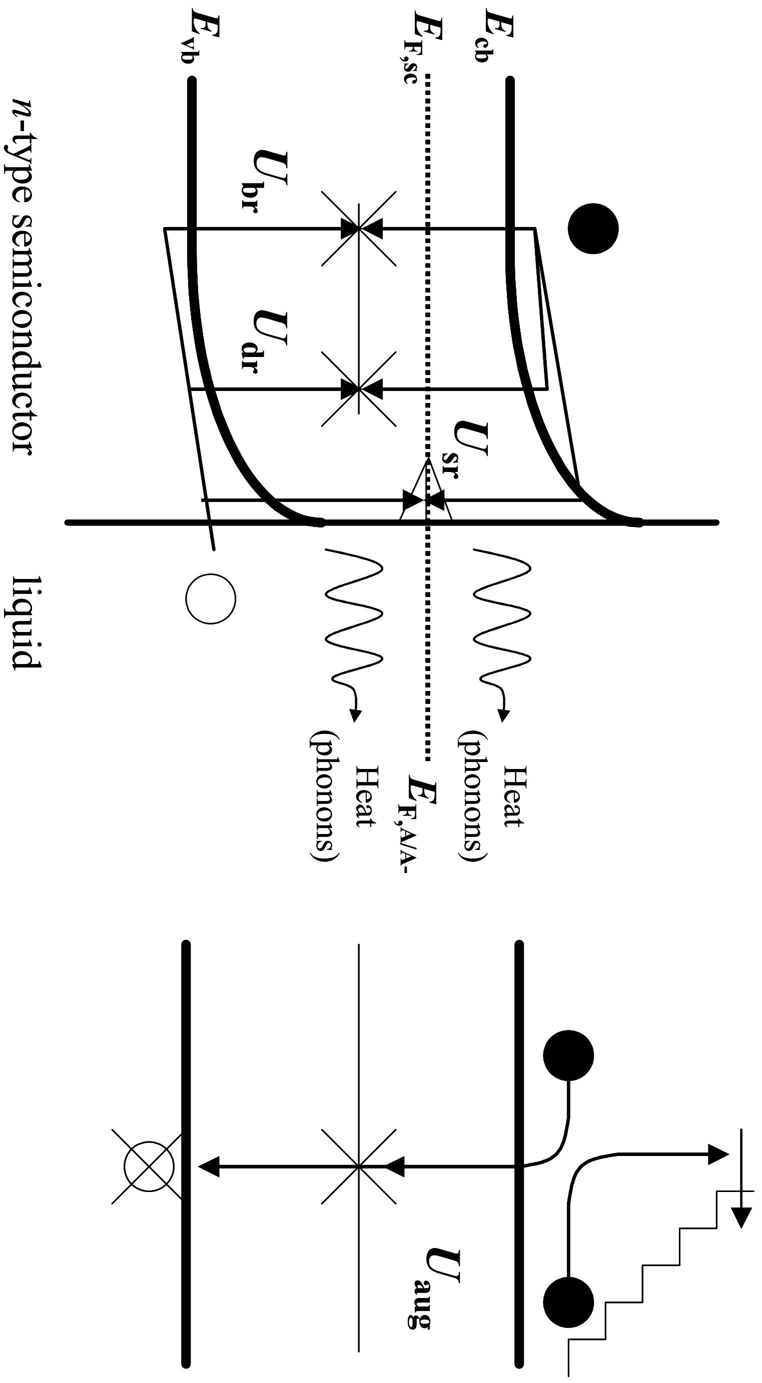
E_{cb}
$E_{F,sc}$
E_{vb}
U_{br}
U_{dr}
U_{sr}
n-type semiconductor
liquid
Heat (phonons)
$E_{F,A/A-}$
Heat (phonons)
U_{aug}

Figure 3.1

Processes involving transitions from R-G centers to energy bands can be treated with the *SRH*-model. The rate of electron or hole capture depends on the existence of electrons or holes to be captured and the availability of the respective trap sites. The rate is directly proportional to the concentration of electrons (n) or holes (p) and the concentration of trap states for electrons or holes, p_T or n_T (units cm^{-3}), respectively. The proportionality constant is the electron capture or hole capture coefficient k_n or k_p (units: cm^3 s^{-1}), respectively. The opposite transition of electron emission can be treated analogously by changing the sign of the rate and by replacing k_n and k_p with the emission coefficients e_n and e_p, respectively. In non-degenerate semiconductors, however, the vast majority of conduction band states or valence band states will be empty (the effective density of states are significantly larger than the dopant density) and do not need to be considered in the rate law. The overall recombination rates (units: number of charge carriers/cm^3-s) for electrons and holes, u_n and u_r, therefore are:

$$u_n \equiv -\left.\frac{\partial n}{\partial t}\right|_{R-G} = k_n \cdot p_T \cdot n - e_n \cdot n_T$$

$$u_p \equiv -\left.\frac{\partial p}{\partial t}\right|_{R-G} = k_p \cdot n_T \cdot p - e_p \cdot p_T \qquad \text{(Eq. 3.1)}$$

The total number of trap states N_T is the sum of p_T and n_T. At steady-state u_n equals u_r. With the simplifying assumption that the emission and capture coefficients remain approximately equal to their equilibrium values under non-equilibrium conditions and by introducing the computable constants n_1 and p_1, the R-G rate U can be written in the following way:

$$U = u_n = u_p = \frac{np - n_i^2}{\frac{1}{k_p N_T} \cdot (n + n_1) + \frac{1}{k_n N_T} \cdot (p + p_1)} = \frac{np - n_i^2}{\tau_p \cdot (n + n_1) + \tau_n \cdot (p + p_1)} \qquad \text{(Eq. 3.2)}$$

$$n_1 = \frac{p_{T0} n_0}{n_{T0}} \; ; \; p_1 = \frac{n_{T0} p_0}{p_{T0}}$$

where n_i denotes the intrinsic charge carrier concentration, and τ_p and τ_n denote the electron and hole carrier lifetime, respectively. The subscript “0” indicates equilibrium values.

If n and p are substituted by $n_0 + \Delta n$ and $p_0 + \Delta p$, respectively, the expression in Eq. 3.2 simplifies drastically for the limiting cases of a n-type material ($n_0 >> p_0$) under high-level injection ($\Delta n = \Delta p >> n_0$) and low-level injection ($\Delta n, \Delta p << n_0$), see Eq. 3.3.

$$U = \frac{\Delta p}{\tau_p} \quad \text{low-level injection}$$

$$U = \frac{\Delta p}{\tau_p + \tau_n} \quad \text{high-level injection} \qquad \text{(Eq. 3.3)}$$

The physical similarity between recombination in the bulk and at the surface leads to an analogous mathematical description of surface recombination. The major difference is that surfaces recombination rates are expressed in (number of charge carriers/cm^2-s). For single-level surface recombination under steady state conditions, the surface recombination is represented by Eq. 3.4

$$U_s = N_{T,s} \frac{k_{n,s} k_{p,s} \Delta p (n_{so} + p_{so} + \Delta p)}{k_{p,s}(n_{so} + \Delta n_s + n_{1,s}) + k_{n,s}(p_{so} + \Delta p + p_{1,s})} \qquad \text{(Eq. 3.4)}$$

Subscript “s” denotes a surface property. The unit of $N_{T,s}$ is now traps/cm^2, whereas the units of n_s remains in number/cm^3 and the units for $k_{n,s}$ and $k_{p,s}$ remain in cm^3 s^{-1}. The quality of surfaces are often described by a surface recombination velocity, SRV. The relationship between the surface recombination velocity, the apparent lifetime,τ, and the bulk lifetime, τ_b, is given in Eq. 3.5

$$\frac{1}{\tau} = \frac{1}{\tau_b} + \frac{2 \cdot SRV}{d} \qquad \text{(Eq. 3.5)}$$

where *d* is the thickness of the sample and where the factor “2” indicates that both surfaces of the semiconductor are participating in the surface recombination.

3.3 EXPERIMENTAL

3.3.1 Digital Simulations

Numerical device simulations were carried out using the TeSCA two-dimensional semiconductor analysis software package developed by Gajewski and co-workers.[37, 38] A detailed description of the mathematical models underlying TeSCA and the adaptations made to account for the behavior of semiconductor/liquid interfaces has been presented previously.[39-44] The code is based upon van Roosbroek’s drift diffusion model.[39, 45] It numerically and self consistently solves a system of differential equations, which includes Poisson’s equation and the continuity equations for electrons and holes. Potential distribution and charge-carrier profiles are computed in accordance with Fermi-Dirac statistics. Optical generation of charge carriers and recombination are explicitly incorporated into the code. The nature of the electrical contacts, gate contacts or ohmic contacts, are defined through appropriate boundary conditions. The gate contact had the physical properties of a Helmholtz layer with a thickness of 3 Å and a dielectric constant of $6\varepsilon_0$, where ε_0 is the permittivity of free space. In order to allow for faradaic charge transfer, the gate contact was specified to be leaky and Marcus-Gerischer theory[46-48] was used to calculate the interfacial charge-transfer current due to the reduction or oxidation of redox species in the electrolyte.

Table 3.1 lists the key parameters used in the simulations discussed herein. All simulations were performed at minimal computational cost on a personal computer equipped with a 1 GHz Pentium® III processor and 750 MB of RAM.

Charge-carrier profiles, the electric potential distribution, and recombination rates as a function of distance were computed at various times after the initial optical excitation pulse. TeSCA requires a reference point at which the charge-carrier concentrations must remain fixed during the entire simulation.[37, 38] Hence one side of the semiconductor must serve as an ohmic or ohmic-selective contact. This is not the situation in actual photoconductivity decay measurements, for which both surfaces are semiconductor/liquid junctions and are subject to recombination and interfacial current flow. To deal with this constraint of the simulation program, the sample thickness in the simulation was increased from 190 μm to 10 cm. The sample then appeared to be semi-infinite on the timescale of interest with respect to the distance from the solid/liquid contact (the y-direction), and consequently recombination at the back contact had minimal influence on the carrier fluxes and dynamics in the 190 μm thick layer adjacent to the semiconductor/liquid interface. In addition, to suppress recombination at the back of the simulated sample, a 1 μm thick, degenerately doped p^+-Si layer (having a hole concentration of 1×10^{18} cm^{-3}) was used as the back ohmic-selective contact in the simulation. Finally, the optical absorption coefficient and light intensity were scaled from their actual values so as to produce a nearly uniform excitation profile at the desired injection level into this increased sample thickness. Photoconductivity decays of charge carriers in the first 95 μm of this sample were then taken to be representative of the photoconductivity decay properties of each side of the actual 190 μm thick semiconductor that was used in the experimental measurements.

The x-dimension of the simulated electrode was chosen such that an optimum triangulation of the adaptive finite-element grid was achieved. Boundary conditions were set such that zero flux and zero recombination occurred at the edges of the 3 μm wide sample. Non-radiative recombination processes were computed at each time increment of the simulations through use of a dynamic trapping model,[38, 44] which reduces at steady state to the well-known Shockley-Read-Hall (SRH) expression.[34, 36, 49] To incorporate the injection of charge carriers into solution as a possible recombination pathway, solution-based charge acceptor states were treated as surface states using the dynamic trapping model. The formal reduction potential of the redox couple was used as the surface trap energy. Only acceptors within 10 Å of the surface were considered as effective charge-carrier traps, so solution concentrations of 10 mM produced effective surface-based acceptor densities of 3×10^{10} cm^{-2}. An average value for the electronic coupling was used to calculate the maximum rate constant for acceptors positioned at this fixed distance from the electrode surface.[48] Capture coefficients for the transfer of electrons and holes were obtained by weighting this rate constant with the corresponding Franck-Condon factors for electron and hole transfer.[50] The four input parameters that generated the various simulations were therefore the barrier height, the redox-active acceptor concentration, the surface trap density, and the initial carrier injection level. A barrier height of 1.03 V, determined experimentally for the n-Si/CH_3OH-$Me_2Fc^{+/0}$ contact,[18, 51, 52] was used to simulate a semiconductor/liquid contact under strong inversion, while a barrier height of 0.65 V, characteristic of the n-Si/CH_3OH-$Me_{10}Fc^{+/0}$ contact,[18, 51, 52] was used for simulations of an n-Si/liquid contact under depletion conditions. The sheet photoconductivity, $\Delta\sigma(y,t)$, at a given time, t, and position, y (perpendicular to the plane of the solid/liquid interface), was computed by multiplying the electron and hole concentrations as a function of distance and time, n*(y,t)* and p*(y,t)*, respectively by the corresponding charge-carrier mobility values, $\mu_n(y,t)$ and $\mu_p(y,t)$, respectively,[1, 53]

$$\begin{aligned}\Delta\sigma(\mathrm{y,t}) &= \mathrm{q}\cdot\left(\mathrm{n(y,t)}\cdot\mu_n(\mathrm{y,t})+\mathrm{p(y,t)}\cdot\mu_p(\mathrm{y,t})\right)-\mathrm{q}\cdot\left(\mathrm{n_0(y)}\cdot\mu_{n,0}(\mathrm{y})+\mathrm{p_0(y)}\cdot\mu_{p,0}(\mathrm{y})\right)\\ \Delta\sigma(\mathrm{t}) &= \frac{2}{\mathrm{d}}\cdot\int_0^{\mathrm{d}/2}\Delta\sigma(\mathrm{y,t})\cdot\mathrm{dy}\end{aligned} \qquad \text{(Eq. 3.6)}$$

where concentrations and mobilities at equilibrium are denoted by a subscript “0”. Several models were tested to compute the mobility of charge carriers. These models ranged from constant mobility values to models incorporating concentration dependencies and the saturation of the charge-carrier drift velocity under the influence of high electric fields.[1, 45, 54, 55] Constant values for the mobility were found to be adequate for the injection levels of interest. Numerical integration over half of the experimental sample thickness (*d/2* = 95 μm) produced the value for the photoconductivity, Δσ*(t)*, for the sample width of interest. Photoconductivity decays were fitted to single and multiple exponentials using a standard-least-square-fitting method (Sigma Plot 5.0) with no weighting applied to the residuals.

3.3.2 Photoconductivity Decay Measurements

The contactless rf conductivity apparatus that was used to measure the photoconductivity decay dynamics as well as the Nd:YAG laser (Spectra-Physics INDI-30, 1064 nm, 10 ns pulses, 10 Hz repetition rate) used to illuminate the sample have been described in detail elsewhere.[19, 33, 56] Using neutral density filters, the power density of the expanded, incident beam was adjusted to either 7×10^{-4} mJ cm^{-2} pulse^{-1} for high-level injection conditions or to 1.3×10^{-6} mJ cm^{-2} pulse^{-1} for low-level injection conditions. After the injected carriers had spread throughout the 190 μm thick Si samples, these power densities produced photogenerated carrier concentrations of 2.8×10^{14} carriers cm^{-3} pulse^{-1}

at high-level injection conditions and 5.2×10^{11} carriers cm^{-3} $pulse^{-1}$ at low-level injection conditions.

Long bulk lifetime (> 200 μs), (111)-oriented float-zone Si wafers were obtained from Virginia Semiconductor, Inc. The wafers were polished on both sides, were 190 – 200 μm in thickness, and were nominally n-type (phosphorous) doped, with resistivities of 3817 – 3826 Ω cm, as specified by the manufacturer. An electron mobility of 1450 cm^2 V^{-1} s^{-1} implies that the free carrier concentration is 1×10^{12} cm^{-3} in such samples.[1] These Si wafers were mechanically cut into approximately 1 cm^2 pieces for use in photoconductivity decay measurements. Prior to use, samples were etched for 15-20 min in 40% $NH_4F_{(aq)}$ (Transene Co.), rinsed with distilled H_2O (18.2 MΩ cm resistivity), and dried under a stream of $N_{2(g)}$.

In the case of photoconductivity measurements involving $N_{2(g)}$ or solvents like CH_3CN or THF, samples were placed into sealed glass vessels and were typically assembled in a $N_{2(g)}$ flushbox. These samples were studied within 20 min of exposure to the ambient of interest. Due to the high rf absorbance of the etching solutions, measurements involving aqueous fluoride solutions were carried out by placing a drop of solution on both sides of the sample and by mounting it between polycarbonate plates. The assembly took place in air and the samples were used within 3 min or less of exposure to the etching solution. With the exception of aqueous fluoride solutions, the photoconductivity decays were stable over at least a 30 min period of data collection. Both sides of the semiconductor sample were exposed during etching and during contact with the electrolyte solutions, and both sides were therefore active surfaces for recombination during the lifetime measurements. Lifetimes for individual samples were obtained by averaging 128 signal decays for each experiment. Mean lifetimes reported for some surface treatments were determined by averaging the lifetimes of at least 3 samples that had been subjected to nominally identical surface treatments.

The observed photoconductivity decay lifetime, τ, can be related to the bulk lifetime, τ_b, and to the surface recombination velocity, *SRV*, through the following expression:[5, 20, 57]

$$SRV = \frac{d}{2}\left(\frac{1}{\tau} - \frac{1}{\tau_b}\right) \tag{Eq. 3.7}$$

where *d* is the sample thickness and both surfaces are electrically active in carrier recombination. Data were fit to a single exponential using a standard-least-square-fitting method (Sigma Plot 5.0) with no weighting applied to the residuals.

The lifetimes measured for Si surfaces in contact with 18 M $H_2SO_{4(aq)}$ have been reported to be useful for setting lower bounds on the bulk lifetime of the Si samples and to obtain *SRV* values for other Si surfaces.[5, 20] For many of the surfaces that will be described below, however, the measured lifetimes approached, or in some cases exceeded, the values of the lifetimes obtained for the same wafer in 18 M $H_2SO_{4(aq)}$. Unless otherwise specified, *SRV* values are reported assuming $\tau_b = \infty$. The reported *SRV* values therefore represent upper limits to the true value of *SRV*.

3.3.3 Measurement of the Built-in Voltage of Si/H_2O Contacts Using Differential Capacitance Measurements

Band-edge positions of semiconductor/liquid contacts are most commonly determined using differential capacitance methods. These methods have been extensively reviewed in the literature.[59-62] In order to justify the significant simplifying approximations made in the determination of the built-in voltage, V_{bi}, a set of stringent conditions have to be met.[59-62] Specifically, no contribution of surface states at the solid/liquid interface, usually evident by a severe frequency dependence of the measured capacitance, should be observed.[59-62]

TABLE 3.1. Physical input parameters of the TeSCA simulations

physical parameter	Value	ref
Silicon		-
dopant density	$N_D = 1.1\times10^{12}$ cm^{-3}	-
dopant density of ohmic selective contact[a]	$N_{A,ohmic} = 1\times10^{18}$ cm^{-3}	-
band gap	$E_g = 1.12$ eV	1
effective density of states in the conduction band	$N_C = 2.8\times10^{19}$cm^{-3}	1
effective density of states in the valence band	$N_V = 1.04\times10^{19}$ cm^{-3}	1
mobility of electrons	$\mu_n = 1460$ cm^2 V^{-1} s^{-1}	1
mobility of holes	$\mu_p = 485$ cm^2 V^{-1} s^{-1}	1
x-y-z dimensions of the simulated electrode		-
x (width of simulated electrode)	3 μm	-
y (thickness of the simulated electrode)	1×10^5 μm	-
z (height of simulated electrode)	100 μm	-
gate contact		-
barrier height of Si/Me$_2$Fc$^{+/0}$ contact	ϕ_B [Si/Me$_2$Fc$^{+/0}$] = 1.03 V	18, 51, 52
barrier height of Si/Me$_{10}$Fc$^{+/0}$ contact	ϕ_B [Si/Me$_{10}$Fc$^{+/0}$] = 0.65 V	18, 51, 52
thickness of Helmholtz layer	$\Delta x_H = 3$ Å	58
dielectric constant	$\varepsilon_H/\varepsilon_o = 6$	58
laser excitation		-
time at which intensity is maximum	$t_{Imax} = 30$ ns	-
full width at half-maximum value	$\tau = 4.3$ ns	-
penetration depth at 1064 nm excitation wavelength	$\alpha = 100$ cm^{-1}	2
concentration of injected charge carriers (low-level injection)	3.3×10^{11} cm^{-3} pulse^{-1}	-
concentration of injected charge carriers (high-level injection)	2.3×10^{14} cm^{-3} pulse^{-1}	-
dynamic trapping model		-
energy of traps with respect to the mid-gap energy level	$\mathbf{E}_T = 0$ eV	-
coefficients for capture of electrons and holes in the bulk	$k_{n,b}, k_{p,b} = 1\times10^{-8}$ cm^3 s^{-1}	2
concentration of traps in the bulk	$N_{T,b} = 5\times10^{10}$ cm^{-3}	-
coefficients for capture of electrons and holes at the surface	$k_{n,s} = 1\times10^{-8}$ cm^3 s^{-1}	1,40,41
	$k_{p,s} = 1\times10^{-8}$ cm^3 s^{-1}	
concentration of surface traps	$N_{T,s} = 1\times10^7 – 1\times10^{13}$ cm^{-2}	-
energy of Me$_2$Fc$^{+/0}$ with respect to the mid-gap energy level	$\mathbf{E}$(Me$_2$Fc$^{+/0}$) = -0.47 eV	-

energy of $Me_{10}Fc^{+/0}$ with respect to the mid-gap energy level	**E**($Me_{10}Fc^{+/0}$) = -0.09 eV	-
capture coefficients of electrons and holes for $Me_2Fc^{+/0}$ [b]	$k_{n,A} = 5\times10^{-10}$ cm^3 s^{-1}	-
	$k_{p,A} = 2\times10^{-13}$ cm^3 s^{-1}	
capture coefficients of electrons and holes for $Me_{10}Fc^{+/0}$ [b]	$k_{p,A} = 1\times10^{-10}$ cm^3 s^{-1}	-
surface concentration of acceptor states	[A] = $3\times10^6 – 3\times10^{10}$ cm^{-2}	-

[a] The thickness of the dopant layer at the ohmic selective contact was 1 μm. The hole concentration was decreased to the bulk concentration using a gaussian distribution (= 10 μm).

[b] Maximum rate constant for charge transfer at a fixed distance of 5×10^{-13} cm^3 s^{-1} was used.[48] This rate constant was weighted by the Franck-Condon factors for electrons and holes assuming a standard free energy change for electrons of 1.03 eV ($Me_2Fc^{+/0}$) and 0.58 eV ($Me_{10}Fc^{+/0}$), respectively, and a standard free energy change for holes of 0.09 eV ($Me_2Fc^{+/0}$) and 0.56 eV ($Me_{10}Fc^{+/0}$), respectively. The reorganization energy for both species in CH_3OH.

n-Si(111) chips (obtained from Wacker) had a dopant density of 6×10^{14} cm^{-3}, a miscut angel of less than 0.5°, and were contacted on the unpolished back side with Ga-In eutectic. p-Si(111) chips (obtained from University Wafer) had a dopant density of 2×10^{15} cm^{-3}, a miscut angel of less than 4° and were contacted on the unpolished back side with Al (annealed at 450°C in 98:2 $N_{2(g)}$:$H_{2(g)}$ for 20 min). The Si chips were approximately 2.5 × 1.5 cm in dimensions. The back contact and the edges of the Si chips were insulated using white epoxy (Loctite 1C Hysol Epoxi-Patch Adhesive). Prior to etching in 40% $NH_4F_{(aq)}$ (Transene Co.) the assembled electrodes were cleaned by sequential immersion in 1,1,1-trichloroethane, acetone, isopropanol and water. Impedance spectra were recorded with a Schlumberger Model 1260 frequency response analyzer (FRA), which was GBIB-controlled using the ZPlot Impedance Analyzer Software (Scribner Associates Inc.). For some impedance spectra the electrochemical cell was placed inside a Faraday cage. Impedance spectra of the n-Si(111)/liquid contacts were obtained using sinusoidal AC signals (10 – 10^5 Hz, 10 mV amplitude). The FRA was interfaced with a Solartron SI 1287 Electrochemcial Interface to apply a DC bias. The n-Si(111) electrodes were typically biased with respect to a saturated calomel electrode (SCE) via a glass fritted bridging tube, or with respect to a Pt-black electrode (Pt-black was galvanostatically deposited on a Pt foil using a current density of 30 mA cm^{-2} for 10 min in a solution containing 0.072 M H_2PtCl_6, 0.13 mM lead acetate) for solutions involving $H_{2(g)}$, or in the case of aqueous fluoride solutions with respect to a Pd-wire saturated with $H_{2(g,sol)}$ (a 7 cm long coil-shaped Pd wire was annealed in an acetylene flame until white hot, then charged and discharge in 5 M $H_2SO_{4(aq)}$ seven times, before being completely charged with $H_{2(g)}$; current 0.1 A). The DC bias range was chosen to ensure that measurements were taken in the desired forward or reverse bias regime. Impedance spectra at varying DC bias were usually obtained by scanning the bias from reverse to forward bias. In some cases the scan direction was reversed or even cycled in order to determine the scan-direction dependence of the recorded impedance spectra. Impedance scans compromised 20 steps per frequency decade and 20 cycles were collected to obtain a high confidence level for the measured impedance at each frequency. Impedance spectra which were obtained under reverse bias were fit to a 3-element equivalent circuit, consisting of a parallel combination of a resistor and a capacitor with both elements being in series with a resistor representing the cell resistance. For all measurements reported herein, there was no frequency dependence of the capacitance and therefore the capacitance was set equal to the space-charge capacitance[59-62] The Mott-Schottky equation, Eq. 1.14, was used to determine the built-in voltage.[1] To probe the influence of surface states, the total parallel capacitance of the n-Si/ liquid contact as a function of both frequency and forward bias was determined in accordance with the method used by Searson *et al.*[31, 32, 63] In addition to differential capacitance measurements, the anodic limiting currents of the Si/H_2O contacts were investigated. Standard potentiodynamic methods were employed using a Solartron SI 1287 Electrochemical Interface (scan direction: open circuit potential to reverse bias and back; scan rate was 20 mV.sec^{-1}) as the potentiostat.

3.3.4 Measurement of the Built-In Voltage of Si/Liquid Contacts Using a Near-Surface Channel Conductance Method

In order to probe the band-edge positions and surface state densities of Si/liquid contacts using the differential capacitance method described above, Si surfaces must be placed under severe reverse and forward bias, making any comparison with the conditions at charge-transfer equilibrium, i.e., conditions approximating those during contact less rf decay measurements, more than ambiguous. In order to address these issues a method used in the past to determine the barrier height of n-Si/CH_3OH-$Me_2Fc^{+/0}$ contacts was adopted.[16]

3.3.4.1 Fabrication of n^+-p-Si(111)-n^+ Devices

Figure 3.2 shows a schematic diagram of the n^+-p-Si(111)-n^+ device fabrication. Test grade (111)-oriented, boron-doped Si wafers (from University Wafer) with a dopant density of 2×10^{15} cm^{-3} and a miscut angle of less than 4° were first cleaned by sequential immersion in RCA solutions (4:1:1 H_2O:NH_4OH:H_2O_2 at 75 °C for 5 min, de-ionized water for 1 min, 50:1 H_2O:HF for 20 sec, and 4:1:1 H_2O:HCl:H_2O_2 at 75 °C for 5min) and de-ionized water (1min) and the wafers were then blown dry with $N_{2(g)}$. A thick oxide layer (10 kÅ) was grown by a commercial foundry (Silicon Quest International Inc.), to provide an effective mask for phosphorous doping. To generate the desired oxide mask, the wafers were first cut into 2 cm × 2 cm pieces and were baked on a digital hotplate at 180 °C for 30 min. A thin layer of AZ 5214 E photoresist (Clariant) was applied by spin coating at 4000 rpm for 60 sec and the chips were subsequently pre-baked for 90 sec at 95 °C on a hot plate. The photoresist-coated chips were exposed for 8 sec to a UV light source (Karl Süss KSM mask aligner, 200 W Hg light bulb) through a glass mask (Microchrome Technology Inc., High Resolution UF Plate, Type 180B; patterns were defined using standard black and white photography), baked for 75 sec at 105 °C, and subsequently flooded with UV light for 20 sec. After the last exposure step, the samples were immersed in AZ 327 MIF developer (Clariant) for 30 sec and were immersed in water for 2 min. The structure were etched in buffered HF solution (Transene Co) for 10 min. The photoresist was removed by sequential immersion in acetone (10 min), isopropanol (1 min), and RCA solutions and the chips were blown dry with $N_{2(g)}$. The thereby exposed regions were doped n-type for 60 min at 1000 °C under flowing $N_{2(g)}$ (flow rate 1 liter per minute) in a tube furnace equipped with a quartz tube solely dedicated for this purpose. The polished side of the patterned Si wafers faced the phosphorous diffusion source (Saint Gobain, Phosphorous planar diffusion source, Source type PH-1000N), which had to be activated prior to the actual doping for at least 8 h at 1000 °C under flowing $N_{2(g)}$ (flow rate:1 liter per minute) using Si dummy wafers to establish constant boundary conditions. After the doping process, the chips were immersed sequentially in a phosphorous glass etch (20:1 H_2O:HF for 2 min) and water (2 min) and were then blown dry with $N_{2(g)}$. Due to the high diffusion constant of phosphorous in Si no drive-in of the dopants was required. The fabrication process was continued by photolithographically defining metal ohmic contacts on the doped regions. The metal contacts were 200 nm thin Al alloyed with 1 wt% Si and were deposited by means of a home-built rf-sputtering system. The photoresist was lifted off by sequential immersion in hot acetone (30 min; ultrasonic cleaning for 5 min) and isopropanol (5 min). The contacts were not annealed. The chips were glued to polycarbonate plates and the ohmic contacts on the transconductance devices were electrically contacted through very stiff, V-shaped pieces of piano wire (McMaster, 0.2 mm diameter). The piano wire clips were in electrical contact with brass screws, which were soldered to tinned copper wires. To avoid electrostatic discharge, the electrical assembly was performed on a grounded metal surface. The chips and the 4 contacts were subsequently encapsulated in white epoxy (Loctite 1C Hysol Epoxi-Patch Adhesive) exposing the center channel and very small amount of the n^+-doped regions adjacent to the center channel. Measurements in 18 M $H_2SO_{4(aq)}$ required insulation with paraffin wax (Paxter Household wax)

3.3.4.2 Method of Characterization & Data Analysis

Working devices had a 4 Ω resistance across a common phosphorous doped contacts (A-C and B-D, see Figure 3.2) and showed a symmetrical double diode across the p-channel (A-B and C-D, see Figure 3.2) with high resistances (> 1 MΩ). Impedance spectra were recorded with a Schlumberger Model 1260 frequency response analyzer (FRA), which was GBIB-controlled using the ZPlot Impedance Analyzer Software (Scribner Associates Inc.). All contacts were grounded during the initialization sequence of the FRA. Measurements for devices in contact with CH_3CN-1.0 M $LiClO_4$ solutions were carried out in a $N_{2(g)}$-purged dry-box (< 0.1 ppm O_2). Measurements in aqueous

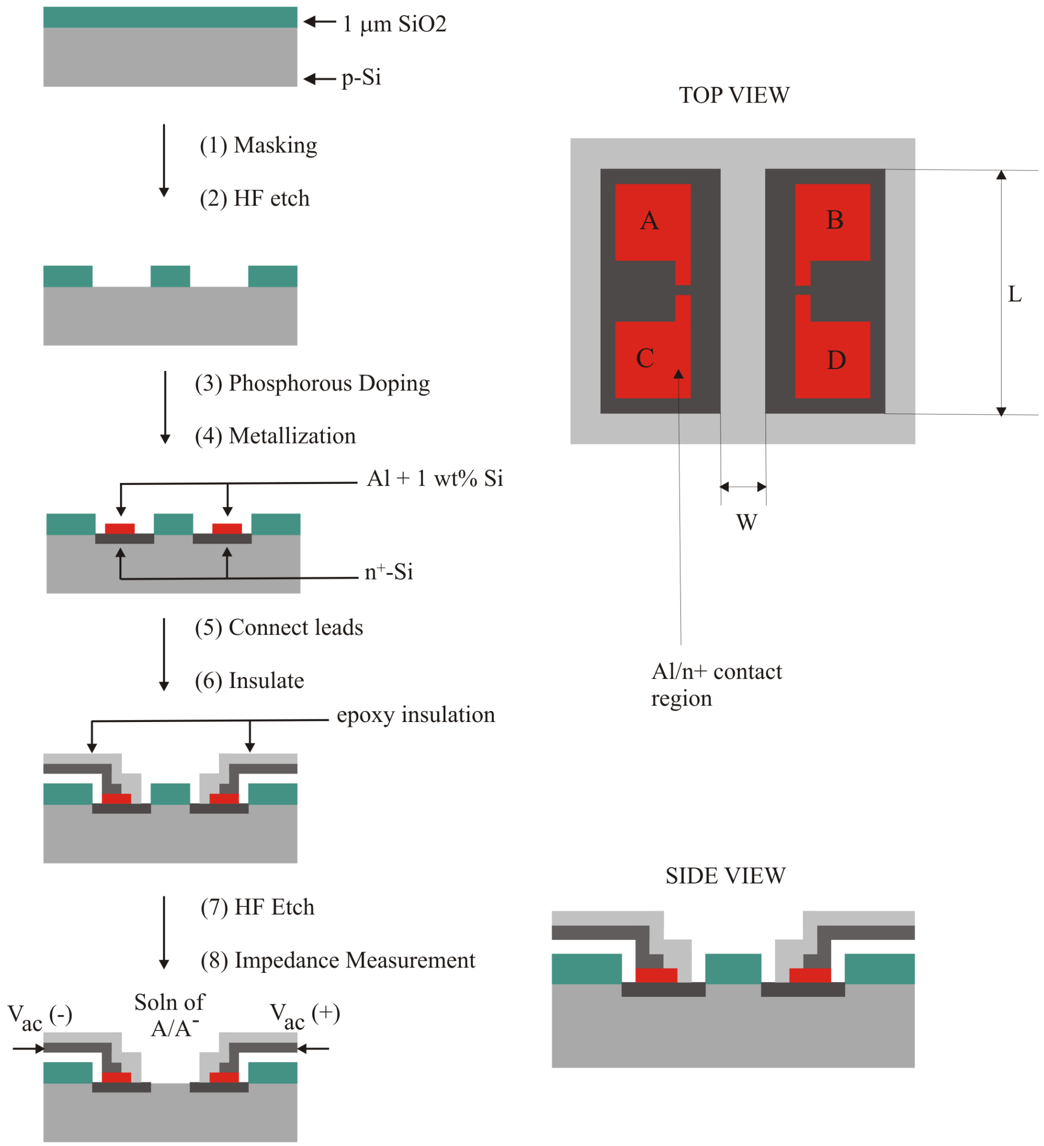

Figure 3.2 Schematic Drawing of the Fabrication of n^+-p-Si(111)-n^+ Devices

fluoride solutions were carried out in ambient. Devices were etched for 10 min in buffered $HF_{(aq)}$ to remove the oxide layer protecting the p-channel and then for 20 min in $NH_4F_{(aq)}$. To re-use a device, the device was immersed for 1 min in buffered $HF_{(aq)}$ and then etched for 20 min in $NH_4F_{(aq)}$, unless otherwise noted. Unless otherwise noted all experiments were carried out in the dark and in unstirred solutions. To acquire an impedance spectra the common contacts were shorted together (A-C and B-D, see Figure 3.2) and a sinusoidal AC signal ($10^{-3} – 10^{6}$ Hz, 10 mV amplitude) was applied across the p-channel. Scans compromised 20 steps per frequency decade and 20 cycles were collected to obtain a high confidence level for the measured impedance at each frequency.

Impedance spectra were fit to a 3-element equivalent circuit, consisting of a a resistor representing the cell resistance in series with a parallel combination of the channel resistor, R_{ch}, and a capacitor. For some spectra, the half circles were significantly suppressed so instead of a capacitor a constant phase element had to be used. The total charge density removed from the semiconductor during inversion, Q_s, is approximately equal to the charge density of minority carriers within the inversion layer, Q_n, and the charge-carrier density necessary to reach inversion, Q_b, see Eq. 3.8[1]

$$Q_s \approx Q_n + Q_b \qquad \text{(Eq. 3.8)}$$

The general formula necessary to calculate the charge carrier densities was developed in Chapter 1.2, see Eq. 1.11. The charge-carrier density necessary to reach inversion (Q_b) can be calculated by Eq. 3.9, by setting the voltage drop ψ equal to the voltage drop necessary to reach inversion, V_i. For the calculation of V_i only the knowledge of the intrinsic electron concentration (N_i) and the acceptor dopant density (N_A) are required, see Eq. 3.9[1]

$$Q_b = \sqrt{2\varepsilon_\mathrm{s} k_\mathrm{B} T N_\mathrm{A}} \cdot F\left(\psi = V_i\right)^{\frac{1}{2}} \quad , V_i = 2 \cdot \frac{1}{\beta} \cdot \ln\left(\frac{N_\mathrm{A}}{N_\mathrm{i}}\right)$$
$$F = \left\{ e^{-\beta\psi} + \beta\psi - 1 + \frac{N_\mathrm{D}}{N_\mathrm{A}} \cdot \left(e^{\beta\psi} - \beta\psi - 1\right) \right\}, \qquad \beta = \frac{q}{k_\mathrm{B} T} \qquad \text{(Eq. 3.9)}$$

In these equations ε_s denotes the permittivity of Si (= 1.05×10^{-12} F cm^{-1}), q is the elementary charge (= 1.6×10^{-19} C), k_B is Boltzmann's constant (= 1.38×10^{-23} J K^{-1}), N_i is the intrinsic carrier concentration (=1.45×10^{10} cm^{-3}) and T is the temperature in K. The acceptor and donor concentrations are represented by N_A and N_D, respectively. The function $F(\psi)$ is defined in Eq. 3.9. For the case of strong inversion, the charge density in the inversion layer can be calculated by

$$Q_\mathrm{n} = \frac{L}{\mu_\mathrm{n} \cdot W \cdot R_\mathrm{ch}} \qquad \text{(Eq. 3.10)}$$

where L denotes the separation between the n^{+}-doped contacts, W the width of the p-doped channel, μ_n is the mobility of electrons and R_ch is the resistance in the p-channel as determined by impedance spectroscopy. The total charge-carrier density, Q_s, can now readily be calculated using Eq. 3.8 and the built-in voltage, V_bi, is calculated by numerically solving Eq. 3.11.

$$Q_S = \sqrt{2\varepsilon_\mathrm{s} k_\mathrm{B} T N_\mathrm{A}} \cdot F\left(\psi = V_\mathrm{bi}\right)^{\frac{1}{2}} \qquad \text{(Eq. 3.11)}$$

3.3.5 Materials & Chemicals

Concentrated, 18 M $H_2SO_{4(aq)}$ and 48% $HF_{(aq)}$ were obtained from EM Science. Buffered $HF_{(aq)}$ and 40% $NH_4F_{(aq)}$ were obtained from Transene Co. Anhydrous THF was purchased from Aldrich Chemical Corp. and was used without further purification.

Anhydrous CH_3CN was purchased from Aldrich Chemical Corp. and was further purified by sequential distillation over $CaH_{2(s)}$ and $P_2O_{5(s)}$ and was collected over activated molecular sieves (3 Å, Aldrich). Bis(cyclopentadienyl)iron or ferrocene (Fc^0) and bis(pentamethylcyclopentadienyl) iron ($Me_{10}Fc^0$) were obtained from Strem Chemicals Inc. and were sublimed before use. Ferrocenium tetrafluoroborate (Fc^+)(BF_4^-) was obtained from Aldrich and was recrystallized from a mixture of THF and CH_3CN. The formal reduction potential of Fc/$Fc^{+/0}$ in CH_3CN and THF, which were used as a reference in these studies, were 0.48 and 0.66 V *vs.* methanolic SCE, respectively. Bis(pentamethylcyclopentadienyl) iron tetrafluroborate ($Me_{10}Fc^+$)(BF_4^-) was synthesized from sublimed $Me_{10}Fc^0$ according to published methods.[64] Cobaltocene ($CoCp_2^0$) was purchased from Aldrich and was purified by sublimation at 45 °C under $N_{2(g)}$. Cobaltocenium hexafluorophosphate ($CoCp_2^+$)(PF_6) was purchased from Aldrich and was recrystallized from a mixture of CH_3CN and diethyl ether.

The formal reduction potentials of redox couples in acetonitrile (CH_3CN) and tetrahydrofuran (THF) were determined by means of cyclic voltammetry using a polished Pt disc working electrode, a Pt mesh counter electrode and a reference electrode with a Luggin capillary. Fused lithium percholrate (0.1 M) served as the supporting electrolyte. For a given solvent, redox potentials were referenced to the ferrocene/ferrocenium ion electrode in that specific solvent. The ferrocene/ferrocenium electrode in a given solvent was referenced with respect to a saturated methanolic calomel electrode. The cell potentials of equimolar solutions used in rf decay measurements closely corresponded to the formal reduction potentials. The formal reduction potentials of $Me_{10}Fc^{+/0}$ *vs.* $Fc^{+/0}$ in CH_3CN and THF were -0.45 and -0.41 V *vs.* $Fc^{+/0}$, respectively. The formal reduction potential of $CoCp_2^{+/0}$ in CH_3CN and THF was -1.36 and -1.38 V *vs.* $Fc^{+/0}$, respectively. All non aqueous solutions were prepared and stored in a $N_{2(g)}$-purged flushbox that contained less than 10 ppm of $O_{2(g)}$ as indicated by the absence of visible fumes from diethyl zinc. All solutions were chemically stable on the timescale of the photoconductivity decay measurements and differential capacitance measurements.

3.4 RESULTS

This chapter presents the results of the digital simulations and the experimental results of photoconductivity decay measurements (Chapter 3.4.1 and Chapter 3.4.2.1, respectively). This investigation is complemented by a study of the surface recombination behavior of Si in contact with aqueous fluoride solutions. The results of photoconductivity decay measurements involving such contacts are presented in Chapter 3.4.2.2. The surface energetics of these contacts are probed by various techniques. The results of differential capacitance measurements are presented in Chapter 3.4.3 and the results of near-surface channel conductance measurements are presented in Chapter 3.4.4.

3.4.1 Digital Simulation of Photoconductivity Decay Dynamics for Si/Liquid Contacts

3.4.1.1 Photoconductivity Decay Dynamics of Silicon/Liquid Contacts Under Strong Inversion

Digital simulations were performed to evaluate the influence of band bending on the effective surface recombination velocity of a semiconductor/liquid contact. Simulations were performed for both low-level and high-level injection conditions as a function of the density of surface states at the solid/liquid interface. The results of the simulations are summarized in Table 3.2. The photoconductivity decay profiles for charge carriers under such conditions were determined in the 95 μm thick region of the semiconductor adjacent to the semiconductor/liquid interface.

Figure 3.3 presents the simulated carrier concentration profiles *vs.* distance for the n-Si/CH_3OH-$Me_2Fc^{+/0}$ contact for both high (1×10^{12} cm^{-2}) surface state densities under both low (a) and high-level injection conditions (b). In both cases, the photoconductivity

TABLE 3.2. Simulation results

	σ_i (Ω^{-1} cm^{-1})[a]	τ_i (ms)[a]	$\Delta p_{1,i}/p_0$ (-)[b]	$\tau_{1,i}$ (ms)[b]	$\Delta p_{2,i}/p_0$ (-)[b]	$\tau_{2,i}$ (ms)[b]	$\Delta p_{3,i}/p_0$ (-)[b]	$\tau_{3,i}$ (ms)[b]	injection level[c]	$N_{T,s}$ (cm^{-2})[d]	liquid contact[e]	[A] (cm^{-2})[f]
I	1.0×10^{-4}	2.1	5.8×10^{3}	2.1	10.5	5.1	0.08	12.8	LLI	1×10^{12}	$Me_2Fc^{+/0}$	3×10^{6}
	0.8×10^{-4}	14.0										
	2.7×10^{-4}	75.6										
II	1.2×10^{-4}	2.2	5.8×10^{3}	2.1	10.5	5.1	0.09	12.5	LLI	1×10^{7}	$Me_2Fc^{+/0}$	3×10^{6}
	0.9×10^{-4}	16.5										
	2.4×10^{-4}	84.9										
IIa	0.9×10^{-4}	2.4	5.8×10^{3}	2.1	10.4	5.1	0.09	12.5	LLI	1×10^{7}	$Me_2Fc^{+/0}$	3×10^{10}
	3.7×10^{-4}	47.3										
III	0.28	3.9	4.5×10^{6}	3.7	4.2×10^{3}	3.7	0.44	5.0	HLI	1×10^{7}	$Me_2Fc^{+/0}$	3×10^{6}
IIIa	0.28	3.9	4.5×10^{6}	3.7	4.2×10^{3}	3.7	0.42	5.0	HLI	1×10^{7}	$Me_2Fc^{+/0}$	3×10^{10}
IV	0.27	3.7	4.2×10^{6}	3.4	4.0×10^{3}	3.5	0.41	5.5	HLI	1×10^{12}	$Me_2Fc^{+/0}$	3×10^{6}

V	0.11	0.002	3.7×10^6	0.001	4.1×10^5	0.001	8.0×10^4	0.001	HLI	1×10^{12}	$Me_{10}Fc^{+/0}$	3×10^6
	0.10	0.009	2.7×10^6	0.009	2.8×10^5	0.009	5.4×10^4	0.009				
	0.06	0.1	1.5×10^6	0.1	1.5×10^5	0.1	3.0×10^4	0.1				
VI	0.28	3.8	16.1×10^6	3.7	1.3×10^6	3.7	0.6×10^6	3.7	HLI	1×10^7	$Me_{10}Fc^{+/0}$	3×10^6
VIa	0.10	0.01	2.7×10^6	0.006	4.4×10^5	0.006	2.3×10^5	0.006	HLI	1×10^7	$Me_{10}Fc^{+/0}$	3×10^{10}
	0.11	0.1	4.7×10^6	0.08	7.4×10^5	0.08	3.8×10^5	0.08				
	0.06	1.5	2.4×10^6	1.3	3.8×10^5	1.3	1.9×10^5	1.3				
VII	4.4×10^{-4}	3.1	1.4×10^4	2.6	2.4×10^3	4.0	1.0×10^3	5.9	LLI	1×10^7	$Me_{10}Fc^{+/0}$	3×10^6
VIIa	1.4×10^{-4}	0.008	4.6×10^3	0.007	660	0.005	400	0.005	LLI	1×10^7	$Me_{10}Fc^{+/0}$	3×10^{10}
	1.9×10^{-4}	0.05	6.0×10^3	0.04	130	0.04	630	0.04				
	0.7×10^{-4}	0.8	1.2×10^3	0.4	190	0.5	170	0.5				
VIII	1.9×10^{-4}	0.001	5.6×10^3	0.001	570	0.001	280	0.001	LLI	1×10^{12}	$Me_{10}Fc^{+/0}$	3×10^6
	1.4×10^{-4}	0.009	2.0×10^3	0.008	190	0.007	97	0.007				
	0.8×10^{-4}	0.2	0.7×10^3	0.1	50	0.09	30	0.09				

a σ_i: pre-exponential factor; summation over all σ_i yields the photoconductivity at time t = 0; τ_i: photoconductivity decay lifetime; subscript 'i' indicates a term in a multiple exponential.

b $\Delta p_{j,i}/p_0$: pre-exponential factor at a selected distance from the liquid contact and is defined as the difference between the hole concentration at time t = 0 and the equilibrium concentration of holes, p_0; normalized with respect to p_0; $\tau_{j,i}$ lifetime of holes at a selected distance from the liquid contact; subscript 'j' indicates position; j=1: bulk (95 µm); j=2: 5 µm ($Me_2Fc^{+/0}$, $Me_{10}Fc^{+/0}$); j=3: 0.8 µm ($Me_2Fc^{+/0}$) and 2 µm ($Me_{10}Fc^{+/0}$); subscript 'i' indicates a term in a multiple exponential.

c LLI: low-level injection (6.3×10^{11} injected charge carriers cm^{-3} $pulse^{-1}$); HLI: high-level injection (4.4×10^{14} injected charge carriers cm^{-3} $pulse^{-1}$)

d surface trap density

e $Me_2Fc^{+/0}$: 1,1'-dimethylferrocene$^{+/0}$; $Me_{10}Fc^{+/0}$: decamethylferrocene$^{+/0}$

f surface acceptor density of redox couple decay was virtually unaffected by the number of surface traps present at this strongly inverted n-Si/liquid contact.

Under low-level injection conditions, holes in the bulk decayed with a lifetime of approximately 2 ms, equivalent to the Shockley-Read-Hall lifetime for holes in the bulk of the sample (Eq. 3.3),[36] for surface trap densities as high as 1×10^{12} cm^{-2}(Table 3.2: **I, II, IIa**). Only when surface trap densities exceeded 1×10^{13} cm^{-2} did the photoconductivity decay profile somewhat vary, due to a gradual unbending of the bands of Si that reduced the extent of hole accumulation and electron depletion at the solid/liquid contact.

Although a single exponential with a lifetime of approximately 2 ms was the dominating decay function of the photoconductivity under low-level injection, obtaining a good fit to the photoconductivity decay also required the addition of a series of exponentials having slower decay times than 2 ms. This behavior is readily understood by examination of the concentration profiles of Figure 3.3 (a). Silicon samples having a donor density of 1.1×10^{12} cm^{-3} form a broad space-charge region, which remains virtually unchanged in width at low carrier injection levels. Inside this space-charge region, charge carriers decay with lifetimes that are significantly larger than the 2 ms bulk lifetime. Since the overall photoconductivity decay reflects a weighted average of all decay processes inside the simulated electrode width, deviations of the overall decay profile from a single exponential are therefore expected.

Similar to the results obtained under low-level injection, the photoconductivity decays for high level injection were virtually unaffected by the surface trap density up to values of $N_{T,s} > 1\times10^{12}$ cm^{-2}. In contrast to the behavior under low-level injection, photoconductivity decays under high-level injection conditions were well described by a single exponential, with a lifetime of approximately 4 ms, equivalent to the high-injection level Shockley-Read-Hall lifetime for holes in the bulk of the sample (Eq. 3.3), for all surface trap densities explored (Table 3.2: **III, IIIa, IV**). The narrow space-charge region

Figure 3.3 Charge-Carrier Concentration Profiles for Si/Me$_2$Fc$^{+/0}$ Contacts.

Barrier height Φ_B = 1.03 V; low-level and high-level injection conditions (2.3×10^{14} injected charge carriers cm^{-3} pulse^{-1}). Profiles are depicted at 1 μs and at 10 ms after optical light excitation and at equilibrium (equil.). For clarity, only the region adjacent to the semiconductor/liquid contact (y = 0 cm) is shown. (a) Simulation **II**: surface trap density $N_{T,s} = 1\times10^{12}$ traps cm^{-2}. Predominant lifetime of holes (p) in the bulk equals 2.1 ms. (b) Simulation **IV**: surface trap density $N_{T,s} = 1\times10^{12}$ traps cm^{-2}. Lifetime of holes (p) in the bulk equals 3.5 ms.

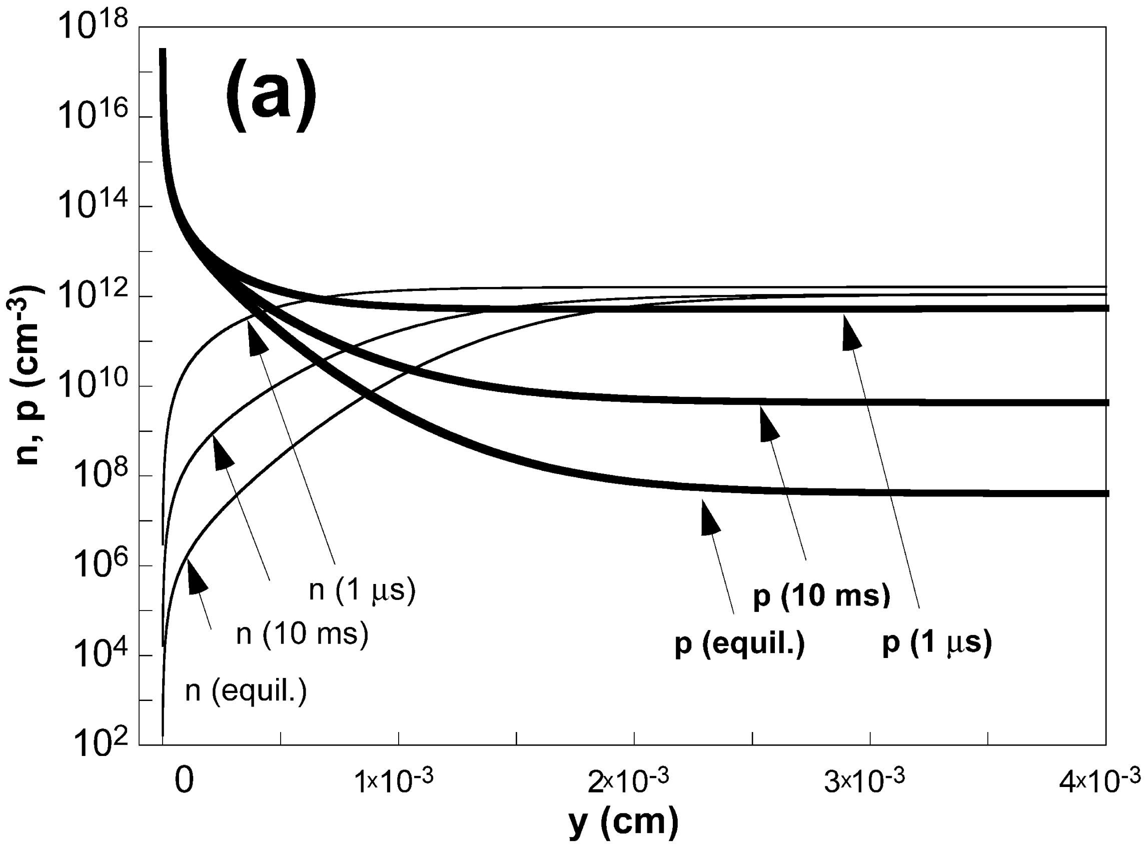
(a)
n, p (cm^{-3})
10^{18}
10^{16}
10^{14}
10^{12}
10^{10}
10^{8}
10^{6}
10^{4}
10^{2}
0
1×10^{-3}
2×10^{-3}
3×10^{-3}
4×10^{-3}
y (cm)
n (1 μs)
n (10 ms)
n (equil.)
p (10 ms)
p (equil.)
p (1 μs)

Figure 3.3 (a)

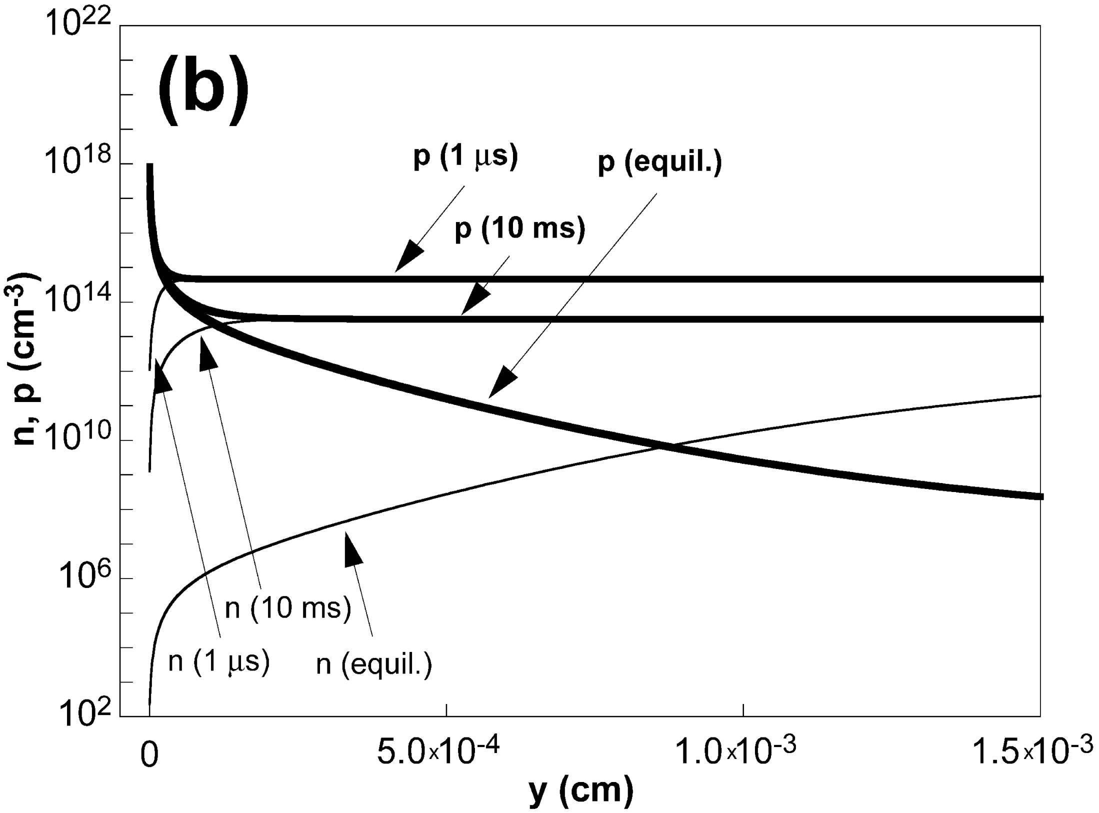
(b)
p (1 μs)
p (equil.)
p (10 ms)
n (10 ms)
n (1 μs)
n (equil.)
n, p (cm-3)
10^22
10^18
10^14
10^10
10^6
10^2
0
5.0×10-4
1.0×10-3
1.5×10-3
y (cm)

Figure 3.3 (b)

under high-level injection conditions produced almost the same decay kinetics for carriers throughout the sample. Furthermore, even under high-level injection, a strong inversion of the charge-carrier profiles at the surface was maintained, which ensured that holes were under accumulation and electrons were under depletion during the photoconductivity decay. The observed lifetime of electrons and holes in the bulk therefore corresponded closely to the high-level injection lifetime of approximately 4 ms predicted by Shockley-Read-Hall theory for this sample.[36] However, it should be noted that the term “high injection” in this work does not imply that the bands of the Si were flat.

The inclusion of electron and hole transfer to acceptor species in solution as an alternative non-radiative recombination process confirmed that in the case of strong inversion acceptor states in solution are not effective as recombination sites (Table 3.2: **IIa, IIIa**).

3.4.1.2 Photoconductivity Decay Dynamics of Silicon/Liquid Contacts Under Depletion

The photoconductivity decay characteristics of n-Si/CH_3OH-$Me_{10}Fc^{+/0}$ contacts exhibited very different behavior. Low surface trap densities produced photoconductivity decay lifetimes similar to those of n-Si/CH_3OH-$Me_2Fc^{+/0}$ and in accord with predictions from Shockley-Read-Hall theory for high-level injection conditions (Table 3.2: **VI**). However, the lifetimes were very sensitive to the surface trap density, and the decay times were a strong function of the value of $N_{T,s}$ (Table 3.2: **V**, **VI**). Similar behavior was observed under low-level injection conditions (Table 3.2: **VII**). The simulations therefore clearly indicate that strong inversion conditions produce long charge-carrier lifetimes even at relatively high surface trap densities and that the effects of increased surface defect levels is pronounced only for semiconductor/liquid contacts in depletion. In contrast to the inversion case, charge transfer to acceptors in solution constitutes an effective recombination pathway for n-Si/CH_3OH-$Me_{10}Fc^{+/0}$ contacts (Table 3.2: **VIa**, **VIIa**). This

Figure 3.4 Charge-Carrier Concentration Profiles for Si/Me$_{10}$Fc$^{+/0}$ Contacts.

Barrier height Φ_B = 0.56 V; high-level injection conditions (2.3×10^{14} injected charge carriers cm^{-3} pulse^{-1}). Profiles are depicted at 1 μs and at 100 μs after optical light excitation and at equilibrium (equil.). For clarity, only the region adjacent to the semiconductor/liquid contact (y = 0 cm) is shown. (a) Simulation V: surface trap density $N_{T,s} = 1\times10^{12}$ traps cm^{-2}. Decay of holes did not follow a single exponential. (b) Simulation VI: surface trap density $N_{T,s} = 1\times10^{7}$ traps cm^{-2}. Lifetime of holes (p) in the bulk equals 3.7 ms.

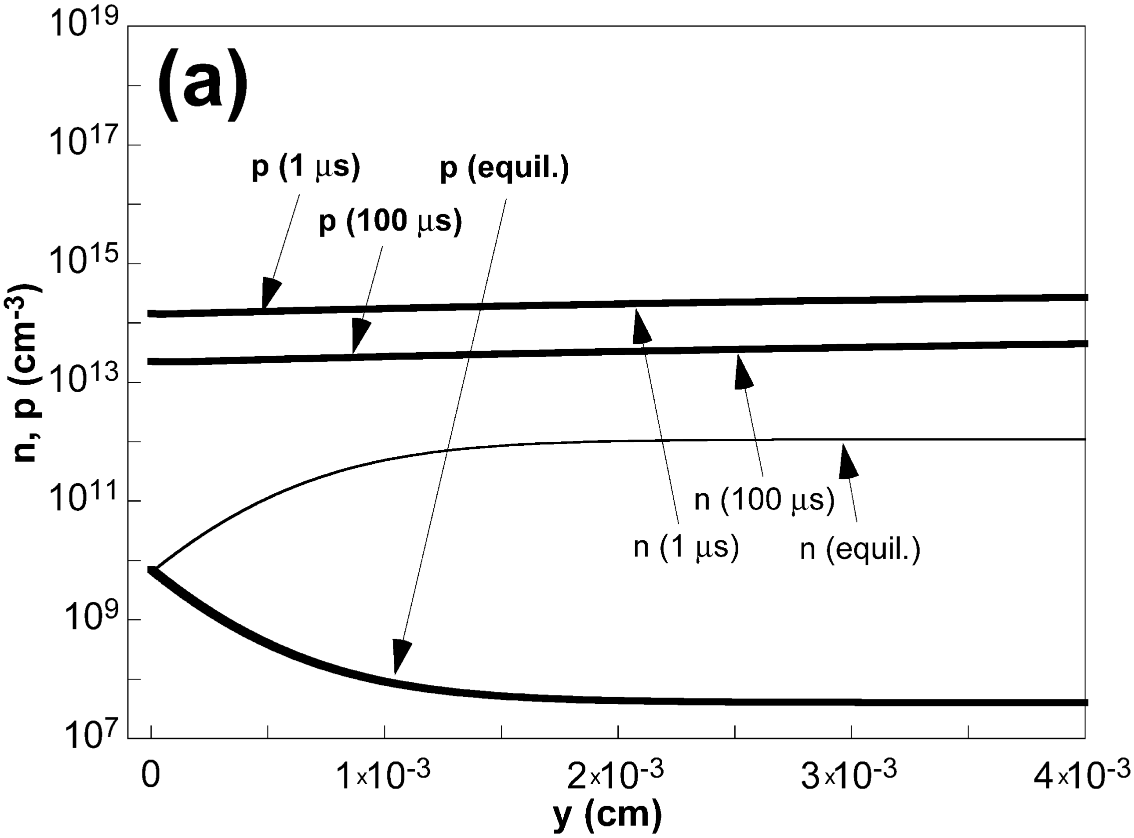
(a)
p (1 μs)
p (equil.)
p (100 μs)
n (100 μs)
n (1 μs)
n (equil.)
10^{19}
10^{17}
10^{15}
10^{13}
10^{11}
10^{9}
10^{7}
n, p (cm^{-3})
0
1×10^{-3}
2×10^{-3}
3×10^{-3}
4×10^{-3}
y (cm)

Figure 3.4 (a)

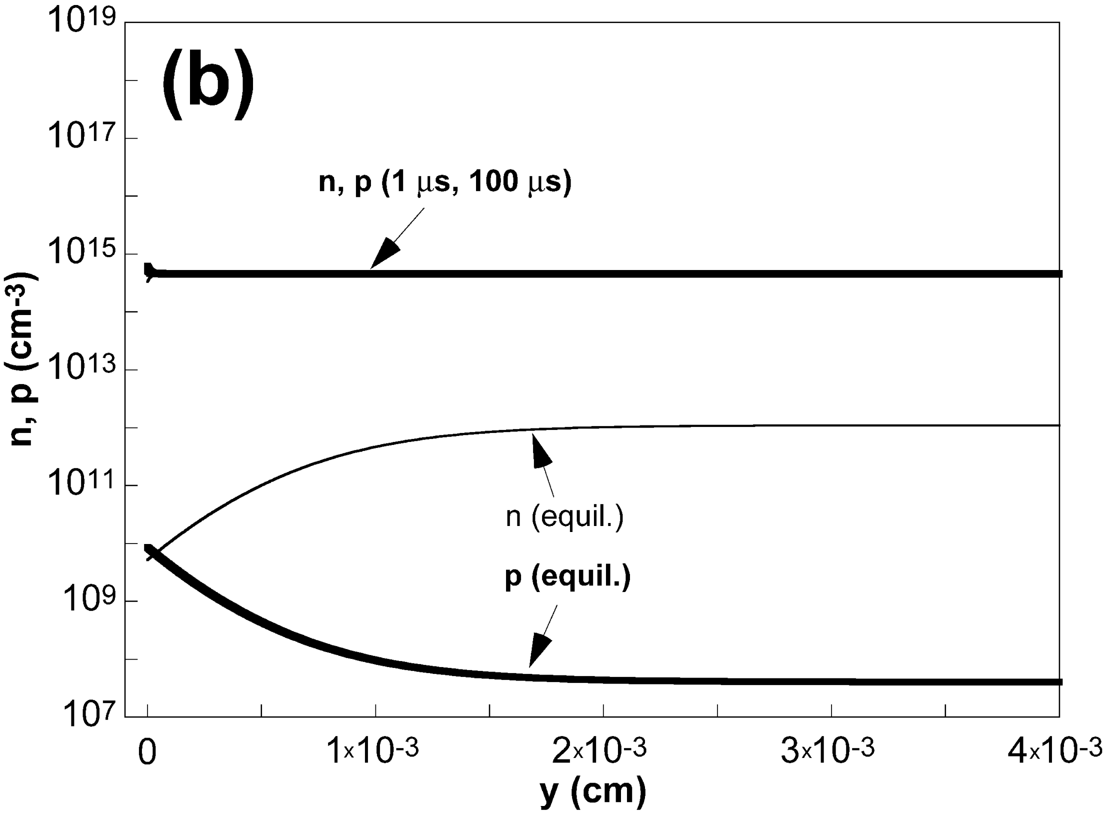
(b)
n, p (1 μs, 100 μs)
n (equil.)
p (equil.)
10^{19}
10^{17}
10^{15}
10^{13}
10^{11}
10^{9}
10^{7}
n, p (cm-3)
0
1x10-3
2x10-3
3x10-3
4x10-3
y (cm)

Figure 3.4 (b)

behavior can be readily understood by the energy level of $Me_{10}Fc^{+/0}$ states, which are close to mid gap thereby forming very effective trap states for both electrons and holes.

3.4.2 Photoconductivity Decay Measurements of Hydrogen-Terminated Si(111)

3.4.2.1 Contact with CH_3CN or THF Solutions Containing $Me_{10}Fc^{+/0}$, $Fc^{+/0}$, or $CoCp_2^{+/0}$

The results of rf conductivity decay measurements for (111)-oriented, H-terminated crystalline Si are summarized in Table 3.3. A representative photoconductivity decay signal for (111)-oriented, H-terminated, crystalline Si is depicted in Figure 3.5.

In this study we only report results for solvents, who are known not to form an alkoxylated surface with oxidants like $Fc^{+/0}$ or I_2, i.e., THF and CH_3CN.[65] Photoconductivity measurements in alkoxylating solvent systems, i.e., CH_3OH containing I_2 or $Fc^{+/0}$, are reported in a different study.[19, 33] The observed carrier lifetime for $NH_4F_{(aq)}$-etched Si samples in contact with THF–0.05 M Fc–0.005 M Fc^+ solutions was quite long, corresponding to *SRV* values under high-level injection of 50±30 cm s^{-1} (Table 3.3: **Ia**). Surface infrared spectroscopic measurements show nearly complete retention of the H-termination after immersion of Si surfaces into THF-Fc^+ electrolytes.[65] Rinsing the H-terminated Si with solvent and contacting the sample with $N_{2(g)}$ produced a high *SRV* value (Table 3.3: **Ib**), and the effect was reversible in that re-immersion into THF–0.05 M Fc–0.005 M Fc^+ (Table 3.3: **Ic**) produced a long carrier decay lifetime even after observation of a short lifetime in contact with $N_{2(g)}$ (Table 3.3: **Ib**).

Use of a species having a more negative redox potential than $Fc^{+/0}$, $Me_{10}Fc^{+/0}$, produced a significantly shorter carrier decay lifetime, and a significantly higher value of *SRV*, regardless of whether the sample had only been etched in $NH_4F_{(aq)}$ or had been etched and then immersed into a THF–Fc^+ solution prior to contact with the THF–$Me_{10}Fc^{+/0}$ solution (Table 3.3: **IIa**, **IIc**). Additionally, removal of the sample from the THF–$Me_{10}Fc^{+/0}$ solution and immersion into the THF–$Fc^{+/0}$ solution restored a low

Figure 3.5 Time-Resolved Photoconductivity Decay.

$NH_4F_{(aq)}$-etched (111)-oriented n-type Si in contact with THF–0.05 M Fc–0.005 M Fc^+ (circles) and in contact with THF–0.05 M $Me_{10}Fc$–0.01M $Me_{10}Fc^+$ (squares). A single-exponential fit to these decays (not shown) yielded time constants of 291 μs and 3.2 μs for the THF–$Fc^{+/0}$-immersed and the THF–$Me_{10}Fc^{+/0}$-immersed samples, respectively. Measurements were made under high-level injection conditions (7.0×10^{-4} mJ cm^{-2} $pulse^{-1}$; 2.7×10^{14} injected charge carriers cm^{-3} $pulse^{-1}$ in a 195 μm thick sample).

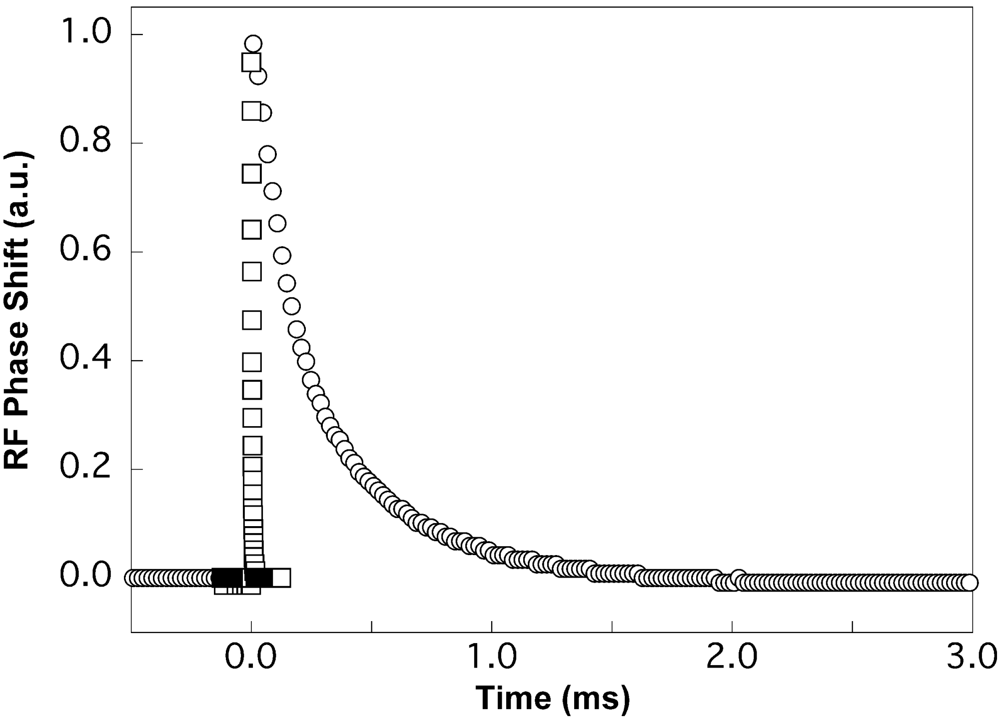

Figure 3.5

effective surface recombination velocity, with *SRV* = 40 ± 10 cm s^{-1} observed under such conditions (Table 3.3: **IId**). This indicates that the electrochemical potential of the electrolyte solution is a critical factor in producing the observed surface recombination velocity values in these systems.

Photoconductivity decay data were also collected for Si surfaces in contact with CH_3CN-$CoCp_2^{+/0}$. These redox systems have a very negative formal reduction potential and are expected to produce an accumulation of electrons at the surface of n-type Si. The average initial decay lifetime for silicon samples in contact with CH_3CN–0.01 M $CoCp_2^{+/0}$ was 370 ± 175 µs (*SRV* = 50 ± 20 cm s-^{1}) for high-level injection and was 375 ± 210 µs (*SRV* = 55 ± 35 cm s^{-1}) for low-level injection (Table 3.3: **IIIa**). Under $N_{2(g)}$ the average lifetime decreased to 6 ± 0.3 µs (*SRV* = 2530 ± 110 cm s^{-1}) and 6 ± 0.1 µs (*SRV* = 2730 ± 40 cm s^{-1}) under high-level and low-level injection, respectively (Table 3.3: **IIIb**). Re-immersion of the silicon samples into the CH_3CN–0.01 M $CoCp_2^{+/0}$ solution produced photoconductivity decay lifetimes that were only slightly longer than the lifetimes measured under $N_{2(g)}$. However, after cleaning in solvent, re-etching in $NH_4F_{(aq)}$, and subsequent re-immersion of these samples into the CH_3CN–0.01 M $CoCp_2^{+/0}$ solution, the photoconductivity decay lifetimes increased to 390 ± 70 µs (*SRV* = 40 ± 10 cm s^{-1}) for high-level injection and 420 ± 100 µs (*SRV* = 40 ± 10 cm s^{-1}) for low-level injection (Table 3.3: **IIIc**).

3.4.2.2 Photoconductivity Decay Measurements of Hydrogen-Terminated Si(111) in Contact with Gaseous Environments, Aqueous Acids or Aqueous Fluoride Solutions

Decays for (111)-oriented, H-terminated Si in contact with various etching solutions are summarized in Table 3.4 and depicted in Figure 3.6 (a)-(b). Each roman numeral indicates a new sample cut from the same wafer. The results are presented in the chronological order of surface treatment. Decays were rapid in air for samples treated with piranha solution or organic solvents. Decay lifetimes were on the order of 5 µs (*SRV* =

TABLE 3.3. Measured lifetimes and surface recombination velocities for H-terminated Si(111) following various surface treatments.

	Surface Treatment	**Low Injection**		**High Injection**	
		τ (μs)	***SRV* (cms^{-1})**	**τ (μs)**	***SRV* (cms^{-1})**
Ia	THF-0.05 M Fc^0-0.005 M Fc^+	280±90	30±10	180±90	50±30
Ib	%, N_2	2.7±0.3	3600±400	2.9±0.3	3400±300
Ic	%, THF-0.05 M Fc^0-0.005 M Fc^+	300±100	30±10	220±160	40±30
Id	%, THF-0.05 M $Me_{10}Fc^0$-0.01 M $Me_{10}Fc^+$	2.6±0.3	3800±400	3.0±0.2	3300±200
IIa	THF-0.05 M $Me_{10}Fc^0$-0.01 M $Me_{10}Fc^+$	3.0±0.7	3300±800	4.0±1.0	2400±600
IIIb	%, N_2	2.7±0.3	3600±400	3.4±0.1	2870±90
IIc	%, THF-0.05 M $Me_{10}Fc^0$-0.01 M $Me_{10}Fc^+$	2.8±0.3	3500±400	3.0±0.4	3300±400
IId	%, THF-0.05 M Fc^0-0.005 M Fc^+	290±90	30±10	250±60	40±10
IIIa	CH_3CN-0.01 M $CoCp_2^0$-0.01 M $CoCp_2^+$[a]	375±210	55±35	375±180	50±25
IIIb	%, N_2	6±0.1	2730±90	6±0.3	2530±40
IIIc	%, CH_3CN-0.01 M $CoCp_2^0$-0.01 M $CoCp_2^+$[a]	420±100	40±10	390±70	40±10

[a] Samples have been cleaned in solvent and re-etched

The symbol "%" indicates that the sample experienced the surface treatment described in the preceding row.

2088 cm s^{-1} , Table 3.4: **IVa**). Immersion of the samples in 48 wt% $HF_{(aq)}$ yielded photoconductivity decays that were very slow and were well fit by a single exponential. The decay lifetimes under high-level injection in $HF_{(aq)}$ were 1049 μs (*SRV* < 9.0 cm s^{-1}, Table 3.4: **IVb**) and 487 μs (*SRV* < 21 cm s^{-1}, Table 3.4: **Vb**) after a piranha etch and 974 ± 51 μs (*SRV* < 10.0±0.5 cm s^{-1}, Table 3.4: **VIa**, averaged over 10 min) after an organic solvent rinse. These values are consistent with the manufacturer's specification that the minority carrier bulk lifetime in these samples, τ_b, is >> 200 μs. Since the thickness dependence of the photoconductivity decay is unknown in this series of measurements the reported *SRV* values only represent an upper bound. Yablonovitch *et al.* measured the lifetime of Si(111)/$HF_{(aq)}$ contacts (pre-treated with piranha etch) as a function of thickness and found that the *SRV* is as low as 0.1 cm s^{-1}.[5, 6, 66] Exposure of a $HF_{(aq)}$-treated Si surface to air produced a rapid decay in the carrier lifetime, with the longest lifetime observed just being on the order of 38 μs (*SRV* = 270 cm s^{-1}, Table 3.4: **IVc**) immediately upon exposure to air. The small τ value was persistent in air and a long lifetime could only be recovered by re-generating the Si(111) surface in a $NH_4F_{(aq)}$ solution (τ = 1093 μs, *SRV* < 9 cm s^{-1}, Table 3.4: **IVd**; τ = 988 μs, *SRV* < 10 cm s^{-1}, Table 3.4: **IVh**), in a $BHF_{(aq)}$ solution (τ = 939 ± 64 μs, *SRV* < 11.0 ± 0.8, Table 3.4**: Ve**), or in $HF_{(aq)}$ after a renewed piranha etch (τ = 945 μs, *SRV* < 11 cm s^{-1}, Table 3.4**: IVg**; τ = 746 ± 92 μs, *SRV* < 14.0 ± 1.6 cm s^{-1}, Table 3.4: **Vf**, averaged over 10 min). After the wafer was rinsed with water and the photoconductivity decay was measured in air, re-immersion into $HF_{(aq)}$ did not necessarily result in slow decays (τ = 33 μs, *SRV* = 304 cm s^{-1}, Table 3.4: **Vd**; τ=60 μs, *SRV* = 169 cm s^{-1}, Table 3.4: **Vg**; τ = 662 ± 28 μs, *SRV* < 15.0 ± 0.6 cm s^{-1} averaged over 10 min, Table 3.4: **VIb**). After the wafer was treated with $NH_4F_{(aq)}$ the lifetime in $HF_{(aq)}$ was very short (τ = 52 μs, *SRV* = 200 cm s^{-1}, Table 3.4: **IVe**). After the wafer was treated with $BHF_{(aq)}$ the lifetime in $HF_{(aq)}$ was appreciably high (τ = 421 ± 16 μs, *SRV* = 24.0 ± 0.9 cm s^{-1} averaged over 7 min, Table 3.4: **VIe**). The longest lifetimes observed in this series were 1136 ± 50 μs (*SRV* < 9 ± 0.4 cm s^{-1} averaged over 10 min, Table 3.4: **VIc**) for samples treated with $NH_4F_{(aq)}$ and 1257 ± 138 μs (*SRV* < 8 ± 0.9 cm s^{-1} averaged over 10 min, Table 3.4: **VId**) for samples contacted with $BHF_{(aq)}$. Repeated and prolonged treatment of a given sample with various aqueous fluoride solutions did yield slightly lower lifetimes and an equilibration period on the order of 10 min was necessary to achieve long lifetimes, see **VIf** and **VIg** in Figure 3.6 (b) and in Table 3.4, respectively. The lifetime of samples in 18 M $H_2SO_{4(aq)}$ were 188 ± 20 μs (*SRV* = 128 ± 14 cm s^{-1}, Table 3.4: **VII**). It should be noted that prolonged exposure of the wafer to 18 M $H_2SO_{4(aq)}$ increased the lifetime to 780 μs (after 30 min)

3.4.3 Measurement of the Built-In Voltage of n-Si(111)/H_2O Contacts Using Differential Capacitance Measurements

To correlate the degree of band bending of n-Si(111) with the results of surface recombination velocity measurements, differential capacitance measurements of a series of n-Si(111)/H_2O contacts were carried out. The results of these measurements are summarized in Table 3.5. In addition to measurements of the flat-band potential, E_{fb}, measurements of the open circuit potential, OCP, were taken before and after the differential capacitance measurements for 10 min and were averaged for the last 5 min of the measurement, see Table 3.5. Values for the E_{fb} and OCP generally showed poor reproducibility even for electrodes taken from the same wafer or for electrodes which were re-etched.

The E_{fb} values for the H-terminated n-Si/$H_2SO_{4(aq)}$ contact ranged from -0.453 to -0.539 V *vs.* SCE (Table 3.5: **I – III**) and there was no apparent difference in E_{fb} between solutions saturated with $H_{2(g)}$ (**I**) or solution degassed with Ar (Table 3.5: **II, III**). The OCP changed dramatically over the course of differential capacitance measurements, but OCP values were always more positive than the E_{fb}, indicating that the surface was

Figure 3.6 Measured Lifetimes of H-terminated Si(111) Following Various Surface Treatments.

(a) A 10 min “Piranha-etch” preceded the immersion of Si(111) in various aqueous fluoride solutions (Table 3.4**: IVa-IVg**). (b) A conventional solvent rinse (water-methanol-acetone-methanol-water) preceded the immersion of Si(111) in various aqueous fluoride solutions. Photoconductivity decays were recorded right after contact between Si(111) and the etchant was established and was then re-measured after 5 min and 10 min, respectively. (time-averaged values, Table 3.4: **VIa-VIg**)

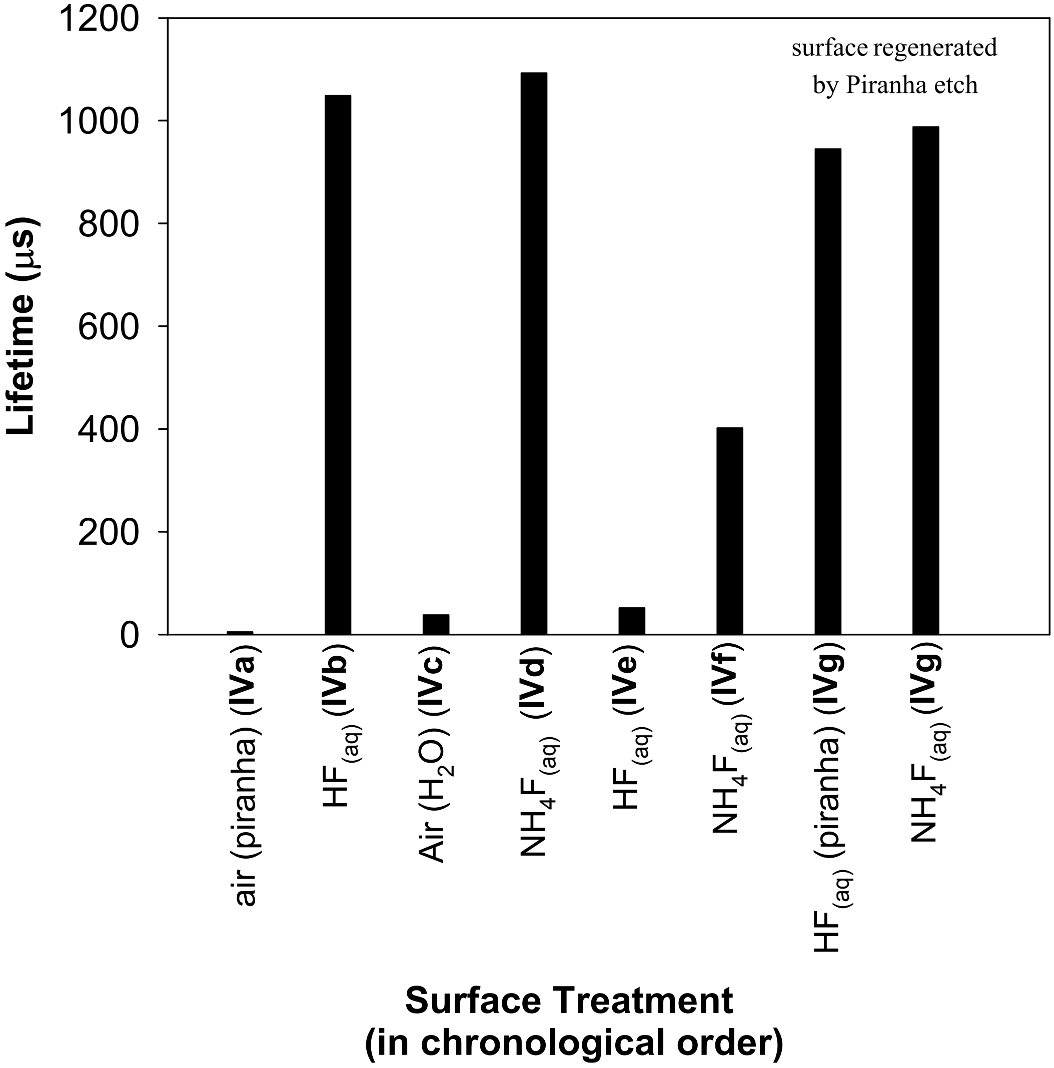
1200
1000
800
600
400
200
0
Lifetime (μs)
surface regenerated by Piranha etch
air (piranha) (IVa)
HF(aq) (IVb)
Air (H2O) (IVc)
NH4F(aq) (IVd)
HF(aq) (IVe)
NH4F(aq) (IVf)
HF(aq) (piranha) (IVg)
NH4F(aq) (IVg)
Surface Treatment
(in chronological order)

Figure 3.6 (a)

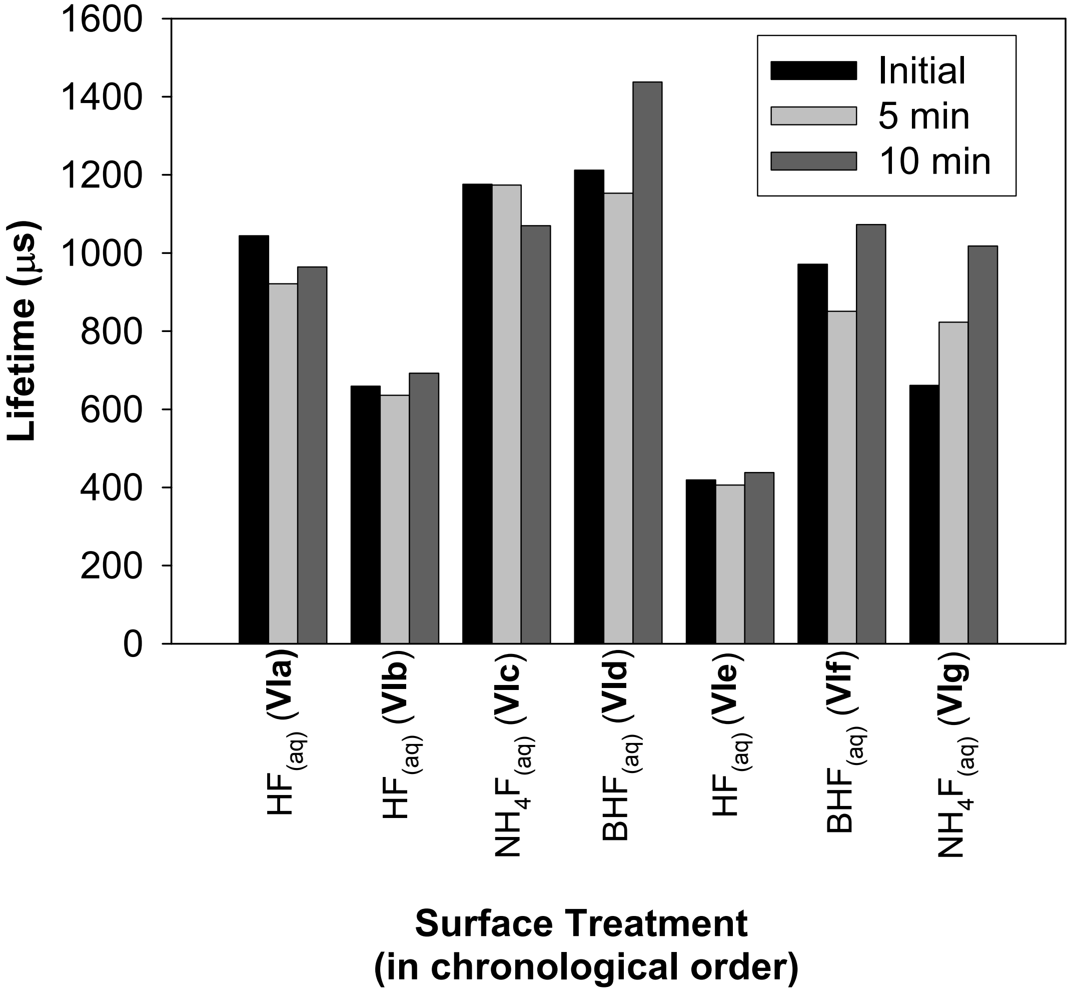
1600
1400
1200
1000
800
600
400
200
0
Lifetime (μs)
Initial
5 min
10 min
HF(aq) (VIa)
HF(aq) (VIb)
NH4F(aq) (VIc)
BHF(aq) (VId)
HF(aq) (VIe)
BHF(aq) (VIf)
NH4F(aq) (VIg)
Surface Treatment
(in chronological order)

Figure 3.6 (b)

TABLE 3.4. Measured lifetimes and surface recombination velocities for $NH_4F_{(aq)}$-etched n-Si(111) following various surface treatments in aqueous solutions.

	Surface Treatment	**High Injection**	
		τ (μs)	***SRV* (cm s^{-1})**
IVa	10 min Piranha etch, H_2O rinse, measured in air	5	2088
IVb	%, in $HF_{(aq)}$	1049	< 9.0
IVc	%, H_2O rinse, measured in air	38	270
IVd	%, in $NH_4F_{(aq)}$	1093	< 9
IVe	%, in $HF_{(aq)}$, after H_2O rinse	52	200
IVf	%, in $NH_4F_{(aq)}$	402	36
IVg	Piranha etch, H_2O rinse, measured in $HF_{(aq)}$	945	< 11
IVh	%, $NH_4F_{(aq)}$	988	< 10
Va	10 min Piranha etch, H_2O rinse, measured in air	2	4499
Vb	%, in $HF_{(aq)}$	487	21
Vc	%, H_2O rinse, measured in air	24	420
Vd	%, in $HF_{(aq)}$	33	304
Ve	%, in $BHF_{(aq)}$, after H_2O rinse (avg. 10 min)	939±64	< 11.0±0.8
Vf	%, in $HF_{(aq)}$ after Piranha etch (avg. 10 min)	746±92	< 14.0±1.6
Vg	%, in $HF_{(aq)}$ after H_2O rinse	60	169
Vh	%, in $BHF_{(aq)}$ after H_2O rinse	800	< 13
Vi	%, in $BHF_{(aq)}$ after Piranha etch (avg. 10 min)	1103±61	< 9±0.5
VIa	in $HF_{(aq)}$, after solvent rinse (avg. 10 min)	974±51	< 10.0±0.5
VIb	%, re-immersed into $HF_{(aq)}$ after water rinse (avg. 10 min)	662±28	15.0±0.6
VIc	%, in $NH_4F_{(aq)}$ (avg. 10 min)	1136±50	< 9±0.4
VId	%, in $BHF_{(aq)}$ (avg. 10 min)	1257±138	< 8±0.9
VIe	%, in $HF_{(aq)}$ (avg. 7 min)	421±16	24±0.9
VIf	%, in $BHF_{(aq)}$ (avg. 10 min)	952±100	< 11±1.2
VIg	%, in $NH_4F_{(aq)}$ (avg. 10 min)	839±117	< 12±1.7
VII	etched in $NH_4F_{(aq)}$, measured in 18 M $H_2SO_{4(aq)}$	188±20	128±14

TABLE 3.5. Flat-band potential and open circuit potential of various H-terminated n-Si(111)/H_2O contacts.

	Conditions	E_{fb} (V) *vs.* SCE	OCP (V) *vs.* SCE
I	1M $H_2SO_{4(aq)}$, 1 atm $H_{2(g)}$	-0.539	-0.419
II	1 M $H_2SO_{4(aq)}$, $Ar_{(g)}{}^a$	-0.520	-0.469; -0.14
III	1 M $H_2SO_{4(aq)}$, $Ar_{(g)}{}^b$	-0.453	-0.25; -0.40
IV	1M $HF_{(aq)}$, KCl (I=1), Ar $_{(g)}$	-0.297	-0.45; -0.4
V	1 M $HF_{(aq)}$, KCl (I=1), Ar $_{(g)}$	-0.292	-0.579; -0.48
VI	1 M $NH_4F_{(aq)}$, 1 atm $H_{2(g)}$	-0.460	-0.37; -0.32
VII	1 M $NH_4F_{(aq)}$, $Ar_{(g)}$	-0.567	-0.85;-0.60
VIII	1 M $NH_4F_{(aq)}$, $Ar_{(g)}{}^c$	-0.646	-0.85
IX	1 M $NH_4F_{(aq)}$, $Ar_{(g)}{}^d$	-0.504	-0.85

a electrode **I** re-measured

b potential scanned from forward bias to reverse bias, then scan direction was reversed; no changes in E_{fb}

c potential scanned from forward bias to reverse bias

d potential is scanned from reverse to forward bias using electrode **VII** depleted. There is no scan-direction dependence of the E_{fb} when the DC bias was cycled (Table 3.5: **III**) .

For the H-terminated n-Si/HF$_{(aq)}$ contact, the values for the E_{fb} were more reproducible (within 5 mV, Table 3.5: **IV, V**). The OCP was always more negative than the E_{fb} indicating that the contact was accumulated.

Comparison of the E_{fb} measured for n-Si(111)/NH$_4$F$_{(aq)}$ contacts (values ranged from -0.504 to -0.567 V *vs.* SCE, Table 3.5: **VII, IX**) with the OCP (values ranged from -0.85 to -0.60 *vs.* SCE, Table 3.5: **VII, IX)**, revealed that the surface was under accumulation, but due to the irreproducibility of both the OCP and the E_{fb}, it cannot be determined with certainty which contact, n-Si/HF$_{(aq)}$ or n-Si/NH$_4$F$_{(aq)}$ was more accumulated. Accumulation was very weak when the solution was saturated with $H_{2(g)}$, see **VI** in Table 3.5. The E_{fb} for n-Si/NH$_4$F$_{(aq)}$ was highly scan-direction dependent with a difference in the E_{fb} between upward and downward scan of approximately 140 mV (Table 3.5: **VIII, IX**).

The pH variation of E_{fb} has been reported for n-Si in contact with aqueous fluoride solutions.[28] The investigated n-Si(111)/HF$_{(aq)}$ and n-Si(111)/NH$_4$F$_{(aq)}$ contacts followed the reported trend, i.e., there is approximately a -45 mV/pH unit shift. Interestingly, the $H_2SO_{4(aq)}$ contact did not follow this trend at all, its E_{fb} was comparable to the E_{fb} of the NH$_4$F$_{(aq)}$ contact. In aqueous fluoride solutions the shift of the E_{fb} with pH seems to suggest that the surface was at least partially covered with OH-groups, which seems to contradict the consensus that Si(111) in contact with aqueous fluoride solutions remains H-terminated at all pH values during anodic oxidation as long as the potential is below the electropolishing potential.[26, 28, 67]

In work relevant to this study, Searson *et al.*[31, 32, 63] studied the surface-state density of n-Si(111) in aqueous fluoride solutions by measuring the surface state capacitance of these contacts under forward bias conditions and using a linear relationship between the surface state capacitance and the surface-state density.[31, 32] In this approach, the potential was always scanned from reverse to forward bias and the total parallel capacitance was determined and corrected for the space-charge capacitance.[31, 32, 63] Figure 3.7 (a) and Figure 3.7 (b) were constructed using Searson's method by plotting the total parallel capacitance *vs.* applied potential for n-Si(111)/$H_2SO_{4(aq)}$ and n-Si(111)/ $NH_4F_{(aq)}$ contacts, respectively. Contrary to Searson's approach, however, the potential in this study was first cycled from forward to reverse bias and then the scanning direction was reversed again. The parallel capacitance was a strong function of the scan direction and the effect was most pronounced for the basic fluoride $NH_4F_{(aq)}$ solutions, a trend which was similar to the scan direction dependence of the E_{fb} reported above.

In this context, the anodic limiting current densities in the dark, $j_{a,lim}$, were studied. These current densities were too large to originate from holes and therefore must stem from electrons being injected from the surface into the conduction band. In accordance with reports from the literature, there was a marked increase of $j_{a,lim}$ with increasing pH. The anodic limiting currents were found to be lowest for H-terminated n-Si(111) in contact with $H_2SO_{4(aq)}$, $j_{a,lim} \approx 10^{-7}$ A cm^{-2}, followed by $HF_{(aq)}$ contacts, $j_{a,lim} \approx 5\times10^{-6}$ A cm^{-2}, and $NH_4F_{(aq)}$, $j_{a,lim} \approx 1\times10^{-5}$ A cm^{-2} and are in accordance with reports in the literature.[28]

Given the complexity of anodic oxidation of Si surfaces in aqueous solutions and its apparent influence on the E_{fb} and the OCP, as evident by the scan-direction dependence of the E_{fb}, the OCP and the surface-state density, it is difficult to correlate the degree of band bending of H-terminated n-Si(111) obtained through these methods with the results from surface recombination velocity measurements. A method which allows the evaluation of band bending at the rest potential is therefore needed. Near-surface channel conductance measurements offer a way of qualitatively, and in some cases even quantitatively, evaluating the degree of band bending without biasing and thereby anodically oxidizing the electrode surface.

Figure 3.7 Parallel Capacitance *vs.* Applied Potential under Forward Bias for H-Terminated n-Si(111)/H_2O Contacts.

The potential was scanned from forward bias to reverse bias and then the scanning direction was reversed. C_p was a function of frequency. The symbol denote the different frequencies used. Circle: 100 kHz, down triangle: 7940 Hz, square: 501 Hz, diamond: 31.6 Hz. (a) n-Si(111) in contact with 1 M $H_2SO_{4(aq)}$. The flat-band potential, E_{fb}, was -0.453 V *vs.* SCE for both scanning directions. (b) n-Si(111) in contact with 1 M NH_4F. The E_{fb} was -0.646 V *vs.* SCE (scanned from forward to reverse bias) and -0.504 V *vs.* SCE (reverse scanning directions).

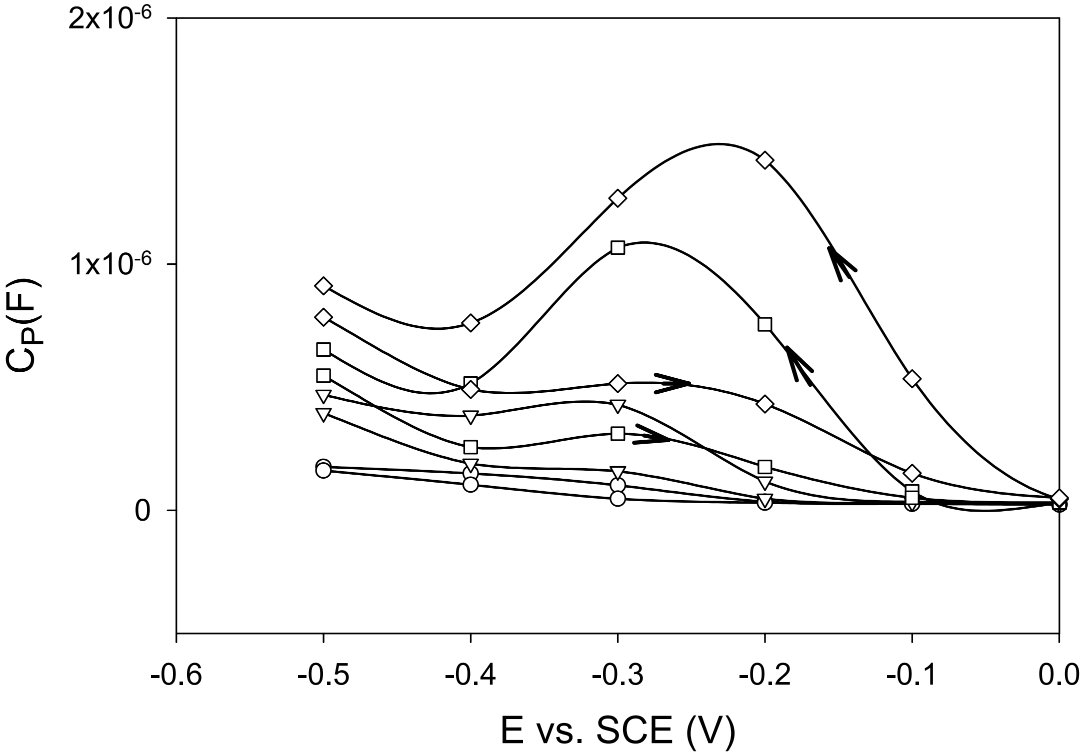

Figure 3.7 (a)

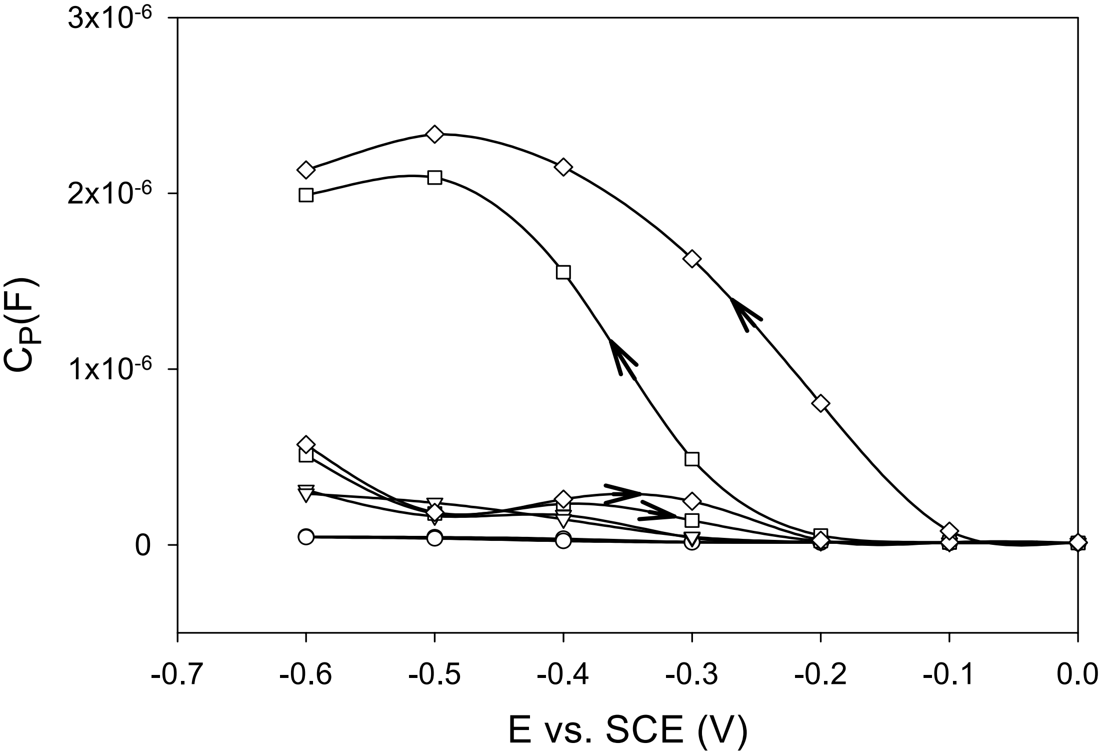

Figure 3.7 (b)

3.4.4 Near-Surface Channel Conductance Measurements

3.4.4.1 Characteristics of n^+- p-Si(111)-n^+ Devices in CH_3CN Solutions Containing $Me_{10}Fc^+$ or $CoCp_2^{+/0}$

The results of the near-surface channel conductance measurements are summarized in Table 3.6 and are depicted in form of Bode plots in Figure 3.12. The Nyquist plot of a n^+- p-Si(111)-n^+ device with a 1-micron-thick silicon dioxide capping layer is shown in Figure 3.9. The impedance spectra consisted of a single half circle. The low-frequency intercept of the half circle was 5.13×10^6 Ω and the CPE had a pre-exponential factor of 2.66×10^{-9} F (Table 3.7: **I**). After etching in various fluoride solutions and transfer to a $N_{2(g)}$ drybox the low-frequency intercept became 2.9×10^4 and the pre-factor of the CPE remained more or less unchanged (Table 3.6: **I**). Contact with the electrolyte was marked by a strong decrease in value of the low-frequency intercept, which became 3231 Ω and 4366 Ω in contact with CH_3CN and CH_3CN + 0.8 M $LiClO_4$, see **III** and **IV** in Table 3.6, respectively. The capacitance of the CPE changed by 2 orders of magnitude to 6.11×10^{-7} F. The suppression of the half circles did not increase significantly. This increase in capacitance is easily explained by the contribution of the double-layer capacitance, C_{dl}, to the impedance at higher frequencies. When the device is outside the electrolyte, C_{dl} does not contribute to the impedance , see Figure 3.8. Compared to the oxide-capped device and the CH_3CN contacts, the $CoCp_2^{+/0}$ contact displayed a significantly lower impedance pathway between the two n^+ contacts. The impedance spectra consisted of two distinct half circles and the spectra were analogous to an inverted p^+- n-Si(111) -p^+/$Me_2Fc^{+/0}$ contact. The half circles in Figure 3.10 were suppressed, and were fit to a 3-element equivalent circuit using a CPE instead of the capacitor. The channel resistance for $CoCp_2^{+/0}$ is 377 Ω (Table 3.6: **VII**) and the observed phase angle approached 0° as the frequency $\omega \rightarrow 0$, which shows that the charge flow takes place in the near-surface channel. If the low impedance pathway were due to faradaic charge flow, the impedance spectra at low frequencies would be dominated by a Warburg impedance and the phase angle would approach 45° at low frequencies.[16] Using Eq. 3.8-Eq. 3.11 the built-in voltage and the barrier height can be calculated. The built-in voltage equaled 0.86 V *vs.* cell potential and the barrier height equaled 1.08 eV. The potential necessary to reach inversion was 0.61 V *vs.* cell potential. The calculated value for the barrier height was larger than the experimentally derived value, which therefore places an upper bound for values of the built-in voltage that can be determined by this method. The poorly rectifying *j-E* characteristics of n-Si/CH_3OH-$Me_{10}Fc^{+/0}$ suggest that p-Si is weakly depleted with respect to holes as well.[68] According to cyclic voltammetry, the formal reduction potential of $Me_{10}Fc^{+/0}$ was 0.91 V more positive than $CoCp_2^{+/0}$. Thus, for a n^+-p-Si(111)- n^+ device in contact with $Me_{10}Fc^{+/0}$ we expect a significantly decreased channel conductance with the low impedance pathway being dominated by a Warburg impedance. Figure 3.11 depicts a typical Nyquist plot for a contact with $Me_{10}Fc^{+/0}$. The parameters of the equivalent circuit for **V** are listed in Table 3.6. The overall impedance was much larger than the impedance for the $CoCp_2^{+/0}$ contact and the impedance spectrum shows at frequencies smaller than approximately 10 Hz a second distinct relaxation process, which appears to be dominated by a Warburg impedance element. The observed change in the near-surface channel conductance was fully reversible and not due to a chemical modification of the surface, as evident from impedance measurements taken right after the device was rinsed with CH_3CN, evacuated and measured in $N_{2(g)}$ (Table 3.6: **VI**). Comparison with this Si/liquid contact therefore not only ensures that the low-impedance pathway observed for $CoCp_2^{+/0}$ arose from a near-surface inversion layer with respect to the majority charge carriers of p-Si, but also demonstrates that the fabricated n^+-p-Si(111)- n^+ devices can be used to correctly probe the inversion of holes in the space-charge layer of p-Si(111) .

3.4.4.2 Characteristics of n^+-p-Si(111)-n^+ Devices in Aqueous Acids or Aqueous Fluoride

Figure 3.8 Equivalent Circuits for the Transconductance Arrangement containing 3 Impedance Pathways.

1: Impedance through the bulk of the semiconductor, which is represented as a resistance R_b in parallel with a capacitance C_b. **2**: Impedance through the near-surface region, which is represented as a near-surface channel resistance R_sc in parallel with a near-surface capacitance C_sc. **3**: Impedance through the electrolyte solution, which is represented as a solution resistance R_Ω in series with a parallel combination of a double layer capacitance C_dl and an impedance, which consists of a charge-transfer resistance R_ct in series with a Warburg impedance W. For a contact under inversion the total impedance is dominated at low frequencies by R_sc and at high frequencies by a capacitance determined by the relative magnitudes of C_dl and C_sc. The phase angle at low frequencies is approaching zero. For a non-inverted contact with the possibility of charge transfer a Warburg element is predicted to dominate the impedance at low frequencies. The phase angle of the impedance is supposed to approach 45^o.

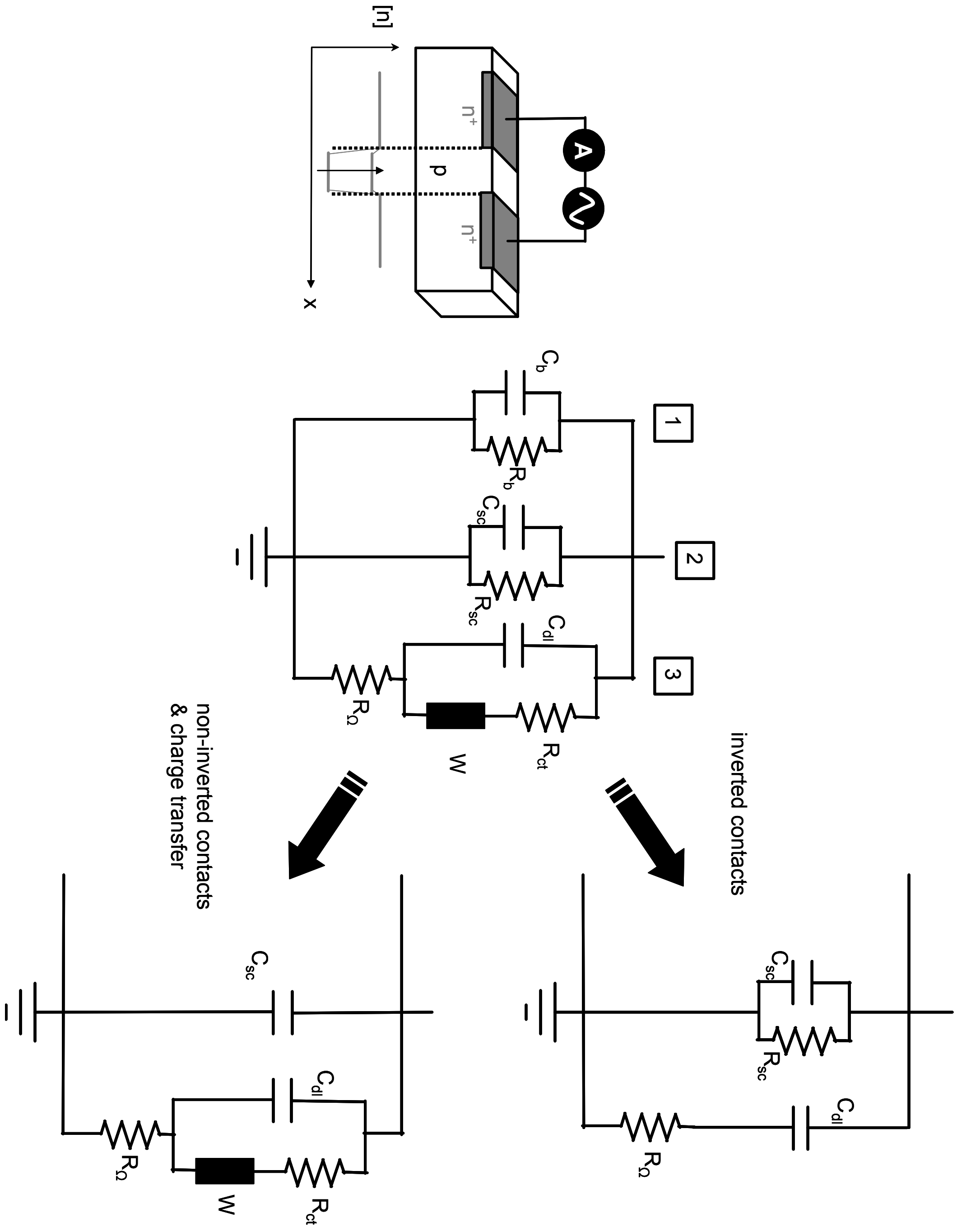
[n]
x
n+
p
n+
A
C_b
R_b
1
C_{sc}
R_{sc}
2
C_{dl}
R_{ct}
R_Ω
W
3
non-inverted contacts
& charge transfer
inverted contacts
C_{sc}
C_{dl}
R_Ω
W
R_{ct}
C_{sc}
R_{sc}
C_{dl}
R_Ω

Figure 3.8

Figure 3.9 Impedance Spectrum of a n^+-p-Si(111)-n^+ Device with a 1-Micron-Thick Capping Layer of SiO_2 in Air.

The amplitude of the sinusoidal AC-signal was 10 mV and the frequencies ranged from 1 to 1×10^5 Hz. No DC-bias was applied. The imaginary part of the impedance, *Z*", was plotted *vs.* the real part of the impedance. The impedance spectra consisted of 1 single relaxation processes. The center of the half circle was not suppressed. The low-frequency intercept of the half circle with the real axis was 5.13×10^6 Ω. The CPE element had a pre-exponential factor of 2.66×10^{-9} F and the exponential factor was 1.00, see **I** in Table 3.7.

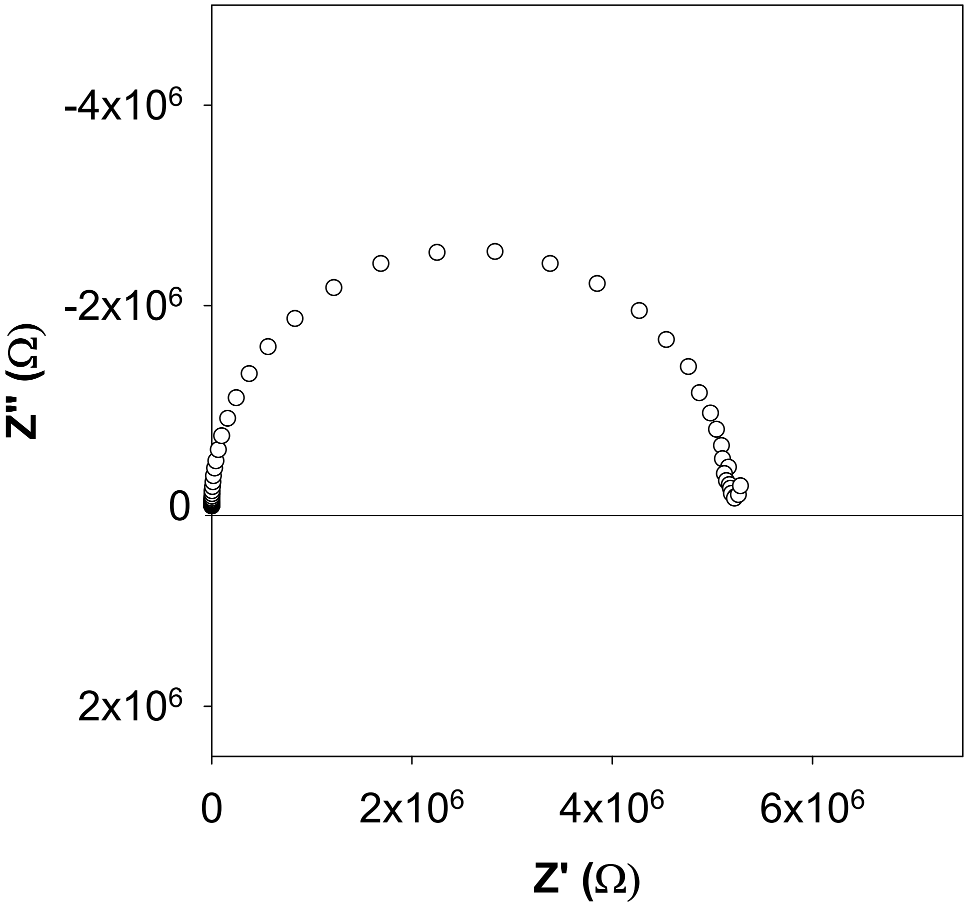

Figure 3.9

Figure 3.10 Representative Impedance Data for a n$^+$- p-Si(111)-n$^+$ Device in Contact with 5 mM CoCp$_2^{+/0}$.

The amplitude of the sinusoidal AC-signal was 10 mV and the frequencies ranged from 1 to 1×10^5 Hz. No DC-bias was applied. The imaginary part of the impedance, Z", was plotted *vs.* the real part of the impedance. The impedance spectra consisted of 2 relaxation processes, half circle and tail. The center of the half circle was suppressed. The low-frequency intercept of the half circle with the real axis was 377 Ω. The CPE element had a pre-exponential factor of 1.2×10^{-6} F and the exponential factor was 0.86 (Table 3.6: **VII**).

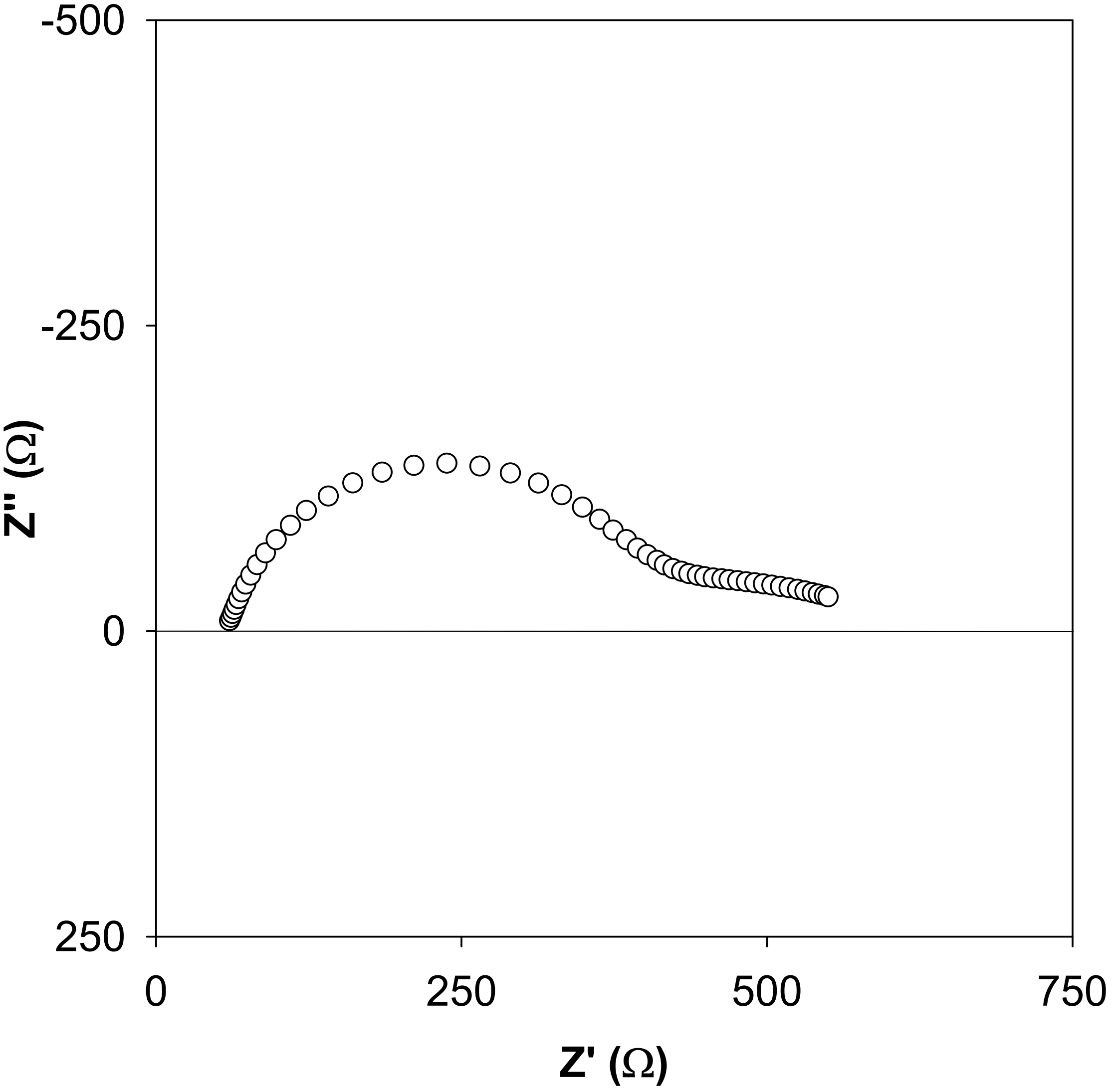

Figure 3.10

Figure 3.11 Representative Impedance Data for a n^+-p-Si(111)-n^+ Device in Contact with 5 mM $Me_{10}Fc^{+/0}$.

The amplitude of the sinusoidal AC-signal was 10 mV and the frequencies ranged from 1 to 1×10^5 Hz. No DC-bias was applied. The imaginary part of the impedance, Z”, was plotted *vs.* the real part of the impedance, Z’. The impedance spectrum consisted of 2 distinct relaxation processes. The first relaxation process consisted of a parallel combination of a resistance with a CPE, the second process was best described by a Warburg impedance. The low-frequency intercept of the half circle with the real axis was 2423 Ω. The CPE element had a pre-exponential of 2.55×10^{-7} F and the exponential factor was 1.0. The Warburg element had a resistance factor of 1.16×10^5 Ω, an effective diffusion time of 36.47 sec and an exponential factor of 0.45, see **V** in Table 3.6.

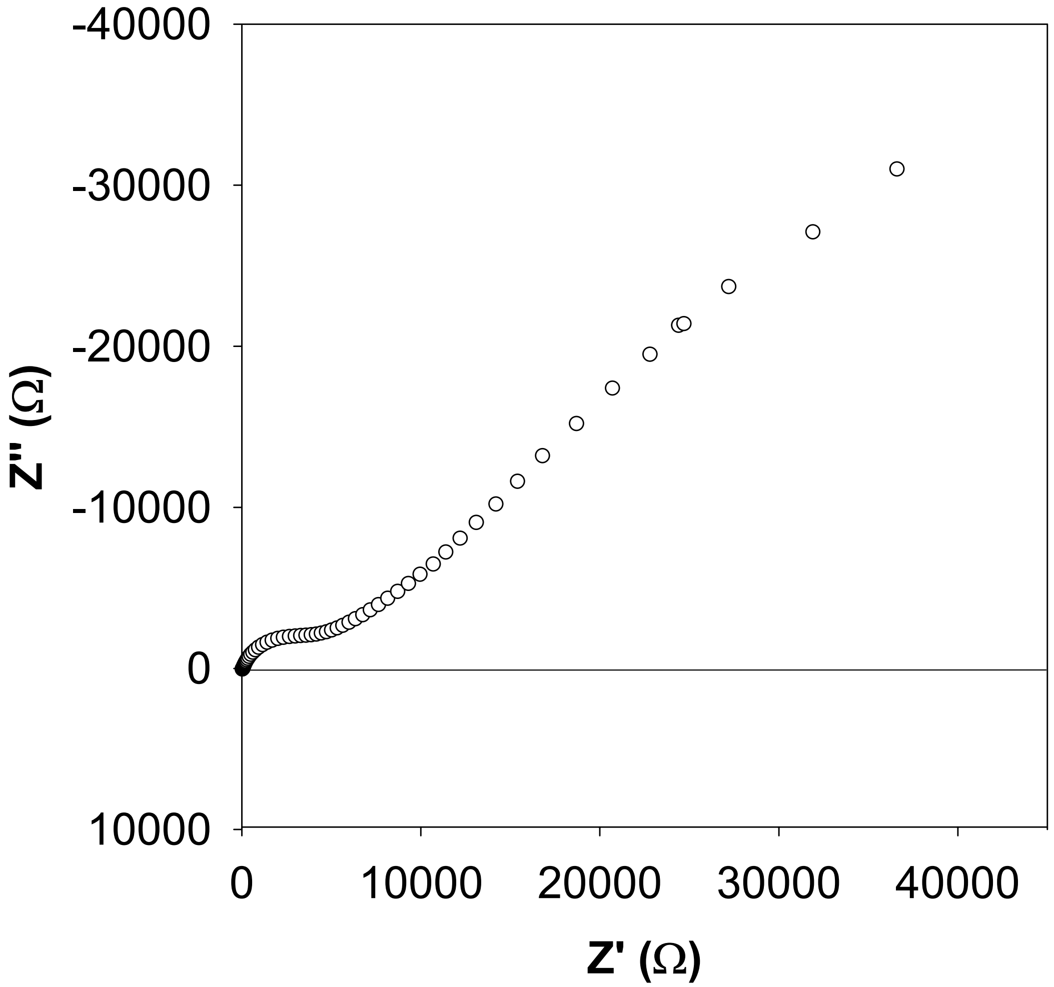
-40000
-30000
-20000
-10000
0
10000
Z'' (Ω)
0
10000
20000
30000
40000
Z' (Ω)

Figure 3.11

Figure 3.12 Representative Impedance Spectra for a n^+-p-Si(111)-n^+ Device in Contact with Various CH_3CN Solutions.

The amplitude of the sinusoidal AC-signal was 10 mV and the frequencies ranged from 1 to 1×10^5 Hz. No DC-bias was applied. The absolute value of the impedance |Z| and the phase angle are plotted *vs.* frequency. Circles correspond to measurements in a CH_3CN solution containing 0.8 M $LiClO_4$ (Table 3.6: **IV**); squares correspond to measurements in CH_3CN, 0.8 M $LiClO_4$, 5 mM $Me_{10}Fc^{+/0}$ (Table 3.6: **V**); “triangles up” corresponds to measurements in $N_{2(g)}$ after a CH_3CN rinse and evacuation in the ante chamber of the drybox (Table 3.6: **VI**); “triangles down” correspond to measurements in CH_3CN, 0.8 M $LiClO_4$, 5 mM $CoCp_2{}^{+/0}$ (Table 3.6: **VII**).

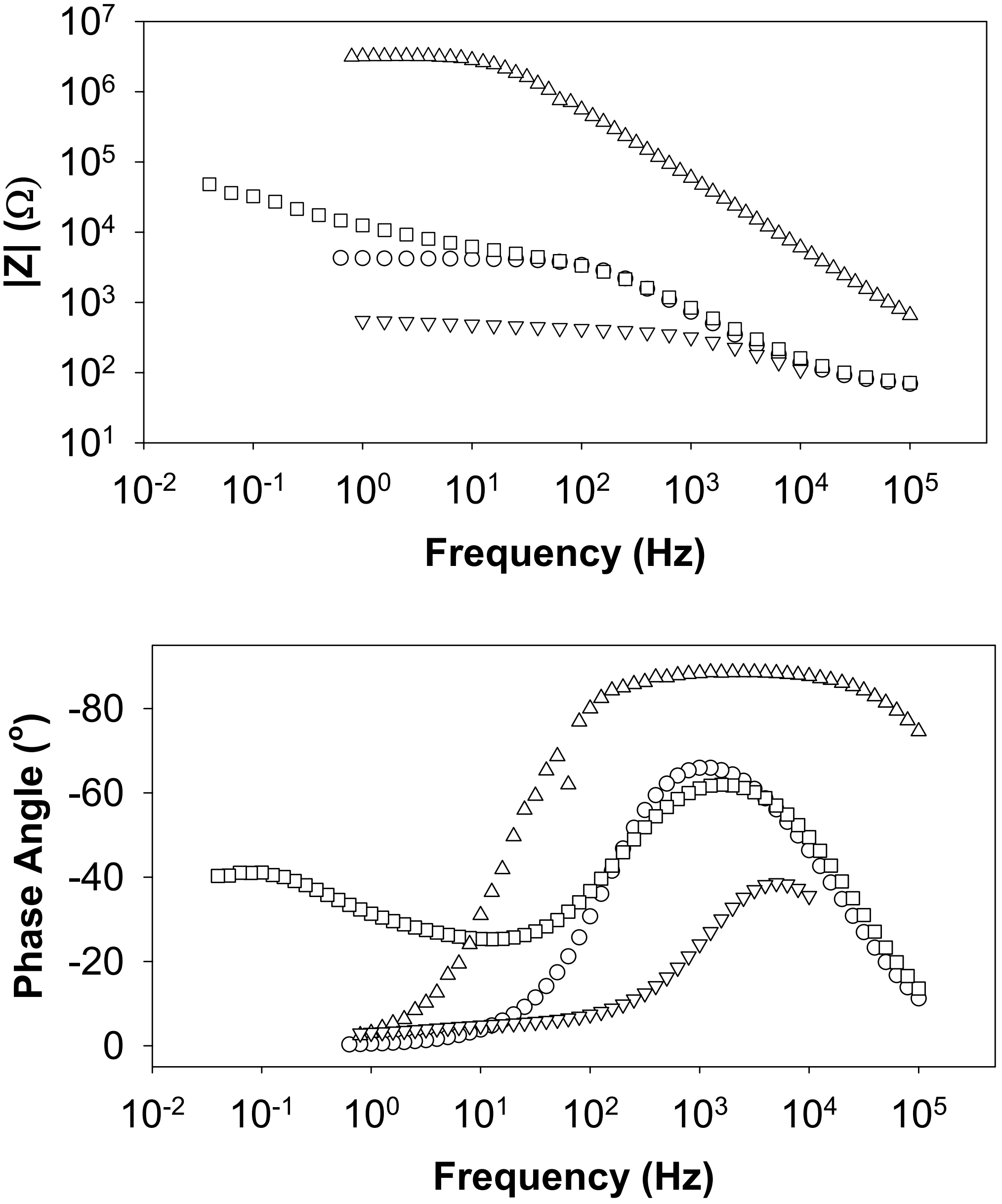
10^7
10^6
10^5
10^4
10^3
10^2
10^1
|Z| (Ω)
10^-2
10^-1
10^0
10^1
10^2
10^3
10^4
10^5
Frequency (Hz)
-80
-60
-40
-20
0
Phase Angle (°)
10^-2
10^-1
10^0
10^1
10^2
10^3
10^4
10^5
Frequency (Hz)

Figure 3.12

TABLE 3.6. Results of near-surface channel conductance measurements of a $NH_4F_{(aq)}$-etched n^+-p-Si(111)-n^+ device in contact with various CH_3CN solutions

	Surface Treatment	**$\lvert Z(\omega \to 0)\rvert$ (Ω)**	**C_{CPE} (F)**	**n_{CPE} (-)**
I	Drybox, in $N_{2(g)}$ *	2.9×10^{4}	3.71×10^{-9}	0.97
II	%, in $N_{2(g)}$ 5 min	7942	4.12×10^{-9}	0.97
III	%, in CH_3CN	3231	6.66×10^{-7}	0.87
IV	%, in CH_3CN + 0.8 M LiClO4	4366	6.11×10^{-7}	0.94
V	%, in CH_3CN + 0.8 M	2423	2.55×10^{-7}	1
	$LiClO_4$ 5 mM $Me_{10}Fc^{+/0}$	WR = 1.16×10^{5}	WT = 36.47 s	WP = 0.45
VI	CH_3CN rinse, evacuation, in $N_{2(g)}$	3.25×10^{6}	2.95×10^{-9}	0.99
VII	%, in CH_3CN + 0.8 M $LiClO_4$, 5 mM $CoCp_2^{+/0}$	377	1.20×10^{-6}	0.86

TABLE 3.7. Results of near-surface channel conductance measurements of a n^+-p-Si(111)-n^+ device in contact with various aqueous fluoride solutions and $H_2SO_{4(aq)}$

	Surface Treatment	**$\|Z(\omega \rightarrow 0)\|$ (Ω)**	**C_{CPE} (F)**	**n_{CPE} (-)**	**V_{bi} *vs.* Cell (V)**
I	Air, 1 μm SiO_2	5.13×10^6	2.66×10^{-9}	1	-
II	$BHF_{(aq)}$ for 10 min, $NH_4F_{(aq)}$ for 20 min, in $NH_4F_{(aq)}$	584	2.76×10^{-7}	0.94	0.84
III	%, in $BHF_{(aq)}$	871	3.88×10^{-7}	0.92	0.82
IV	%, in $NH_4F_{(aq)}$	685	2.94×10^{-7}	0.94	0.83
V	%, in HF(aq)	9.65×10^4	3.95×10^{-7}	0.94	0.65
VI	%, in $NH_4F_{(aq)}$	2841	4.66×10^{-7}	0.91	0.77
VII	%, in $NH_4F_{(aq)}$ after 15 min	2629	3.21×10^{-7}	0.94	0.77
VIII	%, in $BHF_{(aq)}$	3197	3.31×10^{-7}	0.94	0.77
IX	%, in $NH_4F_{(aq)}$	1763	3.53×10^{-7}	0.94	0.79
X	%, in $NH_4F_{(aq)}$ after 60 min	929	4.25×10^{-7}	0.92	0.82
XI*	$H_2SO_{4(aq)}$ after $NH_4F_{(aq)}$ etch	5.69×10^4	2.5×10^{-7}	0.85	0.67

* new transconductance device insulated with paraffin wax.

Solutions

The impedance spectroscopy measurements involving n^+-p-Si(111)-n^+ devices in contact with 18 M $H_2SO_{4(aq)}$ or various aqueous fluoride solutions are summarized in Table 3.7. Bode plots of representative impedance spectra are depicted in Figure 3.13. The effects of different surface treatments on the reproducibility of the low-frequency intercepts in the Nyquist plots are depicted in Figure 3.14. With the exception of $H_2SO_{4(aq)}$, all impedance spectra reported herein were taken for the same n^+-p-Si(111)-n^+ device used in the investigation of CH_3CN contacts containing $Me_{10}Fc^{+/0}$ or $CoCp_2^{+/0}$. After each measurement, a series of impedance spectra were taken in $NH_4F_{(aq)}$ to check for reproducibility. The Nyquist plots of all contacts (not shown) consisted of a single, slightly suppressed semicircle. The low-frequency intercepts of these control experiments varied significantly, as did impedance measurements for a given contact taken over time. The influence of these variations on the electrostatics of the contact, however, were not very pronounced and most of the resulting deviations in the built-in voltage were rather small, see Table 3.7.

The most striking feature of the studied Si/liquid contacts is that n^+- p-Si(111)-n^+ in contact with $NH_4F_{(aq)}$ and buffered $HF_{(aq)}$ had low-frequency intercepts of 584 Ω and 871 Ω, see **II** and **III** in Table 3.7, respectively. These values were significantly lower than the low-frequency intercepts obtained with 48 wt% $HF_{(aq)}$ and 18 M $H_2SO_{4(aq)}$, which were equal to 9.65×10^4 Ω (Table 3.7: **V**) and 5.69×10^4 Ω (Table 3.7: **XI**), respectively. The results for 18 M $H_2SO_{4(aq)}$ are not directly comparable to the other contacts since a different device with paraffin wax insulation and therefore with slightly different dimensions had to be used instead. The fact that p-Si(111) in contact with $H_2SO_{4(aq)}$ is less inverted than $NH_4F_{(aq)}$ or $BHF_{(aq)}$, however, is clearly demonstrated. As in the case of the CH_3CN contacts, all aqueous contacts had to be described by means of a CPE. The unitless exponent was on the order of 0.94, which indicates a very mild suppression of the half circle. As observed for the CH_3CN contacts, the pre-exponential factor changed from 2.66×10^{-9} F (air) to approximately 3×10^{-7} F when the device was contacted with the electrolyte and indicates that the high-frequency impedance is dominated by the double-layer capacitance, see Figure 3.8.

Figure 3.14 indicates that the low surface-channel conductances after immersion in $HF_{(aq)}$ could only be recovered after extensive etching in $NH_4F_{(aq)}$ for 60 min. The lowest surface-channel conductance for the device after $HF_{(aq)}$-etching in $NH_4F_{(aq)}$ was 929 Ω (Table 3.7: **X**). In control experiments using a p^+-n-Si(100)-p^+ device the resistances across the conductance channel were $(2.75 \pm 1.55)\times10^6$ Ω, $(3.14 \pm 1.43)\times10^6$ Ω, 2.00×10^6 Ω, and $(4.38\pm 2.18)\times10^6$ Ω for $NH_4F_{(aq)}$, $BHF_{(aq)}$, $HF_{(aq)}$, and $H_2SO_{4(aq)}$, respectively.

Control experiments were performed, where a near-surface channel transconductance device with a protective oxide capping layer was directly immersed into $HF_{(aq)}$ and the impedance was measured as the oxide layer was gradually removed by etching. The low-frequency intercept of the impedance upon contact of p-Si(111) with $HF_{(aq)}$ was 1.3×10^4 Ω and rose rapidly to 6.5×10^4 Ω. Immersed in $NH_4F_{(aq)}$, the low-frequency intercept of the impedance dropped immediately to 3.4×10^3 Ω and decreased gradually to 540 Ω.

The small amount of $H_{2(g)}$ that might form for $NH_4F_{(aq)}$ or $BHF_{(aq)}$ in the vicinity of the rest potential is not expected to make a significant contribution to any impedance related to faradaic charge flow in the spectra reported herein. Therefore, the low-frequency impedance pathway must be either through the inverted or depleted surface region or through the bulk. The open circuit potential of a p-Si(111) electrode *vs.* a standard calomel electrode were measured and the results are shown in Table 3.8. In accordance with reports from the literature, n-Si(111)/$NH_4F_{(aq)}$ contacts had the most negative open circuit potential of all contacts (-0.82 V *vs.* SCE, see **I** in Table 3.8), followed by $BHF_{(aq)}$ (-0.69 V *vs.* SCE, see **II** in Table 3.8) and followed by $HF_{(aq)}$ (-0.09 V *vs.* SCE, see **IV** in

Figure 3.13 Representative Impedance Spectra for a n^+-p-Si(111)-n^+ Device in Contact with Various Aqueous Fluoride Solutions and 18 M $H_2SO_{4(aq)}$.

The amplitude of the sinusoidal AC-signal was 10 mV and the frequencies ranged from 1 to 1×10^5 Hz. No DC-bias was applied. The absolute value of the impedance |Z| and the phase angle are plotted *vs.* frequency. Circles correspond to measurements of the device capped with an oxide layer in air (Table 3.7: **I**; $|Z(\omega\to0\,| = 5.13\times10^6\ \Omega$); "triangles down" correspond to measurements in $NH_4F_{(aq)}$ (Table 3.7**: II**; $|Z(\omega\to0\,| = 584\ \Omega$) ; "triangles up" corresponds to measurements in $BHF_{(aq)}$ (Table 3.7: **III**; $|Z(\omega\to0\,| = 871\ \Omega$); squares correspond to measurements in 48 wt% $HF_{(aq)}$ (Table 3.7: **V**; $|Z(\omega\to0\,| = 9.65\times10^4\ \Omega$)

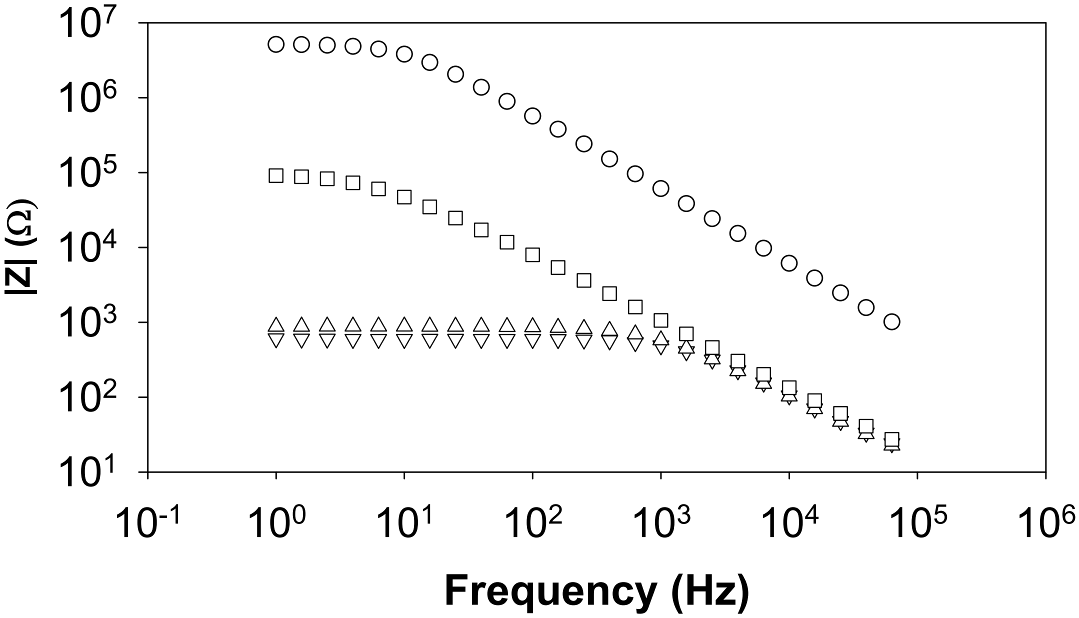

10^7
10^6
10^5
10^4
10^3
10^2
10^1
|Z| (Ω)
10^{-1}
10^0
10^1
10^2
10^3
10^4
10^5
10^6
Frequency (Hz)

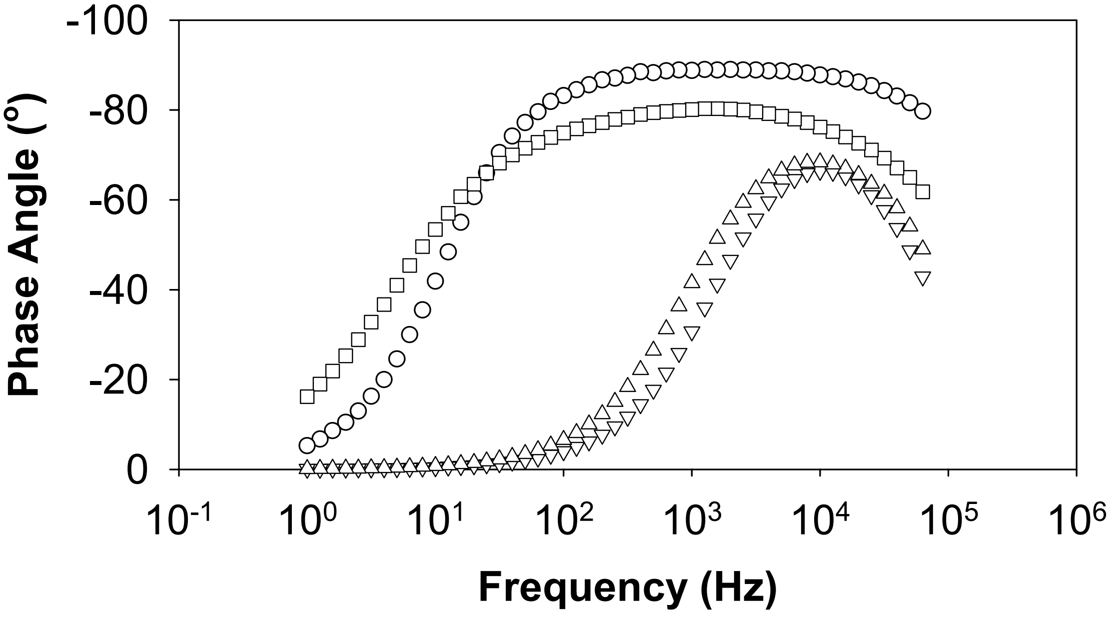

-100
-80
-60
-40
-20
0
Phase Angle (°)
10^{-1}
10^0
10^1
10^2
10^3
10^4
10^5
10^6
Frequency (Hz)

Figure 3.13

Figure 3.14 Low-Frequency Intercepts of the Impedance of H-terminated n^+ -p-Si(111)- n^+ Near-Surface Channel Conductance Devices Following Various Surface Treatments.

The low-frequency intercept of the device with an oxide capping layer in air is 5.13×10^6 Ω (see **I** in Table 3.7). A 10 min $BHF_{(aq)}$ etch followed by a 20 min $NH_4F_{(aq)}$ etch preceded the immersion of the n^+-p-Si(111)-n^+ device into various aqueous fluoride solutions (see **II**-**X** in Table 3.7).

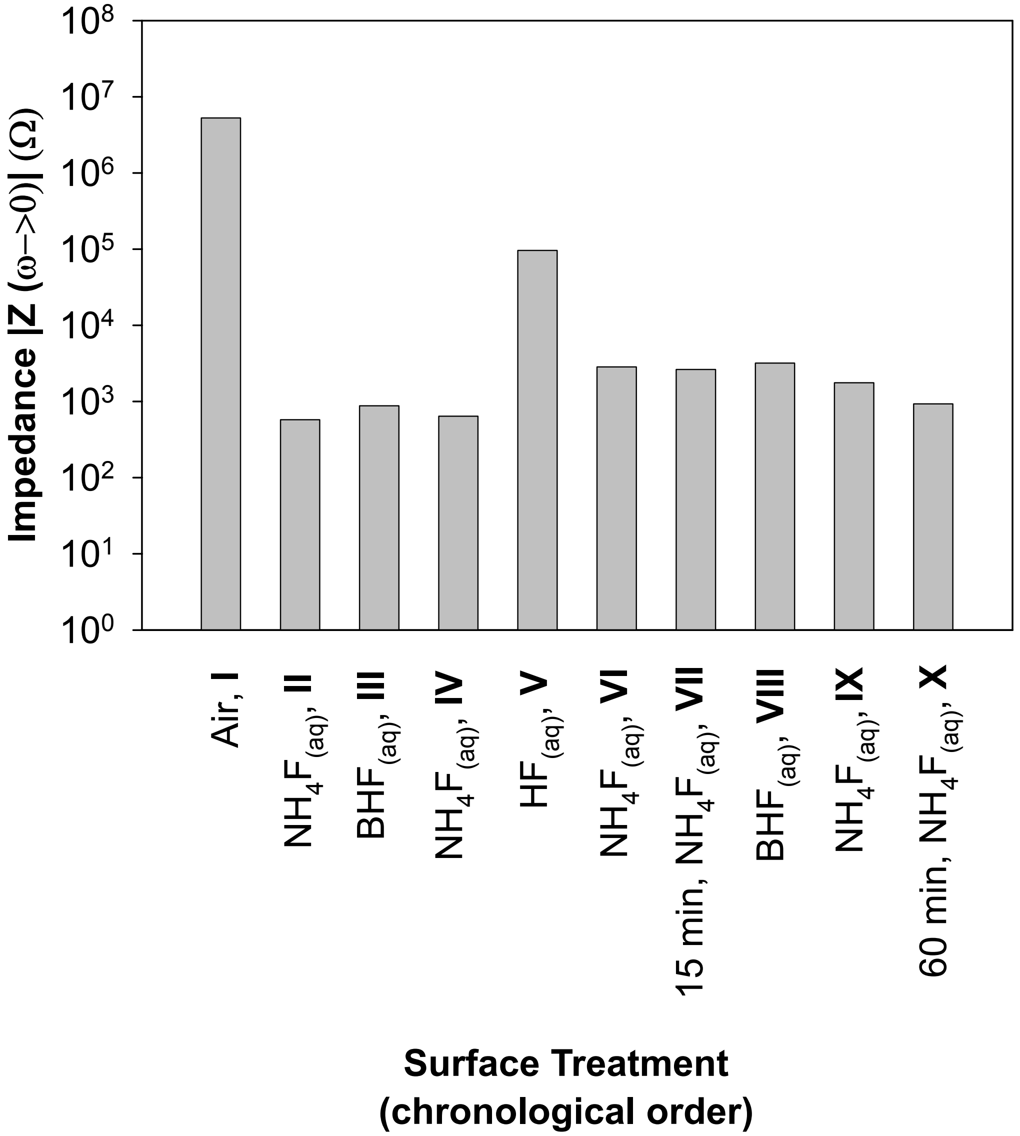
Impedance |Z (ω->0)| (Ω)
10^8
10^7
10^6
10^5
10^4
10^3
10^2
10^1
10^0
Air, **I**
$NH_4F_{(aq)}$, **II**
$BHF_{(aq)}$, **III**
$NH_4F_{(aq)}$, **IV**
$HF_{(aq)}$, **V**
$NH_4F_{(aq)}$, **VI**
15 min, $NH_4F_{(aq)}$, **VII**
$BHF_{(aq)}$, **VIII**
$NH_4F_{(aq)}$, **IX**
60 min, $NH_4F_{(aq)}$, **X**
Surface Treatment
(chronological order)

Figure 3.14

Table 3.8).[26, 27] After contact with $HF_{(aq)}$ the initially low near-surface conductance of $NH_4F_{(aq)}$ was recovered only after prolonged etching (Table 3.8: **V**). The built-in voltage, V_{bi}, for these contacts *vs.* open circuit potential and the total charge density removed from the semiconductor during inversion, Q_s, can be calculated using the relationships given by Eq. 3.8-Eq. 3.11. For $NH_4F_{(aq)}$ $V_{bi} = 0.84$ V *vs.* cell potential ($Q_s = 1.19\times10^{12}$ cm^{-2}, see **II** in Table 3.7) , for $BHF_{(aq)}$ $V_{bi} = 0.82$ V *vs.* cell potential ($Q_s = 5.05\times10^{11}$ cm^{-2}, see **III** in Table 3.7), for $HF_{(aq)}$ $V_{bi} = 0.65$ V *vs.* cell potential ($Q_s = 1.74\times10^{11}$ cm^{-2}, see **V** Table 3.7), and for 18 M $H_2SO_{4(aq)}$ $V_{bi} = 0.67$ V *vs.* cell potential ($Q_s = 1.80\times10^{11}$ cm^{-2}, see **XI** in Table 3.7). The built-in voltage required to reach inversion, V_i, equals 0.61 V, which corresponds to the removal of a charge density $Q_s = Q_b = 1.68\times10^{11}$ cm^{-2}, see Eq. 3.9. It is noted that Eq. 3.8-Eq. 3.11 are very simplified equations and that corrections might be necessary to account for the impedance caused by the n^+- p diode junctions. However, it can be inferred from these experimental results that p-Si(111) in contact with $NH_4F_{(aq)}$ is the most inverted contact, followed by $BHF_{(aq)}$ contacts. With respect to contacts formed with $HF_{(aq)}$ and $H_2SO_{4(aq)}$, inversion might be too weak to justify the use of Eq. 3.8-Eq. 3.11. However, control experiments using p^+-n-Si(100)-p^+ indicate that n-Si is definitely not in strong depletion, let alone inversion with respect to electrons.

With these results it can be argued that n-type Si(111) in contact with $NH_4F_{(aq)}$ is the most accumulated contact with respect to electrons, followed by buffered $HF_{(aq)}$, $HF_{(aq)}$, and $H_2SO_{4(aq)}$ contacts, respectively. The fact that n-Si(111) in contact with aqueous fluoride solutions is accumulated has been reported by Allongue *et al.*,[28] however, the differential capacitance measurements suggest that acidic contacts are more accumulated than basic contacts, which is in contradiction with the measurements presented in this study. Since the Si-electrodes in aqueous fluoride solutions are being etched, i.e., they are not at equilibrium, we refrain from converting the $V_{bi,p}$ of p-Si(111), into a value for the $V_{bi,n}$ for the n-Si(111) samples used in *SRV* measurements.

TABLE 3.8. Measurement of the open circuit potential (OCP) following various surface treatments of p-Si(111) in aqueous fluoride solutions.

	Surface Treatment	**OCP *vs.* SCE (under illumination)**	**OCP *vs.* SCE (in darkness)**
I	$NH_4F_{(aq)}$ for 20 min	-0.82	-1.08
II	%, $BHF_{(aq)}$ for 3 min	-0.69	-0.94
III	%, $NH_4F_{(aq)}$ for 3 min	-0.83	-1.07
IV	%, $HF_{(aq)}$ for 3 min	-0.09	-0.47
V	%, $NH_4F_{(aq)}$ for 7 min	-0.80	-1.03

3.5 DISCUSSION

3.5.1 The Influence of Interfacial Energetics on the Surface Recombination Velocity of Inverted n-Si(111) Contacts

The electrolytes that produced low effective Si surface recombination velocities all had either relatively positive, or very negative, redox potentials relative to the standard calomel electrode (SCE).[68] THF solutions of $Fc^{+/0}$ produce low effective *SRV* values for (111)-oriented crystalline Si surfaces regardless of the chemical state of the Si surface. Similar effects were observed for an electrolyte having a very negative redox potential, $CoCp_2^{+/0}$, in CH_3CN, see Chapter 3.5.3. In contrast, low *SRV* values was observed for Si surfaces in contact with $N_{2(g)}$ or in contact with THF-$Me_{10}Fc^{+/0}$ solutions, indicating that the surface recombination rates observed for such contacts are sensitive to the chemical state of the surface.

This behavior of each contact can be understood in the context of the Shockley-Read-Hall treatment for surface recombination, when the effect of band bending at the semiconductor/liquid contact is considered.[34-36, 69] According to the Shockley-Read-Hall treatment the recombination rate for a surface with traps at a single energy involves the carrier capture rate constants, $k_{\mathrm{n,s}}$ and $k_{\mathrm{p,s}}$, the electron and hole concentrations at the surface of the semiconductor in the dark, n_{so} and p_{so}, respectively, and the injected electron and hole concentrations, n_{s} and p_{s}, respectively (note: $n_{\mathrm{s}} = p_{\mathrm{s}}$):

$$U_{\mathrm{s}} = N_{\mathrm{T,s}} \frac{k_{\mathrm{n,s}} k_{\mathrm{p,s}} \Delta p (n_{\mathrm{so}} + p_{\mathrm{so}} + \Delta p)}{k_{\mathrm{p,s}} (n_{\mathrm{so}} + \Delta n_{\mathrm{s}} + n_{1,\mathrm{s}}) + k_{\mathrm{n,s}} (p_{\mathrm{so}} + \Delta p + p_{1,\mathrm{s}})} \qquad \text{(Eq. 3.12)}$$

In Eq. 3.12, $N_{\mathrm{T,s}}$ is the surface trap density and $n_{1,\mathrm{s}}$ and $p_{1,\mathrm{s}}$ are the electron and hole concentrations, respectively, when the Fermi level is located at the energy of the surface trap.[36, 49]

Figure 3.15 Surface Recombination Velocities and the Corresponding Surface State Trap Densities of Various Si Surfaces.

Si surfaces with a native oxide layer have a $N_{T,s}$ on the order of 10^{12} cm^{-2}. Si(111)-CH_3OH and Si(111)-THF under inversion or accumulation show an effective recombination velocity which corresponds to an apparent surface-state density of 10^{12} cm^{-2}. The best surface to date is Si(111) in contact with $HF_{(aq)}$ as measured by Yablonovitch *et al.* The surface-state density of this contact is as low as 10^7 cm^{-2}.[5, 6, 20]

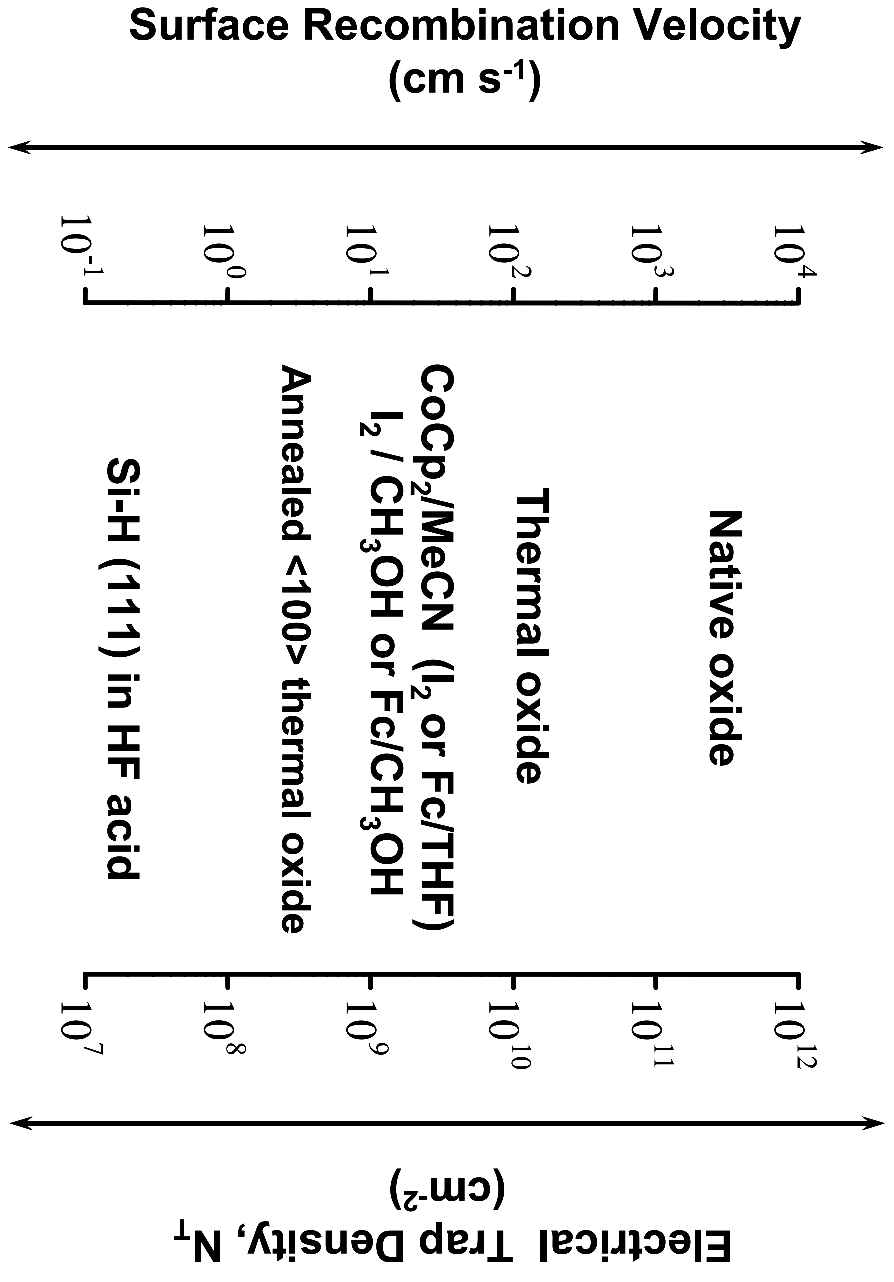
Surface Recombination Velocity
(cm s^{-1})
10^{-1}
10^{0}
10^{1}
10^{2}
10^{3}
10^{4}
Native oxide
Thermal oxide
CoCp$_2$/MeCN (I$_2$ or Fc/THF)
I$_2$ / CH$_3$OH or Fc/CH$_3$OH
Annealed <100> thermal oxide
Si-H (111) in HF acid
10^{7}
10^{8}
10^{9}
10^{10}
10^{11}
10^{12}
Electrical Trap Density, N$_T$
(cm^{-2})

Figure 3.15

The electron and hole concentrations in Eq. 3.12 refer to the values at the solid/ liquid interface and are strong functions of any electric potential drops in the semiconductor. Qualitatively, it is clear that redox couples that have very positive redox potentials are capable of extensive charge transfer from the Si into the electrolyte, allowing for the formation of an inversion layer (and an accumulation of holes) at the surface of n-type Si.[16, 17, 19, 70] Similarly, charge-transfer equilibration with redox couples that have very negative redox potentials will produce an accumulation of electrons at the Si surface. In either case, the lack of one carrier type or the other for participation in steady-state surface recombination (and hence the increased magnitude of the concentration of the other carrier type, either n_s or p_s, in the denominator of Eq. 3.12) will produce a low effective surface recombination velocity even for significant values of $N_{T,s}$. Silicon in contact with air, $N_{2(g)}$, or electrolytes having moderately negative redox potentials (< 0 V *vs.* SCE) such as THF $Me_{10}Fc^{+/0}$, surfaces with significant $N_{T,s}$ values exhibit a higher effective surface recombination velocity than they do under conditions that produce an inversion or accumulation layer at the Si surface. The effect should be rapid and reversible because only electron exchange is required to produce the electrochemically induced change in surface carrier concentration that affects the effective *SRV* value. Removal of the sample from the electrolyte will generally change the surface potential in a direction that reduces the band bending, so the observed value of *SRV* should increase and the variations in $N_{T,s}$ can be reflected in the measurements of *SRV* under these conditions. This expectation is in accord with the experimental observations that the surfaces investigated in this work all exhibited higher *SRV* values in contact with $N_{2(g)}$ than they did in contact with the oxidizing or strongly reducing electrolyte solutions.

Further evidence for charge-transfer control over the effective *SRV* value in these electrolytes can be obtained through reference to near-surface channel conductance measurements in p^{+}-n-p^{+} Si structures exposed to electrolytes containing $Me_2Fc^{+/0}$

(inversion) and $Me_{10}Fc^{+/0}$ (no inversion).[16] Additionally, Mott-Schottky measurements of the n-Si/CH_3OH $Me_2Fc^{+/0}$ contact have indicated an equilibrium barrier height of 1.03 V, [18, 19, 71] which is sufficient to drive the system into carrier inversion. Figure 3.15 shows how the inverted (and accumulated) contacts in this study compare with various Si surfaces in terms of their surface recombination velocity and apparent surface-state density.

3.5.2 Comparison between Digital Simulations and Experimental Observations of the Surface Recombination Velocity as a Function of the Redox Potential of the Electrolyte

The digital simulations confirm the presence of the charge-transfer induced effect on the effective surface recombination velocity and furthermore establish quantitative bounds on when the effect can dominate variations in the surface trap density. For barrier heights of 0.9-1.0 V, even $N_{T,s}$ values as high as 10^{12} cm^{-2} produce a low *SRV*. Thus, for such systems, the surface quality is secondary, and the charge-transfer effect dominates the observed *SRV* value. In contrast, for the Si/CH_3OH-$Me_{10}Fc^{+/0}$ systems or Si/THF-$Me_{10}Fc^{+/0}$, which are not under strong inversion, variation in both $N_{T,s}$ and the solution-based redox acceptor concentration can produce a significant variation in the effective *SRV* value of such contacts.

This effect implies that measurements of the surface recombination velocity can be used to monitor surface defect densities for semiconductor/liquid contacts having moderate band-bending values and small interfacial charge-transfer rates, but not for surfaces under significant inversion or accumulation conditions. This behavior is however beneficial for systems with large amounts of band bending since such surfaces are rather insensitive to surface contamination. Such surfaces will display good electrical properties even if the surface contains a significant density of electrically active defects. However, this type of behavior is only applicable to the solid/liquid contact (or to other contacts capable of sustaining the required charge-transfer equilibrium at the semiconductor surface). As shown herein, both experimentally and through digital simulation, transfer of such surfaces into inert ambients for use in electrical device applications will eliminate the surface charge carrier accumulation phenomenon and will result in high effective surface recombination velocities if the surface actually has a high electrical defect density.

The effect of injection level is also of interest. Generally high-level injection conditions are produced when the concentration of injected majority carriers exceeds the concentration of majority carriers produced by thermal excitation of dopant electrons in the bulk of the sample. High-level injection conditions are therefore often used to minimize any effects of band bending on the observed surface recombination velocities. However, for sufficiently large band-bending values, the minority carrier concentration at the surface of the semiconductor exceeds the majority carrier concentration in the bulk of the sample (or alternatively, in accumulation, the majority carrier concentration at the surface far exceeds the majority carrier concentration in the bulk). Such conditions require significantly higher light intensities than those calculated from the conventional definition of high-level injection in order to flatten the bands in the semiconductor and to minimize the effects of the initial surface-localized electric field on the observed carrier concentration decay dynamics. The simulations presented herein indicate that even though the injected carrier concentrations exceeded those in the bulk by a factor of 1×10^{3}, the carrier concentration dynamics at the surface were still dominated by the effects of the surface electric field as they modulated the carrier concentrations at the semiconductor surface. Hence, the effects observed at high-level injection conditions ought to be parallel to those observed in low-level injection. This expectation is also in accord with the experimental behavior observed in our studies. It should eventually, of course, be possible to flatten the bands at sufficiently high carrier injection levels, but such conditions were not accessible during the course of this study due to a reduction in the bulk lifetime at higher injected carrier concentrations resulting from Auger recombination processes in such samples.

3.5.3 The Influence of Interfacial Energetics on the Surface Recombination Velocity of n-Si(111)/CH_3CN Contacts and n-Si(111)/H_2O Contacts

Through near-surface channel conductance measurements, it was confirmed that n-Si(111)/CH_3CN–$CoCp_2^{+/0}$ contacts form an accumulation region with respect to electrons. The accumulation region arises when a strong reducing agent injects electrons into orbitals that are part of the conduction band of an n-type semiconductor. As pointed out in Chapter 1.2 on page 1-3, these excess electrons do not need to reside with dopant atoms, the supported charge density is not limited by the dopant density, as it is in the case of a depletion layer, but is limited by the atom density in the lattice. Hence, the width of the accumulation layer is supposed to be on the order of 100 Å or less,[62] while the width of the depletion layer in case of an inverted contact is on the order of micrometers.[62] Experimentally, this means that the ability of an accumulated junction to separate charges is greatly reduced relative to strongly depleted or inverted contacts.[72] Photoconductivity decay measurements involving n-Si(111)/CH_3CN–$CoCp_2^{+/0}$ contacts suggest that the carrier concentration dynamics at the surface of an accumulated contact are still dominated by the surface electric field in its ability to modulate the carrier concentrations at the semiconductor surface. Hence, the width of the accumulation layer must be large enough to prevent electrons and holes from tunneling through the energy barrier to trap states residing at the surface. We therefore conclude that the reduction in the surface recombination velocity at accumulated n-Si/CH_3CN–$CoCp_2^{+/0}$ contacts is caused by the same charge-transfer equilibration process, which allows n-Si(111)/THF–$Fc^{+/0}$ to form an inversion layer at the surface and which in turn is responsible for a very low effective surface recombination velocity of inverted contacts compared to depleted contacts, like n-Si(111)/THF–$Me_{10}Fc^{+/0}$.[19, 33]

The surface recombination behavior of electrochemically well-defined, accumulated contacts like n-Si(111)/CH_3CN–$CoCp_2^{+/0}$ contacts are of interest with respect to the charge-carrier dynamics at interfaces obtained by etching (111)-oriented Si surfaces in aqueous fluoride solutions. Silicon in contact with aqueous fluoride solutions show low *SRV* values. Two explanations can account for this high degree of apparent surface passivation. (1) Yablonovitch proposed that the defect density of Si in acidic solutions is reduced by the protonation of basic defect sites.[5] (2) Alternatively, our measurements show that an accumulation of electrons at the surface can lead to low surface recombination velocities.

We will first discuss the limitations of the model regarding the protonation of basic defect sites. According to Yablonovitch *et al.*, the low *SRV* values result from the reversible protonation of a low population of weakly basic surface defect sites, such that in acidic aqueous solutions the defect state density is gradually eliminated (and *SRV* thereby minimized).[5] It has already been noted that no apparent relationship exists between the acidity of the solution and the measured *SRV* value, since weakly dissociating acids like $HF_{(aq)}$ and $H_3PO_{4(aq)}$ essentially yield the same *SRV* values as strong acids like $H_2SO_{4(aq)}$. Yablonovitch does not discuss the *SRV* values in aqueous fluoride solutions other than $HF_{(aq)}$. Searson *et al.* have extended the mechanism of the reversible protonation of basic defect sites to aqueous fluoride solutions of various pH.[31, 32] In a series of measurements aimed at probing the surface state capacitance, Searson *et al.* propose that at low pH values the surface-state density of n-Si(111) in contact with aqueous fluoride solutions is relatively low (2×10^{10} cm^{-2}) and remains relatively constant up to a critical pH value, (pH = 6). For solutions with a pH value larger than the critcial value of 6, the surface-state density increases significantly to 1×10^{12} cm^{-2}.[31, 32] As we have shown in this study, the parallel capacitance that is used in such an approach is a strong function of the scan direction and this effect is most obvious in the case of basic fluoride $NH_4F_{(aq)}$ solutions, see Figure 3.7. This trend is similar to the scan-direction dependence of the E_{fb}, which is most pronounced for $NH_4F_{(aq)}$, see Table 3.5. Provided that the surface-state capacitance can indeed unambiguously be extracted from the parallel capacitance, the question remains whether the increase of the surface-state density with pH is a result of scanning the potential from reverse to forward biases[31, 32] and whether it is justified to assume that this surface-state density corresponds to the surface-state density at the open circuit potential. Similar shortcomings hold for any experimental approach aimed at probing the nature of band bending of Si/H_2O contacts solely based on a comparison between the apparent flat-band potential and the open circuit potential.[28] We have found large deviations in the open circuit potential before and after differential capacitance measurements are conducted. According to Alloungue *et al.*, all n-Si(111)/aqueous fluoride solution contacts are mildly accumulated and the degree of accumulation is more or less invariant with pH.[28] Together with the scan-direction dependence of the flat-band potential at high pH, these measurements make any conclusion regarding the degree of accumulation as a function of the pH of aqueous fluoride solution ambiguous.

To evaluate the relative importance of these two proposed mechanisms, i.e., charge-transfer equilibration process *vs.* reversible protonation of basic defect sites, the question regarding the evolution of band bending of n-Si(111) in aqueous fluoride solutions needs to be revisited. Given the complexity of the anodic oxidation of n-Si(111) surfaces during differential capacitance measurements, which results in irreproducible as well as in scan-direction dependent values for the flat-band potential and the open circuit potential, we have chosen an experimental approach which allows us to determine the degree of band bending at the open circuit potential. These measurements reveal that p-Si(111) in contact with $NH_4F_{(aq)}$ is the most inverted contact followed by $BHF_{(aq)}$ and

$HF_{(aq)}$. In an analogous fashion one can say that n-Si(111) shows the highest degree of accumulation with respect to electrons of all contacts followed by $BHF_{(aq)}$ and $HF_{(aq)}$. Contrary to Allongue's findings,[28] the degree of accumulation increases strongly with increasing pH.

The evolution of band bending in these contacts and the trends in the surface recombination velocity are intimately connected to the mechanisms which govern the chemical and electrochemical etching at the open circuit potential. Contrary to n-Si(111)/ $CH_3CN–CoCp_2^{+/0}$ or n-Si(111)/$CH_3CN–Me_{10}Fc^{+/0}$, n-Si(111) in contact with aqueous fluoride solutions does not have a well-defined redox potential and the *j-E* curves in the dark do not correspond to the type one would expect from an ideal diode.[23, 26-28] Depending on the pH, the dissolution of n-Si in aqueous fluoride solutions at the rest potential is described as being partly chemical and partly electrochemical in nature.[28, 67] Chemical dissolution is described as being anisotropic, since for steric reasons hydrolysis of the Si-H is easiest at step edges and the electrochemical dissolution is isotropic, since for accumulated contacts dissolution starts with the reversible dissociation of a Si-H bond leading to the formation of a negatively charged surface group $Si^{(-)}$. In the case of $HF_{(aq)}$ the dissolution is entirely electrochemical in nature, i.e., isotropic dissolution, which explains why the surface is pitted and roughened during etching. In the case of $BHF_{(aq)}$ the dissolution is predominantly electrochemical but has some chemical contributions and for $NH_4F_{(aq)}$ the contributions are about equal, but chemical enough in nature to ensure anisotropic etching at step edges.[28, 73] The electrochemical dissolution mechanism is responsible for determining the open circuit potential. In this mixed potential approach, the open circuit potential or rest potential is determined by a superposition of a cathodic reduction process of H_3O^+ forming H_2 and an oxidation process resulting in soluble SiF_4 ($pH < 2$) or $HSi(OH)_2F$ ($5 < pH < 9$).[28, 30] The hydrogen evolution in the chemical dissolution mechanism stems from the hydrolysis of the Si-H bond at the surface and of the soluble $HSi(OH)_2F$ product.[28, 30] The open circuit potential shifts with increasing pH to more negative values indicating that more electrons are injected into the conduction band and that the quasi-Fermi level of electrons moves to more negative values. The high anodic limiting currents, which reach a maximum at pH = 7, are a result of this electron injection mechanism.[26, 27] The open circuit potential situation also holds for p-Si under inversion.

As the experimental results have shown, accumulated contacts show low effective surface recombination velocities. An accumulation of electrons at the Si surface will lead to a low effective *SRV* value even for high values of $N_{\mathrm{T,s}}$. In the case of n-Si(111) in contact with aqueous fluoride solutions, the change in the effective *SRV* values is not due to a charge-transfer process which equilibrates the Fermi level of the semiconductor with the Fermi level of the contacting electrolyte, but due to the injection of electrons into the conduction band in the course of the electrochemical dissolution of n-Si(111).

This charge-transfer derived effect provides a natural explanation of the trend in *SRV* with varying pH because the decreases in *SRV* correlate well with conditions that produce an increase in the charge-carrier accumulation at the Si/liquid contact. The surface recombination velocity of n-Si(111)/$HF_{(aq)}$ contacts for instance depends on the pre-treatment of the surface. Only freshly-etched Si(111) or piranha-etched Si(111) shows a high lifetime. A water rinse or treatment with $NH_4F_{(aq)}$ and $BHF_{(aq)}$ effects the lifetime drastically and the lifetimes cannot be recovered in $HF_{(aq)}$, see Figure 3.6 (a). While the origin of this effect is not entirely clear and can probably only be understood through *in-situ* STM studies, the fact that $HF_{(aq)}$ contacts show high *SRV* values under certain circumstances thereby revealing the presence of a high density of trap states, i.e., the true quality of the surface, is corroborated by the fact that the $HF_{(aq)}$ contact is not or very mildly accumulated. When placed in $NH_4F_{(aq)}$ or $BHF_{(aq)}$ a significantly higher lifetime is immediately recovered, which indicates that the accumulation of electrons is responsible for the low effective *SRV* values, not a reduction in trap states, see Figure 3.6 (a). If the reversible protonation of basic defect sites were responsible for low surface state densities, than the result that immersion in more basic fluoride solutions recovers the initially high lifetime in $HF_{(aq)}$ could not be explained. The gradual improvement of the lifetime with etching time in $NH_4F_{(aq)}$ is probably due to both the anisotropic chemical etching, which gradually flattens the surface thereby further reducing the density of surface states and by a further bending of the bands over time, as indicated by a 50 mV increase in the built-in voltage of transconductance devices, see Table 3.7 and Figure 3.14, respectively. Since $H_2SO_{4(aq)}$ does not etch n-Si(111) and since the *j-E* show no indication for electron injection into the conduction band and since no evidence for electron accumulation as found, we conclude that the robust high lifetimes obtained for n-Si (111) in contact with $H_2SO_{4(aq)}$ might indeed be due to the reversible protonation of basic defect sites.

3.6 CONCLUSIONS

The experimentally observed charge-carrier decay dynamics for a variety of chemically treated Si surfaces can be explained in the context of the known electrochemical behavior of Si/liquid contacts. Low effective *SRV* values for Si in contact with oxidizing electrolyte solutions are observed for systems capable of undergoing interfacial charge-transfer reactions that produce an accumulation of holes or an accumulation of electrons at the Si surface. Except for Si surfaces under deep inversion or deep accumulation conditions, these types of Si/liquid contacts are therefore potentially useful for monitoring surface contamination levels above certain trap densities in the wet etching and processing steps of Si, but do not at present appear to provide routes to the effective passivation of Si surfaces for use in applications outside of these specific media. Surfaces in contact with $CH_3CN–CoCp_2^{+/0}$ solutions show low effective surface recombination velocities due to formation of an electron accumulation layer at the Si surface. In conjunction with prior measurements of the near-surface channel conductance for p^+-n-p^+ Si structures in contact with $CH_3OH–Fc^{+/0}$ solutions and for n^+-p-n^+ Si structures in contact with $CH_3CN–CoCp_2{}^{+/0}$ (this study), the data reveal that formation of an accumulation of holes and the formation of an accumulation of electrons, respectively, and not a reduced density of electrical trap sites on the surface, is primarily responsible for the long charge-carrier lifetimes observed for Si surfaces. Digital simulations incorporating a generalized Shockley-Read-Hall model for surface recombination reveal that effective surface recombination velocities < 10 cm s^{-1} can be produced by surfaces having $N_{T,s}$ values $> 10^{12}$ cm^{-2} provided that the surface is in accumulation or inversion due to charge-transfer equilibration with the redox-active electrolyte. Through the correct determination of the nature and the degree of band-bending of Si/H_2O contacts, an analogous effect, derived from interfacial charge-transfer processes in the course of electrochemical etching of Si(111) in aqueous fluoride solutions, was shown to play a significant role in the surface recombination behavior of Si in contact with aqueous fluoride solutions. The reversible protonation of basic defect sites is important for the low surface recombination of n-Si(111)/$H_2SO_{4(aq)}$ contacts but plays a minor role for aqueous fluoride solutions.

3.7 REFERENCES

1 Sze, S. M., *The Physics of Semiconductor Devices*. Wiley: New York, 1981.

2 Fonash, S. J., *Solar Cell Device Physics*. Academic: New York, 1981.

3 Green, M. A., Effects of Pinholes, Oxide Traps, and Surface States on MIS Solar Cells. *Appl. Phys. Lett.* **1978,** 33, (2), 178.

4 Lewis, N. S.; Rosenbluth, M. L., *Theory of Semiconductor Materials*. In *Photocatalysis: Fundamentals and Applications*, Ed. Serpone, N.; Pelizzetti, E., John Wiley & Sons: New York, 1989; 45.

5 Yablonovitch, E.; Allara, D. L.; Chang, C. C.; Gmitter, T.; Bright, T. B., Unusually Low Surface Recombination Velocity on Silicon and Germanium Surfaces. *Phys. Rev. Lett.* **1986,** 57, (2), 249.

6 Yablonovitch, E.; Gmitter, T., Auger Recombination in Silicon at Low Carrier Densities. *Appl. Phys. Lett.* **1986,** 49, (10), 587.

7 Royea, W. J.; Juang, A.; Lewis, N. S., Preparation of Air-Stable, Low Recombination Velocity Si(111) Surfaces through Alkyl Termination. *Appl. Phys. Lett.* **2000,** 77, (13), 1988.

8 Forbes, M. D. E.; Lewis, N. S., Real-Time Measurements of Interfacial Charge Transfer Rates at Silicon/Liquid Junctions. *J. Am. Chem. Soc.* **1990,** 112, (9), 3682.

9 Tan, M. X.; Kenyon, C. N.; Lewis, N. S., Experimental Measurement of Quasi-Fermi Levels at an Illuminated Semiconductor/Liquid Contact. *J. Phys. Chem.* **1994,** 98, 4959.

10 Tan, M. X.; Kenyon, C. N.; Krüger, O.; Lewis, N. S., Behavior of Si Photoelectrodes Under High Level Injection Conditions. 1. Steady-State Current-Voltage Properties and Quasi-Fermi Level Positions Under Illumination. *J. Phys. Chem. B* **1997,** 101, (15), 2830.

11 Reddy, A. J.; Burr, T. A.; Chan, J. K.; Norga, G. J.; Michel, J.; Kimerling, L. C., Silicon Surface Defects: The Roles of Passivation and Surface Contamination. *Defects in Semiconductors - Icds-19, Pts 1-3* **1997,** 258-2, 1719.

12 Stephens, A. W.; Green, M. A., Novel Method for Minority-Carrier Mobility Measurement Using Photoconductance Decay with Chemically Passivated and Plasma Damaged Surfaces. *J. Appl. Phys.* **1996,** 80, (7), 3897.

13 Stephens, A. W.; Green, M. A., Effectiveness of 0.08 molar Iodine in Ethanol Solution as a Means of Chemical Surface Passivation for Photoconductance Decay Measurements. *Sol. Energy Mater. Sol. Cells* **1997,** 45, (3), 255.

14 Msaad, H.; Michel, J.; Lappe, J. J.; Kimerling, L. C., Electronic Passivation of Silicon Surfaces by Halogens. *J. Electron. Mater.* **1994,** 23, (5), 487.

15 Horanyi, T. S.; Pavelka, T.; Tutto, P., Insitu Bulk Lifetime Measurement on Silicon with a Chemically Passivated Surface. *Appl. Surf. Sci.* **1993,** 63, (1-4), 306.

16 Laibinis, P. E.; Stanton, C. E.; Lewis, N. S., Measurement of Barrier Heights of Semiconductor/Liquid Junctions Using a Transconductance Method: Evidence for Inversion at n-SiCH$_3$OH-1,1'-Dimethylferrocene$^{+/0}$ Junctions. *J. Phys. Chem.* **1994,** 98, (35), 8765.

17 Shreve, G. A.; Karp, C. D.; Pomykal, K. E.; Lewis, N. S., Limits on the Corrosion Rate of Si Surfaces in Contact with CH3OH-Ferrocene+/0 and CH$_3$OH-1,1'-Dimethylferrocene$^{+/0}$ Solutions. *J. Phys. Chem.* **1995,** 99, 5575.

18 Pomykal, K. E.; Fajardo, A. M.; Lewis, N. S., Theoretical and Experimental Upper Bounds on Interfacial Charge-Transfer Rate Constants Between Semiconducting Solids and Outer-Sphere Redox Couples. *J. Phys. Chem.* **1996,** 100, (9), 3652.

19 Royea, W. J.; Michalak, D. J.; Lewis, N. S., Role of Inversion Layer Formation in Producing Low Effective Surface Recombination Velocities at Si/Liquid Contacts. *Appl. Phys. Lett.* **2000,** 77, (16), 2566.

20 Yablonovitch, E.; Swanson, R. M.; Eades, W. E.; Weinberger, B. R., Electron-Hole Recombination at the Si-SiO$_2$ Interface. *Appl. Phys. Lett.* **1986,** 48, (3), 245.

21 Matsumura, M.; Morrison, S. R., Anodic Properties of n-Si and n-Ge Electrodes in HF Solution under Illumination and in the Dark. *J. Electroanal. Chem.* **1983,** 147, (1-2), 157.

22 Matsumura, M.; Morrison, S. R., Photoanodic Properties of an Normal-Type Silicon Electrode in Aqueous-Solutions Containing Fluorides. *J. Electroanal. Chem.* **1983,** 144, (1-2), 113.

23 Memming, R.; Schwandt, G., Anodic Dissolution of Silicon in Hydrofluoric Acid Solutions. *Surf. Sci.* **1966,** 4, (2), 109.

24 Turner, D. R., On the Mechanism of Chemically Etching Germanium and Silicon. *J. Electrochem. Soc.* **1960,** 107, (10), 810.

25 Vanmaekelbergh, D.; Searson, P. C., On the Electrical-Impedance Due to the Anodic-Dissolution of Silicon in HF Solutions. *J. Electrochem. Soc.* **1994,** 141, (3), 697.

26 Gerischer, H.; Lubke, M., The Electrochemical-Behavior of n-Type Silicon (111)-Surfaces in Fluoride Containing Aqueous-Electrolytes. *Ber. Bunsen-Ges. Phys. Chem. Chem. Phys.* **1987,** 91, (4), 394.

27 Gerischer, H.; Lubke, M., On the Etching of Silicon by Oxidants in Ammonium Fluoride Solutions - a Mechanistic Study. *J. Electrochem. Soc.* **1988,** 135, (11), 2782.

28 Allongue, P.; Kieling, V.; Gerischer, H., Etching Mechanism and Atomic Structure of H-Si(111) Surfaces Prepared in NH4F. *Electrochim Acta* **1995,** 40, (10), 1353.

29 Hu, S. M.; Kerr, D. R., Observation of Etching of n-Type Silicon in Aqueous HF Solutions. *J. Electrochem. Soc.* **1967,** 114, (4), 414.

30 Eddowes, M. J., Anodic-Dissolution of p-Type and n-Type Silicon - Kinetic-Study of the Chemical Mechanism. *J. Electroanal. Chem.* **1990,** 280, (2), 297.

31 Oskam, G.; Hoffmann, P. M.; Searson, P. C., In Situ Measurements of Interface States at Silicon Surfaces in Fluoride Solutions. *Phys. Rev. Lett.* **1996,** 76, (9), 1521.

32 Oskam, G.; Hoffmann, P. M.; Schmidt, J. C.; Searson, P. C., Energetics and Kinetics of Surface States at n-type Silicon Surfaces in Aqueous Fluoride Solutions. *J. Phys. Chem.* **1996,** 100, (5), 1801.

33 Gstrein, F.; Michalak, D. J.; Royea, W. J.; Lewis, N. S., Effects of Interfacial Energetics on the Effective Surface Recombination Velocity of Si/Liquid Contacts. *J. Phys. Chem. B* **2002,** 106, (11), 2950.

34 Shockley, W.; Read, W. T., Statistics of the Recombination of Holes and Electrons. *Phys. Rev.* **1952,** 87, 835.

35 Hall, R. N., Electron-Hole Recombination in Germanium. *Phys. Rev.* **1952,** 87, 387.

36 Pierret, R. F., *Advanced Semiconductor Fundamentals*. ed. Neudeck, G. W.; Pierret, R. F.; Addison-Wesley Publishing Company: Reading, MA, 1987; VI.

37 Gajewski, H., Analysis und Numerik von Ladungstransport in Halbleitern. *GAMM (Gesellschaft für Angewandte Mathematik und Mechanik) Mitteilungen* **1993,** 16, 35.

38 Gajewski, H.; Glitzky, A.; Griepentrog, J.; Hünlich, R.; Kaiser, H.-C.; Rehberg, J.; Stephan, H.; Röpke, W.; Wenzel, H., Modellierung und Simulation von Bauelementen der Nano- und Optoelektronik. Weierstrass Institute for Applied Analysis and Stochastics (Germany), 1996.

39 Van Roosbroeck, W., Theory of Flow of Electrons and Holes in Germanium and Other Semiconductors. *Bell Syst. Tech. J.* **1950,** 29, 560.

40 Kruger, O.; Jung, C.; Gajewski, H., Computer-Simulation of the Photoluminescence Decay at the Gaas Electrolyte Junction .1. The Influence of the Excitation Intensity at the Flat-Band Condition. *J. Phys. Chem.* **1994,** 98, (48), 12653.

41 Kruger, O.; Jung, C.; Gajewski, H., Computer-Simulation of the Photoluminescence Decay at the Gaas Electrolyte Junction .2. The Influence of the Excitation Intensity under Depletion Layer Conditions. *J. Phys. Chem.* **1994,** 98, (48), 12663.

42 Kruger, O.; Kenyon, C. N.; Tan, M. X.; Lewis, N. S., Behavior of Si Photoelectrodes under High Level Injection Conditions .2. Experimental Measurements and Digital Simulations of the Behavior of Quasi-Fermi Levels under Illumination and Applied Bias. *J. Phys. Chem. B* **1997,** 101, (15), 2840.

43 Anz, S. J.; Kruger, O.; Lewis, N. S.; Gajewski, H., Conditions Under Which Heterogeneous Charge-Transfer Rate Constants Can Be Extracted From Transient Photoluminescence Decay Data of Semiconductor/Liquid Contacts As Determined By 2-Dimensional Transport Modeling. *J. Phys. Chem. B* **1998,** 102, (29), 5625.

44 Anz, S. J.; Lewis, N. S., Simulations of the Steady-State Current Density vs. Potential Characteristics of Semiconducting Electrodes. *J. Phys. Chem. B* **1999,** 103, (19), 3908.

45 Selberherr, S., *Analysis and Simulation of Semiconductor Devices*. Springer-Verlag: Wien New York, 1984.

46 Gerischer, H., Electron-Transfer Kinetics of Redox Reactions at the Semiconductor Electrolyte Contact - a New Approach. *J. Phys. Chem.* **1991,** 95, (3), 1356.

47 Marcus, R. A., Reorganization Free-Energy for Electron Transfers at Liquid Liquid and Dielectric Semiconductor Liquid Interfaces. *J. Phys. Chem.* **1990,** 94, (3), 1050.

48 Royea, W. J.; Fajardo, A. M.; Lewis, N. S., A Fermi Golden Rule Approach to Evaluating Outer-Sphere Electron-Transfer Rate Constants at Semiconductor/Liquid Interfaces. *J. Phys. Chem. B* **1997,** 101, 11152.

49 Blakemore, J. S., *Semiconductor Statistics*. Dover Publications, Inc.: New York, 1987.

50 The free energy for electron transfer was set equal to the difference between the conduction-band edge and the formal potential of the solution. The free energy for hole transfer was set equal to the difference between valence-band edge and the formal potential of the solution.

51 Tomkiewicz, M., Impedance Spectroscopy of Rectifying Semiconductor-Electrolyte Interfaces. *Electrochim. Acta* **1990,** 35, (10), 1631.

52 Kobayashi, H.; Takeda, N.; Sugahara, H.; Tsubomura, H., Silicon-Nonaqueous Solution Interface Studied by Capacitance-Voltage and Conductance-Voltage Techniques. *J. Phys. Chem.* **1991,** 95, 813.

53 Bube, R. H., *Photoconductivity of Solids*. Wiley: New York, 1960.

54 Yamaguchi, K.; Toyabe, T.; Kodera, H., Effect of Field-Dependent Carrier Diffusion on the Two-Dimensional Analysis of a Junction Gate FET. *Jpn. J. Appl. Phys.* **1975,** 14, (7), 1069.

55 Masetti, G.; Severi, M.; Solmi, S., Modeling of Carrier Mobility against Carrier Concentration in Arsenic-Doped, Phosphorus-Doped, and Boron-Doped Silicon. *IEEE Trans. Electron Devices* **1983,** 30, (7), 764.

56 Yablonovitch, E.; Gmitter, T. J., A Contactless Minority Lifetime Probe of Heterostructures, Surfaces, Interfaces and Bulk Wafers. *Solid-State Electron.* **1992,** 35, (3), 261.

57 Kunst, M.; Sanders, A., Transport of Excess Carriers in Silicon-Wafers. *Semi. Sci. Techn.* **1992,** 7, 51.

58 Forker, W., *Elektrochemische Kinetik*. Akademie-Verlag: Berlin, 1989.

59 Lewis, N. S., Progress in Understanding Electron-Transfer Reactions at Semiconductor/Liquid Interfaces. *J. Phys. Chem. B* **1998,** 102, (25), 4843.

60 Fajardo, A. M.; Lewis, N. S., Free-Energy Dependence of Electron-Transfer Rate Constants at Si/Liquid Interfaces. *J. Phys. Chem. B* **1997,** 101, (51), 11136.

61 Lewis, N. S., An Analysis of Charge-Transfer Rate Constants for Semiconductor Liquid Interfaces. *Annu. Rev. Phys. Chem.* **1991,** 42, 543.

62 Morrison, S. R., *Electrochemistry at Semiconductor and Oxidized Metal Electrodes*. Plenum Press: New York, 1980.

63 Natarajan, A.; Oskam, G.; Searson, P. C., Characterization of Silicon Surfaces in HF Solution Using Microwave Reflectivity. *J. Appl. Phys.* **1998,** 83, (4), 2112.

64 Hendrickson, D. H.; Sohn, Y. S.; Gray, H. B., Magnetic Suscpetibility Study of Various Ferricenium and Iron (III) Dicarbollide Compounds. *Inorg. Chem.* **1971,** 10, (8), 1559.

65 Haber, J. A.; Lauermann, I.; Michalak, D.; Vaid, T. P.; Lewis, N. S., Electrochemical and Electrical Behavior of (111)-Oriented Si Surfaces Alkoxylated through Oxidative Activation of Si-H bonds. *J. Phys. Chem. B* **2000,** 104, (43), 9947.

66 Yablonovitch, E., Personal Communication Regarding the Pre-Treatment of Si(111) with Piranha Etch, 2003.

67 Gerischer, H.; Allongue, P.; Kieling, V. C., The Mechanism of the Anodic-Oxidation of Silicon in Acidic Fluoride Solutions Revisited. *Ber. Bunsen-Ges. Phys. Chem. Chem. Phys.* **1993,** 97, (6), 753.

68 Rosenbluth, M. L.; Lewis, N. S., Kinetic Studies of Carrier Transport and Recombination at the n-Silicon Methanol Interface. *J. Am. Chem. Soc.* **1986,** 108, (16), 4689.

69 Schroder, D. K., *Semiconductor Material and Device Characterization*. John Wiley & Sons: New York, 1990.

70 Michalak, D. J.; Lewis, N. S., Use of Near-Surface Channel Conductance and Differential Capacitance versus Potential Measurements to Correlate Inversion Layer Formation with Low Effective Surface Recombination Velocities at n-Si/Liquid Contacts. *Appl. Phys. Lett.* **2002,** 80, (23), 4458.

71 Aberle, A. G.; Glunz, S.; Warta, W., Impact of Illumination Level and Oxide Parameters on Shockley- Read-Hall Recombination at the Si-SiO2 Interface. *J. Appl. Phys.* **1992,** 71, (9), 4422.

72 Tan, M. X.; Laibinis, P. E.; Nguyen, S. T.; Kesselman, J. M.; Stanton, C. E.; Lewis, N. S., *Principles and Applications of Semiconductor Photoelectrochemistry.* In *Progress in Inorganic Chemistry*, Ed. John Wiley & Sons Inc: New York, 1994; 41, 21.

73 Hessel, H. E.; Feltz, A.; Reiter, M.; Memmert, U.; Behm, R. J., Step-Flow Mechanism Versus Pit Corrosion - Scanning-Tunneling Microscopy Observations on Wet Etching of Si(111) by Hf Solutions. *Chem. Phys. Lett.* **1991,** 186, (2-3), 275.

CHAPTER 4 *Electron-Transfer Processes at Metal/Nanogap Junctions*

4.1 INTRODUCTION

Conventional Si-based electronic components are expected to reach a limit of miniaturization within the next 20 years, when the characteristic feature length of electronic devices shrinks below 100 nm. At this point the main technological problem is the onset of quantum phenomena, like electron tunneling, which will render scaled-down devices inoperable. Successor technologies, like the single-electron transistor, use these quantum phenomena advantageously as their operating principle.[1-4] The ultimate device miniaturization are three-terminal devices made from single molecules.

Prototypes of such devices already exist. Early studies go back to the work of Mann and Kuhn.[5] Reliable single-molecule transport measurements were first reported on structures based on single-walled carbon nanotubes.[6] Devices based on simple molecules were first introduced in the seminal work of Reed and Tour in 1997,[7] which triggered a considerable research interest in this field. Especially some of the more recent advances[8-13] were enthusiastically received, but remain controversial.[14] This is mostly due to the fact that the parameters determining the resistance of a simple molecule covalently bound to two metal electrodes are still somehow unclear. Theoreticians have contributed considerably to this field, and there are now a plethora of theoretical predictions regarding the influence of electronic coupling between molecule and metal electrodes, which need to be experimentally verified.[15-23] In addition, electron-tunneling phenomena through molecular bridges and solvents are immediately relevant to understanding the role of electron transfer in a wide variety of fundamentally interesting systems like photosynthetic reaction centers and proteins.[24, 25]

In order to test theoretical predictions that have become available over the last decade ways have to be found to directly address the electron transport through an individual molecular wire.[15, 18, 23] The original break-junction approach by Tour and coworkers, albeit its ease of use and simplicity, did not permit an unambiguous measurement of the electronic transport characteristics of an individual molecule.[7, 15, 26] This also holds for other attempts studying the molecule/metal junction, like the AFM approach by Wold *et al.*[27-29] and Cui *et al.*[30]and the STM approach by Hong *et al.*[31] Addressing individual molecules remains a challenge and there are only a few attempts, where this challenge has actually been met.[6, 26, 32]

A recent example, where the charge transfer characteristics of individual molecular wires were studied, is the elegant approach by Park *et al.* and Liang *et al.* who independently employed an electromigration technique as the experimental vehicle to *directly* explore electron-tunneling events through molecular bridges connecting two metal electrodes.[10, 12] The two groups used the unconventional combination of electron-beam lithography and electromigration to trap single molecules in the electrode gap. Electromigration describes a phenomenon in which the locally inhomogeneous electric field accompanying electron transport acts as a driving force for atom migration. This driving force increases with the applied electric field and a threshold voltage is necessary to induce the migration of atoms, which can ultimately result in the breakage of a nanometer-sized wire. Park *et al.* and Liang *et al.* used electromigration to form gold electrodes with nanometer separations.[10-12, 33]

Trapping is an occasional and lucky event. The fact that a single molecule got trapped, was inferred from electron transport characteristics that originate from two quantum effects, Coulomb blockade and Kondo resonance. The molecules used by Park *et al*. and Liang *et al*. are transition metal coordination compounds.[10-12] The metal atoms form the active region of the device, whereas the ligands provide the connections to the metal electrodes. In terms of electrical transport, the energy cost of adding an extra electron to an object of nanoscopic dimensions can be tuned to zero by applying a voltage to the gate electrode. However, Coulomb repulsion prevents a second electron from hopping at the same time. The first electron must leave the molecule to make way for the second electron resulting in a one-by-one electron motion known as single-electron tunnelling. In addition, electrons each carry one half-unit of spin in the 'up' or 'down' configuration. Spin-flipping, driven by the desire of the system to be in its ground state, forces an exchange of electrons between molecule and electrodes through a quantum effect called the Kondo effect.[10-12] According to the authors, the conduction mechanism is either single-electron tunnelling or electron transport mediated by the Kondo effect. Remarkably, when the Kondo effect dominates, the conductance reaches values close to the Landauer or quantum limit (which is $2e^2/h$, where e is the electron charge and h is Planck's constant) for a perfectly conducting one-dimensional wire. The results of Park *et al.* and Liang *et al.* are quite remarkable considering the intrinsic difficulty of establishing good electrical connection between a molecule and a metal electrode and the inherently catastrophic nature of electromigration.

If electromigration of nanosized metal wires is a method that results in direct electron-tunneling gaps, a very versatile experimental tool would be at hand for the investigation of a variety of tunneling phenomena in molecular wires and solvents.

Surprisingly, all published work to date was exclusively limited to nanogaps formed by breaking chemically modified (thiolated) metal nanowires. The experimental approach chosen by these investigators did not allow the investigation of the electrical behavior of the gap before the molecule was introduced. However, because the behavior of electrodes formed by electromigration is so varied,[33] it is important to measure each electrode set before it is used in measurements involving molecules. Only by looking at the difference between the bare electrodes and the electrodes with the sample molecule in the gap can one truly conclude that the observed data is indicative of only the molecule and not the electrode. Given the remarkable conclusion that a one-dimensional wire bridges the gap, the *J-E* characteristics of bare electrodes should be due to pure electron tunneling. If direct electron tunneling is dominating, the *J-E* characteristics of the metal/

nanogap junction should show a lack of temperature dependence. The possibility of pure electron tunneling in such devices, however, has so far not been unambiguously demonstrated.

In this study the electron-tunneling characteristics of devices in the absence of molecules bridging the gap are investigated in high vacuum as a function of temperature (4 K to RT) and gate bias and are correlated with the results of transmission electron microscopy studies. The metal nanowires consists of a bilayer of Cr and Au (with Cr having various thicknesses), pure Au and Pt. Nanowires with gaps of approximately 20 nm distance were used throughout this study to investigate possible parasitic pathways through the substrate and on the substrate surface. Aluminum nanowires with an Al-oxide tunneling barrier serve as model systems for the temperature and gate-bias dependence of ideal electron-tunnel junctions.

4.2 BACKGROUND

Arnold Sommerfeld and Hans Bethe were the first to theoretically treat the electron-tunneling effect for low and high voltages.[34] The theory was subsequently extended by a number of authors and generalized formulas for all voltage ranges, various barrier shapes, and for electrodes with dissimilar work functions have become available.[35-39] Simmon's equation is considered to be the classic treatment of electron tunneling. The relationship between the current density (*j*) and the applied voltage (*E*) in a symmetrical tunnel junction for a rectangular barrier is given by

$$j = -\frac{q}{4\pi^2 \hbar s^2}\left[\left(\varphi - \frac{qE}{2}\right)\cdot e^{\frac{-2\sqrt{2m}}{\hbar}s\sqrt{\varphi - \frac{qE}{2}}} - \left(\varphi + \frac{qE}{2}\right)\cdot e^{\frac{-2\sqrt{2m}}{\hbar}s\sqrt{\varphi + \frac{qE}{2}}}\right], \qquad \text{(Eq. 4.1)}$$

where φ is the value of the barrier height above the Fermi level of the negatively biased electrode, *E* is the voltage across the tunnel junction, *m* is the mass of the electron, *h* is

Figure 4.1 Energy Band Diagram for Electron Transfer in Electron Tunnel Junctions and Metal Island Films.

(a) The energy band diagram for direct electron tunneling is shown for a symmetrical tunnel junction (infinite electrode) and a rectangular energy barrier. The Fermi-level of the metal is denoted by η, the work function is denoted by ψ , and the barrier height measured with respect to the Fermi-level of the negatively biased electrode is φ. The width of the barrier is denoted by s. The shaded areas indicate available energy states. (b) If the size of the metal electrode is decreased to nanoscopic dimensions, the metal electrodes will have a non-negligible capacitance and the process of charge generation requires a non-negligible charging energy. The energy required to generate a pair of neighboring positively and negatively charged metal islands is denoted by $\boldsymbol{E_c^*}$. The voltage drop is denoted by $q\Delta V$. After tunneling has occurred a hole is left in one finite electrode and a electron is added to the other finite electrode.

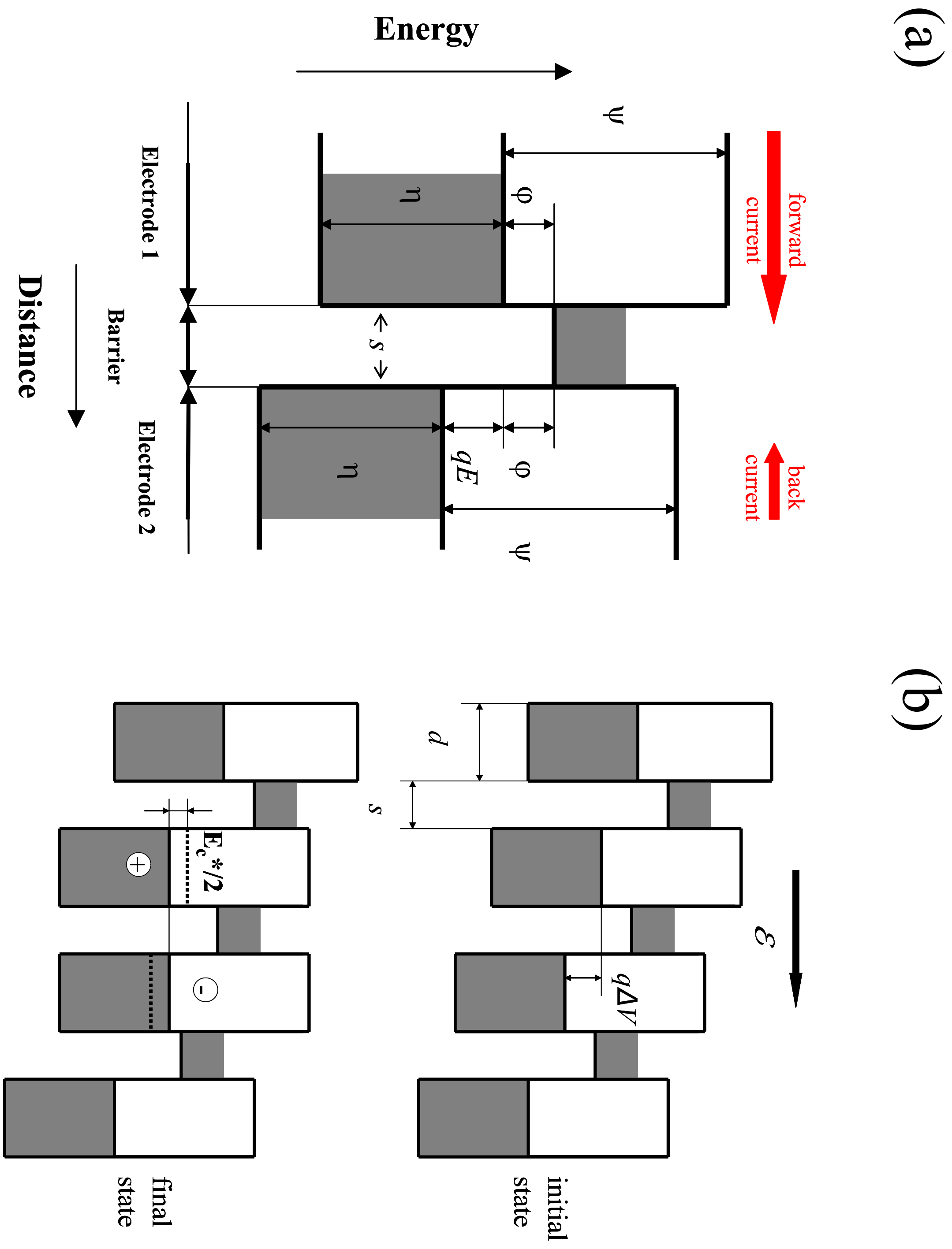
(a)
Energy
Distance
Electrode 1
Barrier
Electrode 2
forward current
back current
ψ
φ
η
s
qE
φ
η
ψ
(b)
d
s
ℰ
qΔV
E_c*/2
+
-
initial state
final state

Figure 4.1

Planck's constant, q is the elementary charge and s the is the distance between the two electrodes. The energy band diagram is shown in Figure 4.1. This equation holds for intermediate voltages ($0< E < \varphi/q$). For low voltages ($E \sim 0$) Eq. 4.1 reduces to:

$$j = \frac{\sqrt{2m}}{s}\left(\frac{q}{h}\right)^2 \cdot \sqrt{\varphi} \cdot e^{\frac{-2\sqrt{2m}}{\hbar} s\sqrt{\varphi}} \cdot E. \qquad \text{(Eq. 4.2)}$$

The j-E characteristics as a function of φ are shown in Figure 4.2. The linear region in the low-bias regime is governed by Eq. 4.2. In the high-voltage regime ($E > \varphi/q$) the tunneling currents are governed by the Fowler-Nordheim equation for field emission:

$$j = \alpha \frac{\left(E/s\right)}{\varphi} \cdot e^{-\beta \cdot s \cdot \varphi^{3/2}/E}, \qquad \text{(Eq. 4.3)}$$

where α and β are a function of the potential barrier.[40] At high temperatures thermionic emission can become prominent. Hartmann *et al.* and Stratton studied the temperature-dependence of the tunneling current by explicitly incorporating the Fermi-Dirac distribution functions.[37, 41, 42] Using Simmon's approach, Hartman derived the following equation for the current density considering an arbitrary shape of the barrier between the two electrodes:[41, 42]

$$\begin{aligned} j &= -\frac{4\pi m q}{h^3 c(V)^2}\left\{\frac{c(V) k_{\mathrm{B}} T}{\sin(\pi c(V) k_{\mathrm{B}} T)}\right\}\left[e^{-b(V)} \cdot \left(1 - e^{-c(V) q V}\right)\right] \\ b(V) &= \frac{4\pi (2m)^{1/2}}{h} \cdot \int_{s_1}^{s_2} \left[\varphi\left(\mathrm{x}, \mathrm{V}\right)\right]^{1/2} \cdot dx \qquad \text{(Eq. 4.4)} \\ c(V) &= \frac{4\pi (2m)^{1/2}}{h} \cdot \int_{s_1}^{s_2} \left[\varphi\left(\mathrm{x}, \mathrm{V}\right)\right]^{-1/2} \cdot dx. \end{aligned}$$

The above formula was used to fit the temperature dependence of the tunneling current in Al-Al_2O_3-Al junctions from 77 K to room temperature. The increase of the tunneling current with temperature was small and amounted to no more than 25 % of the low temperature value.[41, 42]

Figure 4.2 Tunneling Current *vs.* Applied Potential as a Function of the Barrier Height.

Eq. 4.1 was used to compute the tunneling current density (*j*) *vs.* potential characteristics for 3 values of the barrier height: 3 eV (dotted line), 4 eV (dashed line), 5 eV (solid line). The inset shows the low-bias region were the current density is increases linearly with the applied potential, see Eq. 4.2.

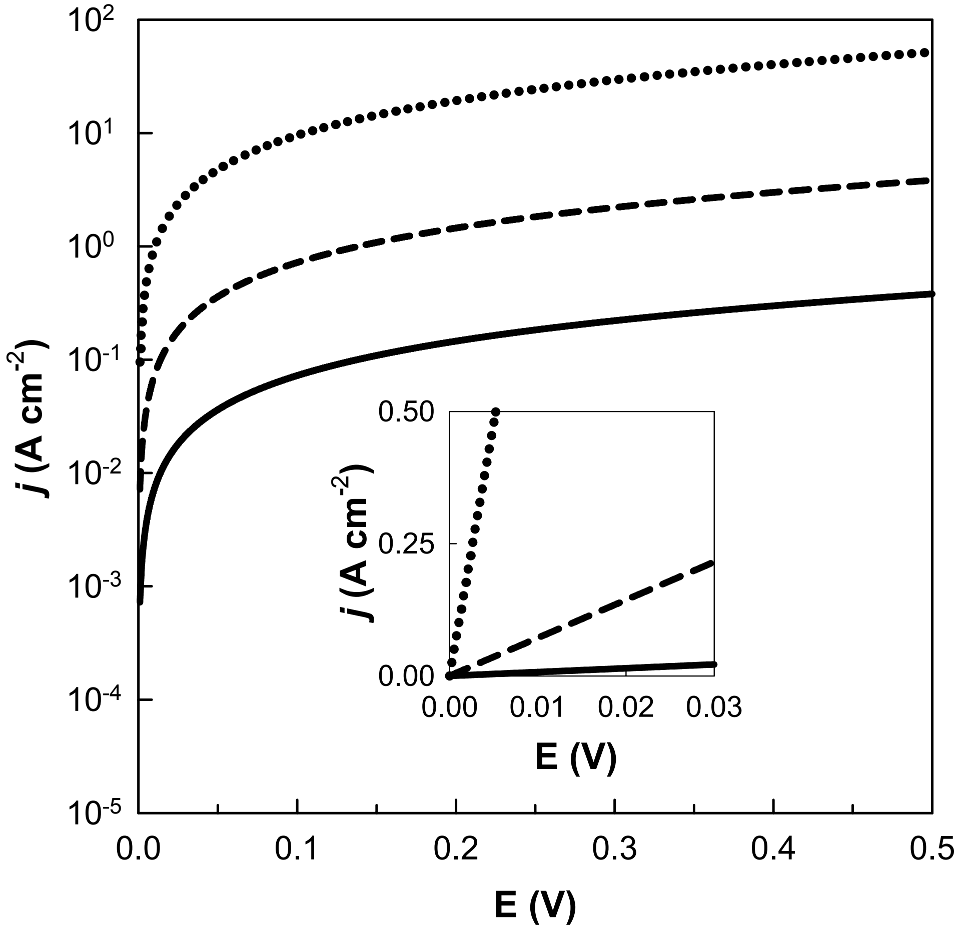

10^2
10^1
10^0
10^{-1}
10^{-2}
10^{-3}
10^{-4}
10^{-5}
j (A cm^{-2})
0.0
0.1
0.2
0.3
0.4
0.5
E (V)
0.50
0.25
0.00
j (A cm^{-2})
0.00
0.01
0.02
0.03
E (V)

Figure 4.2

The situation changes entirely when electron tunneling between metal electrode of nanoscopic dimensions is considered, see Figure 4.1 (b). Such tunneling phenomena are prominent in metal island films, where an electron has to be removed from one neutral metal island and placed on another neutral metal island, thereby creating a positively and a negatively charged metal island (Coulomb blockade effect). Due to the fact that small metal islands have a finite capacitance, the process of electron and hole generation requires a charging energy $\boldsymbol{E}_\mathbf{c}$, which has the general form of

$$\boldsymbol{E}_\mathrm{c} = \frac{q^2}{d} F\left(\frac{s}{d}\right), \tag{Eq. 4.5}$$

where d is the size of the metal island, s is the tunneling distance between the metal islands and F is a function of the shape of the island. The existence of the finite charging energy has far-reaching consequences on the electron transfer properties of such systems. These effects are manifested in both a pronounced temperature dependence and a characteristic electric-field dependence. When the electric field is weak, that is when the voltage drop between neighboring metal islands (ΔV) is significantly smaller than $k_\mathrm{B}T/q$, the charge carrier generation will be thermally activated and transport is due to drift under the influence of the weak electric field. The density of charge carriers follows a Boltzmann distribution and is proportional to $\exp(-\boldsymbol{E}_\mathbf{c}^*/2k_\mathrm{B}T)$. The parameter $\boldsymbol{E}_\mathbf{c}^*$ denotes the energy necessary to create a fully dissociated electron-hole pair. At the lowest temperatures the charging energy can only be overcome by an electric field such that $\Delta V > \boldsymbol{E}_\mathbf{c}^*/\mathrm{q}$.

For metal island films covering an area larger than 10 nm × 10 nm, i.e., an area large enough that the condition $\mathrm{s/d} = const$ and hence $s * \boldsymbol{E}_\mathbf{c}^* = const$ holds, Abeles *et al.* derived a set of equations that describe the temperature and electric-field dependence of metal island films.[43] The low-field conductivity (σ_LF) is given by the product of charge, tunneling probability (see conductivity term in Eq. 4.2), number of carriers (Boltzmann factor), followed by integration over all possible pathways and can be written using the condition $s{*}\boldsymbol{E}_\mathbf{c}{}^{*} = const$ as:

$$\begin{aligned}\sigma_{\mathrm{LF}} &\propto \int\left(\beta(s)\cdot exp\left[2\sqrt{\frac{2m\varphi}{\hbar^2}}\cdot s\right]\cdot exp\left[-\frac{\boldsymbol{E}_\mathbf{c}^*}{2k_\mathrm{B}T}\right]\right)\cdot ds = \\ &= \int\left(\beta(s)\cdot exp\left[2\sqrt{\frac{2m\varphi}{\hbar^2}}\cdot s-\frac{C}{2\sqrt{\frac{2m\varphi}{\hbar^2}}\cdot s\cdot k_\mathrm{B}T}\right]\right)\cdot ds,\end{aligned} \qquad \text{(Eq. 4.6)}$$

where β(s) is the density of percolation pathways. Abeles *et al.* simplify the above equation and suggest the following approximation for σ_{LF}[43]

$$\sigma_{\mathrm{LF}} = \sigma_0\cdot exp\left[-2\cdot\sqrt{\frac{C}{k_\mathrm{B}T}}\right] = \sigma_0\cdot exp\left[-C'\sqrt{\frac{1}{T}}\right], \qquad \text{(Eq. 4.7)}$$

where σ_0 is a temperature-independent constant.[43] This equations was shown to describe the low-field conductivity of a large variety of co-sputtered metal-SiO_2 films.[43]

For the high-field regime at very low temperatures there is a threshold voltage below which tunneling cannot occur. Since $s{*}\boldsymbol{E}_\mathbf{c}{}^{*} = const$, at a given applied voltage only barriers with s larger(!) than $C/q\Delta V$ can tunnel. The high-field conductivity (σ_{HF}) at low temperatures therefore is governed by a tunneling probability related to a barrier thickness of $s = C/q\Delta V = C'/\mathcal{E}$:

$$\sigma_{\mathrm{HF}} = \sigma_{\mathrm{inf}}\cdot exp\left[-C/q\mathcal{E}\,x_o\right] = \sigma_{\mathrm{inf}}\cdot exp\left[-C''/E\right], \qquad \text{(Eq. 4.8)}$$

where $\mathcal{E}$ is the electric field, C'' is a constant and x_o is the average distance between the equipotential surfaces in the metal island film.

4.3 EXPERIMENTAL

State-of-the-art lithography techniques currently do not have the resolution necessary to produce an electron tunneling gap that is 1 nm wide. The best electron-beam lithography equipment can currently fabricate structures with feature sizes as small as approximately 10 nm. Thus, in order to fabricate electrodes with nanometer-scale spacings, electromigration is used in addition to standard electron-beam lithography. In order to create nanometer-scale gaps using electromigration, it is necessary to fabricate electrodes connected by a thin metal section that will eventually be broken by a large current density. Figure 4.3 shows schematically how an electromigration experiment is carried out. It should be noted that little experimental details are available for the fabrication of electromigrated metal/nanogap junctions and the instrumentation used for their study. Therefore, device fabrication and instrumentation have been subject of continued improvement and optimization.

4.3.1 Device Fabrication

Two techniques were employed in the fabrication of the nanostructured electrodes: (1) a shadow evaporation technique, where the two electrodes and the metal weak link are fabricated in a single lithography and evaporation step and (2) a process, where the weak link and the electrodes are fabricated in two subsequent lithography and evaporation steps.

First a 300 nm thick oxide layer was grown on test grade, degenerately doped p-type Si(100) wafers by a commercial foundry (Silicon Quest International Inc.). The wafers were cleaned by subsequent immersion in boiling 1,1,1-trichloroethane (TCE), acetone, and isopropanol (IPA), followed by de-scumming in an UV-ozone dry stripper (SAMCO Model UV-1, O_2 flow rate 0.8 l/s, 65 ^oC, 60 min). Standard photolithography techniques were used to create large pads for interfacing the sample holder with the nanostructured electrodes defined by electron beam lithography. A thin layer of AZ 5214 E photoresist (Clariant) was applied by spin coating at 4000 rpm for 60 sec and the chips were subsequently pre-baked for 90 sec at 95 °C on a hot plate. The photoresist-coated chips were exposed for 8 sec to a UV light source (Karl Süss KSM mask aligner, 200 W

Figure 4.3 Schematic of the Experimental Setup of Electromigration Experiments. Electron-beam lithography is used to fabricate two electrodes (white regions: 4 nm Cr, 100 nm of Au), which are connected by a thin metal section (grey region: 4 nm Cr/25 nm Au, 1 nm Cr/ 25 nm Au, 25 nm Au, or 15 nm Pt) that will eventually be broken by a large current density in high vacuum. Samples were fabricated on various substrates (typically on a Si wafer with 300 nm of thermally grown oxide or on a 30 nm thick silicon nitride membrane). The width and length of the weak link were approximately 70 and 300 nm, respectively. During electromigration, the voltage is ramped continuously. At a critical threshold voltage, a dramatic drop in the current is noticed after which the current drops stepwise. When the gap resistance is larger than the resistance quantum, the voltage is ramped down and the *J-E* characteristics of the junction are measured as a function of temperature. The contrast of the image was digitally enhanced.

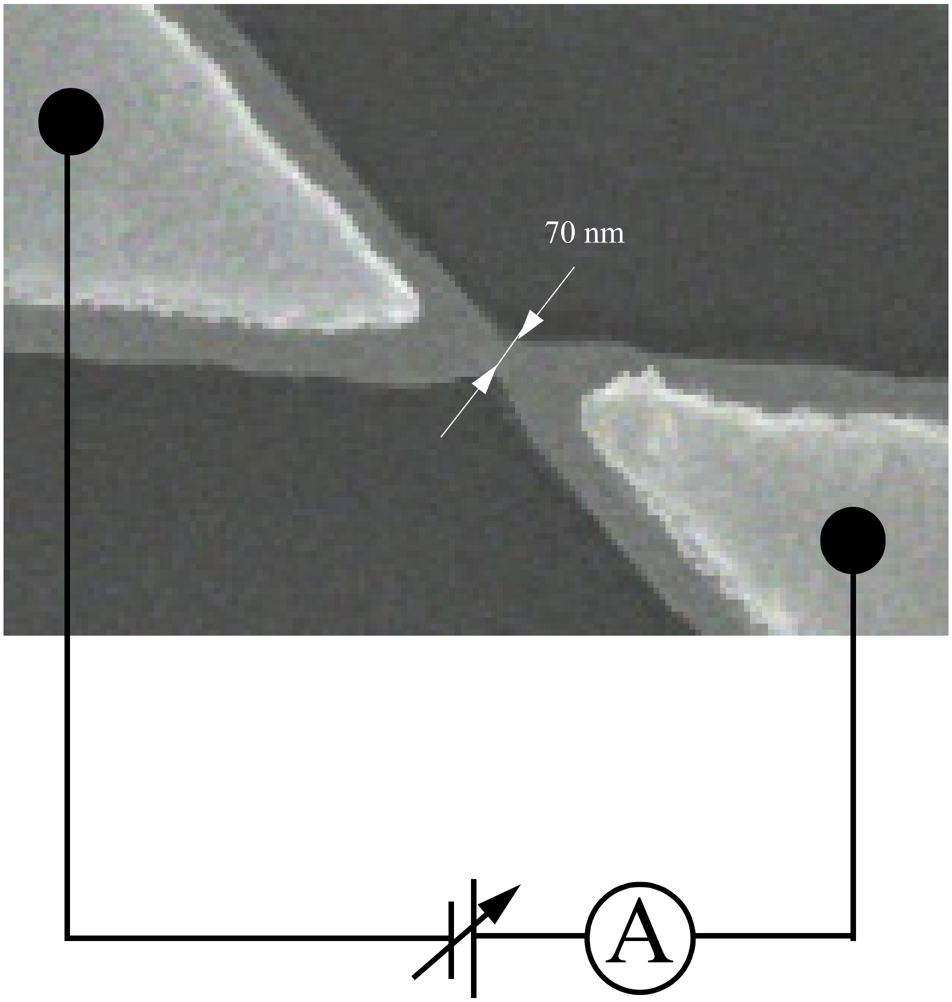

Figure 4.3

Hg light bulb) through a glass mask (Adetk Photomask Montreal Canada; 4” × 4” soda lime glass plate; photo patterns were defined by bright Cr coating; 0.2 μm tolerance in feature size), baked for 75 sec at 105 °C, and subsequently flooded with UV light for 20 sec. After the last exposure step, the samples were immersed in AZ 327 MIF developer (Clariant) for 30 sec and were immersed in water for 2 min. The exposed patterns were cleaned in a ozone dry stripper (SAMCO Model UV-1, O_2 flow rate 0.8 l/s, 65 ^oC, 3 min) Metal was evaporated through the photolithography mask in a thermal evaporator with a vacuum better than 10^{-6} Torr. The metal bilayer consisted of a 4 nm thick Cr adhesion layer and a 100 nm thick Au layer. The photolithography mask was lifted off in hot acetone (10 min, aided by sonication) followed by immersion in IPA (1 min) and de-scumming in a ozone dry stripper (SAMCO Model UV-1, O_2 flow rate 0.8 l/s, 65 ^oC, 60 min).

The fabrication scheme leading to nanostructured electrodes by means of a shadow evaporation technique is shown in Figure 4.4. The resist bilayer consisted of a 400 nm thick layer of Copolymer MMA (8.5) MAA (Microchem, Newton MA; total of 4 layers; each layer was applied by spin coating at 4000 rpm for 60 sec and was subsequently baked at 160 °C on a hot plate for 2 min; this was followed by a final bake of all 4 layers at 160 °C for 40 min) and a 100 nm PMMA C2 950 resist layer (Microchem, Newton MA; resist layer was applied by spin coating at 4000 rpm for 60 sec and subsequently baked at 180 °C on a hot plate for 20 min). Because the MMA resist is more sensitive to the electron beam, than the PMMA layer, a strong undercut profile around the edges of the pattern develops when the pattern is exposed to the electron beam. The lithography pattern was designed such that the strong undercut results in a thin suspended resist-bridge of PMMA in the region where the tips of the 2 electrodes meet. A JEOL JSM-6400 thermionic emission scanning electron microscope (SEM) was used to draw the pattern onto the sample using the NPGS lithography system. The dosage (area exposure) of the electron beam was set to

Figure 4.4 Fabrication of Nanostructured Electrodes Using Shadow Evaporation. A resist bilayer, consisting of a highly sensitive MMA copolymer (blue) and a less sensitive PMMA layer (orange), is exposed to an electron beam, which after development leads to such a strong undercut profile that a suspended PMMA resist bridge results (see SEM picture). During evaporation the sample stage is rotated (+/- 20^{o}; green arrows) such that a 15 -25 nm thin metal layer (1) is deposited underneath the resist bridge. This is followed by evaporation normal to the substrate (red arrow) of a 100 nm thick metal layer (2). The suspended resist bridge covers the thin metal section during straight evaporation. An SEM picture of the resulting structure is shown in Figure 4.3.

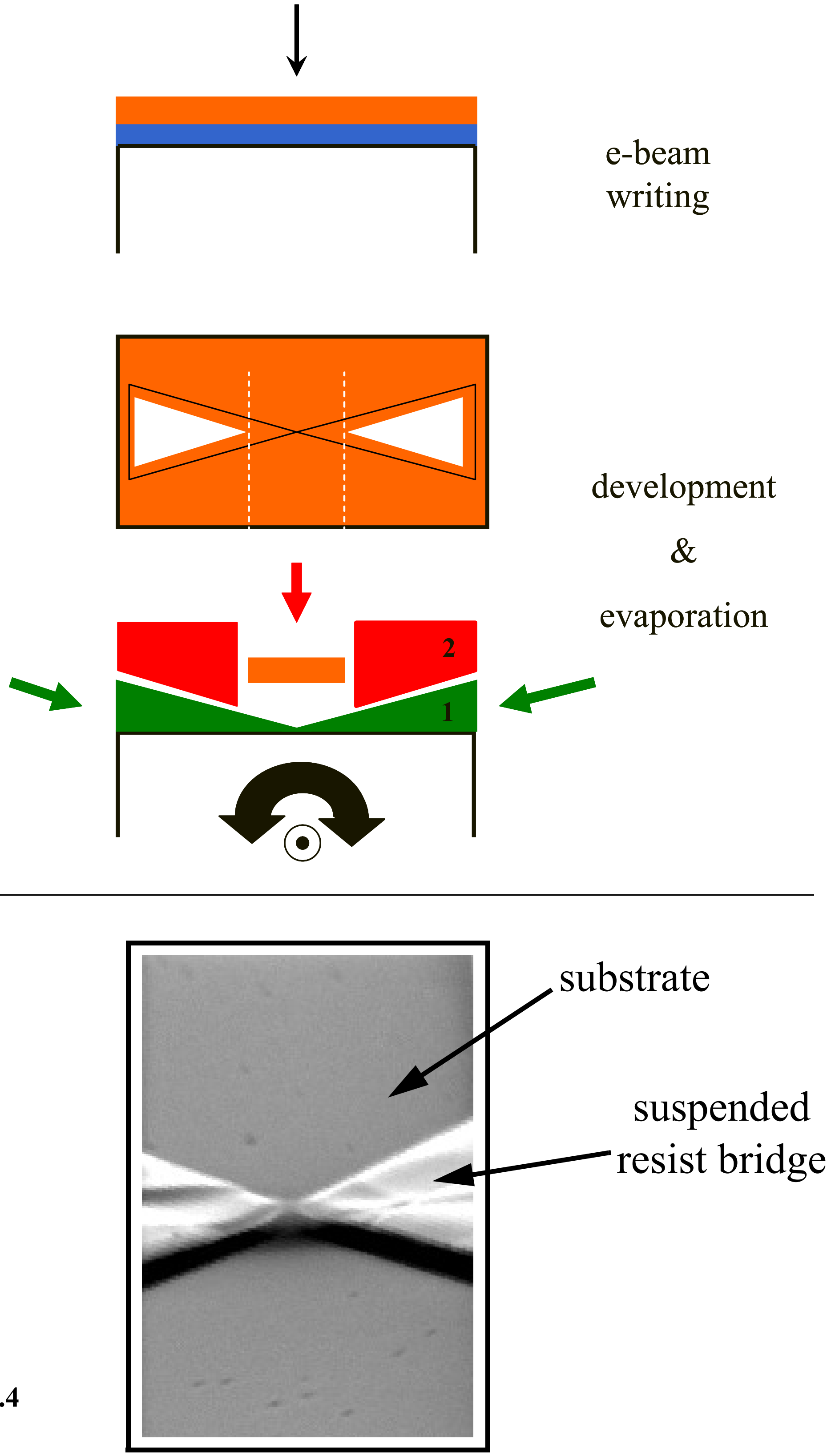
e-beam
writing
development
&
evaporation
2
1
substrate
suspended
resist bridge

Figure 4.4

1000 μC/cm^2. The resist bilayer was developed for 30 seconds in a 3:1 mixture of IPA and methylisobutyl ketone (MIBK) and then rinsed with IPA. The resist-bridge covers the area that will eventually be the thin metal section connecting the two electrodes. When metal is evaporated normal to the substrate surface, the bridge prevents metal from being deposited. However, when the substrate is rotated, a small amount of metal may get under the resist-bridge. A thin metal layer was first evaporated onto the sample at angels of +/- 20^o, creating the thin metal that will eventually be broken. The thin metal section consisted either of 1-4 nm thick Cr followed by 25 nm thick Au, 25 nm thick Au without an adhesion layer, or 15 nm of Pt without an adhesion layer. Platinum was evaporated using an electron-beam evaporator (Temescal BJD-1800, pressure better than 4×10^{-7} Torr). Chromium and Au were deposited using a thermal evaporator with a pressure better than 10^{-6} Torr. All evaporation sources were pre-evaporated for at least 1 min prior to opening the shutter. The resist layer was lifted off by immersing the sample in concentrated acetic acid (60 ^{o}C, 8 hours).

Tunnel junctions consisting of Al/Al-oxide/Al were fabricated using the same shadow evaporation technique. A film of Al (thickness: 300 nm) was evaporated at an angle of 20^o. High purity oxygen (99.998 %, Matheson Tri Gas) was subsequently introduced into the system (0.3 Torr, 5 min). The system was evacuated again and 400 nm of Al were evaporated at an angle of -20^o. The little overlap of oxidized Al and Al metal formed the electron-tunnel junction.

Several structures were fabricated on silicon nitride membranes in an attempt to correlate the *J-E* characteristics with images obtained through high resolution transmission electron microscopy (TEM). To fabricate membranes, Si with 30 nm silicon nitride was etched from the back face in a concentrated KOH solution (50 wt% KOH, 80^o C). The silicon nitride on the back face served as the etch mask. This mask was defined through photolithography and a dry silicon nitride etch (flow rate 20 sccm Ar, 10 sccm

NF_3 at 30 mTorr, 300 W RF power with a DC bias of -100 V for 30 seconds). TEM images were made using a Phillips EM 430 transmission electron microscope.

A more recent and in many aspects optimized way of making nanostructured electrodes utilizes a fabrication scheme based on two separate electron-beam lithography and evaporation steps. A wafer patterned with photolithographically defined contacting pads was covered with a thin metal layer (1 nm Cr, 25 nm Au), that will eventually form the thin metal weak link of the electrodes. The substrate can be cleaned by O_2 plasma cleaning or ion milling without breaking the vacuum prior to metal deposition step. The PMMA bilayer consists of a PMMA C2 495 layer (applied by spin coating at 6000 rpm and baking at 180 ^oC for 10 min) and a PMMA C2 950 layer (applied by spin coating at 6000 rpm and baking at 180 ^oC for 10 min). A Leica EBPG 5000+ e-beam writer (area exposure: 1300 $\mu C/cm^2$, 100kV, 20 nm point to point distance, 20nm line to line distance) was used to define a 70 nm wide and approximately 500 nm long nanowire terminating in larger areas that connect to the photolithographically defined contacting pads. The structures were developed in 3:1 IPA:MIBK mixture for 40 sec and were subsequently immersed in IPA for 10 sec and blown dry with $N_{2(g)}$. A 50 nm thick layer of Ni was evaporated on the structures and after liftoff the Ni layer served as a mask during ion milling (MRI reactive ion etcher, 20 sccm Ar, 20 mTorr , 100 W RF power, 3 min). The sample was briefly dipped into buffered HF (Transene Co.) The Ni mask was removed by etching in a saturated $FeCl_3$ solution (room temperature, 2 min), the structures were subsequently rinsed with de-ionized water and blown dry with $N_{2(g)}$. The nanowires were connected to the photolithographically-defined bonding pads in a second electron-beam writing step (1000 $\mu C/cm^2$, 100 kV, 20 nm point to point distance, 20 nm line to line distance), with dimensions slightly recessed from those of the nanowire, followed by the evaporation of 100 nm of Au. The advantage of this approach over the shadow evaporation technique is, that the substrate can be carefully cleaned prior to the deposition of the thin metal layer which will eventually form the metal nanowire. The suspended PMMA resist bridge on the other hand is very delicate and de-scumming the substrate underneath the resist bridge prior to metal deposition is not possible.

All samples intended for electromigration experiments were thoroughly cleaned right before they were mounted into the sample holder, typically by immersion in concentrated acetic acid, which removes any PMMA resist residues (even when heavily crosslinked), followed by subsequent immersion in IPA and O_2-plasma cleaning (ECR etcher, 20 mTorr O_2 , 20 sccm flow rate, 300 W power, 0 V DC bias, 2 min). The measurement system did not allow in-situ cleaning of the devices.

4.3.2 Electrical Measurements

Early devices were broken in a dipstick containing 0.5 Torr of He exchange gas. The dipstick was placed in a liquid He bath to cool the sample and variable temperature measurements were carried out using resistive heating. The sample was electrically connected to the measurement system using thin Au wire and silver print. Eventually a measurement system was built that uses spring-loaded pins (PogoPins, Ostby Barton Pylon, distributed by Newark Electronics) to make electrical contact and a liquid He continuos flow cryostat (Janis Research, ST 200 Tubular System combined with 6’ super insulated liquid He transfer line) to cool the sample. In this setup, the sample is broken and measured in a vacuum system capable of reaching pressures as low as 10^{-9} Torr using a turbo pump. The setup is shown in Figure 4.5. Because it is important that the gaps are ultra-clean, the samples must be measured in high vacuum (HV). The sample holder consists of a machined piece of Macor, which holds the sample chip. The sample chip and the Macor cup are pressed against eight PogoPins that make electrical contact to the photolithographically-defined pads on the sample chip. To promote better thermal contact between the cryostat and the sample holder, the Macor cup was replaced by a machined

Figure 4.5 Measurement System for the Electrical Characterization of Electron Tunneling Gaps as a Function of Temperature and Gate Bias.

The sample holder, consisting of a chip (holding the nanostructured electrodes, top left) and a Cu or Macor cup (shown in the picture), is mounted on top of a continuous liquid He flow-cryostat and can be pressed against spring-loaded pogo pins that provide electrical contact and interface the nanostructured electrodes with the measurement equipment. The flow cryostat is mount into a UHV system. The system can reach pressures as low as 10^{-9} Torr. The temperature can be varied between 4.2 K and room temperature.

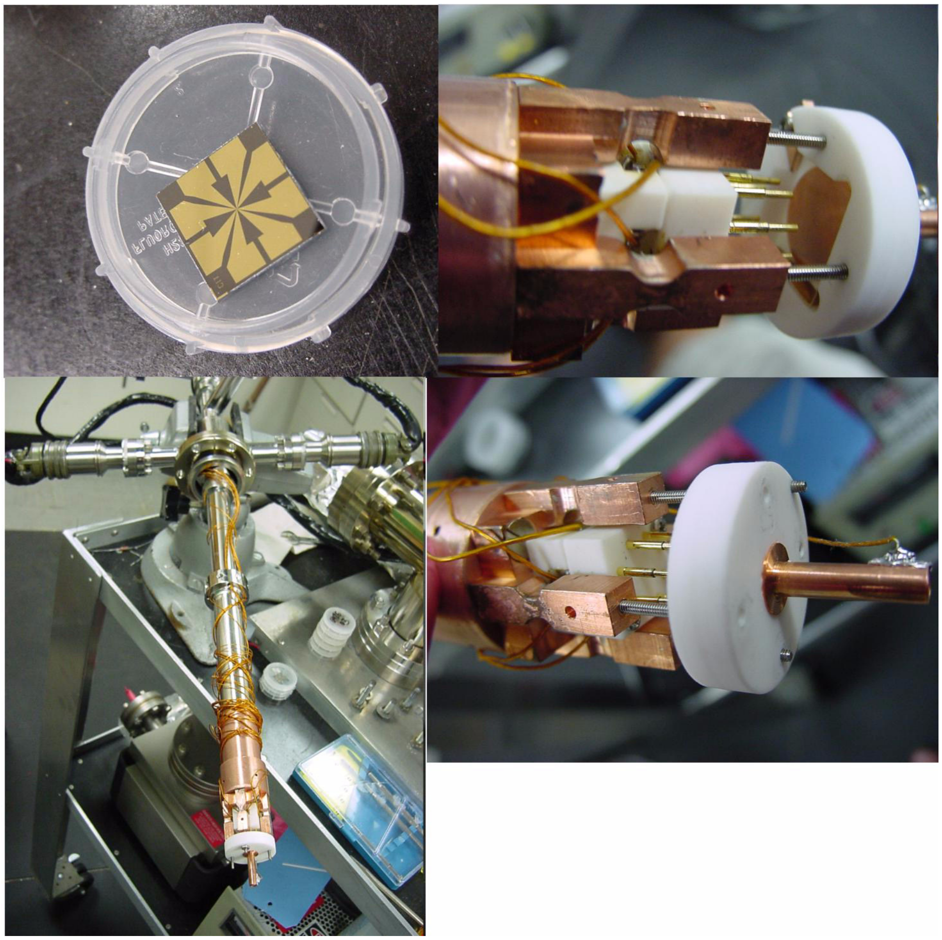

Figure 4.5

piece of Cu, which was electrically isolated from the cryostat using single crystal sapphire washers (Swiss Jewel Company, Philadelphia PA). These washers have excellent thermal conductivity at cryogenic temperatures. The PogoPins were cleaned in boiling TCE, acetone, and IPA prior to the measurement system assembly, and were lubricated with graphite to prevent them from mechanically freezing at low temperatures. The PogoPins are electrically connected to a switch box that allows interfacing between the sample and measurement equipment. The entire assembly inside the vacuum system may be cooled down to 4.2 K using the liquid He flow cryostat. To increase the temperature the flow of liquid He was slowly reduced and the system was allowed to warm up at a rate of approximately 0.5 K min^{-1}.

Each photolithographically defined pad was electrically accessed through a switch box that keeps each connection to the sample grounded when not in use. It is extremely important to prevent static electricity or charge buildup on the sample, as the thin metal section tends to fully break at potentials under a few volts. The switching circuit (Figure 4.6 (a)) prevents any accidental charging of the sample and isolates the sample from initialization glitches from the instruments. Two different sets of equipment were used for breaking and measuring the metal/nanogap junctions. Initially, the samples were electromigrated using a Keithley 230 DC source and an HP 34401A multimeter acting as an ammeter. The instruments were controlled via GPIB with a LabVIEW program that stepped up the DC voltage while monitoring the current flowing across the electrodes. When the current dropped suddenly, indicating that the sample had broken, the program quickly ramped down the applied voltage, thus terminating the electromigration process. The differential conductance (*dJ/dE vs. E*) curves were measured using an HP 1134 function generator, a Stanford Research SR830 lock-in amplifier, an Ithaco 1211 current preamplifier, and HP and Agilent 34401A multimeters (Figure 4.6 (c)). The function generator created an AC signal for the lock-in amplifier to track while at the same time ramping up the DC offset. One of the multimeters was used along with the Ithaco current preamplifier to trace out the *J-E* curve, while the differential conductance curve was created using data from the lock-in amplifier. Again, all equipment was controlled via GPIB using a LabVIEW program.

Though the above setup worked extremely well for measuring single *J-E* and differential conductance curves, the integration time on the multimeters limited the data acquisition speed to approximately 6 points per second. Moreover, the voltage resolution of the Keithley DC source was not small enough (5 mV for the desired range) and the response of some of the equipment over the GPIB interface was not fast enough.

Eventually all of the analog inputs and outputs were moved over to a National Instruments PCI-6036E DAQ card (using a BNC-2090 breakout box). The DAQ card was calibrated using a special LabVIEW file to ensure that the card was within its specifications. Electromigration is accomplished using one of the analog outputs and one of the analog inputs connected to either the Ithaco current preamplifier or a 10 Ω resistor as a ammeter (Figure 4.6 (b)). To measure *J-E* curves, one of the analog outputs is divided down by approximately 20-fold (to get higher resolution) and connected to the sample. The current is measured using the Ithaco current preamplifier connected to one of the analog inputs (Figure 4.6 (d)). Differential conductance curves are created by simple numeric differentiation of the *J-E* data. With this system much quicker measurements are achieved, a necessity for doing high-resolution gate potential dependence measurements. The voltage resolution is approximately 15 μV for *J-E* curves and 305 μV for electromigration experiments.

The outcome of electromigration proofed to be relatively insensitive to parameters like the ramp rate. The final, optimized measurements were performed at a ramp rate of 30 mV/sec. To provide a smooth ramp, the voltage was increased in 300 μV steps.

Figure 4.6 Electrical Circuit Diagrams for Switch System, Electromigration Experiments, Differential Conductance Measurements and Measurement of the *J-E* Characteristics.

The switching circuit (a) prevents any accidental charging of the sample and isolates the sample from initialization glitches from the instruments. All of the analog inputs and outputs were connected to a National Instruments PCI-6036E DAQ card (via a BNC-2090 breakout box). Electromigration (b) is accomplished using one of the analog outputs and one of the analog inputs connected to either a 10 Ω resistor or the Ithaco current preamplifier. Differential conductance curves are created by simple numeric differentiation of the *J-E* data or by electrical measurements using circuit (c). To measure *J-E* curves, one of the analog outputs is divided down by approximately 20-fold (to get higher resolution) and connected to the sample. The current is measured using the Ithaco current preamplifier connected to one of the analog inputs.

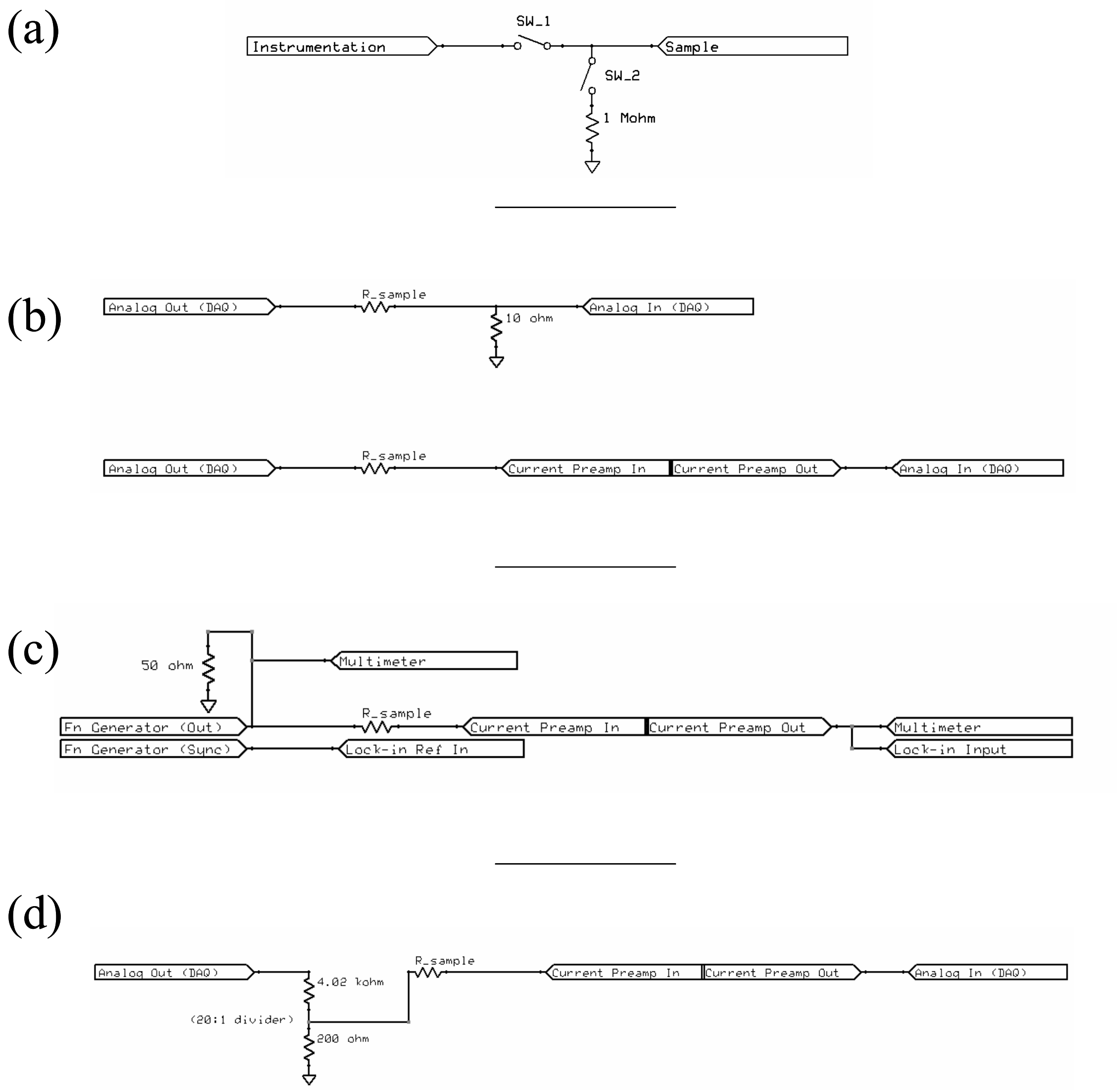
(a)
Instrumentation
SW_1
Sample
SW_2
1 Mohm
(b)
Analog Out (DAQ)
R_sample
Analog In (DAQ)
10 ohm
Analog Out (DAQ)
R_sample
Current Preamp In
Current Preamp Out
Analog In (DAQ)
(c)
50 ohm
Multimeter
Fn Generator (Out)
R_sample
Current Preamp In
Current Preamp Out
Multimeter
Fn Generator (Sync)
Lock-in Ref In
Lock-in Input
(d)
Analog Out (DAQ)
4.02 kohm
(20:1 divider)
200 ohm
R_sample
Current Preamp In
Current Preamp Out
Analog In (DAQ)

Figure 4.6

4.4 RESULTS

This chapter presents the current *vs.* voltage characteristics (*J-E* characteristics) of a large variety of metal/nanogap junctions formed by electromigration. The *J-E* characteristics were investigated as a function of temperature and if applicable as a function of gate bias. In the case of Au nanowires, devices were studied with and without an adhesion layer. The weak link that was eventually broken consisted either of a 4 nm thick Cr and 25 nm thick Au bilayer (type **I:** devices **A** and **B**), bilayers of Cr and Au where Cr had a thickness smaller than 1 nm (type **II**: devices **C** and **D**), Au of 25 nm thickness (type **III**), or 15 nm thick Pt (type **IV**: device **E**, **F**, and **G**). Although little experimental details are available for the experiments of Park *et al.* and Liang *et al.*, the junctions studied in these reports apparently belong to type **I** or type **II**.[10-12, 33, 44] At least ten device of each type were investigated. Representative junctions are identified by bold capital letters and are referred to throughout the text. In addition to these electromigration devices, the electron-tunneling characteristics of model electron-tunnel junctions, Al/Al-oxide/Al (device **H**), with geometries similar to those of the metal/nanogap junctions formed by electromigration are presented. Unless otherwise noted, all experiments were carried out in a sample holder mounted on top of a liquid He flow cryostat, as depicted in Figure 4.5.

The *J-E* characteristics of the junctions were measured as a function of temperature after electromigration was carried out at 4.2 K. Only devices with measurable currents (> 100 fA) within a voltage range of ±1 V and with a low-bias resistance larger than the resistance quantum were considered to be operational. During electromigration, the yield of operational devices was found to be very sensitive to both the breaking method as well as the quality of the electrical instrumentation. Especially, glitches created by the digital electrical equipment were found to potentially destroy a device. The best yield was achieved when the applied potential was increased smoothly (using a rate of approximately 30 mV s^{-1}) until the sample showed signs of breaking (i.e., the gap resistance became larger than the resistance quantum) and then was quickly ramped down to zero. The applied potential was never immediately set to 0 V, because the possibility of a sudden glitch associated with the instrumentation tended to destroy the device.

Figure 4.7 (a) and (b) show the changes in current and conductance during electromigration experiments. After the measurement system and device fabrication were optimized, samples that were fabricated following a specific fabrication scheme, broke at very similar potentials approximately within a range of 50 mV of one another. Devices with weak links formed by Cr/Au (**I**, **II**) broke at around 0.65 V, which is close to the value reported by Park *et al.,*[33] while Pt devices (**IV**) broke at somewhat larger potentials of approximately 1.2 V. Given the refractory character of Pt, the higher threshold voltage for electromigration involving weak links formed by Pt as compared to Cr/Au makes intuitive sense. Though electromigration was often seen as a self-terminating process, devices with resistances larger than the resistance quantum still tended to undergo physical re-arrangements when a large potential was applied between the electrodes. Thus, it was important to ensure that the electromigration procedure adequately defined a current-drop threshold for stopping electromigration. It was also necessary to make sure that the potential across the electrodes in subsequent *J-E* measurements was not too large. Even potentials as low as 0.4 V were found to cause irreproducible changes in the *J-E* curves, especially at higher temperatures.

During electromigration, the conductance decreased more or less stepwise. Sometimes, the heights of the conductance steps were on the same order of magnitude as the conductance quantum, although very often the conductance quantization showed irregularities. The quantization of the conductance has been used by Park *et al.*[10, 11, 33] and Liang *et al.*[12] to confirm that electromigration results in the gradual pinching off of conductance channels ultimately leading to a single row of metal atoms that can be

Figure 4.7 Current and Conductivity Changes during Electromigration. Representative current and conductivity changes during electromigration experiments are shown as a function of the applied potential for (a) device **C** (type **II**) and (b) device **F** (type **IV**)**.** Electromigration took place at 4.2 K. Devices of type **I** and type **II** typically broke at 0.65 ± 0.05 V, while devices of type **IV** broke at higher voltages of 1.2 ± 0.05 V. The conductance decreased more or less stepwise, the step height is on the same order of magnitude as the conductance quantum (~ 0.8×10^{-4} S).

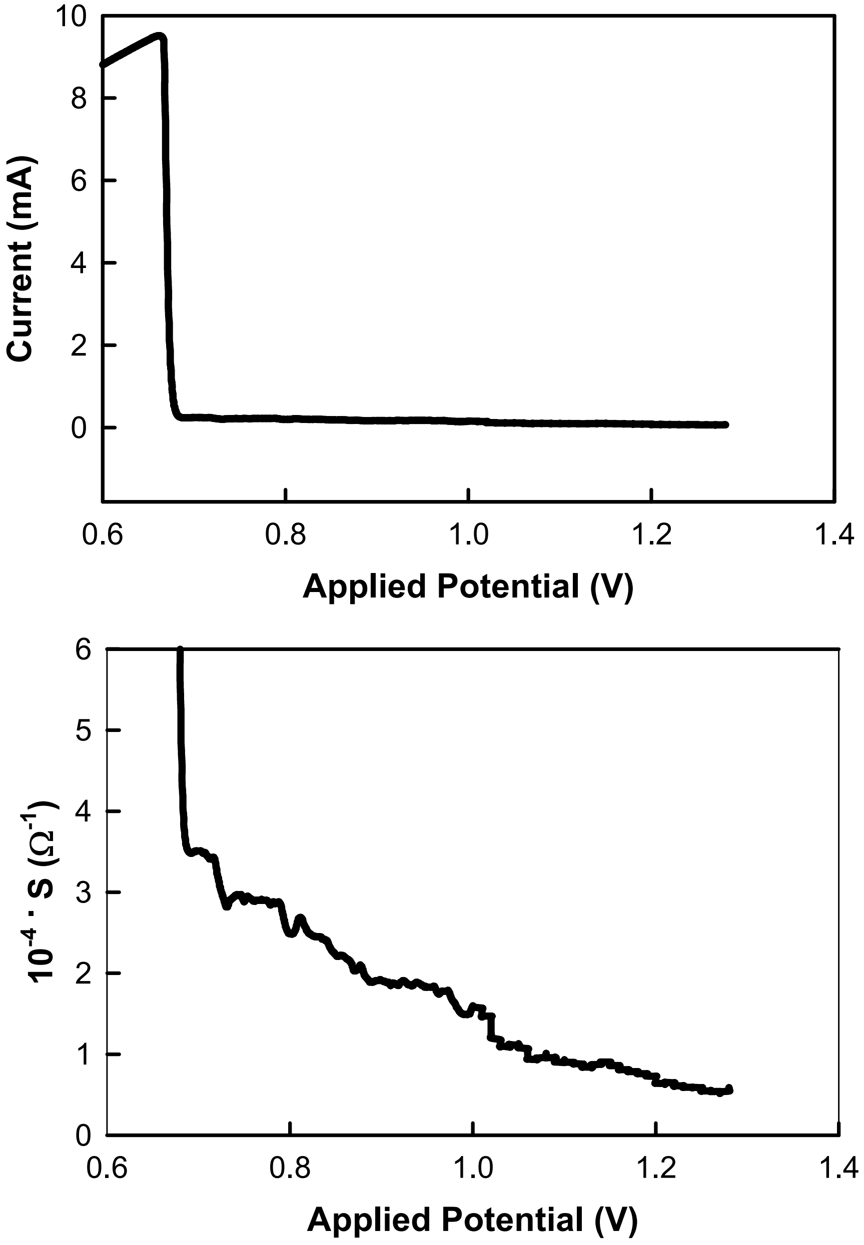
10
8
6
4
2
0
Current (mA)
0.6
0.8
1.0
1.2
1.4
Applied Potential (V)
6
5
4
3
2
1
0
$10^{-4} \cdot S\ (\Omega^{-1})$
0.6
0.8
1.0
1.2
1.4
Applied Potential (V)

Figure 4.7 (a)

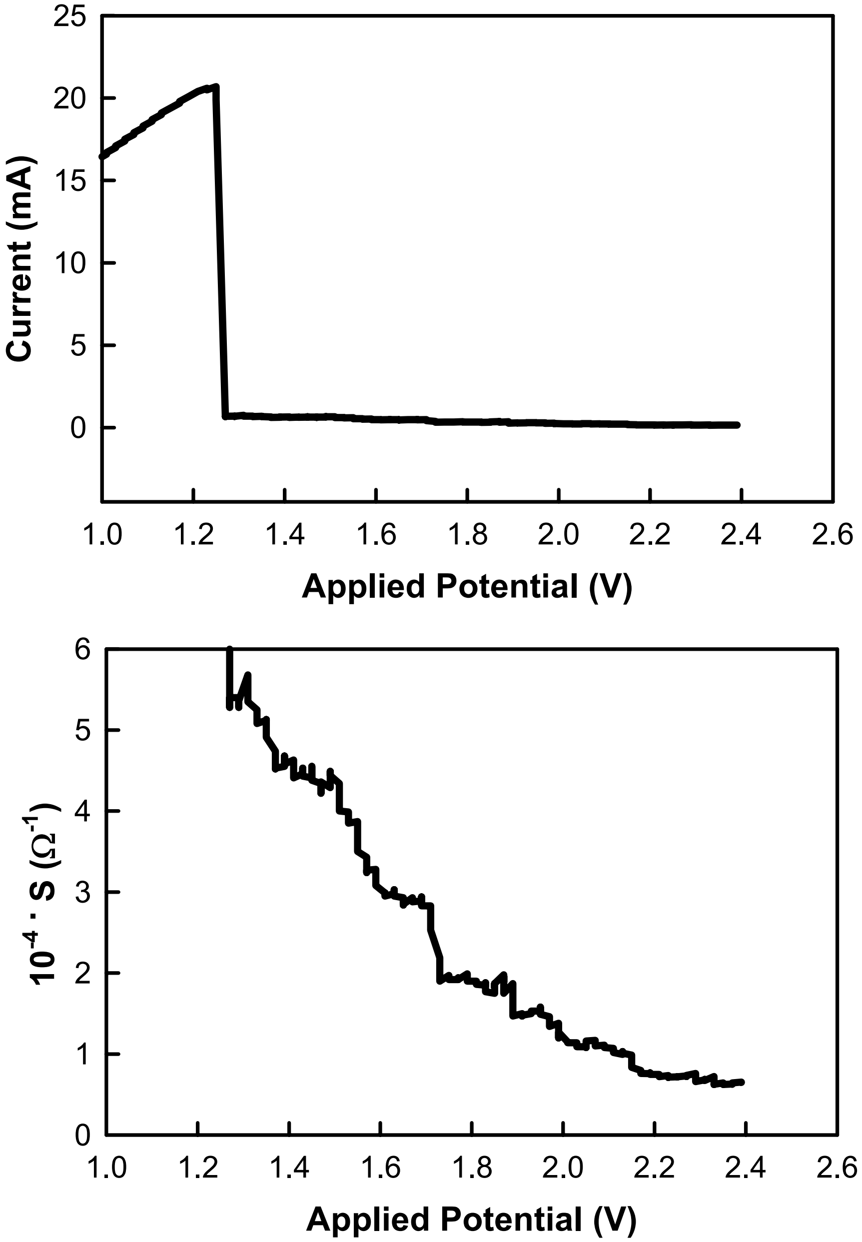
25
20
15
10
5
0
Current (mA)
1.0
1.2
1.4
1.6
1.8
2.0
2.2
2.4
2.6
Applied Potential (V)
6
5
4
3
2
1
0
$10^{-4} \cdot S\ (\Omega^{-1})$
1.0
1.2
1.4
1.6
1.8
2.0
2.2
2.4
2.6
Applied Potential (V)

Figure 4.7 (b)

broken. It should be noted, however, that abrupt reductions in the cross section can give rise to irregular conductance quantization as well as the pinching off of conductance channels during the gradual thinning down of the contact region. At cryogenic temperatures there is no thermal healing of internal defects, hence conductance quantization is less pronounced and more prone to depart from ideality as it was observed here.[45]

Due to imperfect measurement equipment and imperfect electromigration procedures, the yield of samples surviving electromigration was initially quite poor, approximately 10%-20%. After optimizing both the device fabrication and the measurement equipment, approximately 90% of the devices had measurable *J-E* characteristics following an electromigration event. The samples were routinely investigated following electromigration experiments by means of scanning electron microscopy (SEM). The effects of electromigration on the electrodes were clearly visible, but due to the limited resolution of SEM the exact make-up of the gap region could not be studied. A typical example is the SEM image shown at the bottom of Figure 4.10 (c).

Electromigrated nanowires in some cases did not exhibit detectable currents even when biased in the ± 1.0 V range. SEM investigations showed that these devices had gaps larger than 10 nm. In *lieu* of specifically designed control experiments, these junctions served a good purpose in confirming that parasitic conduction pathways were absent for electrodes that were in very close proximity of each other but not within tunneling distance. Junctions that did yield measurable currents displayed *J-E* curves with a variety of shapes, current magnitudes, and temperature dependences. Based on the results reported herein, the following general classification regarding metal/nanogap junctions can be made: (a) devices with no measurable currents, (b) devices with Coulomb blockade features at low temperatures and a pronounced temperature dependence of the low-bias resistance, (c) devices with no apparent indication of Coulomb blockade, but a pronounced temperature dependence of the low-bias resistance, (d) devices with a limited temperature dependence of the *J-E* characteristics.

The *J-E* characteristics of some early devices fabricated on 300 nm thick, thermally grown Si oxide substrates (device **A**) and of devices fabricated on Si nitride membranes (device **B)** were measured in He exchange gas and the results are depicted in Figure 4.8 (a). The weak links of these devices were fabricated by means of the aforementioned shadow evaporation technique and were composed of a 4 nm thick Cr adhesion layer and a 25 nm thick Au top layer (type **I**). At 6 K device **A** showed zero conductivity over a voltage range of approximately ± 60 mV , which was attributed to a Coulomb blockade effect. The region of zero conductivity did indeed vanish as the temperature was increased. The low-bias resistance showed a pronounced temperature dependence as revealed by the *J-E* curves that were recorded at 6 K, 77 K, 200 K, and 295 K. The low-bias resistance at room temperature was 585 kΩ. Using equations Eq. 4.7 and Eq. 4.8, proposed by Abeles[43] to account for the temperature dependence of the low-bias resistance and the electric-field dependence of the low-temperature, high-field differential resistance, respectively, the electron transport properties of these junctions were interpreted in terms of the transport characteristics of granular metal films. The low-bias resistance was determined in a voltage range of ± 0.02 V and the differential resistance (*dE/dJ*) at 6 K was determined for voltages larger than 0.125 V. The results are shown in Figure 4.8 (b) for device **A** and a similar device (**A2)**. The data was well-fit by these equations. The results from the fit are summarized in Table 4.1. Device **B** was fabricated on a 30 nm thick Si-nitride membrane so that the gap region could eventually be imaged with high resolution transmission electron microscopy (TEM). It should be noted that samples on membranes can not directly be compared to junctions fabricated on other substrates, since free standing Si-nitride membranes did not provide enough heat sinking during electromigration and thus the electromigration was more catastrophic than on

Figure 4.8 (a) *J-E* Characteristics of Devices of Type I. (b) Plot of Low-Bias resistance vs. $T^{-1/2}$ and Plot of Differential Resistance vs. E^{-1}. (c) TEM Images After Electromigration.

(a) *J-E curves* of devices fabricated with a weak link consisting of Cr (4 nm) and Au (25 nm) by means of shadow evaporation. Top figure (Device **A**): At 6 K the sample had zero conductivity over a voltage range of ~ ±60 mV. The low-bias resistance had a pronounced temperature dependence: circles, squares, triangles-down, and diamonds denote data recorded at 6 K, 77 K, 200 K, and 295 K, respectively. The low-bias resistance at 295 K was 585 kΩ. Bottom figure (Device **B**): *J-E curves* of a device whose TEM image is shown in Figure 4.8 (c): squares, triangles-down, and diamonds denote data recorded at 77 K, 200 K, and 298 K, respectively. (b) The electron transport characteristics of device **A** were further investigated by plotting the low-bias resistance (determined in a voltage range of ±0.02 V) *vs.* $T^{-1/2}$ and by plotting the differential resistance (*dE/dJ*) at 6 K (for voltages larger than 0.125 V) *vs.* E^{-1} according to Abeles's model.[43] The linear regression fits are shown. Circles correspond to device **A**; squares correspond to device **A2**. (c) TEM images of devices (type **I**) fabricated on Si nitride membranes. The TEM image at the top corresponds to device **B** after electromigration and *J-E* measurements, while the TEM image at the bottom belongs to a device which showed no measurable currents. A continuos, very thin underlayer, which in the case of device **B** bridges the particulate matter in the gap region with the electrodes, is highlighted in both cases for clarity.

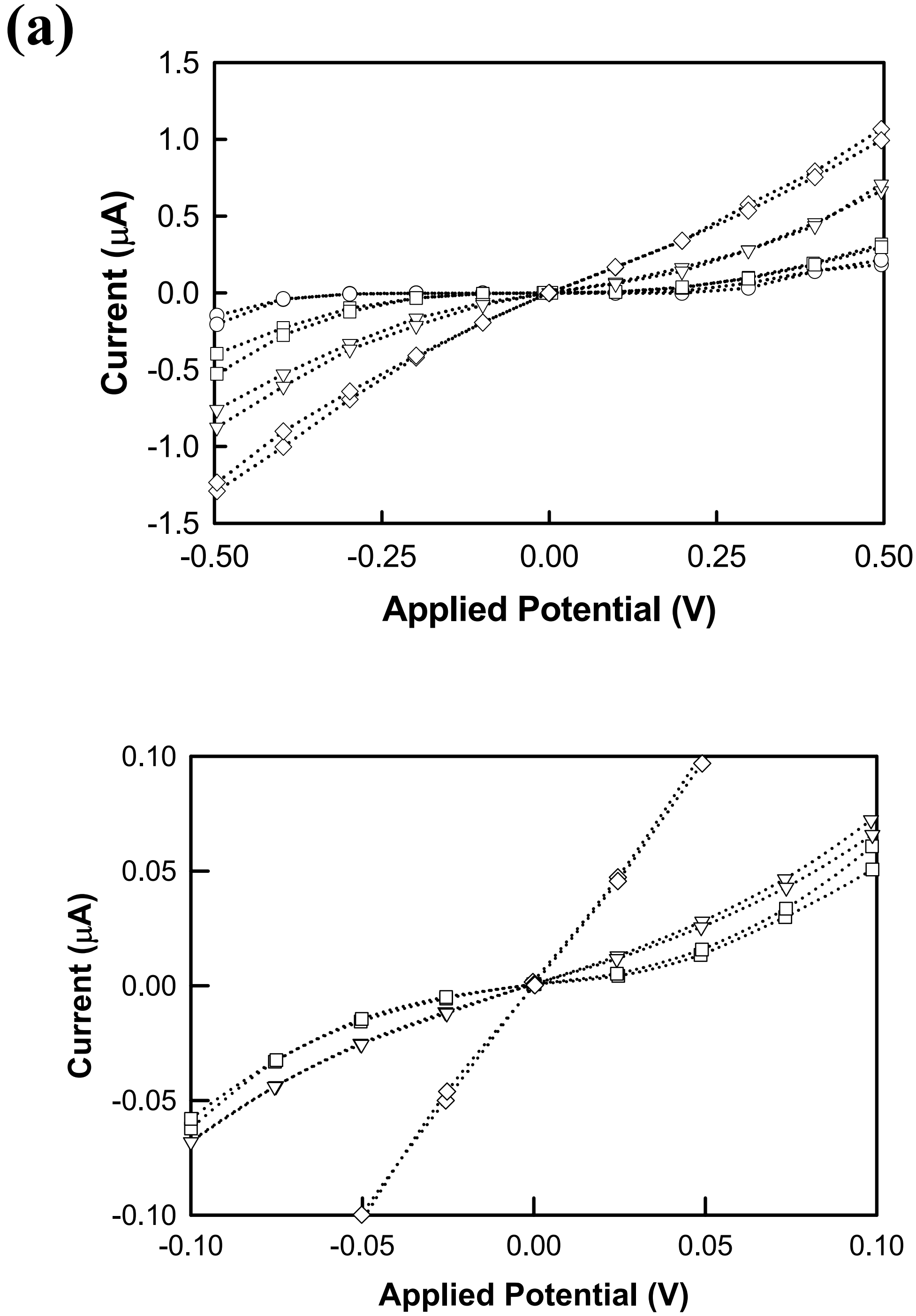
(a)
1.5
1.0
0.5
0.0
-0.5
-1.0
-1.5
Current (μA)
-0.50
-0.25
0.00
0.25
0.50
Applied Potential (V)
0.10
0.05
0.00
-0.05
-0.10
Current (μA)
-0.10
-0.05
0.00
0.05
0.10
Applied Potential (V)

Figure 4.8 (a)

(b)

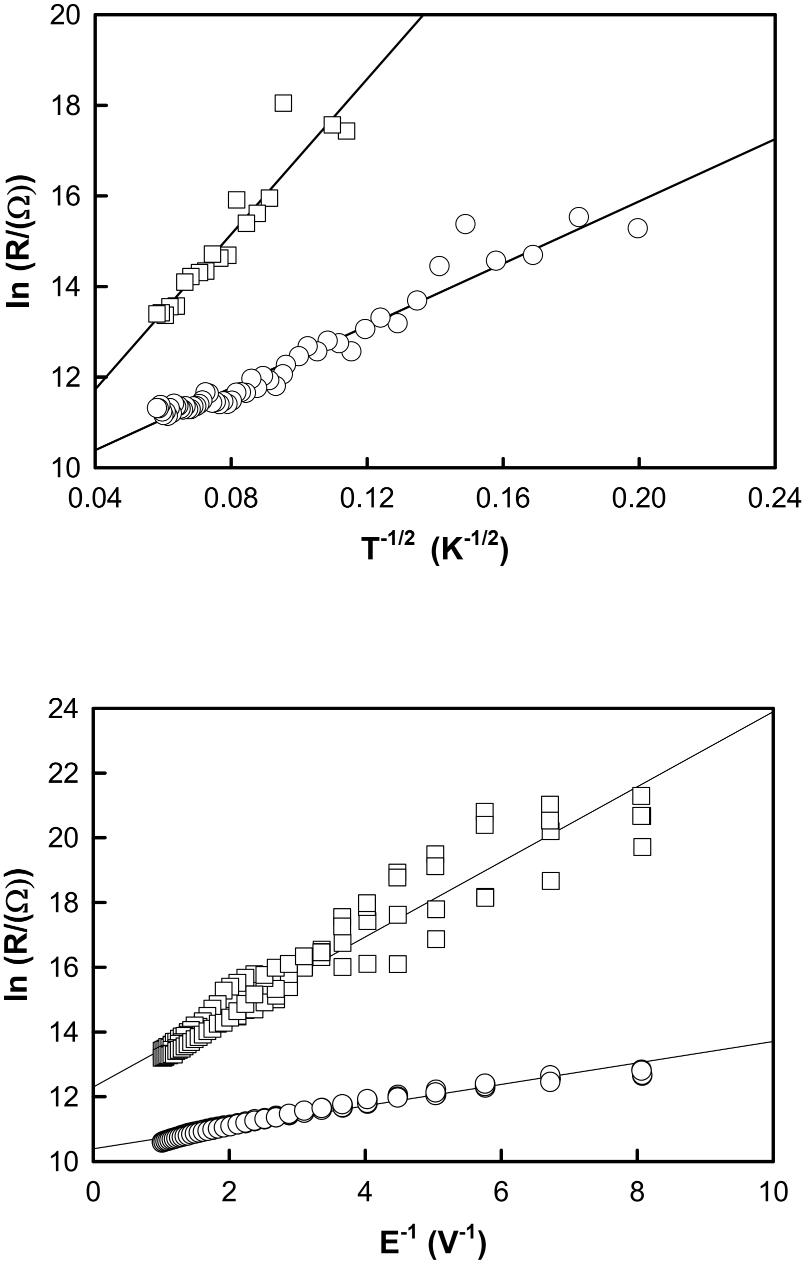
20
18
16
14
12
10
0.04
0.08
0.12
0.16
0.20
0.24
ln (R/(Ω))
T^-1/2 (K^-1/2)
24
22
20
18
16
14
12
10
0
2
4
6
8
10
ln (R/(Ω))
E^-1 (V^-1)

Figure 4.8 (b)

(c)

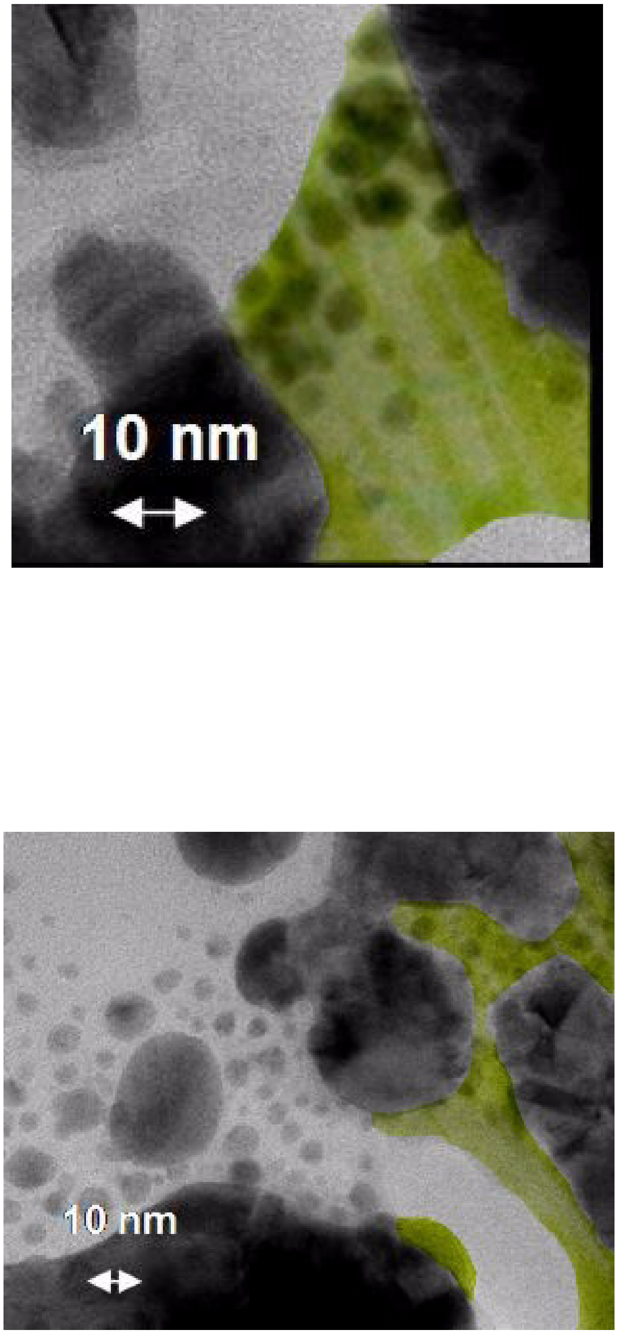

Figure 4.8 (c)

supported oxide substrates. The TEM images of device **B** together with a reference sample are shown in Figure 4.8 (c). The reference sample did not exhibit any measurable tunneling currents, while device **B** behaved both in terms of the magnitude of the measured currents and in terms of the temperature dependence of the low-bias resistance similarly to junctions formed on supported silicon oxide substrates. The more catastrophic nature of electromigration on membranes notwithstanding, the *J-E* characteristics of junctions fabricated on membranes were found to be comparable with those obtained for junctions fabricated on supported substrates, and thus the information provided by TEM images was very valuable. First, the high tunneling currents that were measured cannot be explained by a tunneling distance of 2 nm (smallest distance between the particulate matter) and the small cross sections that can be inferred from the TEM images, see Figure 4.8 (c). It is important to note that device **B** exhibited a thin underlayer connecting all debris to the electrodes. This underlayer has been highlighted in Figure 4.8 (c) for clarity. This underlayer does not connect the electrodes in the reference sample, which did not exhibit any measurable currents, although the small particulate matter has dimensions and distances similarly to device **B**, which showed large currents.

Eventually it was learned that when using a Cr adhesion layer it might be important to keep the thickness of the Cr smaller than 1 nm.[44] At this thickness the Cr layer is considered not to be continuous, but rather to consist of small islands. It is thought that the size and spacing of these islands help define the resulting gap size and shape, as the islands will give the Au atoms definite locations to stick to. The *J-E* characteristics of representative devices are shown in Figure 4.9 (a). Device **C** had a finite low-bias resistance at 4.2 K of 161 kΩ. The *J-E* curves, however, changed continuously with temperature. No abrupt changes in the *J-E* characteristics, indicative of structural re-arrangements were found. The low-bias resistance at room temperature was 42.3 kΩ.

Figure 4.9 ***J-E*** **Characteristics of a Device of Type II as a Function of Temperature** (a) 3-dimensional representations of the *J-E* curves as a function of temperature (4 -300 K) of devices fabricated with a weak link consisting of Cr (<1 nm) and Au (25 nm thick) by means of the improved fabrication scheme (see Chapter 4.3 for details). The *J-E* curves changed continuously with temperature (top figure: device **C**). The device was further electromigrated at 4.2 K (bottom figure: device **D**). (b) The electron transport characteristics were further investigated by plotting the low-bias resistance (determined in a voltage range of ±0.02 V) *vs.* $T^{-1/2}$ and by plotting the high-field differential resistance (*dE/dJ*) at 9K for voltages larger than 0.125 V *vs.* E^{-1} according to Abeles's model.[43] The linear regression fits are shown. Circles denote device **C**; squares denote device **D**.

(a)

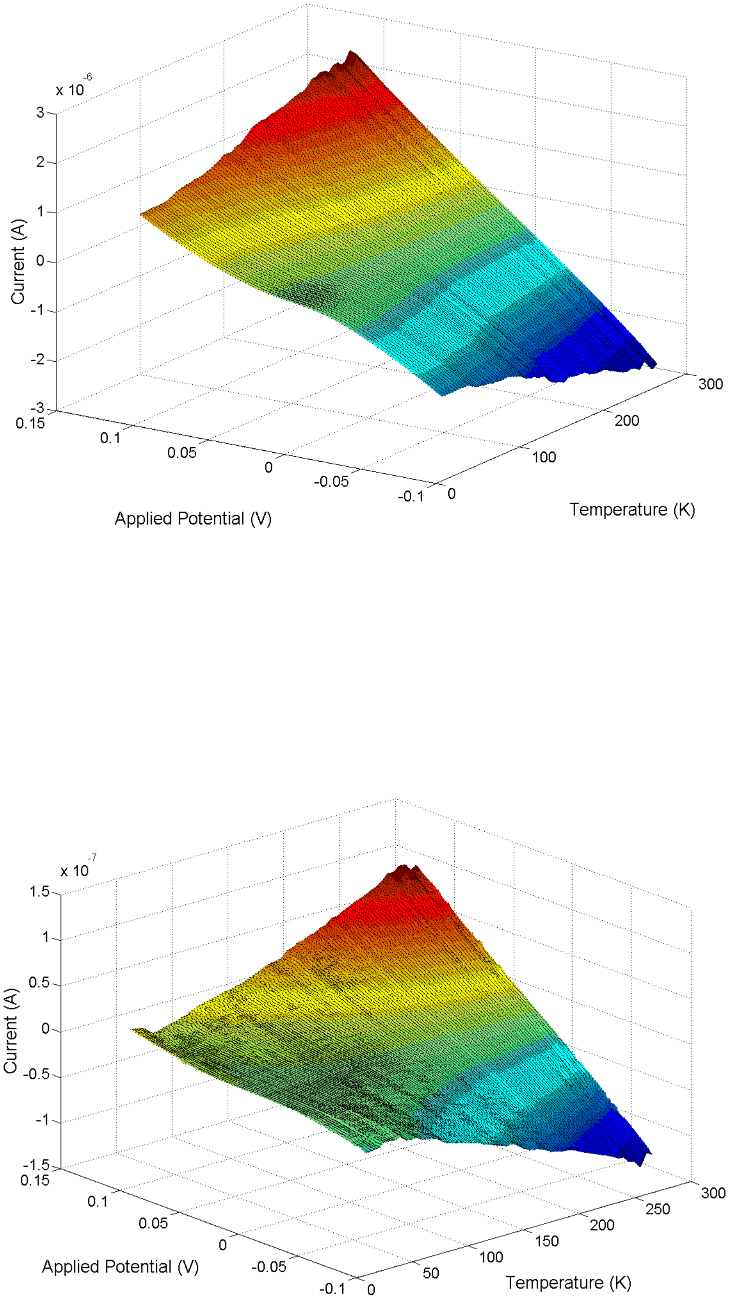
x 10^-6
3
2
1
0
-1
-2
-3
Current (A)
0.15
0.1
0.05
0
-0.05
-0.1
Applied Potential (V)
0
100
200
300
Temperature (K)
x 10^-7
1.5
1
0.5
0
-0.5
-1
-1.5
Current (A)
0.15
0.1
0.05
0
-0.05
-0.1
Applied Potential (V)
0
50
100
150
200
250
300
Temperature (K)

Figure 4.9 (a)

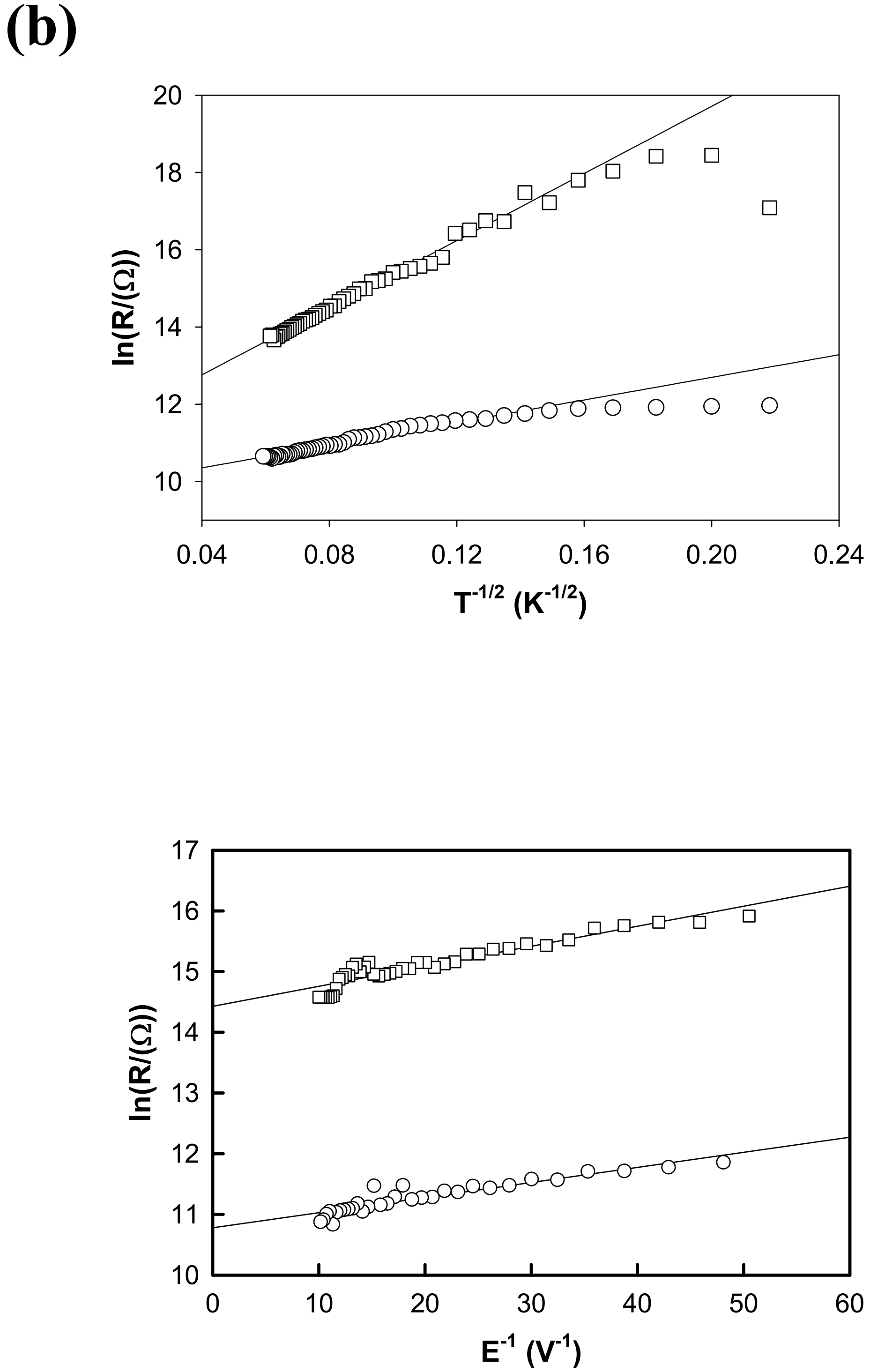
(b)
20
18
16
14
12
10
ln(R/(Ω))
0.04
0.08
0.12
0.16
0.20
0.24
T^-1/2 (K^-1/2)
17
16
15
14
13
12
11
10
ln(R/(Ω))
0
10
20
30
40
50
60
E^-1 (V^-1)

Figure 4.9 (b)

The electron transport characteristics were further investigated by plotting the low-bias resistance (determined in a voltage range of ±0.02 V) *vs.* $T^{-1/2}$ according to Eq. 4.7, and by plotting the differential resistance at 4.2 K (determined for voltages > 0.02 V) *vs.* $E^{-1/2}$ according to Eq. 4.8, see Figure 4.9 (b). At temperatures smaller than 20 K,[46] the low-bias resistance deviated from the linear trend somewhat. It should be noted, that the temperatures in that particular phase of the experiments were increased very slowly and approximately 10 minutes at each temperature were allocated for the system to reach some kind of steady state. After the temperature-dependent *J-E* measurements were carried out, device **C** was again cooled down to 4.2 K and subjected to more electromigration resulting in device **D**. The threshold potential for which a significantly larger resistance was measured was approximately 2 V. The low-bias resistance of this junction was 19.7 MΩ. The *J-E* curves showed a pronounced temperature dependence and the currents increased smoothly with increasing temperatures. At 265 K the low-bias resistance was 954 kΩ, which corresponds to a decrease in the low-bias resistance by more than 2 orders of magnitude compared to the value at 4.2 K. The temperature dependence of he low-bias resistance as well as the field dependence of the low-temperature, high-field differential resistance was equally well described by Eq. 4.7 and Eq. 4.8, respectively. The results of the linear regression fits are summarized in Table 4.1.

Attempts were made to fabricate Au/nanogap junctions without the use of a Cr adhesion layer in the weak link bridging the electrodes. All junctions investigated yielded significantly lower currents than junctions using 1-4 nm thick Cr adhesion layers. The junction currents were typically on the order of 1 nA or lower at 0.4 V bias. However, the temperature dependence could not be studied in terms of Abeles' model, since the Au/nanogap junctions exhibited *J-E* curves which showed very abrupt and irregular changes as the temperature was increased and sometimes even changed at a constant temperature setting as the applied potential was slowly increased in the course of *J-E* measurements. .

.

This behavior prompted the investigation of Pt as the metal that forms the weak link. No adhesion layer was used in these experiments as well. The electromigration and temperature dependence data for such a junction (device **E**) are shown in Figure 4.10 (a). A broad region of zero conductance from -0.15 to 0.1 V was found at 4.2 K. Coulomb blockade effects disappeared as the temperature was increased. The voltage range of zero conductance was effectively modulated by means of a gate potential applied to the back gate. Though there was little capacitive coupling between the gate and the device (the gate oxide of the back gate was 300 nm thick) significant gate bias dependence was observed, see Figure 4.10 (a). At 10 V gate bias the region of zero conductance ranged from 0-0.05 V. The SEM image corroborated the existence of the Coulomb blockade effect and showed a 10×100 nm large Pt island in the mid-gap region, see Figure 4.10 (b). The SEM image of a device of type **I** with finite resistances near 0 V and an Abeles-like temperature and field dependence is shown for comparison. Device **E** exhibited rather irregular an abrupt changes in its *J-E* characteristics as the temperature was increased, quite contrary to devices with a Cr adhesion layer and Au top layer, which typically showed a smooth and continuos increase in the junction current with temperature. The overall magnitude of the current in device **E** did not change dramatically as the temperature was increased. The low-bias resistance decreased with temperature, but reflected the irregular temperature dependence of the *J-E* characteristics and was not well fit by Abeles' model.

Other devices of type **IV** showed a variety of *J-E* characteristics. The two extreme cases that were observed regarding the *J-E* behavior for this type of junctions are shown in Figure 4.11 (a). Device **F** showed limited temperature dependence of the current at the vertices of the applied potential, however the low-bias resistance changed with increasing temperature from 147 kΩ (4.2 K) to 34 kΩ (298 K). However, it was unclear from the fits

Figure 4.10 (a) ***J-E*** **Characteristics of a Device of Type IV as a Function of Temperature and Gate Bias. (b) SEM Images of Electromigrated Devices.**
The weak link of device **E** consisted of 15 nm thick Pt (no adhesion layer). A broad region of zero conductance (-0.15 to 0.1 V) was found at 4.2 K that vanished with increasing temperatures. The voltage range of the region of zero conductance was modulated by means of a gate potential (circles 0 V, squares 10 V gate potential). The differential conductance is shown (dotted line 0 V, solid lines 10 V). The gate oxide of the back gate was 300 nm thick. See text for details. (b) The SEM image at the top (device **E**) corroborates these findings and shows a 10×100 nm large Pt island in the mid-gap region. The SEM image of a device with finite resistances near 0 V is shown for comparison (bottom).

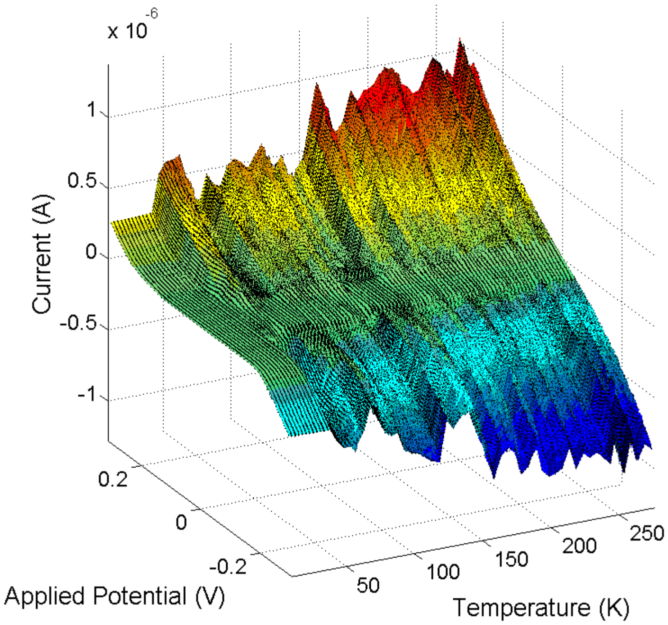
x 10^-6
1
0.5
0
-0.5
-1
Current (A)
0.2
0
-0.2
Applied Potential (V)
50
100
150
200
250
Temperature (K)

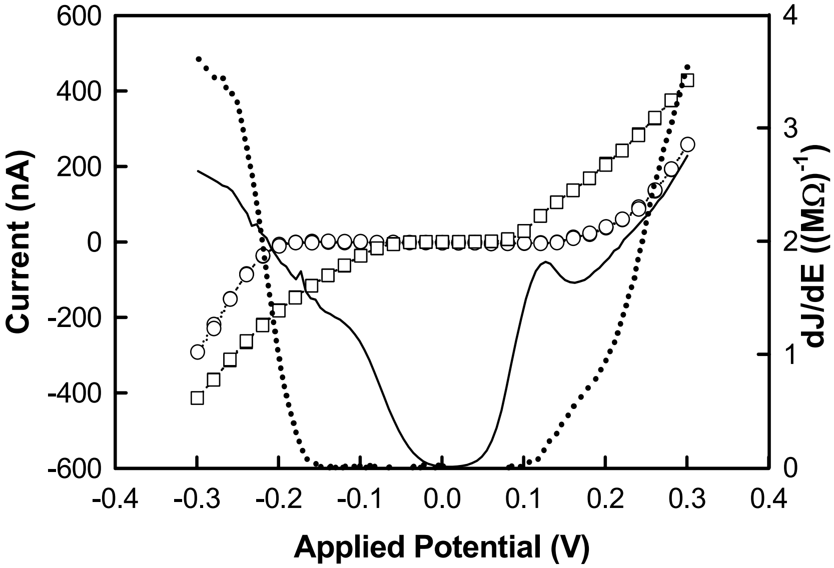
600
400
200
0
-200
-400
-600
Current (nA)
4
3
2
1
0
dJ/dE ((MΩ)^-1)
-0.4
-0.3
-0.2
-0.1
0.0
0.1
0.2
0.3
0.4
Applied Potential (V)

Figure 4.10 (a)

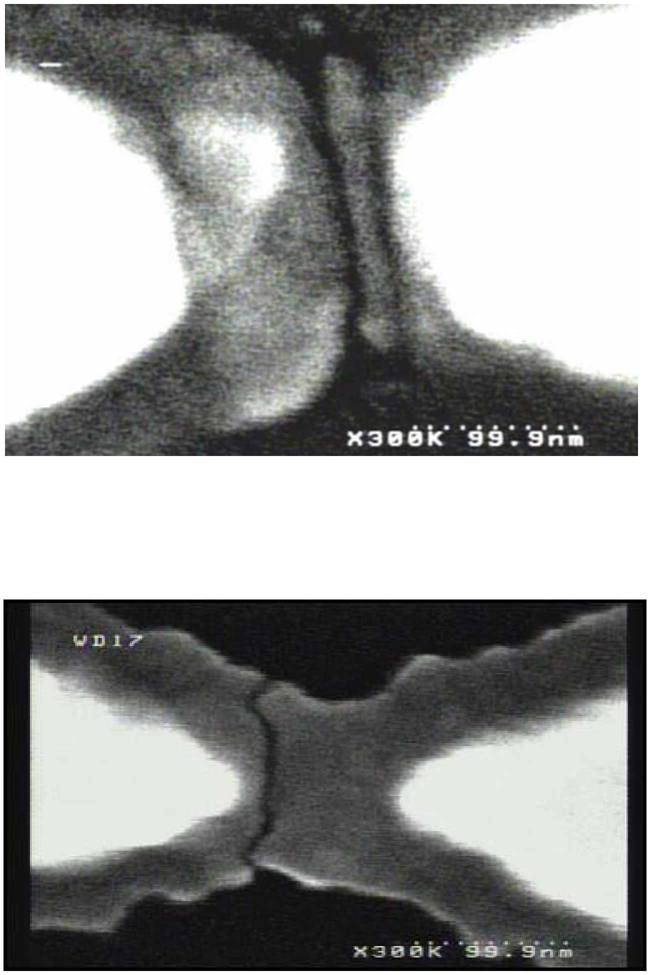

Figure 4.10 (b)

Figure 4.11 (a) *J-E* Characteristics of a Device of Type IV as a Function of Temperature. (b) Low-Bias Resistance *vs.* $T^{-1/2}$ and Plot of the Differential Resistance vs. E^{-1}.

(a) The *J-E* characteristics of 2 devices, device **F** (top) and device **G** (bottom) with a weak link consisting of 15 nm of Pt (no adhesion layer) are shown as a function of temperature. A finite resistance near 0 V was found for both devices. (b) The electron transport characteristics were further investigated by plotting the low-bias resistance (determined in a voltage range of ±0.02 V) over $T^{-1/2}$ and the differential resistance (*dE/dJ*) at 4.2 K for voltages larger than 0.10 V over E^{-1} according to Abeles's model.[43] The linear regression fits are shown. Circles correspond to device **F** and squares correspond to device **G**.

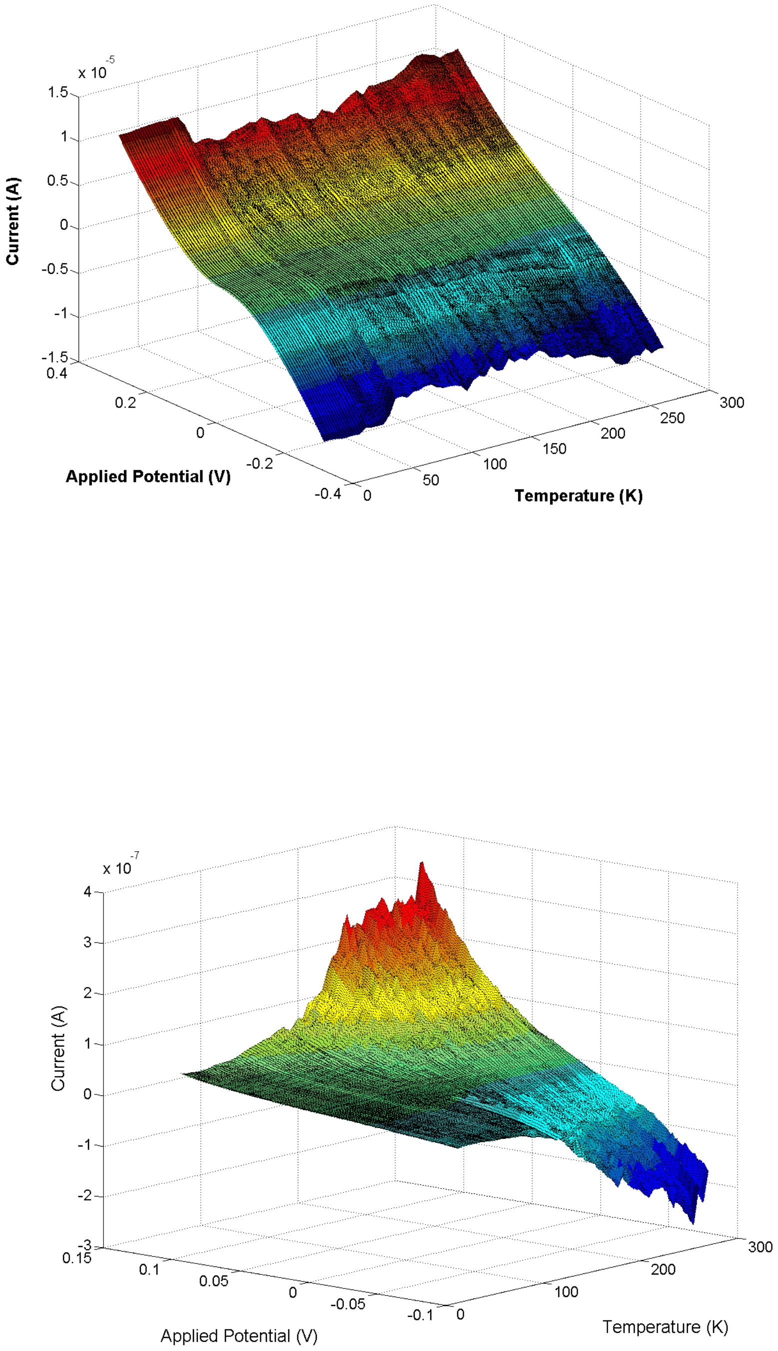
x 10^-5
1.5
1
0.5
0
-0.5
-1
-1.5
Current (A)
0.4
0.2
0
-0.2
-0.4
Applied Potential (V)
0
50
100
150
200
250
300
Temperature (K)
x 10^-7
4
3
2
1
0
-1
-2
-3
Current (A)
0.15
0.1
0.05
0
-0.05
-0.1
Applied Potential (V)
0
100
200
300
Temperature (K)

Figure 4.11 (a)

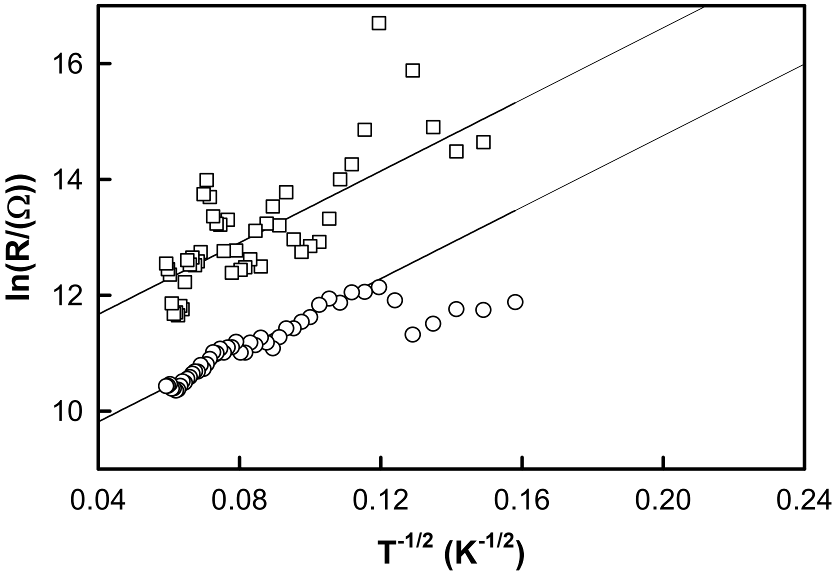
16
14
12
10
ln(R/(Ω))
0.04
0.08
0.12
0.16
0.20
0.24
T^-1/2 (K^-1/2)

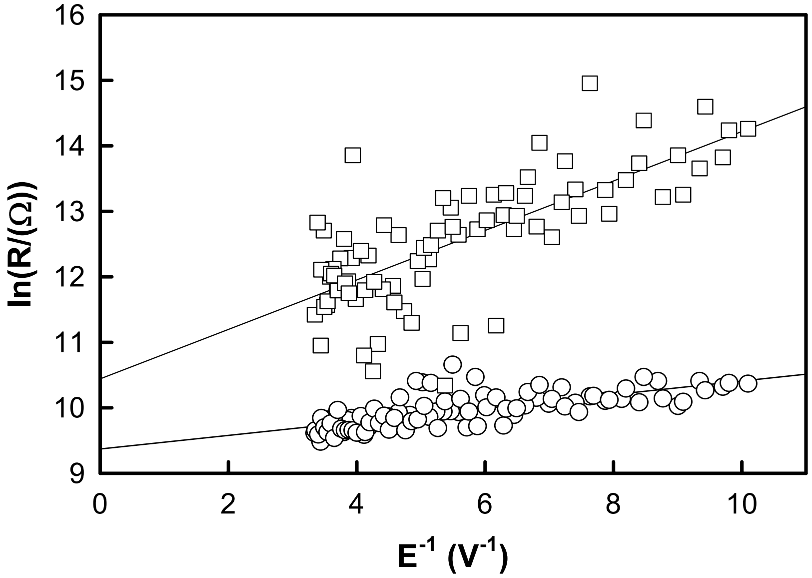
16
15
14
13
12
11
10
9
ln(R/(Ω))
0
2
4
6
8
10
E^-1 (V^-1)

Figure 4.11 (b)

for the temperature dependence of the low-bias resistance and the electric-field dependence of the high-field differential resistance at 4.2 K whether the *J-E* characteristics can be explained with Abeles' model, see Table 4.1 and Figure 4.11 (b). Device **G** showed a more pronounced and smooth increase of the junction current with increasing temperature at all potentials. The low-bias resistance decreased from 16.4 MΩ to 280 kΩ . The fits obtained with Abeles' model are shown in Figure 4.11 (b) and are summarized in Table 4.1

Finally, a model system for electron tunneling was fabricated, which had a geometry similar to the devices used in electromigration experiments. The electron-tunnel junction consisted of 2 Al electrodes separated by a tunneling barrier of Al oxide which is approximately 2 nm thick.[47] The AFM image shown in Figure 4.12 indicated that the cross section for electron tunneling is approximately 200×200 nm^2. As expected from theory and from reports in the literature,[37, 40-42] the temperature dependence of the electron-tunneling current was negligible, see Figure 4.12. The low-temperature resistance at 4.2 K and 250 K were 1.82 MΩ and 2.00 MΩ, respectively. .

4.5 DISCUSSION

This investigation represents the first attempt to understand the electron-tunneling characteristics of metal/nanogap junctions fabricated by a combination of electron-beam lithography and electromigration in the absence of molecules bridging the gap. The investigations were carried out in high vacuum as a function of temperature (4.2 K to room temperature) and the results of the current *vs.* voltage measurements were correlated with TEM studies.

Despite the recent popularity of such devices in the electron transport studies of single molecules, it was found that metal/nanogap junctions without molecules displayed Coulomb staircase features (similar to those reported for electrodes bridged by

Figure 4.12 Electron Tunneling Current *vs. E* and AFM Image of a Al/Al-oxide/Al junction.

The *J-E* characteristics of Al/Al-oxide/Al tunnel junctions (device **H**) with geometries similar to those of the electromigration devices show no apparent temperature dependence (4.2-250 K). The Al oxide thickness is approximately 2 nm and the tunneling cross section is 200×200 nm^2. The details of the device fabrication are given in Chapter 4.3.

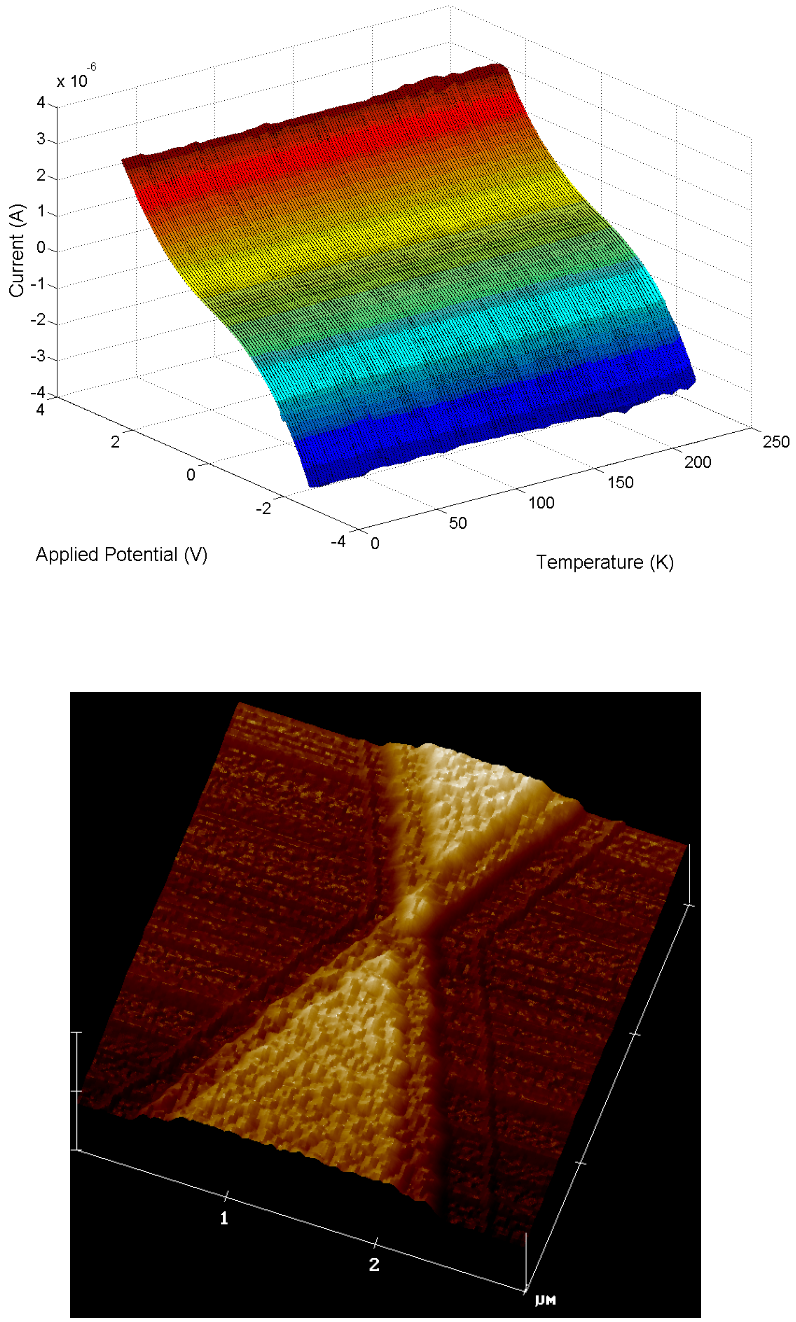
x 10^-6
4
3
2
1
0
-1
-2
-3
-4
Current (A)
4
2
0
-2
-4
Applied Potential (V)
0
50
100
150
200
250
Temperature (K)
1
2
μm

Figure 4.12

TABLE 4.1. Temperature dependence of the low-bias resistance and electric-field dependence of the low-temperature differential resistance.

Device	**R_{LB}(kΩ) at 4.2 K**	**R_{LB}(kΩ) at RT**	**Temperature dependence Abeles' model** **σ_0^{-1} (kΩ), C'($K^{1/2}$), r^2(-)***	**Field dependence Abeles' model** **σ_{inf}^{-1} (kΩ), C"(V^{-1}), r^2(-)***
A	infinite	585	8.2, 34.34, 0.94	327, 0.33, 0.98
A2	infinite	656	4.2, 85.65, 0.91	220, 1.16, 0.93
C	161	42.3	17.5, 14.63,0.98	47.1,0.03,0.89
D	19700	954**	635, 42.96, 0.99	1849,0.03,0.90
F	147	34	5.3, 30.90 0.94	11.8, 0.1, 0.51
G	16400	280	33.9, 30.95, 0.45	26.1, 0.42, 0.53
H	1820	2005***	-	-

* compare with Eq. 4.7 and Eq. 4.8; r^2 denotes regression factor of linear fits

** data was recorded at 265 K

*** data was recorded at 250 K

molecules),[10-12] as well as a pronounced temperature dependence, which makes an understanding of electron tunneling very complicated. The possibility of pure electron tunneling in such devices has so far not been unambiguously demonstrated. Because of the inherently catastrophic nature of electromigration, it is likely that a significant fraction of gaps will be formed containing metallic debris of varying size and thus exhibiting corresponding Coulomb blockade features.

In this study, the *J-E* characteristics as well as the differential conductance versus voltage (*dJ/dE vs. E*) characteristics of a wide variety of chemically unmodified metal electrodes (Cr/Au, Au, Pt) were extensively investigated as a function of temperature and gate bias. The thickness of the Cr adhesion layer was systematically varied. During electromigration, right before the transition from ohmic conduction to tunneling occurs, the conductance exhibited very often quantized steps, which were on the order of the conductance quantum. This might indicate that single metal atoms were moved apart as these gaps formed. The irregularities of the conductance quantization, however, suggests that abrupt changes in the cross section of the nanowire were responsible for the conductance quantization.[45]

Pure electron-tunneling currents should display a distinctive shape of the *J-E* curves. The *J-E* behavior is supposed to be ohmic in the low-bias regime and is supposed to gradually change to displaying a current that is exponentially dependent on the applied potential, see Figure 4.2. However, at the potentials that were applied to the devices in this study, the tunneling equation predicts either low currents and exponential behavior at the extremes (large gaps) or high currents and ohmic behavior over the entire range of potentials (small gaps) using standard values for metal work functions as the barrier height. Many of our devices exhibited both high currents and exponential behavior at the extremes of the biases. Unfortunately, without accurate knowledge of the cross-sectional area of the tunneling gap and the gap distance, it is not possible to conclusively extract useful information (for instance the actual barrier height) from fits of any know electron tunneling equation to our data. The tunneling gap distances and tunneling cross sections obtained from TEM studies did not allow us to compute tunneling currents with standard analytical equations for electron tunneling found in the literature.

In the absence of this vital information the variation of the low-bias resistance with temperature and the behavior of the high-field, low-temperature resistance with applied bias was examined. From the low-field tunneling equation (see Eq. 4.2 and Eq. 4.4) it is apparent that there should be no significant temperature dependence to the low-bias electrical behavior of direct electron-tunneling gaps. This fact has been confirmed by numerous reports in the literature[37, 40-42] and by the results of this investigation regarding the lack of temperature dependence found for electron-tunneling in Al/Al-oxide/Al junctions. The Fowler-Nordheim description of field emission current also lacks significant temperature dependence. An increase in thermal energy may slightly increase tunneling probabilities, but should not have a drastic effect on a stable and clean tunneling gaps. Physical changes in the electrode geometry are likely to occur with electromigration devices where the metal is not adequately attached to the substrate, such as in the case of devices with only Au or Pt in the thin metal section. Thus the strong temperature dependence exhibited by the Au/nanogap junctions without a Cr adhesion layer and to a certain extent by Pt/nanogap junctions is characterized by abrupt and sudden changes in the *J-E* curves as the temperature is raised. This behavior is easily explained by physical movement of the gap edges.

This is in stark contrast to the temperature dependence of the *J-E* characteristics displayed by Cr/Au/nanogap junctions. The *J vs. E* curves showed no abrupt and sudden changes as the temperature was increased. Some *J vs. E* curves showed regions of zero conductivity at low bias. Such features were absent in the data collected for other tunneling junctions. These differences notwithstanding, a common pattern was discerned in that the low-bias resistances of all junctions (with measurable currents) decreased by an order of magnitude or more with increasing temperature. The temperature dependence of currents flowing through discontinuous granular metal films has been well characterized by the work of Abeles and coworkers.[43] Plots of the natural logarithm of the low-bias resistance *vs.* the inverse root temperature demonstrate that Cr/Au/nanogap junctions irrespective of the thickness of the adhesion layer did indeed follow the predicted temperature dependence. The fact that these devices did exhibit the temperature dependence described for granular metal films instead of the lack of temperature dependence characteristic of pure tunneling currents implies that small metal islands did indeed exist between the electrodes. It should be noted that the temperature dependence of the low-bias resistance also exhibits a reasonable linear variation with other models like the $T^{-1/4}$ variation that is found for Mott-thermionic emission.[40] However, the variations of the tunneling resistance with temperature and the behavior of the high-field resistance with bias observed for our junctions are only predicted by Abeles' equations. In the high-bias ($V >> k_B T/q$, at 4.2 K this corresponds to $V >> 0.3$ mV), low temperature regime this model predicts the differential resistance to depend exponentially on the applied electric field. The results regarding the temperature and electric field dependence obtained for Cr/Au devices, follows Abeles model very well, supporting the conclusion that our devices are exhibiting tunneling through gaps containing small metal islands. It should, however, be noted that Abeles model was created for granular metal films with cross section of at least 10×10 nm^2. Since scanning electron microscopy currently does not have the resolution to image these tunneling gaps no microscopic evidence or lack thereof can currently be provided. The TEM images obtained for Cr/Au pointed to the presence of a thin underlying film that bridges the electrodes. Further investigations are clearly necessary to correlate TEM images with the temperature dependence of the *J-E* behavior.

Not a single metal/nanogap junction among approximately 100 electromigrated nanowires was found that displayed a lack of temperature dependence.

4.6 CONCLUSIONS

Electromigration induced breaking of metal nanowires is a promising new method that has been recently employed to form metal-molecule-metal tunnel junctions.[10-12, 33] Investigations thus far have focused on measurements of the electrical characteristics of nanometer spaced electrodes that contain molecules in the gaps.[10-12] The electrical characteristics of unmodified electrodes have not been thoroughly studied. In this work, we have explored in detail the current versus voltage (*J vs. E*) characteristics of unmodified tunnel junctions formed through electromigration of metal nanowires.

Junctions that did yield measurable currents displayed *J vs. E* curves with a variety of shapes and magnitudes. The low temperature *J vs. E* curves of Cr/Au junctions showed regions of zero conductivity at low bias. Such features were absent in the data collected for other Cr/Au tunnel junctions. These differences notwithstanding, a common pattern was discerned in that the low-bias resistances of all junctions (with measurable currents) decreased by an order of magnitude or more with increasing temperature. The features detected in our data are completely consistent with the Coulomb blockade effect. Patterns characteristic of Coulomb blockade were also detected in *J-E* curves measured as a function of gate bias at low temperatures. We attribute the blockade behavior to metal atom clusters and islands located in the gap region. This assignment is compatible with the mechanism of electromigration. In support of our interpretation, we found that the low-bias resistance *vs.* temperature curves were well described by Abeles' model for electron tunneling in granular metal junctions. Additional support for the assignment was obtained from TEM studies of gold junctions with chromium adhesion layers, where the images showed the presence of a thin underlying film that bridges the electrodes.

4.7 REFERENCES

1 Goldhaber-Gordon, D.; Shtrikman, H.; Mahalu, D.; Abusch-Magder, D.; Meirav, U.; Kastner, M. A., Kondo Effect in a Single-Electron Transistor. *Nature* **1998,** 391, (6663), 156.

2 Kastner, M. A., The Single-Electron Transistor. *Rev. Mod. Phys.* **1992,** 64, (3), 849.

3 Klein, D. L.; Roth, R.; Lim, A. K. L.; Alivisatos, A. P.; McEuen, P. L., A Single-Electron Transistor Made from a Cadmium Selenide Nanocrystal. *Nature* **1997,** 389, (6652), 699.

4 Postma, H. W. C.; Teepen, T.; Yao, Z.; Grifoni, M.; Dekker, C., Carbon Nanotube Single-Electron Transistors at Room Temperature. *Science* **2001,** 293, (5527), 76.

5 Mann, B.; Kuhn, H., Tunneling through Fatty Acid Salt Monolayers. *J. Appl. Phys.* **1971,** 42, (11), 4398.

6 Tans, S. J.; Devoret, M. H.; Dai, H. J.; Thess, A.; Smalley, R. E.; Geerligs, L. J.; Dekker, C., Individual Single-Wall Carbon Nanotubes as Quantum Wires. *Nature* **1997,** 386, (6624), 474.

7 Reed, M. A.; Zhou, C.; Muller, C. J.; Burgin, T. P.; Tour, J. M., Conductance of a Molecular Junction. *Science* **1997,** 278, (5336), 252.

8 Collier, C. P.; Wong, E. W.; Belohradsky, M.; Raymo, F. M.; Stoddart, J. F.; Kuekes, P. J.; Williams, R. S.; Heath, J. R., Electronically Configurable Molecular-Based Logic Gates. *Science* **1999,** 285, (5426), 391.

9 Collier, C. P.; Mattersteig, G.; Wong, E. W.; Luo, Y.; Beverly, K.; Sampaio, J.; Raymo, F. M.; Stoddart, J. F.; Heath, J. R., A 2 Catenane-Based Solid State Electronically Reconfigurable Switch. *Science* **2000,** 289, (5482), 1172.

10 Park, J.; Pasupathy, A. N.; Goldsmith, J. I.; Chang, C.; Yaish, Y.; Petta, J. R.; Rinkoski, M.; Sethna, J. P.; Abruna, H. D.; McEuen, P. L.; Ralph, D. C., Coulomb Blockade and the Kondo Effect in Single-atom Transistors. *Nature* **2002,** 417, (6890), 722.

11 Park, J. W.; Pasupathy, A. N.; Goldsmith, J. I.; Soldatov, A. V.; Chang, C.; Yaish, Y.; Sethna, J. P.; Abruna, H. D.; Ralph, D. C.; McEuen, P. L., Wiring Up Single Molecules. *Thin Solid Films* **2003,** 438, 457.

12 Liang, W. J.; Shores, M. P.; Bockrath, M.; Long, J. R.; Park, H., Kondo Resonance in a Single-Molecule Transistor. *Nature* **2002,** 417, (6890), 725.

13 Service, R. F., Molecules Get Wired. *Science* **2001,** 294, (5551), 2442.

14 Service, R. F., Molecular Electronics - Next-Generation Technology Hits an Early Midlife Crisis. *Science* **2003,** 302, (5645), 556.

15 Yaliraki, S. N.; Ratner, M. A., Molecule-Interface Coupling Effects on Electronic Transport in Molecular Wires. *J. Chem. Phys.* **1998,** 109, (12), 5036.

16 Yaliraki, S. N.; Kemp, M.; Ratner, M. A., Conductance of Molecular Wires: Influence of Molecule-Electrode Binding. *J. Am. Chem. Soc.* **1999,** 121, (14), 3428.

17 Yaliraki, S. N.; Roitberg, A. E.; Gonzalez, C.; Mujica, V.; Ratner, M. A., The Injecting Energy at Molecule/Metal Interfaces: Implications for Conductance of Molecular Junctions from an Ab Initio Molecular Description. *J. Chem. Phys.* **1999,** 111, (15), 6997.

18 Nitzan, A.; Ratner, M. A., Electron Transport in Molecular Wire Junctions. *Science* **2003,** 300, (5624), 1384.

19 Seminario, J. M.; Zacarias, A. G.; Tour, J. M., Molecular Alligator Clips for Single Molecule Electronics. Studies of Group 16 and Isonitriles Interfaced with Au Contacts. *J. Am. Chem. Soc.* **1999,** 121, (2), 411.

20 Lang, N. D.; Avouris, P., Electrical Conductance of Individual Molecules. *Phys. Rev. B* **2001,** 6412, (12), art. no.

21 Di Ventra, M.; Lang, N. D., Transport in Nanoscale Conductors from First Principles. *Phys. Rev. B* **2002,** 6504, (4), art. no.

22 Di Ventra, M.; Lang, N. D.; Pantelides, S. T., Electronic Transport in Single Molecules. *Chem. Phys.* **2002,** 281, (2-3), 189.

23 Di Ventra, M.; Pantelides, S. T.; Lang, N. D., First-Principles Calculation of Transport Properties of a Molecular Device. *Phys. Rev. Lett.* **2000,** 84, (5), 979.

24 Gray, H. B.; Winkler, J. R., Electron Transfer in Proteins. *Annu. Rev. Biochem.* **1996,** 65, 537.

25 Fleming, G. R.; Martin, J. L.; Breton, J., Rates of Primary Electron-Transfer in Photosynthetic Reaction Centers and Their Mechanistic Implications. *Nature* **1988,** 333, (6169), 190.

26 Xu, B. Q.; Tao, N. J. J., Measurement of Single-Molecule Resistance by Repeated Formation of Molecular Junctions. *Science* **2003,** 301, (5637), 1221.

27 Wold, D. J.; Frisbie, C. D., Formation of Metal-Molecule-Metal Tunnel Junctions: Microcontacts to Alkanethiol Monolayers with a Conducting AFM Tip. *J. Am. Chem. Soc.* **2000,** 122, (12), 2970.

28 Wold, D. J.; Frisbie, C. D., Fabrication and Characterization of Metal-Molecule-Metal Junctions by Conducting Probe Atomic Force Microscopy. *J. Am. Chem. Soc.* **2001,** 123, (23), 5549.

29 Wold, D. J.; Haag, R.; Rampi, M. A.; Frisbie, C. D., Distance Dependence of Electron Tunneling through Self-Assembled Monolayers Measured by Conducting Probe Atomic Force Microscopy: Unsaturated versus Saturated Molecular Junctions. *J. Phys. Chem. B* **2002,** 106, (11), 2813.

30 Cui, X. D.; Primak, A.; Zarate, X.; Tomfohr, J.; Sankey, O. F.; Moore, A. L.; Moore, T. A.; Gust, D.; Harris, G.; Lindsay, S. M., Reproducible Measurement of Single-Molecule Conductivity. *Science* **2001,** 294, (5542), 571.

31 Hong, S.; Reifenberger, R.; Tian, W.; Datta, S.; Henderson, J. I.; Kubiak, C. P., Molecular Conductance Spectroscopy of Conjugated, Phenyl-Based Molecules on Au(111): the Effect of End Groups on Molecular Conduction. *Superlattices Microstruct.* **2000,** 28, (4), 289.

32 Bumm, L. A.; Arnold, J. J.; Cygan, M. T.; Dunbar, T. D.; Burgin, T. P.; Jones, L.; Allara, D. L.; Tour, J. M.; Weiss, P. S., Are Single Molecular Wires Conducting? *Science* **1996,** 271, (5256), 1705.

33 Park, H.; Lim, A. K. L.; Alivisatos, A. P.; Park, J.; McEuen, P. L., Fabrication of Metallic Electrodes with Nanometer Separation by Electromigration. *Appl. Phys. Lett.* **1999,** 75, (2), 301.

34 Sommerfeld, A.; Bethe, H., *Handbucher der Physik*. ed. Geiger, H.; Schell, K.; Julius Springer Verlag: Berlin, 1933; 24/2.

35 Simmons, J. G., Electric Tunnel Effect between Dissimilar Electrodes Separated by a Thin Insulating Film. *J. Appl. Phys.* **1963,** 34, (9), 2581.

36 Simmons, J. G., Generalized Formula for Electric Tunnel Effect between Similar Electrodes Separated by a Thin Insulating Film. *J. Appl. Phys.* **1963,** 34, (6), 1793.

37 Stratton, R., Volt-Current Characteristics for Tunneling through Insulating Films. *J. Phys. Chem. Solids* **1962,** 23, (SEP), 1177.

38 Bardeen, J., Tunnelling from a Many-Particle Point of View. *Phys. Rev. Lett.* **1961,** 6, (2), 57.

39 Harrison, W. A., Tunneling from an Independent-Particle Point of View. **1961,** 123, (1), 85.

40 Guentherodt, H.-J.; Wiesendanger, R., *Scanning Tunneling Microscopy I : General Principles and Applications to Clean and Adsorbate-Covered Surfaces*. ed. Springer-Verlag: Berlin, New York, 1992; 1.

41 Hartman, T. E.; Chivian, J. S., Electron Tunneling through Thin Aluminum Oxide Films. **1964,** 134, (4A), 1094.

42 Hartman, T. E., Tunneling through Asymmetric Barriers. *J. Appl. Phys.* **1964,** 35, (11), 3283.

43 Abeles, B.; Sheng, P.; Coutts, M. D.; Arie, Y., Structural and Electrical Properties of Granular Metal-Films. *Adv. Phys.* **1975,** 24, (3), 407.

44 Park, J. W., Personal Communication Regarding the Thickness of Cr Adhesion Layers in Electromigration Experiments, 2003.

45 Bratkovsky, A. M.; Sutton, A. P.; Todorov, T. N., Conditions for Conductance Quantization in Realistic Models of Atomic-Scale Metallic Contacts. *Phys. Rev. B* **1995,** 52, (7), 5036.

46 Park, J. W., Personal Communication Regarding the Temperature Dependence of J-E curves. Impact of the Temperature on the J-E curves was noticed at T > 20 - 40 K, 2003.

47 Pashkin, Y. A.; Nakamura, Y.; Tsai, J. S., Room-Temperature Al Single-Electron Transistor made by Electron-Beam Lithography. *Appl. Phys. Lett.* **2000,** 76, (16), 2256.